



Provided by the author(s) and University of Galway in accordance with publisher policies. Please cite the published version when available.

Title	Computational modelling of the coupled electro-mechanical behaviour of neurons
Author(s)	Cinelli, Ilaria
Publication Date	2019-01-22
Publisher	NUI Galway
Item record	<a href="http://hdl.handle.net/10379/14852">http://hdl.handle.net/10379/14852</a>

Downloaded 2024-04-23T10:32:25Z

Some rights reserved. For more information, please see the item record link above.



# Computational Modelling of the Coupled Electro-Mechanical Behaviour of Neurons



**NUI Galway**  
**OÉ Gaillimh**

*A Thesis submitted to*  
**National University of Ireland Galway**  
*(Galway, Republic of Ireland)*

*For the Degree of*  
**Doctor of Philosophy**  
*(Structured Ph.D. Program)*

***Discipline of Biomedical Engineering, College of Engineering and Informatics***

**Dec. 2013 – Dec. 2018**

*Supervisors*

Professor Peter E. McHugh

Dr Maeve Duffy

Professor Michel Destrade

*Student*

[Ilaria Cinelli](#)

# Index

Certificate .....	6
The Author Acknowledges .....	7
Funding Acknowledgments .....	8
Abstract.....	9
List of Publications .....	11
i. First-Author Journal Publications .....	11
ii. Conference Proceeding Papers .....	11
iii. Posters.....	12
Invited Talks .....	12
List of Figures.....	14
List of Tables .....	21
Chapter 1. Introduction and Thesis Structure .....	22
1.1 Introduction.....	22
1.2 Context.....	23
1.3 Aim .....	24
1.4 Significance of the Problem and Motivation .....	24
1.5 Contribution to the Research Field .....	25
1.6 Objectives .....	27
1.7 Thesis Structure .....	27
References Chapter 1 .....	30
Chapter 2. Background.....	33
2.1 The Nervous Cell.....	33
2.2 The Hodgkin-Huxley Model.....	34
2.3 The Membrane Capacitance .....	37
2.4 Biophysical Phenomena at the Nerve Membrane .....	38
2.4.1 Electrostriction.....	39
2.4.2 Piezoelectricity.....	42
2.5 Emerging Theories about Nerve Pulses .....	43
2.5.1 The Soliton Theory .....	44
2.5.2 The Pressure Pulse Theory.....	45
2.5.3 The Mechanical Surface Waves Theory .....	46
2.6 A Modelling Perspective .....	47
2.6.1 An Overview on Brain Modelling .....	47
2.6.2 Multiscale Modelling of Neural Electrical Activity .....	48
2.6.3 Multiscale Modelling of Nerve Structures.....	51

2.7	Discussion.....	53
	References Chapter 2.....	55
Chapter 3.	Electro-Thermal Equivalent 3D Finite Element Model of a Single Neuron 62	
3.1	Introduction.....	63
3.2	Materials and Methods.....	65
3.2.1	Theory of the Equivalence .....	65
3.2.2	Neuron Structure.....	67
3.2.3	Material Properties.....	69
3.2.4	Subthreshold Model: Mesh and Boundary Conditions .....	71
3.2.5	Active Membrane Model: Mesh and Boundary Conditions .....	72
3.2.6	Equivalent Coupled Electro-Mechanical Model: Mesh and Boundary Conditions.....	73
3.3	Results.....	74
3.3.1	Subthreshold Model.....	75
3.3.2	Active Membrane Model .....	76
3.3.3	Equivalent Electro-Mechanical Coupling.....	76
3.4	Discussion.....	78
3.5	Conclusion .....	82
	References Chapter 3.....	83
Chapter 4.	Electro-Mechanical Response of a 3D Nerve Bundle Model to Mechanical Loads Leading to Axonal Injury .....	88
4.1	Introduction.....	89
4.2	Method.....	92
4.2.1	Model .....	92
4.2.2	Damage Evaluation.....	93
4.2.3	Implementation .....	94
4.2.4	Boundary Conditions .....	94
4.2.5	Validation.....	96
4.3	Results.....	98
4.3.1	Model Analysis .....	98
4.3.2	Mechanical Loading Cases of Interest.....	101
4.4	Discussion.....	104
4.5	Conclusion .....	106
	References Chapter 4.....	108
Chapter 5.	Effects of Nerve Bundle Geometry on Neurotrauma Evaluation .....	112
5.1	Introduction.....	113
5.2	Method.....	116

5.2.1	Material Properties.....	116
5.2.2	Boundary Conditions .....	117
5.3	Results.....	118
5.3.1	Pressure Loads .....	118
5.3.2	Displacement Loads.....	120
5.4	Discussion.....	127
5.5	Limitations .....	130
5.6	Conclusion .....	131
	References Chapter 5 .....	132
Chapter 6.	Electro-Mechanical Alterations in Nerve Fibres of the Human Corpus Callosum	138
6.1	Introduction.....	138
6.2	Method.....	138
6.3	Results.....	140
6.4	Limitations .....	146
6.5	Conclusion .....	147
	References Chapter 6.....	149
Chapter 7.	Head-To-Nerve Analysis of Electro-Mechanical Impairments of Diffuse Axonal Injury	151
7.1	Introduction.....	152
7.2	Method.....	156
7.2.1	Material Properties.....	156
7.2.2	Boundary Conditions .....	156
7.3	Results.....	157
7.4	Discussion.....	161
7.5	Clinical Applications .....	164
7.6	Conclusion .....	164
	References Chapter 7 .....	166
Chapter 8.	Conclusions and Recommendations .....	170
8.1	Thesis Summary .....	170
8.2	Recommendations for Future Research .....	172
8.3	Conclusions and Final Remarks.....	174
	References Chapter 8.....	176
	Appendix A.....	177
A.1.	Subthreshold Model.....	177
A.2.	Active Membrane Model .....	178
A.3.	Validation of the Active Membrane Model .....	179
	References Appendix A.....	183

Appendix B .....	184
B.1. Myelinated Fibre.....	184
B.2. Method.....	185
B. 2.1. Geometry and Material Properties .....	185
B. 2.1. Mesh.....	187
B. 2.2. Boundary Conditions .....	188
B.3. Results.....	188
References Appendix B .....	189
Appendix C.....	190
Appendix D.....	193
Appendix E .....	194
Appendix F .....	195
Acronyms.....	198

## **Certificate**

This is to certify that this thesis work entitled “*Computational Modelling of the Coupled Electro-Mechanical Behaviour of Neurons*” submitted by Ilaria Cinelli B.Eng. M.Eng. is a bona-fide thesis work carried out under the supervision and guidance of Professor Michel Destrade, Dr Maeve Duffy and Professor Peter E. McHugh.

This thesis is conformed to the standard required at the National University of Ireland Galway (Galway, Republic of Ireland) for the degree of Doctor of Philosophy. The work embodied in this thesis has not been submitted elsewhere for a degree.

## The Author Acknowledges

Years ago, I read the quote “Life is about *giving*”. So, I started to read more about *giving*.

The Ph.D. is the part of my life called *learning*. Learning for improving: knowledge, skills and Awareness. When I started my Ph.D., I knew that I had to grow for *giving*. Eventually, this was a personal and professional growth for me. Having a degree does not directly mean being capable of making a good use of the received education. Self-Awareness is what makes the difference, especially in personal development.

The topic of this thesis touches a personal story. In science, words, such as DAI, TBI and tumours, are usually used to highlight clinical applications and to keep running the business behind research. However, behind medical conditions, there are people. Not papers. Compelling (personal) reasons are what keeps the growth constant, and what add real meaning to the *giving*.

I am a very curious person with high ambitions. During my Ph.D., I have been very successful in disciplines and projects *not* related to my research here at NUIG. Fulfilment is the motivation for which I am doing more activities. It is the happiness in doing, so what add feeling to the *giving*. My greatest lessons come from my failures. And, there is no failure if there is no risk. Failures taught me the importance of: time, effective execution and vision. This is the base of the action for the *giving*. The University helps in developing technical skills, and those are needed for shaping the *giving*. Then, the significance of the *giving* is in the recognition of the *life* itself.

I am truly grateful to my Family for their support, love and understanding in these years. Truly. I am not a perfect human being, I have lot to learn. This is why I am truly grateful of being loved and love back.

So, *life* is about *giving*. And giving is *love*. The quality of the *giving* is in the integration of the different forms of *love*. As for an individual, as for Humanity. I hope to keep growing and doing research for Humanity. There is no *giving* if there is no *Life*.

I thank the National University of Ireland Galway, my Supervisors, all the Professors, lectures and all the other employees for making this journey valuable!

*Ilaria Cinelli*

Email: [i\\_cinelli@yahoo.it](mailto:i_cinelli@yahoo.it)

ORCID ID: <https://orcid.org/0000-0003-1302-1188>

## **Funding Acknowledgments**

The author gratefully acknowledges funding from the Galway University Foundation, the Biomechanics Research Centre and the Power Electronics Research Centre, College of Engineering and Informatics of the National University of Ireland Galway (Galway, Republic of Ireland).

## Abstract

Recent experimental evidence has uncovered complex biophysical phenomena accompanying the electrical activity of nervous cells. Now emerging theories refer to the electric pulse, i.e. the Action Potential (AP), as an electro-mechanical phenomenon, highlighting its multi-disciplinary nature.

Due to its complexity, a unified theory explaining the multiphysics behind neural electrical activity has not yet appeared in the literature. Thus, neural electrical activity and its associated mechanics are frequently studied independently.

This work aims at broadening the understanding of electro-mechanical neural activity in relation to brain injuries. Focus is given to injuries that initiate Diffuse Axonal Injury (DAI), a progressive pathogenesis that induces damage at the cellular level.

The work performed in this thesis proposes a coupled 3D electro-mechanical modelling framework to investigate the interaction between neural electrical activity and neural structural mechanics in finite element analysis, considering DAI-induced electrical changes following brain injury.

This work is based on a novel approach for simulating the interdependence of multi-domain phenomena, where electrical conduction is implemented through the use of electro-thermal equivalences, as the most appropriate and computationally efficient way to couple the electrical and mechanical domains in finite element analysis.

The nerve modelling framework developed in this thesis is capable of simulating the real-time electro-mechanical phenomena of electrostriction and piezoelectricity, and their effects on the AP, which have been observed experimentally in the nerve membrane. It includes a modulated threshold for activation of the AP and independent alteration of the neural electrical properties as a function of (elastic and plastic) strain, voltage, space and time. This modelling approach is assessed and validated against experimental observations and data from the literature.

A multiscale approach is then taken to investigate brain injury, by linking the nerve modelling framework at the *microscale* with a structural mechanics model of the head at the *macroscale* that is capable of simulating head impacts. The combined use of these models replicates both the neural micro-electro-mechanical environment and the brain macro-mechanical environment.

The work considers the electro-mechanical behaviour of nerve fibres and fibre bundles, both with and without a myelin layer. The results of the simulations indicate that the structure of the nerve fibre is critically important in determining its electro-mechanical behaviour. Results also show that the insulating layer around myelinated fibres plays an important mechanical role during loading, by redistributing plastic strains within the nerve,

and protecting the fibre from mechanical failure and electrophysiological impairments. Additionally, an analysis of the electro-mechanical behaviour in fibres of different calibre and type, reveals that disconnection is more likely to occur in fibres with large diameters because of elastic strains, while plastic strains seem to affect unmyelinated fibres with small calibre to a greater extent.

The work reported in this thesis may contribute to the advancement of computational neuro electro-mechanics, leading to an enhancement in the understanding of the link between mechanical and electrical phenomena. It has also generated further insights into the electro-mechanical effects of nerve trauma due to brain injury that could have implications for improving the diagnosis and treatment of DAI. In the long-term, this modelling approach could also be used for studying communication between dendritic cells to aid the understanding of the alteration of neural networks as a result of injury or disease.

## List of Publications

### i. First-Author Journal Publications

Cinelli, I., M. Destrade, M. Duffy, and P. E. McHugh. 2017. “Electro-thermal equivalent 3D Finite Element Model of a Single Neuron”, IEEE Transactions on Biomedical Engineering, DOI 10.1109/TBME.2017.2752258, <http://ieeexplore.ieee.org/document/8038069/>

Cinelli, I., M. Destrade, M. Duffy, and P. E. McHugh. 2017. “Electro-Mechanical Response of a 3D Nerve Bundle Model to Mechanical Loads Leading to Axonal Injury”, International Journal for Numerical Methods in Biomedical Engineering, DOI 10.1002/cnm.2942 <http://onlinelibrary.wiley.com/doi/10.1002/cnm.2942/abstract#>

Cinelli, I., M. Destrade, P. E. McHugh, and M. Duffy. 2017. “Effects of Nerve Bundle Geometry on Neurotrauma Evaluation”, International Journal for Numerical Methods in Biomedical Engineering, [online] 34(April), pp.517–520. Available at: <https://onlinelibrary.wiley.com/doi/abs/10.1002/cnm.3118>

Cinelli, I., Destrade, M., McHugh, P., Trotta, A., Gilchrist, M., and Duffy, M. 2018. Head-to-nerve analysis of electromechanical impairments of diffuse axonal injury. Biomechanics and Modeling in Mechanobiology. <https://doi.org/10.1007/s10237-018-1086-8>

### ii. Conference Proceeding Papers

Cinelli, I., M. Destrade, M. Duffy, and P. McHugh, 2017 “Neurotrauma Evaluation in a 3D Electro-Mechanical Model of a Nerve Bundle”, in Neural Engineering (NER), 2017 8th International IEEE/EMBS Conference on, DOI 10.1109/NER.2017.8008402, <http://ieeexplore.ieee.org/document/8008402/>

Cinelli, I., M. Destrade, M. Duffy, and P. McHugh. 2017 “Effects of Nerve Bundle Geometry on Neurotrauma Evaluation“, in Neural Engineering (NER), 2017 8th International IEEE/EMBS Conference on, DOI 10.1109/NER.2017.8008403, <http://ieeexplore.ieee.org/document/8008403/>

Cinelli, I., M. Destrade, M. Duffy, and P. McHugh. 2017. “Electro-Mechanical Response of a 3D Nerve Bundle Model to Mechanical Loads Leading to Axonal

Injury” Engineering in Medicine and Biology Society (EMBC), 2017 39th Annual International Conference of the IEEE, DOI 10.1109/EMBC.2017.8036989, <http://ieeexplore.ieee.org/document/8036989/>

Cinelli, I., M. Duffy, and P. E. McHugh. 2015. “Thermo-Electrical Equivalents for Simulating the Electro-Mechanical Behaviour of Biological Tissue”, Engineering in Medicine and Biology Society (EMBC), 2015 37th Annual International Conference of the IEEE, DOI 10.1109/EMBC.2015.7319263, <http://ieeexplore.ieee.org/document/7319263/>

Cinelli, I., Duffy, M., and McHugh, P. (2015). Thermo-electrical equivalents for simulating the electro-mechanical behavior of biological tissue. In IEEE (Ed.), *Proceedings of the Annual International Conference of the IEEE Engineering in Medicine and Biology Society*, EMBS (Vol. 2015–November, pp. 3969–3972). Milan: IEEE. <https://doi.org/10.1109/EMBC.2015.7319263>

### **iii. Posters**

Cinelli, I., M. Duffy, and P. E. McHugh, “Thermo-Electrical Equivalences in a Mixed Fibre Bundle”, Engineering in Medicine and Biology Society (EMBC), 2016 38th Annual International Conference of the IEEE

Cinelli, I., M. Duffy, and P. E. McHugh, “Finite Element Modelling of Electro-Mechanical Coupling in Nerves”, Engineering in Medicine and Biology Society (EMBC), 2016 38th Annual International Conference of the IEEE

### **Invited Talks**

Cinelli, I., M. Destrade, M. Duffy, and P. McHugh, “Neurotrauma Evaluation in a 3D Electro-Mechanical Model of a Nerve Bundle” Engineering in Medicine and Biology Society (EMBC), 2017 39th Annual International Conference of the IEEE, *Modelling of Modern Devices and Technologies with Computational Human Phantoms Panel*.

Cinelli, I., M. Destrade, M. Duffy, and P. McHugh, “Permanent Electro-Mechanical Changes in a 3D Model of a Nerve Bundle,” Engineering in Medicine and Biology Society (EMBC), 2017 39th Annual International Conference of the IEEE, *Modelling of Modern Devices and Technologies with Computational Human Phantoms Panel*.

Cinelli, I., M. Duffy, and P. McHugh, “Electro-thermal equivalent implementation of the Cable Equation in nerve bundles”, *6<sup>th</sup> Postgraduate Research Day NUI-Galway-UL Alliance, Final Best PhD thesis*, [https://nuigulresearchday2016.files.wordpress.com/2016/04/nuigul-2016\\_paper\\_106.pdf](https://nuigulresearchday2016.files.wordpress.com/2016/04/nuigul-2016_paper_106.pdf)

Cinelli, I., M. Duffy, and P. McHugh, “Thermo-electrical equivalents for simulating the electro-mechanical behaviour of biological tissue”, *5<sup>th</sup> Postgraduate Research Day NUI-Galway-UL Alliance, Final Best PhD thesis*, [https://nuigulresearchday2015.files.wordpress.com/2015/04/nuigul-2015\\_submission\\_9.pdf](https://nuigulresearchday2015.files.wordpress.com/2015/04/nuigul-2015_submission_9.pdf)

## List of Figures

<b>Fig. 2.1</b> Figure reprinted from 2002 Encyclopaedia Britannica, Inc., showing unmyelinated and myelinated axons.....	34
<b>Fig. 2.2</b> Electrical circuit representing the nerve membrane. Conductances are $GNa$ , $GK$ and $Gl$ [ $mS\ cm^{-2}$ ]; membrane voltage, $V$ [ $mV$ ]; intracellular medium voltage, $Vi$ [ $mV$ ]; extracellular medium voltage, $Ve$ [ $mV$ ]; ionic potential drop $VNa = -115\ mV$ , $VK = 12\ mV$ and $Vl = -10.63\ mV$ ; ionic currents ( $INa$ , $IK$ , $Il$ and $Ic$ [ $mA\ cm^2$ ]); membrane current, $Im$ ; membrane capacity per unit area, $Cm$ , equal to $1\ \mu F\ cm^2$ (Hodgkin and Huxley, 1952). Figure reprinted and adapted from (Plonsey and Malmivuo, 1995). .....	35
<b>Fig. 2.3</b> Sodium and potassium conductance ( $GNa$ and $GK$ ), their sum ( $Gm$ ), and the membrane voltage ( $V$ ) during a propagating nerve impulse. Here, the membrane resting potential is $Vr$ , and is equal to $-65\ mV$ . Figure reprinted and adapted from (Plonsey and Malmivuo, 1995). .....	37
<b>Fig. 2.4</b> Biological membranes, especially nerve membrane, have similar electrical properties to those exhibited by parallel-plate capacitors. In (a), a parallel-plate capacitors and, in (b), the nerve membrane. In both cases, the two conductive layers are separated by a non-conductive medium. Figure reprinted from www.PhysiologyWeb.com. ....	38
<b>Fig. 2.5</b> Electrostriction effects upon charging the membrane capacitor. A force generated by an applied potential difference, $\Psi$ , compresses the membrane layer which reaches a state with larger area, $A$ , and smaller thickness, $d$ . Figure reprinted from (Mosgaard et al., 2015). .....	40
<b>Fig. 2.6</b> On the top, capacitive susceptibility, $Cm$ , as a function of voltage. The shaded area indicates the excess charge of the voltage-induced transition. The dashed line is the voltage dependent capacitance, $Cm$ . On the bottom, the changes in membrane thickness and area. Figure reprinted from the paper (Heimburg, 2012). .....	42
<b>Fig. 2.7</b> Thickness changes of a squid axon during the AP as a function of time (solid line). The dashed line represents the voltage change. Figure reprinted from (Heimburg et al., 2014). .....	43
<b>Fig. 2.8</b> The pressure pulse manifests itself as an increase in the axon diameter, associated membrane area expansion, and radial contraction. Figure reprinted from the paper (Rvachev, 2010). .....	46
<b>Fig. 2.9</b> A nerve fibre in which the AP is an electromechanical pulse traveling along the axon. In orange, the changes in potential. Figure reprinted from (El Hady and Machta, 2015). .....	46
<b>Fig. 2.10</b> Temporal and spatial scales of organization in the nervous system. The proper spatial scale of “Cognition and Behaviour” depends on how it is being viewed and modelled. Scale overlap can be seen by noting that dendrite, cell and column share scale in both time and space, reflecting the fact that the same neural signals are being processed at these different levels. Figure reprinted from (Lytton et al., 2017). .....	49
<b>Fig. 2.11</b> Overview of the presented modelling methods and mathematical tools for brain dynamics. Figure reprinted from (Siettos and Starke, 2016). .....	50
<b>Fig. 2.12</b> Inertial loads of the head lead to the shearing of brain tissue. At the cellular level, this shearing of brain tissue results in the stretching of neural axons which is thought to be one of the primary injury mechanisms of DAI. Figure reprinted from web3MD.com. ....	52
<b>Fig. 3.1</b> In (a), a schematic illustration of the unmyelinated nerve and myelinated nerve. The ECM, membrane and ICM are highlighted. The length of the fibre is $l$ . The radius of a nerve fibre from the ICM to the ECM is $a_{Fibre}$ . In (b), frontal and lateral views of the mesh of the 3-layer cylindrical model of the nervous cell with $500\ \mu m$ length are shown. The ICM and membrane radii are $a_{ICM}$ and $a_M$ respectively. The membrane and ECM	

thicknesses are  $bM$  and  $bECM$ , respectively. In (b), the 3-layer axisymmetric model of the membrane. Underneath, the 3-layer axisymmetric models of squid giant axon, crab nerve fibre and garfish olfactory nerve fibre with diameters equal to  $500 \mu m$  (Hodgkin and Huxley, 1952; Rall, 1977),  $30 \mu m$  (Hille, 1977) and  $0.25 \mu m$  (Easton, 1971) respectively. .... 69

**Fig. 3.2** Flowchart of the code describing the active behaviour of the nerve's membrane: on the left the HH dynamics (Hodgkin and Huxley, 1952) and on the right the 1-way coupled HH dynamics. Here, a Gaussian voltage distribution elicits the AP in a 3D model of a nervous cell. By using electro-thermal equivalences, the HH dynamics are implemented as an equivalent thermal process, in which the membrane's conductivity changes as in (Hodgkin and Huxley, 1952) and the capacitance,  $Cm$ , changes as in (Alvarez and Latorre, 1978). .... 75

**Fig. 3.3** Voltage boundary condition. (a) Spatial variation of the membrane voltage  $V$ , here NT11, in steady state ( $\omega = 0$ ) is shown for  $n = 2$  (Tahayori et al., 2012), see Eq. 3.6. The azimuthal coordinate is  $\theta$ . In (b), the voltage distribution in the axial direction at the membrane layer, at  $x = 1 \mu m$ ,  $y = 0 \mu m$ , from  $z = 0 \mu m$  to  $z = 5 \mu m$  of the 3 layer cylinder model. Here  $V2 = 20 nVm$  and  $s = 1 \mu m$  (Tahayori et al., 2012), see Eq. 3.6 - Eq. 3.8. .... 76

**Fig. 3.4** Voltage clamp procedure with  $80 mV$  clamped voltage, (a), and generated ionic currents in (b). Space clamp procedure and  $18 mA cm^{-2}$  current stimulus of  $0.2 ms$  (c) and generated ionic currents in (d). .... 78

**Fig. 3.5** Quantitative comparison with three experimentally favoured systems of garfish olfactory nerve (column a), crab nerve (column b) and squid giant axon (column c) using model and parameters as described in the text. Columns (a)-(c) present the spatial distribution of the voltage and mechanical responses for the three different cases. Column (d) shows the time dependency of the mechanical features for the squid giant axon case only. The results refer to the 1-way coupling of the HH model. The results are taken in the middle of the membrane layer at  $y = 0$ , where the  $y$ -axis is the axis of symmetry of the model and the  $x$ -axis is the radial distance. For each case, the width of the AP is taken from the experimental literature (El Hady and Machta, 2015). Displacement, strain and stress are taken in the radial direction. In (d), stresses and strains are estimated using different Young's Moduli, refer to Case I (Alvarez and Latorre, 1978; El Hady and Machta, 2015) and Case II (Abolfathi et al., 2009). .... 80

**Fig. 4.1** (a): frontal view and (b): isometric view of the 3-layer nerve bundle, made of four fibres. Fibre #3 is the active fibre, i.e. the fibre activated by a Gaussian voltage distribution (El Hady and Machta, 2015). Fibres #1, #2 and #4 are activated by the charges diffusing from Fibre #3. (c): the ECM; (d): the membrane; (e): the ICM. In the case of myelinated fibres, the membrane layer is periodically-partitioned along the fibre length to model the insulation sheath of the myelin layer, see (d.1), and the Ranvier node, see (d.2). The myelin layer length is  $1 \mu m$  and the Ranvier's node length is  $2 \mu m$ , while the radial thickness of the layer is equal to  $3 \mu m$  (Cinelli et al., 2017d, 2017c, 2015a; Einziger et al., 2005). .... 93

**Fig. 4.2** Flowchart of the code describing the active behaviour of the nerve's membrane: on the left, the HH dynamics (Hodgkin and Huxley, 1952) and on the right, the fully coupled HH dynamics (or 2-way coupling). Here, a Gaussian voltage distribution elicits the AP in a 3D model of a nervous cell. By using electro-thermal equivalences, the HH model is implemented as an equivalent thermal process, in which the membrane's conductivity changes as in (Hodgkin and Huxley, 1952) and the capacitance,  $Cm$ , changes as in (Alvarez and Latorre, 1978). The HH parameters are changing based on the temperature (which is the equivalent quantity of voltage (Cinelli et al., 2017d)) and strain at the membrane (Jérusalem et al., 2014). The strain  $\epsilon$  generated in the model is a function

of temperature,  $T$ , and thermal expansion coefficients, see Eq. 3.4 and Eq. 4.1. Voltage, current, strain and stresses distribution are only a few of the 3D results released by Abaqus by equivalence. In Chapter 4 plasticity is not included; in Chapter 5 the analysis includes isotropic plasticity..... 95

**Fig. 4.3** (a) the membrane's potential in Case I, AP ( $LS = 0mV$ ;  $AC = 0$ ); Case II, damaged traumatized membrane ( $LS = 20mV$ ;  $AC = 1$ ). In \*, the reversal ionic potentials have constant values as in (Boucher et al., 2012), and, in \*\*, they change according to equation Eq. 4.1, as in (Jérusalem et al., 2014). In (b), the Current Density [ $A/\mu m^2$ ] on Fibre #3 for the cases considered..... 99

**Fig. 4.4** (a): mechanical displacement of the unmyelinated nerve membrane; (b): displacement of a myelinated nerve membrane of the Fibre #3 in the four cases considered (see text) along the radial direction in the bundle (i.e. the  $x - axis$ ),  $Ux$  ..... 100

**Fig. 4.5** Frontal and isometric views of the total displacement [ $\mu m$ ] in (a) an unmyelinated and (e) a myelinated nerve bundle model. In (b) and (f), the ECM; in (c) and (g), the ICM of the two bundle types. In (d), the isometric view of the nerve membrane and, in (h), the Ranvier nodes and the myelin sheath of the myelinated bundle. (a)-(d) and (e)-(h) are Case II (\*\*) (Jérusalem et al., 2014) applied to an unmyelinated and myelinated nerve bundle. Data are taken at the peak of the membrane potential in both cases..... 100

**Fig. 4.6** (a) Membrane Potential [ $mV$ ] and (b) Current Density [ $A\mu m^2$ ] on Fibre #3 in the unmyelinated bundle under mild ( $25kPa$ ), moderate ( $68kPa$ ) and severe ( $192kPa$ ) pressures (Hosmane et al., 2011). The extreme case of  $P = 1GPa$  is also considered.  $AC$  is the fraction of affected ionic channels by the strain:  $AC = 0$  is for an intact membrane and  $AC = 1$  for a traumatized membrane (Boucher et al., 2012). Data are the maximum radial displacement of a node on Fibre #3. .... 102

**Fig. 4.7** Radial displacement [ $nm$ ] of (a) an unmyelinated bundle and (b) a myelinated bundle. Uniform applied pressures are classified as mild ( $25kPa$ ), moderate ( $68kPa$ ) and severe ( $192kPa$ ) pressures (Hosmane et al., 2011). Data are the maximum radial displacement of a node on Fibre #3 in both cases..... 103

**Fig. 4.8** (a)-(b) Membrane Potential [ $mV$ ] and (c)-(d) Current Density [ $A\mu m^2$ ] on Fibre #3 in the unmyelinated bundle and myelinated bundle, respectively, under 5% and 14% of total deformation  $\epsilon$  applied (Bain and Meaney, 2000).  $AC$  is the fraction of affected ionic channels by the strain:  $AC = 0$  is for an intact membrane and  $AC = 1$  for a traumatized membrane (Boucher et al., 2012). Data are taken at the maximum displacement along the bundle middle axis, i.e.  $z - axis$ , on Fibre #3. .... 104

**Fig. 4.9** Voltage distribution ( $NT11$ ) in an unmyelinated nerve bundle, in (a)-(d), and in a myelinated nerve bundle, in (e)-(h), for 5% elongation. Frontal and isometric view of an unmyelinated and myelinated nerve bundle model in (a) and (b), respectively. In (b) and (f), the ECM, in (c) and (g) the ICM of the two bundle types. In (d), the isometric view of the nerve membrane and, in (h), the Ranvier nodes and the myelin sheath of the myelinated bundle. .... 105

**Fig. 5.1** (a) Membrane Potential [ $mV$ ] on Fibre #3 in a small unmyelinated bundle (SBUN). (c)-(e) Radial displacement [ $nm$ ],  $Ux$ , of a SBUN and an unmyelinated big bundle (BBUN). (b) Membrane Potential [ $mV$ ] on Fibre #3 in a small myelinated bundle (SBMY). (d)-(f) Radial displacement [ $nm$ ],  $Ux$ , of SBMY and a myelinated big bundle (BBMY). The uniform applied pressures are classified as mild ( $25kPa$ ) and severe ( $192kPa$ ) pressures (Hosmane et al., 2011). Data are the maximum radial displacement of a node on Fibre #3 in both cases..... 118

**Fig. 5.2** Voltage distribution ( $NT11$ ), at the AP peak, in (a) SBUN, (b) SBMY, (c) BBUN and (d) BBMY for  $25kPa$  pressure with  $AC = 0$ . The box shows the membrane layer of each model. .... 121

**Fig. 5.3** (a)-(b) Membrane Potential [ $mV$ ] on Fibre #3 in SBUN and SBMY, under 5% to 60% of elongation (Bain and Meaney, 2000). The load is applied from 2 ms to 67 ms, only.  $AC$  is the fraction of affected ionic channels by the strain:  $AC = 0$  is for an intact membrane and  $AC = 1$  for a traumatized membrane (Boucher et al., 2012). Data are taken at the maximum displacement along the bundle middle axis, i.e.  $z - axis$ , on Fibre #3. .... 123

**Fig. 5.4** (a), (c) show the peak values of the membrane potential [ $mV$ ] in the SB and BB, respectively. (b), (d) show the maximum values of the maximum principal plastic strain ( $PEz$ ) at the node of interest, along the bundle axis. Data are taken on Fibre #3 at the node at which the displacement along the bundle axis is maximum. Displacement boundary conditions are equal to 5%, 14%, 25%, 30% and 60%. In BB, failure occurs at 60% applied displacement..... 124

**Fig. 5.5** (a), (c) show the peak values of the membrane potential [ $mV$ ] found on Fibre#3, in the SB and BB, respectively. In (b), (d), the maximum value of the total strain ( $ETot$ ) is the maximum found on Fibre#3. Displacement boundary conditions are equal to 5%, 14%, 25%, 30% and 60%. In BB, failure occurs at 60% applied displacement. .... 126

**Fig. 5.6** Isometric view of (a) SBUN and (b) SBMY for 60% elongation; and, (c) BBUN and (d) BBMY for 30% elongation with  $AC = 0$ . Data are taken at the peak of the AP. NT11 is the equivalent voltage variable in [ $V$ ]. The box shows the membrane layer of each model. .... 127

**Fig. 6.1** Diagram of the HCCMY. In (a), the HCCMY is made of repeated units of myelin sheath with length equal to 750  $\mu m$ , separated by the Ranvier's Node regions with length equal to 1.5  $\mu m$  (not drawn to scale). The four fibres are surrounded by the extracellular medium (EC). Here, we assumed that the fibres are parallel and identical. Thanks to the symmetry, the coloured part is the part modelled in Abaqus. In (b), a section of a fibre of the HCCMY. The intracellular medium (ICM) radius is 0.5  $\mu m$ , the nerve membrane (NM) thickness is 3 nm, and the myelin sheath thickness is 90 nm. The darker grey part of the nerve membrane section is pure resistive material, while the light grey part is the Ranvier's Node region where the Action Potential can be elicited. .... 139

**Fig. 6.2** The HCCMY is long 375.75  $\mu m$ , see (a), and has a diameter of 2.96  $\mu m$ , see (b). The myelin sheath is 375  $\mu m$  while the Ranvier's node is 0.75  $\mu m$ . In (c), a side of the HCCMY is shown, made by a 15  $\mu m$  long myelinated section and a 0.75  $\mu m$  is shown. In (d), the myelin and the membrane nodes are shown without the extracellular medium around. Then, (e) shows the membrane layer, where the active part, i.e. the Ranvier's Node, has a length equal to 0.75  $\mu m$ , see (f)..... 140

**Fig. 6.3** Data are nodal quantities when displacement boundary conditions (from 5 % to 30 %) are applied at the small myelinated bundle (SBMY) and the human corpus callosum bundle (HCCMY) with  $AC=0$  and  $AC=1$ . Data are taken on Fibre #3 at the node at which the displacement along the bundle axis is maximum. (a) shows the peak values of the membrane potential [ $mV$ ] at the node. Then, (b) shows the maximum principal value of the plastic strain [%], and, in (c), the total strain at the node of interest, along the bundle axis..... 141

**Fig. 6.4** Data are the maximum quantities of Fibre #3 when displacement boundary conditions (from 5 % to 30 %) are applied at the small myelinated bundle (SBMY) and the human corpus callosum bundle (HCCMY) with  $AC=0$  and  $AC=1$ . (a) shows the peak values of the membrane potential [ $mV$ ] on Fibre #3. Then, (b) shows the maximum principal value of the plastic strain [%], and, in (c), the total strain on Fibre #3. .... 142

**Fig. 6.5** Isometric view of the small bundle model made by myelinated fibres under 30% applied deformation. The voltage distribution [ $V$ ] is taken at the peak of the membrane potential with  $AC=0$  in (a)-(b), and  $AC=1$  in (c)-(d). .... 143

**Fig. 6.6** The HCCMY is shown at the peak of the membrane potential when a 30% displacement boundary conditions is applied with  $AC=0$ . In (b), the frontal and back view of the HCCMY. In (c), a section of the HCCMY including the myelin and the Ranvier's Node. In (d), the myelin and the Ranvier's node without the extracellular medium and intracellular medium. In (e), the membrane section, where the conductive part, the Ranvier's node, is shown in (f)..... 144

**Fig. 6.7** The HCCMY is shown at the peak of the membrane potential when a 30% displacement boundary conditions is applied with  $AC=1$ . In (b), the frontal and back view of the HCCMY. In (c), a section of the HCCMY including the myelin and the Ranvier's Node. In (d), the myelin and the Ranvier's node without the extracellular medium and intracellular medium. In (e), the membrane section, where the conductive part, the Ranvier's node, is shown in (f)..... 145

**Fig. 6.8** The maximum principal of the total strain,  $ETot$ , the total plastic strain,  $PETot$ , and the thermal strain through the membrane thickness,  $THEr$ , of the HCCMY are plotted against the applied strain. These values refer to Fibre #3..... 146

**Fig. 7.1** The UCD Head Model (Horgan and Gilchrist, 2003, 2004): in (a), the face, scalp, cortical and trabecular bone, and cephalic fluid; in (b), gray matter, white matter, cerebellum and brain stem. .... 155

**Fig. 7.2** Variation in the maximum principal value of the nominal strains [%] in the Head Model vs. the speed impact values,  $v$  [ $m/s$ ], used in the frontal head impacts of the Head Model. Linear regression fit also included. .... 157

**Fig. 7.3** (a)-(c) the Head Model (Horgan and Gilchrist, 2003, 2004) and in (d)-(i) the Nerve Bundle Model. The head impacts the floor at 7.5 m/s, in (a), and, at the instant of contact with the floor, maximum principal nominal strains are shown for the cerebellum, see (b), and white matter regions of the Head Model, see (c). A displacement boundary condition is applied to the Nerve Bundle Model with magnitude determined from the maximum value of the strain found in the white matter, see (c), for the same case of impact. The voltage (NT11) is shown during elongation, at the peak of the membrane potential. The voltage distribution is shown for: BBUN (d), BBMY (e), SBUN (f) and SBMY (g). In (h) and (i) a representation of the mesh and geometry of SB and BB used in this work. The maximum value of each contour plot is reported here in brackets for clarity. For the Head Model the maximum of the nominal strain is **12.02**, for the cerebellum is **0.5319**, and for the White Matter is **48.71**. Then, peak of the voltage in the BBUN is **-1.320 mV**, for the BBMY is **0.2905 mV**, for the SBUN **-1.309 mV** and for the SBMY is **-4.016 mV**. ..... 158

**Fig. 7.4** Variation in the maximum principal value of the plastic strains [%] in the Nerve Bundle Model, read at the nerve membrane, vs. the maximum principal value of the nominal strains [%] in the Head Model for (a) SBUN, (b) SBMY, (c) BBUN and (d) BBMY. Regression fits also included..... 160

**Fig. 7.5** The membrane potential peak [mV], read at the nerve membrane, vs. the maximum principal value of the nominal strains [%] found in the Head Model; (a) and (c) show the potential values during elongation, while (b) and (d) show the potential values after elongation. On the top, (a) and (b), are for the membrane potential peak, read on Fibre#3. On the bottom, (c) and (d), are for the membrane baseline..... 161

**Fig. A. 1** Current boundary condition. (a) Spatial variation of the membrane voltage  $V$ , here NT11, in steady state ( $\omega = 0$ ) is shown for  $n = 2$  (Tahayori et al., 2012). In (b), the voltage distribution in the axial direction at the membrane layer, at  $x = 1\mu m$ ,  $y = 0\mu m$ , from  $z = 0\mu m$  to  $z = 50\mu m$ . Here  $J2 = 5000\mu A/m$  and  $s = 10\mu m$  (Tahayori et al., 2012), see Eq. 3.6 and Eq. 3.7..... 177

<b>Fig. A. 2</b> Normalized voltage taken at membrane, with voltage and current boundary along the $z$ –axis of the nerve cell model with membrane thicknesses equal to <b>3, 5, 7 and 10 nm</b> . .....	179
<b>Fig. A. 3</b> Voltage clamp procedure with <b>60 mV</b> (from (a) to (e)) and <b>80 mV</b> (from (f) to (l)) clamped voltage. The results are shown for clamped voltage as input in (a) and (f); the dynamics of gating activation (no units) in (b) and (g); sodium and potassium conductance in (c) and (h); sodium, potassium and membrane currents in (d) and (i); and capacitive current in (e) and (j). Currents are in [ <b>mAc<sub>m</sub>2</b> ]. .....	181
<b>Fig. A. 4</b> Space clamp procedure with 6 (from (a) to (e)) and <b>18 mA cm – 2</b> (from (d) to (j)) current stimulus of <b>0. 2 ms</b> each. The results are shown for current stimulus as input in (a) and (f); the dynamics of gating activation (no units) in (b) and (g); sodium and potassium conductance in (c) and (h); sodium, potassium and membrane currents in (d) and (i); and capacitive current in (e) and (j). Currents are in [ <b>mAc<sub>m</sub>2</b> ]. .....	182
<b>Fig. B. 1</b> Cross sections of a general representation of myelinated (Einzigler et al., 2005) and unmyelinated (Cinelli et al., 2015c) fibre, respectively in (a) and (b). The periodic black sections in (a) along the length of the fibre (z-axis) are the myelinated units, instead the region with maximum conductivity are labelled with <b>Lr</b> , see (a) and (b). Here <b>Lp = 1</b> and its width is <b>Lr = 0. 002</b> (Einzigler et al., 2005). The radius of the neurite (axoplasm and central section) is indicated with the letter <i>a</i> . .....	186
<b>Fig. B. 2</b> In (a) and (b), a general and a focus view of the 4-layers MNM and 3-layers M-MNM. In the MNM, the myelin sheath is a solid part with periodic profile around the membrane, instead in the M-MNM the central sections have been partitioned at regularly space intervals with conductive and isolating properties. ....	187
<b>Fig. B. 3</b> In (a) a focus view of the normalized transmembrane potential over <b>5 μm</b> of the whole fibre length for the MNM, A-MNM and M-MNM. The results are compared with the analytical solution for a point source (Einzigler et al., 2005). In (b) and (c) the contour plots of voltage and current density in the M-MNM in the central section. ....	188
<b>Fig. C. 1</b> Variation in the maximum principal value of the plastic strains [%] in the Nerve Bundle Model, read at the nerve membrane, vs. the speed impact values, <b>v</b> [m/s], used in the frontal head impacts of the Head Model. Regression fits are also shown; the fits refer to SBUN, SBMY, BBUN and BBMY in (a) to (d), respectively. ....	191
<b>Fig. C. 2</b> The membrane potential peak [mv], read at the nerve membrane, vs. the speed of impact values, <b>v</b> [m/s] used in the Head Model; (a) and (c) show the potential values during elongation, while (b) and (d) show the potential values after elongation. On the top, (a) and (b), are for the membrane potential peak, read on Fibre#3. On the bottom, (c) and (d), are for the membrane baseline. ....	192
<b>Fig. D. 1</b> (a)-(e) selecting the region of interest. In (a), isometric view of the Small Myelinated Bundle (SBMY); in (b), the membrane section that includes the myelin layer and the membrane nodes; in (c), the membrane nodes, and in (d) the membrane nodes of the active fibre, Fibre#3. (e)-(g) extracting nodal quantities when displacement boundary conditions are applied. In (e)-(f), the active membrane nodes at the membrane peak where the maximum refers to the maximum displacement along the <b>z – axis</b> . In (g), the voltage [V] at the node of interest where the displacement is maximum. Here, (e)-(g) refer to a <b>30 %</b> applied deformation with <b>AC = 0</b> . ....	193
<b>Fig. E. 1</b> Data collection procedure: extracting nodal quantities when displacement boundary conditions are applied at the Ranvier’s node regions of HCCMY. In (a) and (d) the displacement along the <b>z – axis</b> in the Ranvier’s node regions, in (b) and (e) an isometric view of the active node on Fibre #3. In (c) and (f) the voltage [V] distribution on the active node. ....	194

**Fig. F. 1** Data refer to the node at the nerve membrane that undergoes maximum displacement during elongation. (a) show the nodal potential, (b) the max principal value of the total plastic strain, ***PEtot.***, and axial strain, ***PEz.***, and (c) the thermal strains through the nerve membrane thickness. .... 196

**Fig. F. 2** Data refer to the maximum found at the nerve membrane during elongation. (a) show the membrane potential, (b) the max principal value of the total plastic strain, ***PEtot.***, and axial strain, ***PEz.***, and (c) the total strain, ***Etot.*** ..... 197

## List of Tables

<b>Table 2.1</b> Dynamics of gating activation for sodium, potassium and leak ions (Hodgkin and Huxley, 1952).....	36
<b>Table 3.1</b> Electrical-Thermal Equivalences .....	67
<b>Table 3.2</b> Material Electrical Properties.....	71
<b>Table 5.1</b> Displacement peak and strain on Fibre#3 when compression is applied. ....	120

# Chapter 1. Introduction and Thesis Structure

This chapter summarises the context and motivation for the work presented in the thesis. It also presents the objectives and the structure of the thesis.

## 1.1 Introduction

Thanks to recent progress in technology, experimental studies now report evidence of the multiphysical nature of many phenomena occurring in our body, for example in the case of nervous cells (Mueller and Tyler, 2014).

Recent experimental evidence has brought to light important multiphysical phenomena in nervous cells (El Hady and Machta, 2015; Mosgaard et al., 2015; Mueller and Tyler, 2014) that are not included in the Nobel Prize biophysically-based model of Hodgkin and Huxley (HH) (Hodgkin and Huxley, 1952), that describes neural electric activity. As a result, neural activity is no longer thought to be an electrical phenomenon only, but rather an electro-thermo-mechanical phenomenon (El Hady and Machta, 2015; Mosgaard et al., 2015; Mueller and Tyler, 2014).

Thanks to the growing interest in understanding the complexity of neural activity, different theories have emerged to describe the multiphysical phenomena of nervous cells, including the soliton theory (Heimburg and Jackson, 2005) and the axoplasmic pressure pulse theory (Rvachev, 2010). However, up to now, the electro-mechanical features of neural electrical activity have not yet been described by an exhaustive theory, that is capable of explaining the full range of experimental data generated thus far.

The experimental literature discusses the importance of including these phenomena in future studies, and reports attempts to describe aspects of the multi-domain complexity of the neural activity (El Hady and Machta, 2015; Heimburg and Jackson, 2005; Heimburg et al., 2014; Mosgaard et al., 2015; Mueller and Tyler, 2014).

Against this backdrop, the work of this thesis is concerned with neural electro-mechanical phenomena and, in particular, is focused on the development of a computational modelling framework capable of representing electro-mechanical *coupling* in nervous cells, and on the use of this modelling framework to assess the effects of brain injuries on nervous cells. This work is a computational study carried out in finite element analysis with Abaqus CAE 6.13-3.

## 1.2 Context

A head injury is any sort of injury that occurs to the brain, skull or scalp, while a brain injury refers to injury that cause alterations of the brain function, as neurological dysregulation (Tse et al., 2015). However, brain injury and head injury are often interchangeable terms as it is not trivial to make a clear distinction between injuries to the brain or to the skull only (McAllister, 2011; Tse et al., 2015).

Traumatic brain injury (TBI), a type of brain injury, is an insult to the brain, caused by external physical force, that may lead to altered state of consciousness, resulting in a permanent or temporary impairment of cognitive, physical and psychological functions (Jérusalem et al., 2014; McAllister, 2011; Stocchetti et al., 2008; Wright and Ramesh, 2012). TBI may result from falls, vehicle accidents, sport injuries, military incidents, etc. (Ma et al., 2016; Wright and Ramesh, 2012; Zhang et al., 2014). In Europe, TBIs cause 37% (Majdan et al., 2016) of all injury-related deaths, and are associated with increased mortality and decreased life expectancy compared with the general population.

TBI can be classified based on occurrence, location or severity, or can be categorized as primary or secondary brain injury, resulting from initial trauma or from the evolution of the initial injury and its subsequent complications, respectively (McAllister, 2011; Tse et al., 2015). TBI could have clinical implications whose severity and treatment might vary based on the location, and it might cause pathologies which range from focal damage of brain tissue to widespread injury at the cellular level (Jérusalem et al., 2014; McAllister, 2011; Tse et al., 2015; Wright and Ramesh, 2012). The most common pathological feature of mild and severe cases of TBI at the cellular and subcellular levels is called Diffuse Axonal Injury (DAI), i.e. the diffuse form of TBI (Smith and Meaney, 2000; Wright and Ramesh, 2012), initiated in the deep white matter regions of the brain at the moment of injury (Ma et al., 2016; Wright and Ramesh, 2012).

DAI is a pathogenesis with progressive course (Ma et al., 2016), responsible for long-lasting neurological impairments and neurodegenerative diseases initiated by trauma, associated with high rates of mortality (Lajtha et al., 2009; Smith and Meaney, 2000; H. C. Wang and Ma, 2010). Currently, no diagnostic criteria, nor clinically approved treatment strategies are available and the clinical diagnosis of DAI is definitive only following post-mortem examination (Lajtha et al., 2009; Ma et al., 2016). A better understanding of DAI is urgently needed to improve diagnosis, clinical treatments and prognosis (Lajtha et al., 2009; Ma et al., 2016).

Analysing the changes in multiphysical phenomena in nervous cells during DAI events, and in particular in coupled electro-mechanical phenomena, provides a way to contribute

to the understanding of the interdependence of electrical and mechanical phenomena in neural activity and the progressive course of axonal pathogenesis.

Eventually, the electro-mechanical analysis of injury at the cellular level for nervous cells could improve the understanding of communication between dendritic cells (both cell-to-cell and communication between group of cells) when the neural network is altered by injury or disease.

### **1.3 Aim**

Because current medical technology is limited in its capacity to detect DAI (Lajtha et al., 2009; Ma et al., 2016), computational modelling is crucially important as a tool for representing and quantifying nerve damage at the microscale, that cannot be measured directly using conventional methods.

In this context, this thesis presents a computational modelling investigation (using finite element analysis) of DAI-induced changes in the electro-mechanical phenomena in nervous cells. A computational modelling framework is developed to replicate the coupling of electrical and mechanical features of neural activity, i.e. where changes in electrical activity lead to mechanical effects and vice versa.

The overall aim of the work is to develop this coupled electro-mechanical computational modelling framework for nervous cells, and to use the framework to assess the effects of brain injuries on nervous cells, and in particular the generation of axonal damage due to DAI-induced loading.

It is also intended that the work will generate further insights into neural electro-mechanical activity and advance our understanding of neural structural and functional damage induced by DAI. The findings may help the understanding of trauma at the cellular level and the potential electrophysiological impairments generated by mechanical loads.

### **1.4 Significance of the Problem and Motivation**

Computational models are often used as tools to understand the biomechanics of TBI, and to develop protective equipment and protocols with a view to preventing and mitigating injury (Horgan and Gilchrist, 2003; Jérusalem et al., 2014; Sahoo et al., 2016; Wright and Ramesh, 2012). The accuracy of these models depends on the incorporation of the appropriate level of structural details, material behaviour and appropriate boundary conditions.

Although some progress has been made in understanding the injury mechanisms and biomechanics of TBI and DAI (Horgan and Gilchrist, 2003; Jérusalem et al., 2014; Sahoo et al., 2016; Wright and Ramesh, 2012) the electrical activity of the nervous cells is usually neglected. One reason for this is the high computational cost required for the combined use of dedicated electrical modelling software codes and mechanical engineering design software (Crozier et al., 2016). Thus, research into the biomechanics of, and the electrical signalling in, the brain is frequently conducted independently, and are often considered as two independent research fields.

However, inclusion of neural electrical activity in the biomechanical analysis of the brain is needed to improve the predictive capabilities of current computational models. Thanks to the integration of multidisciplinary fields, computational electro-mechanical models, that couple mechanics and electrophysiology, may improve the understanding of neurophysiological and neuropathological processes, and neurocognitive damage, associated with brain injuries (Jérusalem et al., 2014; Wright and Ramesh, 2012). Additionally, the incorporation of electro-mechanical features in the study of nerve tissue mechanics may contribute to the development of clinical diagnosis and treatment strategies to target and treat dysfunctional axons.

The investigation of DAI at the microscale is a key aspect in simulating both structural damage and functional damage in a mechanically injured nerve fibre. Quantifying the induced electro-mechanical changes at the microscale may help to differentiate the severity of a given injury and to understand the alteration in signal propagation at cellular and nerve bundle levels. These results have the potential to improve diagnosis and treatment methods for traumatic brain injuries, supporting the use of finite element models as powerful tools to investigate neural electro-mechanical activity.

## **1.5 Contribution to the Research Field**

This work provides a framework for improving the reliability of predictive finite element models for neural engineering applications, by simulating electro-mechanical phenomena in nerves and the effects of injury on the neural electro-mechanical behaviour.

Recent experimental literature on neural activity highlights some biophysical phenomena at the nerve membrane layer that can no longer be ignored in nerve modelling (El Hady and Machta, 2015; Mosgaard et al., 2015; Mueller and Tyler, 2014). In particular, axonal swelling, piezoelectricity (Zhang et al., 2001) and electrostriction (Alvarez and Latorre, 1978) are significant electro-mechanical phenomena associated with neural

electrical activity (El Hady and Machta, 2015; Mosgaard et al., 2015; Mueller and Tyler, 2014).

This thesis presents a fully coupled 3D electro-mechanical model of the neuron implemented in finite element analysis, which includes the representation of electrostriction and piezoelectricity (El Hady and Machta, 2015; Mosgaard et al., 2015; Mueller and Tyler, 2014). Mechanical loads are applied to induce damage at the nerve membrane layer, reproducing previously observed changes in neuronal membrane excitability (Jérusalem et al., 2014) and propagation (Boucher et al., 2012) in response to electro-mechanical alterations (Mueller and Tyler, 2014).

In this work, the electro-mechanical coupling incorporates the use of a thermal analogy to account for electrical conduction in nervous cells. Here, equivalent thermal material properties are analogues of electrical properties, which are then applied to model simultaneous inter-dependence of electrical and mechanical phenomena using established thermo-mechanical modelling tools. For the work of the thesis, this modelling approach is found to be the most computationally efficient way for establishing real-time electro-mechanical coupling in finite element analysis.

In the initial phase of the work, the electro-mechanical coupling is evaluated as a *1-way coupling* in which only the effects of electrical quantities on the mechanical structure are considered. Following this, the coupling is evaluated as fully coupled (or *2-way coupling*), where the electrical properties and activity of the nerve membrane are both changed due to mechanical deformation.

To represent permanent damage in the nerve tissue, plasticity is included in the model and this is seen to have a significant effect on the computed DIA-induced local mechanical state (stress and strain) of the tissue. The coupled modelling framework is tested and evaluated on single nerve fibres and on nerve bundles to establish the influence of neuron morphology on the predicted results.

Finally, the University College Dublin Brain Trauma Model (Horgan and Gilchrist, 2003, 2004) is used to simulate a short-duration frontal head impact under a series of DAI-inducing velocity levels. The resulting simulated deformation of the deep region of the white matter is used to generate boundary conditions for application in the nerve bundle model (utilising the coupled electro-mechanical modelling framework), for estimating electrophysiological and electro-mechanical changes in the nerve bundle at the microscale. This procedure enables accurate estimation of the impact of DAI on neural electro-mechanical activity.

This framework can be easily reproduced and used in other studies to improve the quality of brain tissue research or in other biological fields, which exhibit coupled electro-mechanical phenomena.

## 1.6 Objectives

The specific objectives of this work are:

1. To establish a modelling framework to simulate simultaneous mechanical and electrical phenomena, using finite element analysis ([Chapter 3](#)).
2. To develop a framework that can simulate fully coupled electro-mechanical phenomena in the nerve membrane (including neural activity, electrostriction and piezoelectricity) ([Chapter 4](#)).
3. To evaluate the effects of material non-linearity (i.e. plasticity) on simulated neural activity that cause permanent tissue damage under mechanical loads ([Chapter 5](#)).
4. To quantify electro-mechanical changes at the cellular level due to strain levels produced during frontal head impacts and to relate TBI-induced mechanical forces applied to the head at the macroscale level to the injury developing at the cellular level ([Chapter 6](#)).

Each of these objectives are investigated and discussed in Chapter 3 to Chapter 6 of this thesis and they also form the basis of journal publications/submissions.

## 1.7 Thesis Structure

Below, the main features of each chapter are listed.

### **Chapter 1** – Introduction and Thesis Structure

This chapter summarises the context, motivation and the objectives of this Ph.D. thesis, and an overview of the thesis structure is provided, highlighting the different stages of the research.

### **Chapter 2** – Background

That chapter outlines the background literature relevant for modelling neural activity. It includes details on: the nervous cell structure and function, biophysical phenomena associated with nerve pulses, and the biomechanics of diffuse axonal injury.

### **Chapter 3** – Electro-Thermal Equivalent 3D Finite Element Model of a Single Neuron

An electro-mechanical coupling (or *1-way* coupling) based on the theory of equivalences in finite element analysis is proposed as a first step in modelling complex neural multiphysical phenomena. This modelling approach is validated against published experimental literature on the squid giant axon, crab nerve fibre and garfish olfactory nerve fibre.

**Chapter 4** – Electro-Mechanical Response of a 3D Nerve Bundle Model to Mechanical Loads Leading to Axonal Injury

A fully coupled model (or *2-way* coupling) is presented that includes the representation of mechano-electrical changes in the neural activity induced by strain applied to the nerve. This real-time coupling includes a modulated threshold for activation of the action potential and independent alteration of the electrical properties for each multi-layer nerve fibre within a nerve bundle as a function of strain. The model is validated against published experimental literature on DAI considering the case of unmyelinated and myelinated nerve bundles.

**Chapter 5** – Effects of Nerve Bundle Geometry on Neurotrauma Evaluation

By applying the fully coupled model, the effects of geometrical changes and damage to the neuron structure are investigated in two scaled nerve bundle models, one consisting of myelinated nerve fibres and the other of unmyelinated nerve fibres. Here, the effects of non-linear mechanical behaviour (i.e. plasticity) are included, to investigate the contribution to permanent changes in neural activity, as observed following brain injuries.

**Chapter 6** – Electro-Mechanical Alterations in Nerve Fibres of the Human Corpus Callosum

The electro-mechanical coupling is tested in a nerve bundle model, whose dimensions are those of the Human Corpus Callosum (HCC). Here, the myelin layer is modelled with a finite thickness as in the HCC. The use of different modelling approaches allows for validation of the framework by using anatomically accurate dimensions.

**Chapter 7** – Head-to-nerve analysis of electromechanical impairments of diffuse axonal injury

The mechanical state in the brain following traumatic brain injury (as frontal head impact) is simulated at the macroscale using a 3D finite element head model. Taking the macroscale simulation results as boundary conditions, the nerve bundle models from Chapter 5 are used to investigate the changes in the neural electro-mechanical responses at

the cellular level (microscale). An analysis is carried out to quantify the cellular level impairments following frontal head impacts.

### **Chapter 8 – Conclusions and Recommendations**

The main findings of each chapter are summarised, and overall conclusions are drawn. Finally, recommendations for future work identify potential studies that can be carried out, based on the thesis outcomes.

---

## References Chapter 1

- Alvarez, O., and Latorre, R. (1978). Voltage-dependent capacitance in lipid bilayers made from monolayers. *Biophysical Journal*, 21(1), 1–17. [https://doi.org/10.1016/S0006-3495\(78\)85505-2](https://doi.org/10.1016/S0006-3495(78)85505-2)
- Boucher, P. A., Joós, B., and Morris, C. E. (2012). Coupled left-shift of Nav channels: Modeling the Na<sup>+</sup>-loading and dysfunctional excitability of damaged axons. *Journal of Computational Neuroscience*, 33(2), 301–319. <https://doi.org/10.1007/s10827-012-0387-7>
- Crozier, A., Augustin, C. M., Neic, A., Prassl, A. J., Holler, M., Fastl, T. E., Plank, G. (2016). Image-based personalization of cardiac anatomy for coupled electromechanical modeling. *Annals of Biomedical Engineering*, 44(1), 58–70. <https://doi.org/10.1007/s10439-015-1474-5>
- El Hady, A., and Machta, B. B. (2015). Mechanical surface waves accompany action potential propagation. *Nature Communications*, 6(6697), 6697. <https://doi.org/10.1038/ncomms7697>
- Heimburg, T., Blicher, A., Mosgaard, L. D., and Zecchi, K. (2014). Electromechanical properties of biomembranes and nerves. *Journal of Physics: Conference Series*, 558, 12018. <https://doi.org/10.1088/1742-6596/558/1/012018>
- Heimburg, T. and Jackson, A.C. (2005). On soliton propagation in biomembranes and nerves. *Proceedings of the National Academy of Sciences*, 102(28), 9790–9795. <https://doi.org/10.1073/pnas.0503823102>
- Hodgkin, A. L., and Huxley, A. F. (1952). A quantitative description of membrane current and its application to conduction and excitation in nerve. *Journal of Physiology*, 117, 500–544. [https://doi.org/10.1016/S0092-8240\(05\)80004-7](https://doi.org/10.1016/S0092-8240(05)80004-7)
- Horgan, T. J., and Gilchrist, M. D. (2003). The creation of three-dimensional finite element models for simulating head impact biomechanics. *International Journal of Crashworthiness*, 8(4), 353–366. <https://doi.org/10.1533/ijcr.2003.0243>
- Horgan, T. J., and Gilchrist, M. D. (2004). Influence of FE model variability in predicting brain motion and intracranial pressure changes in head impact simulations. *International Journal of Crashworthiness*, 9(4), 401–418. <https://doi.org/10.1533/ijcr.2004.0299>

- Jérusalem, A., García-Grajales, J. A., Merchán-Pérez, A., and Peña, J. M. (2014). A computational model coupling mechanics and electrophysiology in spinal cord injury. *Biomechanics and Modeling in Mechanobiology*, 13(4), 883–896. <https://doi.org/10.1007/s10237-013-0543-7>
- Lajtha, A., Javitt, D., and Kantrowitz, J. (2009). Handbook of neurochemistry and molecular neurobiology. Brain and spinal cord trauma. (N. Banik & K. R. Swapan, Eds.), *Springer Reference* (3rd Edition, Vol. 281). Springer. <https://doi.org/10.1016/j.jns.2009.03.019>
- Ma, J., Zhang, K., Wang, Z., and Chen, G. (2016). Progress of research on diffuse axonal injury after traumatic brain injury. *Neural Plasticity*, 2016, 7. <https://doi.org/10.1155/2016/9746313>
- Majdan, M., Plancikova, D., Brazinova, A., Rusnak, M., Nieboer, D., Feigin, V., and Maas, A. (2016). Epidemiology of traumatic brain injuries in Europe: A cross-sectional analysis. *The Lancet Public Health*, 1(2), e76–e83. [https://doi.org/10.1016/S2468-2667\(16\)30017-2](https://doi.org/10.1016/S2468-2667(16)30017-2)
- McAllister, T. W. (2011). Neurobiological consequences of traumatic brain injury. *Dialogues in Clinical Neuroscience*, 13(3), 287–300. Retrieved from <https://www.ncbi.nlm.nih.gov/pubmed/22033563>
- Mosgaard, L. D., Zecchi, K. A., and Heimburg, T. (2015). Mechano-capacitive properties of polarized membranes. *Soft Matter*, 11(40), 7899–7910. <https://doi.org/10.1039/C5SM01519G>
- Mueller, J. K., and Tyler, W. J. (2014). A quantitative overview of biophysical forces impinging on neural function. *Physical Biology*. <https://doi.org/10.1088/1478-3975/11/5/051001>
- Rvachev, M. M. (2010). On axoplasmic pressure waves and their possible role in nerve impulse propagation. *Biophysical Reviews and Letters*, 5(2), 73–88. <https://doi.org/10.1142/S1793048010001147>
- Sahoo, D., Deck, C., and Willinger, R. (2016). Brain injury tolerance limit based on computation of axonal strain. *Journal of Accident Analysis and Prevention*, 92, 53–70. <https://doi.org/10.1016/j.aap.2016.03.013>

- Smith, D. H., and Meaney, D. F. (2000). Axonal damage in traumatic brain injury. *The Neuroscientist*, 6(6), 483–495. <https://doi.org/10.1177/10738584000600611>
- Tse, L., Barr, A. M., Scarapicchia, V., and Vila-rodriguez, F. (2015). Neuroleptic Malignant Syndrome : A Review from a Clinically Oriented Perspective. *Current Neuropharmacology*, 13, 395–406. Retrieved from <https://www.ncbi.nlm.nih.gov/pmc/articles/PMC4812801/pdf/CN-13-395.pdf>
- Wang, H. C., and Ma, Y. Bin. (2010). Experimental models of traumatic axonal injury. *Journal of Clinical Neuroscience*, 17(2), 157–162. <https://doi.org/10.1016/j.jocn.2009.07.099>
- Wright, and Ramesh, K. T. (2012). An axonal strain injury criterion for traumatic brain injury. *Biomechanics and Modeling in Mechanobiology*, 11(1–2), 245–260. <https://doi.org/10.1007/s10237-011-0307-1>
- Zhang, Y. P., Cai, J., Shields, L. B. E., Liu, N., Xu, X. M., and Shields, C. B. (2014). Traumatic brain injury using mouse models. *Translational Stroke Research*, 5(1), 454–471. <https://doi.org/10.1007/s12975-014-0327-0>
- Zhang, P.-C., Keleshian, A. M., and Sachs, F. (2001). Voltage-induced membrane movement. *Nature*, 413(6854), 428–432. <https://doi.org/10.1038/35096578>

---

## Chapter 2.      **Background**

This chapter summarises some background in neurophysiology, with focus on the recent findings concerning biophysical phenomena related to neural electrical activity. Mathematical models for describing the effects of these phenomena on neural electrical activity are also reviewed.

### 2.1    **The Nervous Cell**

Neurons or nervous cells consist of a cell body, dendrite and long cylindrical nerve fibre called the axon, see Fig. 2.1, which connects between the neuron extremities or dendrites, as described by Rall (1977). A thin membrane sheath separates the axon (i.e. axoplasm or intracellular media) from the external saline solution (extracellular media or extracellular space). Neurons can be classified as myelinated or unmyelinated nerve fibres, depending on whether a myelin sheath surrounds the axon of the fibre or not.

According to previous publications (Meffin et al., 2012; Tahayori et al., 2012), a *neurite* (or dendrite) refers to a part of the body of a nervous cell (axon) that consists of two structurally distinct regions (axoplasm and membrane). In contrast, a *fibre* usually refers to an axon (as axoplasm and membrane) with a myelin layer. However, the term *axon* can also be used to indicate the full length of the conductive part of the cell, i.e. the fibre.

Neurons are electrically excitable cells carrying electrical signals. When a stimulus of current or voltage depolarises the resting membrane potential beyond the threshold voltage, then the membrane will respond with an electrical impulse called the Action Potential (AP).

If the axon is encased in a myelin sheath, transmission of the AP signal along the fibre is faster than in an unmyelinated axon. The myelin layer is considered to be an electrical insulator, which increases the velocity of transmission by shifting the exchange of ionic charges to specific periodic regions, called *Ranvier's nodes*, see Fig. 2.1. In contrast, this structure is not present in unmyelinated axons, where the ionic gate channels are uniformly distributed along the fibre length, see Fig. 2.1.

Experimental literature, based on morphological data, shows that AP conduction velocities and firing rates are proportional to the fibre diameter, which differs widely in calibre throughout the Central Nervous System (Björnholm et al., 2017; Perge et al., 2012).

Efficiency in communication is the reason for this morphological variation. In relation to the brain, available space constrains its design and different fibre calibres are needed to achieve the best balance of energy consumption and signalling efficiency (Perge et al., 2012).

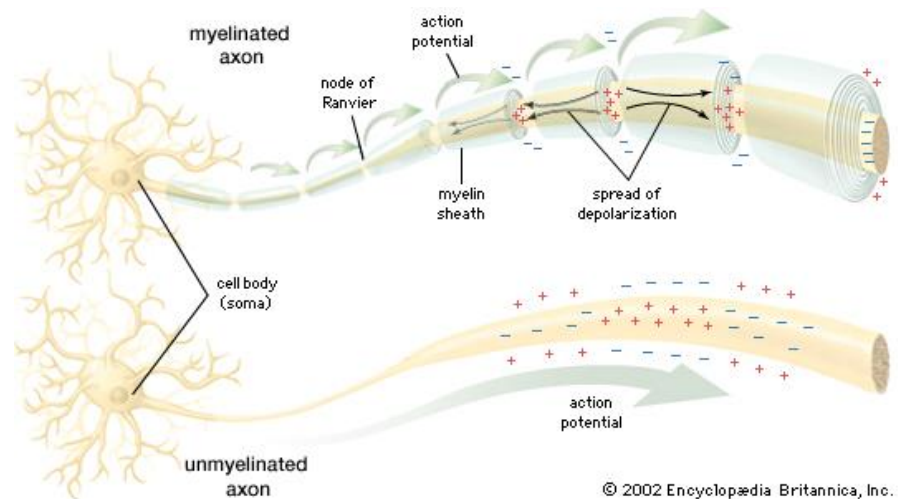


**Fig. 2.1** Figure reprinted from 2002 Encyclopaedia Britannica, Inc., showing unmyelinated and myelinated axons.

## 2.2 The Hodgkin-Huxley Model

The Hodgkin-Huxley (HH) model won the 1963 *Nobel Prize in Physiology or Medicine* for being the first biophysically-based model of the electrophysiology of a single cell, based on a series of experiments on a squid giant nerve fibre (Hodgkin and Huxley, 1952). This model describes the depolarisation and repolarisation of the nerve membrane through the AP, where ionic currents flow in and out through the ionic gate channels of the membrane.

The AP is an “all or nothing” phenomenon generated by changes in ion mobility that occurs after an initial activation event (Hodgkin and Huxley, 1952). When the membrane is depolarised over the threshold voltage of about  $-55\text{ mV}$  (Hodgkin and Huxley, 1952), the flow of ions hyperpolarises the trans-membrane potential from the resting potential, about  $-60\text{ mV}$ , to a peak overshoot value,  $\sim 40\text{ mV}$  (Hodgkin and Huxley, 1952).

The HH model is a mathematical description of this phenomenon, based on first-order differential equations, see Eq. 2.1 and Fig. 2.2 (Hodgkin and Huxley, 1952). In this model, the electrical behaviour of the axon membrane is represented by the equivalent electrical circuit shown in Fig. 2.2. Here, three membrane currents are considered to flow in parallel to a membrane capacitance,  $C_m$ , corresponding to sodium ( $\text{Na}^+$ ), potassium ( $\text{K}^+$ ) and

leak ions ( $l^-$ ), mainly chloride anions, respectively. Each current is determined by a driving force conveniently measured as an electrical potential difference,  $V_i$ , and a permeability coefficient which has the dimensions of conductance per area (indicated by  $G_i$  with  $i = Na^+, K^+ \text{ or } l^-$ ), see Fig. 2.2. The driving voltage of each branch of the circuit is the Nernst potential of each ion species, and this is known as the Ohmic conductance hypothesis (Hodgkin and Huxley, 1952).

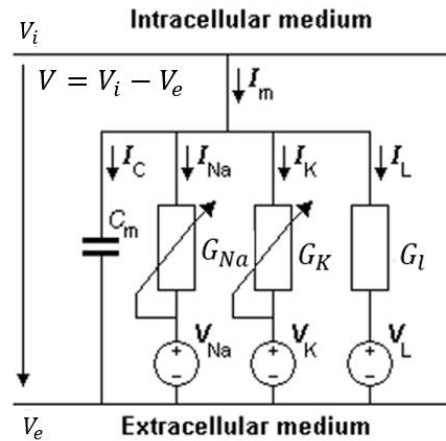


**Fig. 2.2** Electrical circuit representing the nerve membrane. Conductances are  $G_{Na}$ ,  $G_K$  and  $G_l$  [ $mS\ cm^{-2}$ ]; membrane voltage,  $V$  [ $mV$ ]; intracellular medium voltage,  $V_i$  [ $mV$ ]; extracellular medium voltage,  $V_e$  [ $mV$ ]; ionic potential drop  $V_{Na} = -115\ mV$ ,  $V_K = 12\ mV$  and  $V_l = -10.63\ mV$ ; ionic currents ( $I_{Na}$ ,  $I_K$ ,  $I_l$  and  $I_c$  [ $mA/cm^2$ ]); membrane current,  $I_m$ ; membrane capacity per unit area,  $C_m$ , equal to  $1\ \mu F/cm^2$  (Hodgkin and Huxley, 1952). Figure reprinted and adapted from (Plonsey and Malmivuo, 1995).

The electrophysiological behaviour of the membrane is described by the net flow of ions through a large number of ion channels, generating the AP (Hodgkin and Huxley, 1952). The behaviour of the membrane can be examined in terms of the behaviour of individual ion channels, and then as the summation of the behaviour of a large number of ion channels, through the equation provided by HH (Hodgkin and Huxley, 1952) .

The dynamics of ion channel particle gating is governed by Eq. 2.1 for each ion type, where  $\alpha_p$  determines the rate constants of ion transfer from outside to inside the membrane, while  $\beta_p$  is the rate of transfer in the opposite direction (Hodgkin and Huxley, 1952). The rate constants vary with voltage only,  $V$ , (Hodgkin and Huxley, 1952). Table 2.1 lists all the equations in greater details.

$$dp/dt = \alpha_p \cdot (1 - p) - \beta_p \cdot p \quad \text{with } p \in \{n, m, h\} \quad \text{Eq. 2.1}$$

The variables  $n$ ,  $m$  and  $h$  of Eq. 2.1 quantify the proportion of the particles on either side of the membrane for potassium, sodium and leak ions, respectively. They are applied

in Eq. 2.2 to calculate the conductance of the three ion types. The variables range between 0 and 1 (no units) (Hodgkin and Huxley, 1952). The initial estimates for  $n$ ,  $m$  and  $h$  are 0.315, 0.042 and 0.608, respectively (Hodgkin and Huxley, 1952), representing the concentration of the three ions at physiological conditions when the membrane potential is the resting membrane potential, and no AP is elicited.

The change in membrane current due to gating activation is described in Eq. 2.3 for each particle type. Table 2.1 presents the maximum values for each ion conductance (Hodgkin and Huxley, 1952). For the HH model, the expression for the total transmembrane current density,  $I_m$ , is the sum of the capacitive,  $I_c$ , and ionic components, see Eq. 2.3, Eq. 2.4 and Fig. 2.3.

$$G_K = \bar{g}_K n^4; \quad G_{Na} = \bar{g}_{Na} m^3 h; \quad G_l = \bar{g}_l \quad \text{Eq. 2.2}$$

$$I_m = C_m \frac{dV}{dt} + \bar{g}_K n^4 (V - V_K) + \bar{g}_{Na} m^3 h (V - V_{Na}) + \bar{g}_l (V - V_l) \quad \text{Eq. 2.3}$$

The last three terms of the total transmembrane current density, Eq. 2.3, can be identified as the individual contribution of each ionic current density as:

$$I_K = \bar{g}_K n^4 (V - V_K); \quad I_{Na} = \bar{g}_{Na} m^3 h (V - V_{Na}); \quad I_l = \bar{g}_l (V - V_l) \quad \text{Eq. 2.4}$$

Furthermore, the variation of the membrane voltage over time is linearly related to its variation over space (i.e.  $x$ , the fibre length), so that the membrane potential satisfies Eq. 2.5 where  $\theta$  is the propagation speed, independent of the voltage.

$$\frac{\partial^2 V}{\partial t^2} = \theta^2 \frac{\partial^2 V}{\partial x^2} \quad \text{Eq. 2.5}$$

**Table 2.1 Dynamics of gating activation for sodium, potassium and leak ions (Hodgkin and Huxley, 1952).**

Gating activation coefficients [ms <sup>-1</sup> ]	Maximum ion conductance [mS cm <sup>-2</sup> ]
$\alpha_n = (0.01(V + 10)) / (\exp((V + 10)/10) - 1)$	$\bar{g}_K = 36$
$\beta_n = 0.125 * \exp(V/80)$	
$\alpha_m = (0.1(V + 25)) / (\exp((V + 25)/10) - 1)$	$\bar{g}_{Na} = 120$
$\beta_m = 4 * \exp(V/18)$	
$\alpha_h = 0.07 * \exp(V/20)$	$\bar{g}_l = 0.3$
$\beta_h = 1 / (\exp(V + 30/10) + 1)$	

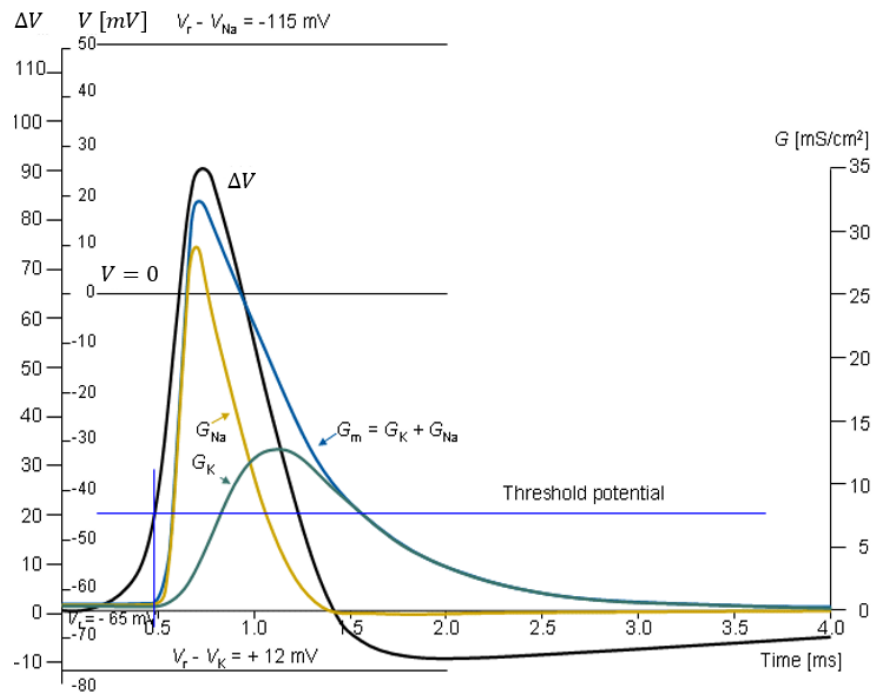


**Fig. 2.3 Sodium and potassium conductance ( $G_{Na}$  and  $G_K$ ), their sum ( $G_m$ ), and the membrane voltage ( $V$ ) during a propagating nerve impulse. Here, the membrane resting potential is  $V_r$ , and is equal to  $-65$  mV. Figure reprinted and adapted from (Plonsey and Malmivuo, 1995).**

## 2.3 The Membrane Capacitance

The nerve membrane is a lipid bilayer with thickness about  $7.5 - 10$  nm (Plonsey and Malmivuo, 1995). The structure of the membrane is the result of an energetically favourable arrangement in water of the hydrophilic polar head part and the hydrophobic chains (Plonsey and Malmivuo, 1995).

Since 1952 (Hodgkin and Huxley, 1952), it has been thought that the nerve membrane is equivalent to a homogenous parallel plate capacitor with constant dimensions in which the internal dielectric part is the hydrophobic part of the lipid bilayer, where integral membrane proteins are neglected. Fig. 2.4 shows the equivalent representation of a parallel plate capacitor in (a), and a lipid bilayer membrane in (b). The non-conductive medium is air or vacuum in (a) and is the hydrophobic membrane core in (b). The thickness of the non-conductive inner core is about  $3$  nm (Plonsey and Malmivuo, 1995). In both cases, the charge,  $Q$ , is stored across the bilayer and generates an electrical potential difference across the layer, see Fig. 2.4. Then, Eq. 2.6 describes the stored charge on two capacitor plates at a fixed voltage that, here, is the membrane voltage,  $V$ . Eq. 2.7 is the capacitance for a parallel plate capacitor (Heimburg, 2012). The membrane capacitance per unit area,  $C_m$ , is the capacitance,  $C$ , divided by the area.

In the HH model (Hodgkin and Huxley, 1952), the capacitance is a constant quantity whose value is calculated based on the membrane area,  $A$ , and the membrane thickness,  $d$ , and it is equal to  $1 \mu\text{F}/\text{cm}^2$  (Hodgkin and Huxley, 1952). The dielectric permittivity,  $\epsilon$ , is, thus, a constant value, a product of the vacuum permittivity,  $\epsilon_0 = 8.85410 \cdot 10^{-12} \text{ F/m}$ , and the dielectric constant of the nerve membrane, which varies between  $\epsilon_r \approx 2 - 4$  (Heimburg, 2012).

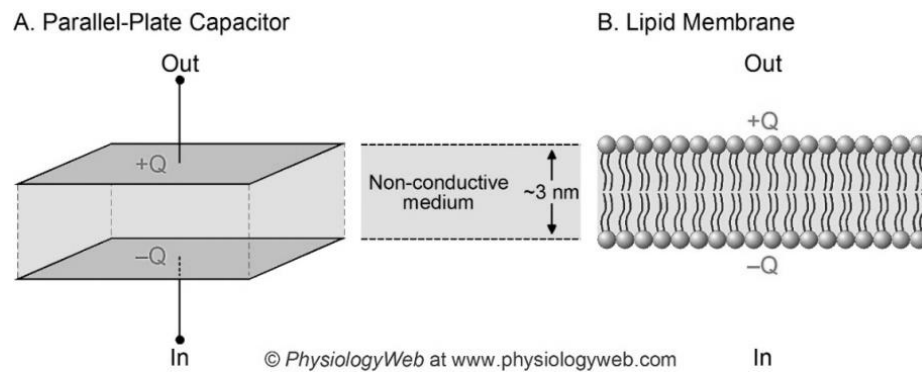


**Fig. 2.4 Biological membranes, especially nerve membrane, have similar electrical properties to those exhibited by parallel-plate capacitors. In (a), a parallel-plate capacitors and, in (b), the nerve membrane. In both cases, the two conductive layers are separated by a non-conductive medium. Figure reprinted from www.PhysiologyWeb.com.**

$$Q = C_m V \quad \text{Eq. 2.6}$$

$$C = \epsilon_0 \epsilon_r \frac{A}{d} = \epsilon \frac{A}{d} \quad \text{Eq. 2.7}$$

Depending on the stimulus applied on the nervous cell, sodium, potassium, and chloride ions flow in and out of the membrane, through the ionic channels. The HH model describes the flux of ionic currents as a Resistor-Capacitor (RC) circuit consisting of two variable resistances, one constant resistance and a capacitor. The total membrane current is derived from the current balance by applying Ohm's Law (Hodgkin and Huxley, 1952).

## 2.4 Biophysical Phenomena at the Nerve Membrane

The parallel plate assumption of the HH model neglects the electrolytes, containing ions, in the medium surrounding the nerve membrane, so that electrical conductivity of the extracellular medium is zero. This is equivalent to considering the thickness of the extracellular medium to be inferior to  $1 \text{ nm}$ , i.e. the distance over which a charge is shielded by ions in a solution (usually called Debye length) (Mosgaard et al., 2015). With

this assumption, the AP is described by the ionic currents flowing across the ionic channel proteins of the nerve membrane thickness. Here, the capacitance is constant.

Now, assuming the nerve membrane is surrounded by a conductive electrolyte solution (or surrounded by an extracellular medium with thickness greater than  $1\text{ nm}$ ), the charges on the capacitor generates mechanical forces on the membrane layers that can alter the dimension of the capacitor. This leads to a non-constant membrane capacitance, which increases when the applied electric field reduces the membrane thickness and increases its area (Mosgaard et al., 2015). This is called electrostriction, and a recent publication (Mosgaard et al., 2015) suggests that the nerve membrane should be described as a non-linear capacitor for a more realistic representation, because small changes in voltage can result in large changes in thickness and capacitance.

Furthermore, Heimburg and Jackson (2005) show that reversible heat occurs in signalling, during which the lipid bilayer transitions from a fluid to a gel state with a related change in membrane density. An initial temperature increase is found at the nerve membrane during the AP, followed by cooling with repolarisation (Heimburg and Jackson, 2005). Heimburg and Jackson (2005) show that this transition is accompanied by an increase in membrane volume and area. During the melting transition, the change in phase generates fluctuations in membrane volume (about 4% (Heimburg and Jackson, 2005)) and surface area (about 25% (Heimburg and Jackson, 2005)) during which material properties, such as heat capacity, volume and area compressibility, bending elasticity and relaxation times, become maximal (Heimburg, 1998; Heimburg and Jackson, 2005).

Hence, there is interest and scope to further develop the HH model to account for complex biophysical interactions at the nerve membrane (Appali et al., 2010; Heimburg, 2012; Hodgkin and Huxley, 1952).

For the purpose of this thesis, emphasis is given to the electro-mechanical phenomena of the neural electrical activity, rather than the electro-thermo-mechanical phenomena, as mentioned in Section 1.1.

### 2.4.1 Electrostriction

Mechanical forces arise on the two membrane layers when the dielectric between them is placed in an external electric field. These forces lead to a change in the membrane capacitor dimensions. In contrast to the HH model assumption of constant capacitance (Hodgkin and Huxley, 1952), experimental observations show that the capacitance of the biological membrane is generally not constant (Heimburg, 1998; Mosgaard et al., 2015). Fig. 2.5 illustrates the increase in capacitance due to compressive forces on the membrane

layers generated by an applied voltage difference. *Electrostriction* of the nerve membrane is the effect describing the changes induced under electrical fields in the membrane capacitance due to mechanical changes in the capacitor, and vice versa (Mosgaard et al., 2015, 2014).

In Fig. 2.5, compressive forces increase the area and reduce the thickness of the capacitor, increasing the capacitance of the membrane that undergoes gel-to-fluid transition (Mosgaard et al., 2015). Eq. 2.8 describes the changes in membrane capacitance as function of voltage only, when the membrane density undergoes transition fluid-to-gel during signalling. Experiments show that the membrane capacitance in the fluid state,  $C_m^{Fluid}$ , is about 1.49 times greater than in the gel state,  $C_m^{Gel}$ , thanks to changes in compressibility, assuming 16.3% decrease in thickness and 24.6% increase in area, while the volume of the lipid membrane remains constant (Heimburg, 2012), see Eq. 2.8.

$$C_m^{Fluid} = \varepsilon \frac{A_{Gel}(1 + 0.246)}{d_{Gel}(1 - 0.163)} C_m^{Gel} \cong 1.49 C_m^{Gel} \quad \text{Eq. 2.8}$$

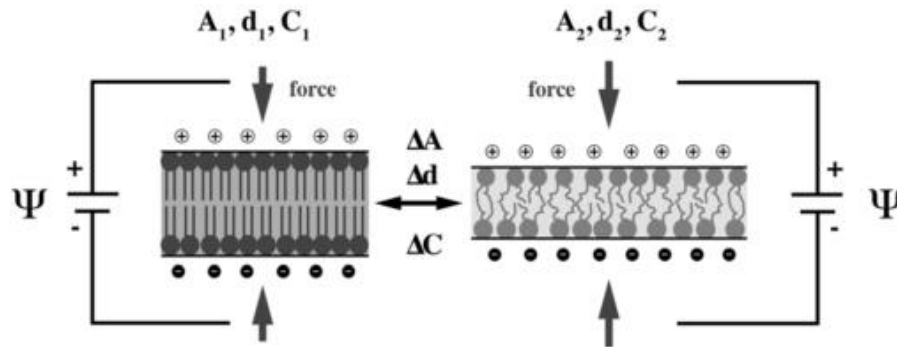


**Fig. 2.5** Electrostriction effects upon charging the membrane capacitor. A force generated by an applied potential difference,  $\Psi$ , compresses the membrane layer which reaches a state with larger area,  $A$ , and smaller thickness,  $d$ . Figure reprinted from (Mosgaard et al., 2015).

Then, Eq. 2.9 describes the forces,  $F$ , generated by electrostatic attraction of the charges on the two capacitor plates due to the thinning of the membrane. As mentioned before, assuming a uniform dielectric constant in the membrane interior (Heimburg, 2012), the electric field across the membrane,  $\Psi$ , is equal to the membrane voltage,  $V$ , divided by the membrane thickness,  $d$ , (Mosgaard et al., 2015). So, substituting Eq. 2.6, the force is proportional to the membrane capacitance and to the square of voltage (Mosgaard et al., 2015), see Eq. 2.9.

$$F = \frac{1}{2} \Psi Q = \frac{1}{2} \frac{C_m V^2}{d} \quad \text{Eq. 2.9}$$

Alvarez and Latorre (1978) describe the capacitance as in Eq. 2.10, proportional to the square of voltage, where  $C_m(0)$  is the capacitance at physiological conditions (i.e. when the membrane potential is equal to the resting membrane potential) and  $\alpha$  is the fractional increase in capacitance per squared volt, which in experimental literature is found to be equal to  $0.02 V^{-2}$  (Alvarez and Latorre, 1978).

$$C_m(V) = C_m(0)[1 + \alpha(V + \Delta V^2)] \quad \text{Eq. 2.10}$$

However, in contrast to Eq. 2.8, the changes of the membrane capacitance can also be described as function of voltage and temperature (Mosgaard et al., 2014). Because of electrostriction, an increase in voltage can induce a melting transition and the compressibility of the membrane is thus dependent on both temperature,  $T$ , and voltage, see Eq. 2.11 (Mosgaard et al., 2014). Heimburg (2012) shows that the charge stored in the capacitor changes as described in Eq. 2.12, a more realistic representation than Eq. 2.6. The second term in Eq. 2.12 does not contribute when assuming that the changes of the capacitance are independent of voltage, as in the HH model (Hodgkin and Huxley, 1952). That is, the membrane dimensions are not altered in the HH model by the phenomena of electrostriction and dielectric phase transitioning, in contrast to experimental observations (Iwasa et al., 1980; Mosgaard et al., 2012).

During the melting transition, the changes in capacitance can also be represented by the capacitance susceptibility,  $\widehat{C}_m$ , see Eq. 2.13, in which the second term on the right is the excess in capacitance due to voltage variation at body temperature (311 K) (Heimburg et al., 2014; Mosgaard et al., 2012). During the AP, the voltage changes from the resting potential, about  $-60 mV$ , to a peak overshoot value,  $\sim 40 mV$  (Hodgkin and Huxley, 1952), as discussed in Section 2.2. If the voltage is constant or if the membrane capacitance is independent of voltage as in the HH model, then the capacitive susceptibility and the capacitance are identical, see Eq. 2.13 and Fig. 2.6 (Heimburg, 2012). This is equivalent to the absence of the AP in the fibre, or to the exclusion of the melting transition phase of the membrane density during signalling, i.e. the second term on the right in Eq. 2.13 (Heimburg et al., 2014; Mosgaard et al., 2012).

$$C_m = \varepsilon \frac{A(T, V)}{d(T, V)} \quad \text{Eq. 2.11}$$

$$\frac{dQ}{dt} = \frac{d}{dt}(C_m V_m) = C_m \frac{dV_m}{dt} + V_m \frac{dC_m}{dt} \quad \text{Eq. 2.12}$$

$$\hat{C}_m = \frac{dQ}{dV_m} = \frac{d(C_m V_m)}{dV_m} = C_m + V_m \frac{\partial C_m}{\partial V_m} \quad \text{Eq. 2.13}$$

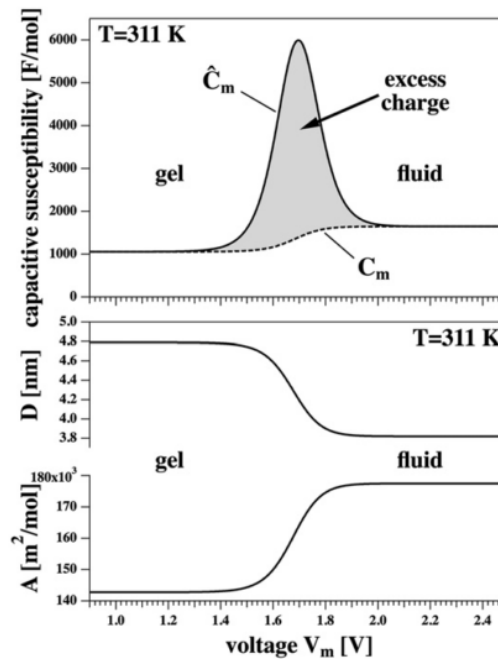


Fig. 2.6 On the top, capacitive susceptibility,  $\hat{C}_m$ , as a function of voltage. The shaded area indicates the excess charge of the voltage-induced transition. The dashed line is the voltage dependent capacitance,  $C_m$ . On the bottom, the changes in membrane thickness and area. Figure reprinted from the paper (Heimburg, 2012).

Different aspects of electrostriction occur with different degrees of asymmetry in the distribution of lipids (such as the charged lipids that are located in the inner core of the lipid bilayer), and spontaneous electrical dipole moments can be generated in the absence of an externally applied potential difference (Mosgaard et al., 2015; Petrov, 2002). Petrov (2002) shown that the polarisation effects may be caused by the inclusion of different lipid types within the same biological membrane or by geometrical deformation, such as changes in curvature. Shape alterations can induce a pressure on the membrane, resulting in a relative dipole orientation on the two layers (Mosgaard et al., 2015; Petrov, 2002). Spontaneous polarisation originating from curvatures is called *flexoelectricity*, as shown in the paper (Petrov, 2002).

## 2.4.2 Piezoelectricity

The piezoelectric effect is the ability of certain materials to generate an electric charge in response to applied mechanical stress and vice versa, as discussed in the paper (Heimburg, 2012). Piezoelectricity is a well-accepted property of several biological tissues

(such as bones, cochlear and others) (Dong et al., 2002). In the nerve membrane, this electromechanical effect can be seen as a pressure-induced change across the nerve membrane (Giizelsu and Akcasu, 1960). The experimental literature on the modulation of membrane tension by transmembrane voltage through indentation reports linear changes of thickness with voltage, of about  $1 \text{ nm}$  per  $100 \text{ mV}$  (Zhang et al., 2001). Fig. 2.7 shows that the changes in thickness or nerve fibre swelling occur simultaneously to the AP in a squid axon (Heimburg et al., 2014; Iwasa et al., 1980). So, the piezoelectric effect is linear with the voltage, while the electrostriction varies with the voltage squared.

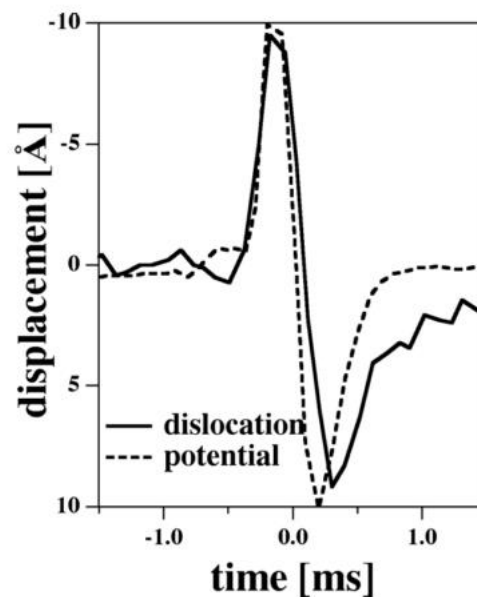


**Fig. 2.7** Thickness changes of a squid axon during the AP as a function of time (solid line). The dashed line represents the voltage change. Figure reprinted from (Heimburg et al., 2014).

## 2.5 Emerging Theories about Nerve Pulses

Scientific investigations of neural mechanisms are a matter of great interest for the understanding of cognitive, sensory and motor functions. An example is the current development of medical devices and the use of diagnostic imaging systems utilizing mechanical energy, as ultrasound imaging (Mueller and Tyler, 2014). The consideration of the mechanobiological processes of the cellular activity has been preferred to electrical- and chemical stimulating devices for treatment and diagnosis (Mueller and Tyler, 2014), as the cell membrane has been shown to generate output signals when forces are applied, as a way to communicate the changes of the surrounding environment by external factors (Haswell et al., 2012; Mueller and Tyler, 2014). It is thought that the local mechanical fluctuations could affect the ion channel kinetics (so the AP) due to the conversion of

mechanical energy from ultrasound to thickness variations of the nerve membrane (Mueller and Tyler, 2014). Then, another example is in general anaesthesia, where inhibitors of pain are currently investigated for their ability to depress the melting point transition in lipid membranes which leads to hydrostatic pressure reversal, increasing the calcium concentration, decreasing pH and to lower body temperature (Heimburg and Jackson, 2007; Mueller and Tyler, 2014).

As mentioned in Section 2.2, the HH model is a mathematical description of an electrical signal propagating in a nerve fibre (Hodgkin and Huxley, 1952), which does not account for motion of the nerve surface generating swelling, reversible mechanical dislocations, or changes in volume and temperature, as shown in experiments (Heimburg and Jackson, 2005; Iwasa et al., 1980; Tasaki and Byrne, 1990).

Recent studies on biomembranes have unearthed important biophysical phenomena regulating neuronal activity (El Hady and Machta, 2015; Mosgaard et al., 2015; Mueller and Tyler, 2014), as previously mentioned. Ionic gate channels in nerve fibres are thought to be sensitive channels to mechanical alterations where the AP can be initiated either by mechanical impulses (such as pressure waves, as discussed in the paper (Rvachev, 2010) or bending (Petrov, 2002)) or ionic currents (Barz and Barz, 2014; Engelbrecht et al., 2016).

Thus, a unified theory is needed to investigate the multiphysics behind neural activity, in order to increase the understanding of current experimental evidence relating to neural conduction. Because of the complexity of simulating the biophysical phenomena accompanying the nerve pulse, up to now, there is no theoretical consensus or preferred theory that can be utilized to replicate all the measured phenomena within one framework. Below, three examples of emerging theories, explaining the multiphysics behind the neural electrical activity, are summarised.

### **2.5.1 The Soliton Theory**

Recently, an alternative representation of the AP has been proposed as an electro-mechanical soliton propagating in the axon membrane (Heimburg and Jackson, 2005). The electrical signal is described as a localised density excitation, propagating as a soliton along the fibre in the membrane, which is in a fluid state at physiological temperatures. The soliton model of the nerve pulse is studied in thermodynamic theory, which includes the phase transitions accompanying the changes in membrane potential and the mechanical implications of these transitions (Heimburg and Jackson, 2005).

So, biomembranes can exist either in liquid phase or in gel phase, and carry mechanical impulses accompanying signal propagation (Heimburg and Jackson, 2005; Barz and Barz,

2014; Engelbrecht et al., 2016). Thanks to the elastic properties of the nerve membrane, mechanical impulses can be carried along the fibre. Mechanical impulses are associated to thermodynamic processes (Barz and Barz, 2014; Engelbrecht et al., 2016). Then, those processes associated with the pulse are in phase with it, and are adiabatic and reversible (Heimburg and Jackson, 2005). This is in contrast with the HH model, which is based on irreversible processes of ionic currents across the nerve membrane. The soliton shape results from the balance of non-linear and dispersive effects, related to the propagation of an isentropic pulse (Heimburg and Jackson, 2005). Heimburg also shows that the thickness changes of the membrane layer are in phase with the voltage changes, see Fig. 2.7 (Heimburg and Jackson, 2005). Then, the energy carried by the soliton and the electrostatic energy both have a similar time dependence (Heimburg and Jackson, 2005). This theory is focused on lipid membranes, but it can be applied to all 1D systems that undergo transitions. Further studies have analysed this model from the point of view of wave mechanics to investigate boundary conditions, shape and velocity of solitary pulses (Engelbrecht et al., 2016).

## 2.5.2 The Pressure Pulse Theory

Although the soliton theory is an established representation of the biophysics of neural activity, it cannot explain the propagation velocity in axons with different calibre and type, according to Rvachev (2010). Rvachev (2010) argues that the propagation of the nerve pulse may involve an axoplasmic pressure wave that is synchronous to the depolarisation wave at the nerve membrane. When an AP is elicited, an axoplasmic pressure wave propagates faster than (or at least as fast as) the electrical pulse straggling the ionic currents prior to activation of the sodium channels (Rvachev, 2010). Here, the activation of ionic channels is driven by both stretch and depolarisation. Then, a local HH type voltage spike develops for the mechano-electrical activation of the ionic channels, widening the transmembrane pores. This facilitates the inflow of calcium particles to cross the nerve membrane. These ions are responsible for the radial contraction of the lipid bilayer, augmenting or generating axoplasmic pressure waves, see Fig. 2.8 (Rvachev, 2010). This auto-sustainable cycle counteracts the pressure pulse decay due to viscosity.

Rvachev (2010) shows that this theory includes electro- and mechano-generation of the AP in the propagation of an axoplasmic pulse wave, with propagation velocity measured to be close to the velocity of the nerve impulse. Overall, this theory explains the dependence of nerve impulse velocity on fibre diameter, type and temperature (Rvachev, 2010). Then, Rvachev (2010) argues that learning and memory in neurons may be linked

to the strength and duration of the pressure-induced contraction, and the underlying mechanisms may be similar to those that regulate muscle cell strength.

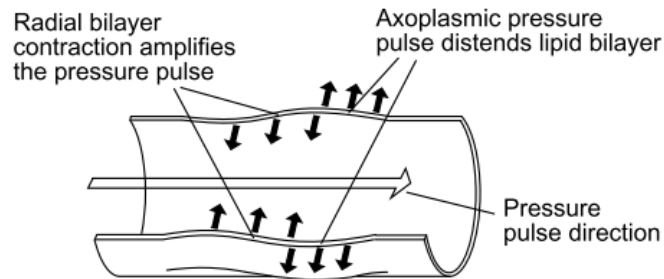


**Fig. 2.8** The pressure pulse manifests itself as an increase in the axon diameter, associated membrane area expansion, and radial contraction. Figure reprinted from the paper (Rvachev, 2010).

### 2.5.3 The Mechanical Surface Waves Theory

This theory recognises the evidence of movement of the nerve membrane surface, during the propagation of the AP, and hence the presence of mechanical waves arising from the driving forces of surface waves (El Hady and Machta, 2015). In contrast to (Heimburg and Jackson, 2005), the AP is considered to be an electrically driven phenomenon, so that the generated mechanical modes are driven by the exchange of charges only across the nerve membrane during AP propagation, as in Fig. 2.9.

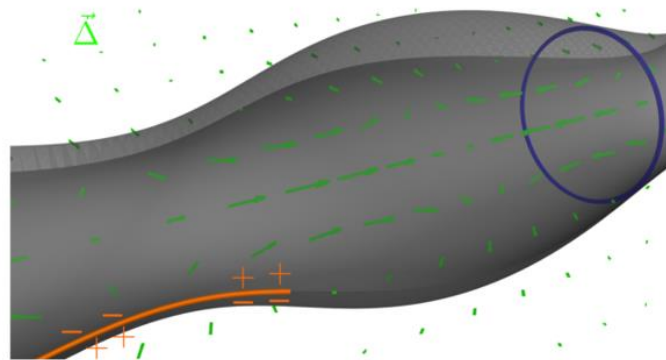


**Fig. 2.9** A nerve fibre in which the AP is an electromechanical pulse traveling along the axon. In orange, the changes in potential. Figure reprinted from (El Hady and Machta, 2015).

The mechanical and electrical features of the propagation are co-propagating and orthogonal waves, so that the resulting shape of the electro-mechanical wave is a soliton wave arising from the AP dynamics (not from mechanical nonlinearities as in (Heimburg

and Jackson, 2005)). From this, the generated strain is proportional to the square of the membrane voltage, as shown in (Alvarez and Latorre, 1978).

Considering a nerve as a tube made of an elastic core surrounded by a dielectric layer, as the AP passes, a co-propagating displacement is generated by the exchange of energy between the elastic core and the viscous extracellular medium. The displacements generated in the inner core of the axons is negligible, so that the mechanical wave is synchronous and linearly related with the AP (El Hady and Machta, 2015). This theory considers thermal affects arising from the electro-mechanical soliton, and that the heat production associated with the AP propagation is a near isothermal process. In contrast to (Heimburg and Jackson, 2005), this theory assumes that the heat exchange occurs faster than milliseconds, as in (Hodgkin and Huxley, 1952), neglecting other potential sources of heat (such as viscous heating and dissipation).

## 2.6 A Modelling Perspective

In this section, an overview of the multiscale approach for evaluation of neural functionality and neural damage is reported, highlighting the differences between the electrical and mechanical domains of neuronal investigation. For the purpose of this thesis, this section focuses on modelling techniques of computational neuroscience only, neglecting *in-vitro* and *in-vivo* studies of nervous cells and brain tissue.

### 2.6.1 An Overview on Brain Modelling

Current research interests in brain modelling aim at understanding head injury (Dixit and Liu, 2017; Garcia-Gonzalez et al., 2018; Hatam Samaka and Faris Tarlochan, 2013; Horgan and Gilchrist, 2003, 2004; Wright, 2012; Young et al., 2015), axonal injury (Garcia-Grajales et al., 2015; Jérusalem et al., 2014; Mohammadipour and Alemi, 2017; Wright and Ramesh, 2012), sport concussions (McCrorry et al., 2017), neuronal morphology (Abdellah et al., 2018; Kanari et al., 2018), and brain connectivity (Wazen et al., 2014) when medical conditions are present, such as Alzheimer's disease, depression and epilepsy (Wazen et al., 2014). Brain models vary according to application (Dixit and Liu, 2017; Samaka and Tarlochan, 2013), and can be based on computed tomography and magnetic resonance tomography images (Horgan and Gilchrist, 2003, 2004) or can be based on magnetic resonance imaging (Garcia-Gonzalez et al., 2017; Garcia-Gonzalez et al., 2018; Wazen et al., 2014). Accuracy and precision of finite element models of the brain are achieved by design, where the brain anatomy is replicated by the inclusion of a certain number of layers, and where material properties aim to conform to reality (Dixit and Liu, 2017; Samaka and Tarlochan, 2013). However, most macro-scale brain models do not

account for a detailed representation of the micro-scale structure of nervous cells to limit the computational cost (Dixit and Liu, 2017; Samaka and Tarlochan, 2013; Mohammadipour and Alemi, 2017; Wright and Ramesh, 2012), although cell models have been developed in this regard (Abdellah et al., 2018; Garcia-Grajales et al., 2015; Jérusalem et al., 2014; Kanari et al., 2018; Mohammadipour and Alemi, 2017; Wright and Ramesh, 2012). Recent published works of finite element models of nervous cells tend to simulate both the mechanical structure and the functionality of the cell (Garcia-Grajales et al., 2015; Jérusalem et al., 2014; Mohammadipour and Alemi, 2017), as its relevance has been demonstrated in experimental works (El Hady and Machta, 2015; Galbraith et al., 1993; Mosgaard et al., 2015; Mueller and Tyler, 2014; Zhang et al., 2001).

## 2.6.2 Multiscale Modelling of Neural Electrical Activity

Computational neuroscience has combined with computational systems biology, and neural multiscale modelling to simulate the neural electrical activity, including microscale modelling of cellular biology, neuronal networks, up to the macroscale of cognition and behaviour (Lytton et al., 2017). To advance the understanding of functionality and disease of the Central Nervous System, fundamental analysis of the phenomenon at both the micro and macroscale (i.e. cellular-to-tissue scale or tissue-to-cellular scale) is required (Lytton et al., 2017). The abstraction level of representation of a phenomenon or of a system is defined by the assumptions of the model both in space and time, see Fig. 2.10.

At the microscale or macroscale, different levels of details may or may not be included, depending on the general scope of the model. Therefore, the representation of a system at a certain scale has advantages and disadvantages in both simplified and detailed models.

In contrast, multiscale modelling provides a representation of the complexity of a system allowing for the integration of different phenomena (such as drug delivery at the cellular scale to traumatic brain injury) by connecting phenomena that occur at different space and time-scales, see Fig. 2.10. This approach opens the way to multiscale multiphysical modelling, exceeding what is possible with statistical analysis or highly simplified models.

Generally, there are two main directions for describing and analysing neural electrical activity: bottom-up, or top-down. The bottom-up approach refers to the analysis of the dynamics of neurons and/or groups of neurons that enhances the understanding of complex emergent behaviour in the brain activity. Here, the models include biophysical models (such as the HH model) and phenomenological models (such as the FitzHugh–Nagumo model and others (Siettos and Starke, 2016)). Microscale models have a limited

computational cost because of the high level of simplification where various aspects of the neuronal anatomy, synaptic and network functions are neglected. However, models such as the HH model or the Rössler Oscillator (Siettos and Starke, 2016)) are universal models that can capture both the dynamics observed in single neurons and the dynamics of groups of neurons and brain areas (Siettos and Starke, 2016).

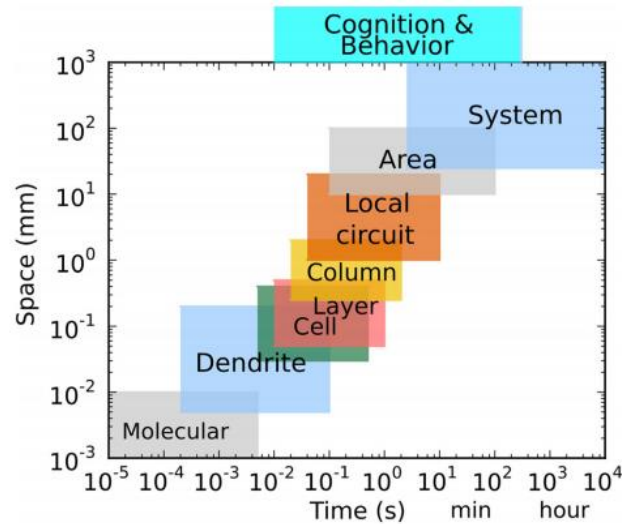


**Fig. 2.10** Temporal and spatial scales of organization in the nervous system. The proper spatial scale of “Cognition and Behaviour” depends on how it is being viewed and modelled. Scale overlap can be seen by noting that dendrite, cell and column share scale in both time and space, reflecting the fact that the same neural signals are being processed at these different levels. Figure reprinted from (Lytton et al., 2017).

In contrast, the top-down approach is a data-driven approach using data collected from medical imaging techniques (EEG, MEG, fMRI and others) to investigate the brain dynamics at the macroscale, while other models are used to extract the interactions of neurons at the microscopic scale (Siettos and Starke, 2016). Detailed models incorporating several measurable physiological variables suffer from high dimensionality, so constructing large network models of the brain or specific area of the brain can be computationally very expensive.

Fig. 2.11 shows the top-down approach (on the left, *linear* and *non-linear*) and the bottom-up approach (on the right, *biophysical* and *phenomenological*). This diagram summarises the procedures and methods to use in each case (Siettos and Starke, 2016). The best modelling approach is the one that generates the best representation of the system in question.

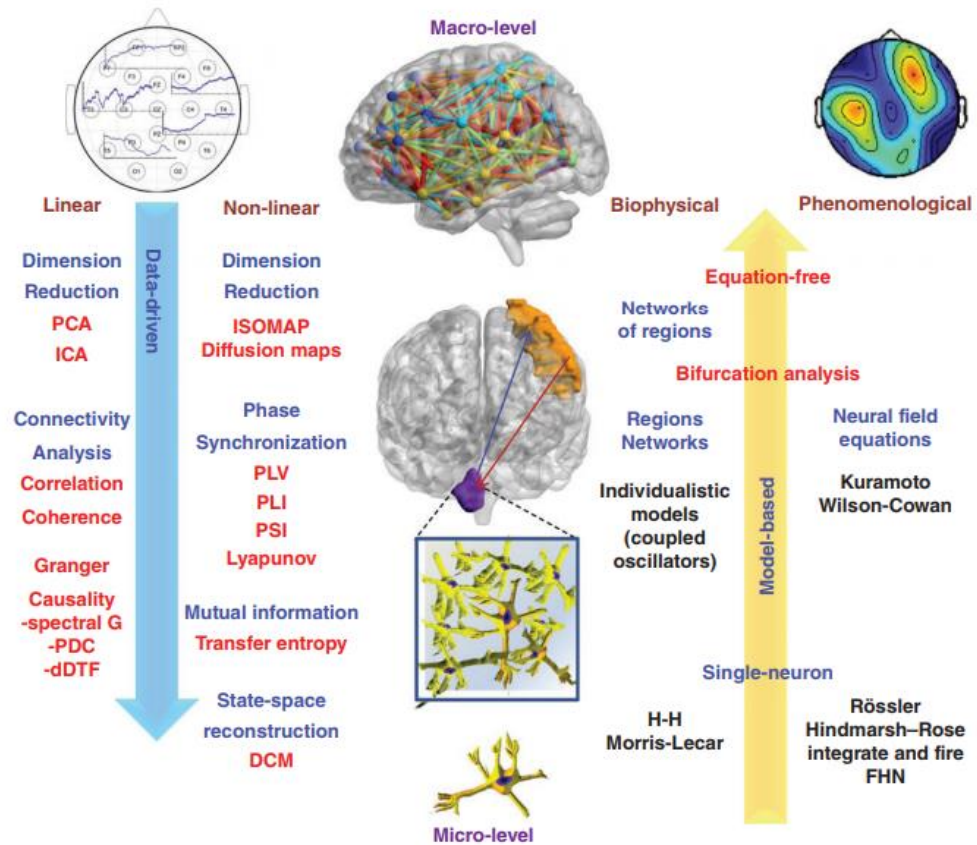


Fig. 2.11 Overview of the presented modelling methods and mathematical tools for brain dynamics. Figure reprinted from (Siettos and Starke, 2016).

As a result, the representation of neural electrical activity, as described by the HH model (Hodgkin and Huxley, 1952), is often implemented in computational modelling approaches that allows for the selection of a specific time step, using software such as MATLAB (Bossetti et al., 2008; Drapaca, 2015; Johnson and Chartier, 2017), NEURON (Voßen et al., 2007), NEURITE (Jérusalem et al., 2014), C/C++ and others. Here, the user defines a virtual representation of a single neuron or group of neurons, in which their physical representation and structure is implicit in the code. Although importing 3D medical images of the brain or anatomical images of neurons is an option, not all these software packages have the same capabilities for analysing neural electrical activity in a virtual network or from real images. A virtual investigation of the neural behaviour is usually less computationally expensive and is more flexible than using 3D/2D medical images.

COMSOL Multiphysics (Elia et al., 2009; Meffin et al., 2012) has been used to generate a 2D representation of the HH dynamics in a nerve model (Elia et al., 2009) or a 3D representation of the subthreshold stimulation of a nerve membrane (Meffin et al., 2012). COMSOL is a multiphysics software package, based on finite element analysis, which

allows the user to define a system geometry from a computer-aided design (CAD) model. Although the use of a 3D visualisation of the system has benefits, papers reporting 3D CAD models of neurons or brain regions are small in number compared to those that use the virtual representations described above, because of the high computational cost associated with the representation of electrical problems in three dimensions.

### 2.6.3 Multiscale Modelling of Nerve Structures

Similar to the representation of neural electrical activity, computational models of nerve structures and nerve structural mechanics are found both in the fields of biomechanics and cellular mechanics. Regardless of the specific modelling approach, such studies are typically computational investigations of the mechanical features only, neglecting the neuronal electrical activity. Published computational studies, such as (Chang et al., 2015; Jérusalem and Dao, 2012; Karami et al., 2009) amongst others, are typically focused on the evaluation of the mechanical performance of nervous cells, nerve fibres or brain tissue under mechanical loading, with a view to improving the mathematical characterisation of the constituent materials, and improving methods for medical diagnosis and disease treatments.

Such modelling approaches allow, for example, for the simulation of the conversion of energy from an external head impact into the local mechanical response in the brain tissue. Such local responses could initiate injury both at tissue and cellular level, initiating ischemia, necrosis and neurodegenerative pathologies (Lytton et al., 2017).

Inertial loads (such as sudden rotations or accelerations) lead to dynamic deformations that increase the risk of stretch and shear injuries for axons distributed throughout the brain parenchyma (Lajtha et al., 2009; Wright and Ramesh, 2012). As discussed in the previous chapter, Diffuse Axonal Injury (DAI) is a type of injury involving damage to the neural axons in the deep white matter regions of the brain. Damage in these regions can lead to the development of cognitive deficits. DAI is initiated by Traumatic Brain Injury (TBI) (Wright and Ramesh, 2012), but classified as an independent category of disease from TBI (Wright and Ramesh, 2012). This injury is considered to be a diffuse form of TBI (Ma et al., 2016; Wright and Ramesh, 2012).

Under inertial loading, the brain undergoes large deformations at constant volume (because it is confined in the skull). Deformations of brain tissue locally deform (stretch and shear) the axons, and the correlation between the magnitude of traumatic force and the degree of axonal damage varies depending on the location and the spatial orientation of the nerve fibre, as discussed by Lajtha et al., (2009), see Fig. 2.12. Axonal damage involves

damage of the axonal cytoskeleton, resulting in a loss of membrane integrity and impairment of axoplasmic transport, leading to changes in electrical signal propagation (Galbraith et al., 1993; Yu et al., 2012; Zhang et al., 2014). Although large-scale traumatic forces can result in uniform mechanical stresses at the microscopic scale, axonal damage is unevenly distributed throughout in the tissue because the myelin distribution varies between neighbouring axons (Lajtha et al., 2009; Su and Bell, 2016).

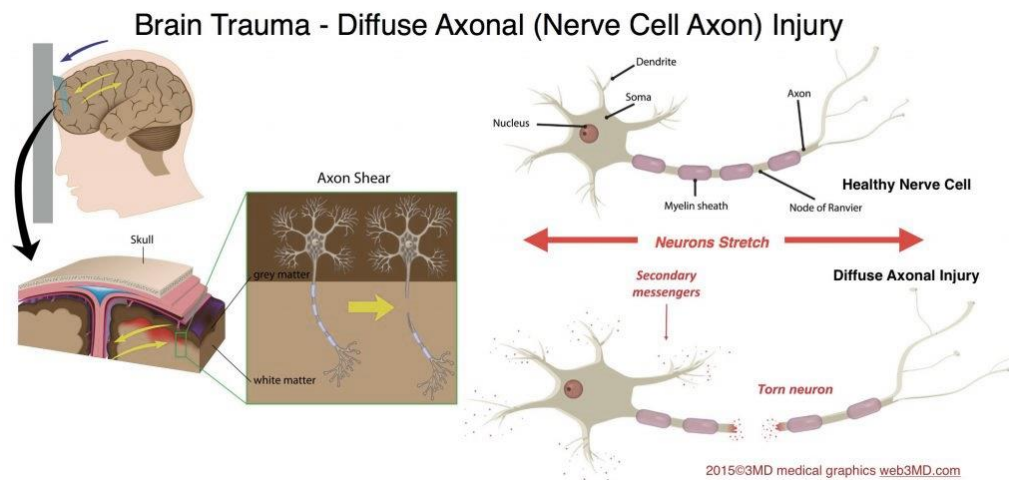


**Fig. 2.12** Inertial loads of the head lead to the shearing of brain tissue. At the cellular level, this shearing of brain tissue results in the stretching of neural axons which is thought to be one of the primary injury mechanisms of DAI. Figure reprinted from web3MD.com.

Experiments on neuronal cultures have shown axonal separation after trauma in unmyelinated axons for dynamic elongation greater than 65% (Lajtha et al., 2009; Smith et al., 1999). Higher risk of disconnection was found for unmyelinated axons compared to myelinated axons, for both shearing of axonal fibres due to trauma and physical stretch due to deformation of the brain (Su and Bell, 2016). Progressive demyelination occurs with DAI in myelinated axons, which may atrophy the surrounding white matter (Lajtha et al., 2009; Su and Bell, 2016). The severity of the axonal injury (called axotomy (Smith and Meaney, 2000) depends on fibre type and size (unmyelinated vs. myelinated nerve fibre), intra-axonal changes, and strain rate (Lajtha et al., 2009; Su and Bell, 2016; Smith and Meaney, 2000).

DAI damage decreases axonal elasticity and limits the recovery of the initial configuration following an impact. A general classification terms *primary axotomy* as primary disruption or disconnection produced during impact, and *secondary axotomy* as progressive or delayed alterations which occurs after a few milliseconds from the initial injury (Lajtha et al., 2009; Povlishock and Christman, 1995; Smith et al., 1999; Su and Bell, 2016; Smith and Meaney, 2000). Pathological features of DAI include a wide-ranging

variety of tissue lesions of the white matter (such as swelling of axonal mitochondria, thinning of the intermodal axoplasm, and development of myelin intrusions (Maxwell and Graham, 1997)), focal haemorrhages, contusions and other brain injuries (Lajtha et al., 2009; Ma et al., 2016; Smith et al., 1999; Wright and Ramesh, 2012). These features can develop over minutes, days or months (Smith et al., 1999). However, biological responses to rapid deformations are still not well understood (Lajtha et al., 2009).

Conventional medical imaging modalities often fail to identify DAI at the cellular level due to the lesions of the neighbouring tissue. Although the progressive course of this injury provides a window of time for therapeutic intervention, the inability to visualize the injury in-vivo allows the disease to progress, resulting in increasing difficulties in clinical treatments (Lajtha et al., 2009; Ma et al., 2016). DAI is, thus, responsible for long-lasting neurological impairments following TBI, with associated high rates of mortality (Lajtha et al., 2009; Smith et al., 1999; H. Wang and Ma, 2010). Computational models are, therefore, highly appropriate tools to generate insights into and further understand this injury and its effects.

## 2.7 Discussion

This chapter presents the HH model and its assumptions for describing the ionic mobility at the membrane of nervous cells (Hodgkin and Huxley, 1952). Up to now, the HH model is the only model capable of capturing the electrophysiology of neurons (Hodgkin and Huxley, 1952), and it has been extensively used in different fields of biomedical engineering (such as neural engineering and signal processing). However, recent articles discuss the importance of biophysical phenomena (such as electrostriction and piezoelectricity) occurring during the AP propagation to advance the understanding of cell-to-cell communications and neural networks (Mosgaard et al., 2015; Tyler et al., 2016). Based on this evidence, emerging theories about nerve pulses are competing to describe the experimentally observed multiphysics behind neural electrical activity. The mechanical soliton theory is an example of such an emerging theory. This is a thermodynamic theory that includes the phase transitions of the nerve membrane during the AP propagation, and the mechanical implications of these transitions (Heimburg and Jackson, 2005). Another theory proposes that pressure waves accompanying the AP are key for understanding the multiphysics of the neural electrical activity, and its propagation in axons with different calibre and type, as shown in the paper (Rvachev, 2010). Instead, another theory suggests to consider the mechanical waves generated by the exchange of

charges only across the nerve membrane during AP propagation (El Hady and Machta, 2015).

Although recent computational modelling efforts have been made to implement these emerging theories, technical limitations arise from the integration and coupling of multiphysical domains by using current computational software. Thus, describing the multiphysics of the neural electrical activity is both a theoretical challenge and a technical challenge with the current technology. Therefore, it is necessary to find a solution that may help the progress in this specific research context.

Against these limitations, this thesis proposes a novel approach to overcome the technical difficulties encountered in finite element modelling for coupling the electrical and mechanical activities only, shown to appear in nerve fibres. As in the published literature (El Hady and Machta, 2015; Rvachev, 2010), the AP is described by the HH model and, here, an extended version of the same model is tested and validated to include mechanical changes, as discussed in Chapters 3 and 4. Then, this approach is applied to the investigation of the electro-mechanical changes in fibres with different calibres, in Chapters 5 and 6. Further studies may include thermodynamic and optical effects as an additional step forward in developing the approach presented in this thesis.

---

## References Chapter 2

- Abdellah, M., Hernando, J., Eilemann, S., Lapere, S., Antille, N., Markram, H., and Schürmann, F. (2018). NeuroMorphoVis: A collaborative framework for analysis and visualization of neuronal morphology skeletons reconstructed from microscopy stacks. *Bioinformatics*, 34(13), i574–i582. <https://doi.org/10.1093/bioinformatics/bty231>
- Alvarez, O. and Latorre, R. (1978). Voltage-dependent capacitance in lipid bilayers made from monolayers. *Biophysical Journal*, 21(1), 1–17. [https://doi.org/10.1016/S0006-3495\(78\)85505-2](https://doi.org/10.1016/S0006-3495(78)85505-2)
- Appali, R., Petersen, S. and Van Rienen, U. (2010). A comparison of Hodgkin-Huxley and soliton neural theories. *Advances in Radio Science*, 8, 75–79. <https://doi.org/10.5194/ars-8-75-2010>
- Barz, H., and Barz, U. (2014). Pressure waves in neurons and their relationship to tangled neurons and plaques. *Medical Hypotheses*, 82(5), 563–566. <https://doi.org/10.1016/j.mehy.2014.02.012>
- Björnholm, L., Nikkinen, J., Kiviniemi, V., Nordström, T., Niemelä, S., Drakesmith, M., ... Paus, T. (2017). Structural properties of the human corpus callosum: Multimodal assessment and sex differences. *NeuroImage*, 152(February), 108–118. <https://doi.org/10.1016/j.neuroimage.2017.02.056>
- Bossetti, C.A., Birdno, M.J. and Grill, W.M. (2008). Analysis of the quasi-static approximation for calculating potentials generated by neural stimulation. *Journal of Neural Engineering*, 5(1), 44–53. <https://doi.org/10.1088/1741-2560/5/1/005>
- Chang, C.T., Chen, Y.-H., Lin, C.-C.K. and Ju, M.S. (2015). Finite element modeling of Hyper-viscoelasticity of peripheral nerve ultrastructures. *Journal of Biomechanics*, 48(10), 1982–1987. <https://doi.org/10.1016/j.jbiomech.2015.04.004>
- Dixit, P., and Liu, G. R. (2017). A Review on Recent Development of Finite Element Models for Head Injury Simulations. *Archives of Computational Methods in Engineering*, 24(4), 979–1031. <https://doi.org/10.1007/s11831-016-9196-x>

- Dong, X., Ospeck, M. and Iwasa, K.H. (2002). Piezoelectric reciprocal relationship of the membrane motor in the cochlear outer hair cell. *Biophysical Journal*, 82(3), 1254–1259. [https://doi.org/10.1016/S0006-3495\(02\)75481-7](https://doi.org/10.1016/S0006-3495(02)75481-7)
- Drapaca, C.S. (2015). An electromechanical model of neuronal dynamics using Hamilton’s principle. *Frontiers in Cellular Neuroscience*, 9, 271. <https://doi.org/10.3389/fncel.2015.00271>
- El Hady, A. and Machta, B.B. (2015). Mechanical surface waves accompany action potential propagation. *Nature Communications*, 6, 6697. <https://doi.org/10.1038/ncomms7697>
- Elia, S., Lamberti, P., and Tucci, V. (2009). A finite element model for the axon of nervous cells. In COMSOL (Ed.), *COMSOL Europe Conference* (pp. 1–7). Milan: COMSOL Conference 2009 Milan. <https://doi.org/http://www.comsol.com/paper/a-finite-element-model-for-the-axon-of-nervous-cells-6735>
- Engelbrecht, J., Peets, T., Tamm, K., Laasmaa, M. and Vendelin, M. (2016). On modelling of physical effects accompanying the propagation of action potentials in nerve fibres. *arXiv [physics.bio-ph]*, (January). Retrieved from <http://arxiv.org/abs/1601.01867>
- Engelbrecht, J., Tamm, K. and Peets, T. (2015). On mathematical modelling of solitary pulses in cylindrical biomembranes. *Biomechanics and Modeling in Mechanobiology*, (1980), 159–167. <https://doi.org/10.1007/s10237-014-0596-2>
- Galbraith, J.A., Thibault, L.E. and Matteson, D.R. (1993). Mechanical and electrical responses of the squid giant axon to simple elongation. *Journal of Biomechanical Engineering*, 115(1), 13–22. <https://doi.org/10.1115/1.2895464>
- Garcia-Gonzalez, D., Jayamohan, J., Sotiropoulos, S. N., Yoon, S. H., Cook, J., Siviour, C. R., ... Jérusalem, A. (2017). On the mechanical behaviour of PEEK and HA cranial implants under impact loading. *Journal of the Mechanical Behavior of Biomedical Materials*, 69(January), 342–354. <https://doi.org/10.1016/j.jmbbm.2017.01.012>
- Garcia-Gonzalez, D., Race, N. S., Voets, N. L., Jenkins, D. R., Sotiropoulos, S. N., Acosta, G., ... Jérusalem, A. (2018). Cognition based bTBI mechanistic criteria; A tool for preventive and therapeutic innovations. *Scientific Reports*, 8(1), 1–14. <https://doi.org/10.1038/s41598-018-28271-7>

- Garcia-Grajales, J. A., Rucabado, G., Garcia-Dopico, A., Pena, J. M., and Jerusalem, A. (2015). Neurite, a finite difference large scale parallel program for the simulation of electrical signal propagation in neurites under mechanical loading. *PLoS ONE*, 10(2), 1–22. <https://doi.org/10.1371/journal.pone.0116532>
- García-Grajales, J. A., Rucabado, G., García-Dopico, A., Peña, J. M., and Jérusalem, A. (2015). Neurite, a finite difference large scale parallel program for the simulation of electrical signal propagation in neurites under mechanical loading. *PLoS ONE*, 10(2), 1–22. <https://doi.org/10.1371/journal.pone.0116532>
- Giizelsu, A. N., and Akcasu, A. (1960). A piezoelectric model for nerve conduction. *Annals of the New York Academy of Sciences - Wiley Online Library*, 238(1). Retrieved from <http://onlinelibrary.wiley.com/doi/10.1111/j.1749-6632.1974.tb26802.x/pdf>
- Hatam, S., and Faris, T. (2013). Finite Element (FE) Human Head Models: Literature Review. *International Journal of Scientific & Technology Research*, 2(7), 17–31. [https://doi.org/Cranial study](https://doi.org/Cranial%20study)
- Heimburg, T. (1998). Mechanical aspects of membrane thermodynamics. Estimation of the mechanical properties of lipid membranes close to the chain melting transition from calorimetry. *Biochimica et Biophysica Acta - Biomembranes*, 1415(1), 147–162. [https://doi.org/10.1016/S0005-2736\(98\)00189-8](https://doi.org/10.1016/S0005-2736(98)00189-8)
- Heimburg, T. (2012). The capacitance and electromechanical coupling of lipid membranes close to transitions: The effect of electrostriction. *Biophysical Journal*, 103(5), 918–29. <https://doi.org/10.1016/j.bpj.2012.07.010>
- Heimburg, T. and Jackson A.C. (2005). On soliton propagation in biomembranes and nerves. *Proceedings of the National Academy of Sciences*, 102(28), 9790–9795. <https://doi.org/10.1073/pnas.0503823102>
- Heimburg, T. and Jackson A.C. (2007). The thermodynamics of general anaesthesia. *Biophysical Journal*, 92(9), 3159–3165. <https://doi.org/10.1529/biophysj.106.099754>
- Heimburg, T., Blicher, A., Mosgaard, L.D. and Zecchi, K. (2014). Electromechanical properties of biomembranes and nerves. *Journal of Physics: Conference Series*, 558, 12018. <https://doi.org/10.1088/1742-6596/558/1/012018>

- Hodgkin, A. L., and Huxley, A. F. (1952). A quantitative description of membrane current and its application to conduction and excitation in nerve. *Journal of Physiology*, 117, 500–544. [https://doi.org/10.1016/S0092-8240\(05\)80004-7](https://doi.org/10.1016/S0092-8240(05)80004-7)
- Iwasa, K., Tasaki, I. and Gibbons, R. (1980). Swelling of nerve fibers associated with action potentials. *Science*, 210(4467), 338–339. <https://doi.org/10.1126/science.7423196>
- Jérusalem, A., and Dao, M. (2012). Continuum modeling of a neuronal cell under blast loading. *Acta Biomaterialia*, 8(9), 3360–3371. <https://doi.org/10.1016/j.actbio.2012.04.039>
- Johnson, M. G., and Chartier, S. (2017). Spike neural models (part I): The Hodgkin-Huxley model. *The Quantitative Methods for Psychology*, 13(2), 105–119. <https://doi.org/10.20982/tqmp.13.2.p105>
- Kanari, L., Dłotko, P., Scolamiero, M., Levi, R., Shillcock, J., Hess, K., and Markram, H. (2018). A Topological Representation of Branching Neuronal Morphologies. *Neuroinformatics*, 16(1), 3–13. <https://doi.org/10.1007/s12021-017-9341-1>
- Kanari, L., Dłotko, P., Scolamiero, M., Levi, R., Shillcock, J., Hess, K., and Markram, H. (2018). A Topological Representation of Branching Neuronal Morphologies. *Neuroinformatics*, 16(1), 3–13. <https://doi.org/10.1007/s12021-017-9341-1>
- Karami, G., Grundman, N., Abolfathi, N., Naik, A. and Ziejewski, M. (2009). A micromechanical hyperelastic modeling of brain white matter under large deformation. *Journal of the Mechanical Behavior of Biomedical Materials*, 2(3), 243–254. <https://doi.org/10.1016/j.jmbbm.2008.08.003>
- Lajtha, A., Javitt, D., and Kantrowitz, J. (2009). Handbook of Neurochemistry and Molecular Neurobiology. Brain and Spinal Cord Trauma. (N. Banik & K. R. Swapan, Eds.), *Springer Reference* (3rd Edition, Vol. 281). Springer. <https://doi.org/10.1016/j.jns.2009.03.019>
- Lytton, W.W., Arle, J., Bobashev, G., Ji, S., Klassen, T.L., Marmarelis, V.Z., Sanger, T.D. (2017). Multiscale modeling in the clinic : Diseases of the brain and nervous system. *Brain Informatics*, 4(4), 219–230. <https://doi.org/10.1007/s40708-017-0067-5>

- Ma, J., Zhang, K., Wang, Z. and Chen, G. (2016). Progress of research on Diffuse Axonal Injury after Traumatic Brain Injury. *Neural Plasticity*, 2016, 7. <https://doi.org/10.1155/2016/9746313>
- Maxwell, W. L., and Graham, D. I. (1997). Loss of axonal microtubules and neurofilaments after stretch-injury to guinea pig optic nerve fibers. *Journal of Neurotrauma*, 14(9), 603–614. <https://doi.org/10.1089/neu.1997.14.603>
- Mcallister, T. W. (2011). Neurobiological consequences of traumatic brain injury. *Dialogues in Cinical Neuroscience*, 13(3), 287–300. Retrieved from <https://www.ncbi.nlm.nih.gov/pubmed/22033563>
- McCrory, P., Feddermann-Demont, N., Dvořák, J., Cassidy, J. D., McIntosh, A., Vos, P. E., ... Tarnutzer, A. A. (2017). What is the definition of sports-related concussion: A systematic review. *British Journal of Sports Medicine*, 51(11), 877–887. <https://doi.org/10.1136/bjsports-2016-097393>
- Meffin, H., Tahayori, B., Grayden, D.B. and Burkitt, A.N. (2012). Modeling extracellular electrical stimulation: I. Derivation and interpretation of neurite equations. *Journal of Neural Engineering*, 9(6), 65005. <https://doi.org/10.1088/1741-2560/9/6/065005>
- Mohammadipour, A., and Alemi, A. (2017). Micromechanical analysis of brain's diffuse axonal injury. *Journal of Biomechanics*, 65, 61–74. <https://doi.org/10.1016/j.jbiomech.2017.09.029>
- Mosgaard, L. D., Jackson, A. D., and Heimburg, T. (2012). Low-frequency sound propagation in lipid membranes. *Advances in Planar Lipid Bilayers and Liposomes*, 16, 51–74. <https://doi.org/10.1016/B978-0-12-396534-9.00002-7>
- Mosgaard, L. D., Zecchi, K. A., and Heimburg, T. (2014). Electrical properties of polar membranes. *arXiv*, 1411.6883v(3), 10. Retrieved from <http://arxiv.org/abs/1411.6883>
- Mosgaard, L.D., Zecchi, K. A. and Heimburg, T. (2015). Mechano-capacitive properties of polarized membranes. *Soft Matter*, 11(40), 7899–7910. <https://doi.org/10.1039/C5SM01519G>

- Mueller, J. K., and Tyler, W. J. (2014). A quantitative overview of biophysical forces impinging on neural function. *Physical Biology*. <https://doi.org/10.1088/1478-3975/11/5/051001>
- Perge, J. A, Niven, J.E., Mugnaini, E., Balasubramanian, V. and Sterling, P. (2012). Why do axons differ in caliber? *The Journal of Neuroscience*, 32(2), 626–638. <https://doi.org/10.1523/JNEUROSCI.4254-11.2012>
- Petrov, A.G. (2002). Flexoelectricity of model and living membranes. *Biochimica et Biophysica Acta - Biomembranes*, 1561(1), 1–25. [https://doi.org/10.1016/S0304-4157\(01\)00007-7](https://doi.org/10.1016/S0304-4157(01)00007-7)
- Plonsey, R. and Malmivuo, J. (1995). Bioelectromagnetism - Principles and applications of bioelectric and biomagnetic fields. (*University Press, Oxford*). Retrieved from <http://www.bem.fi/book/>
- Povlishock, J.T. and Christman, W. C. (1995). The pathology of traumatically induced axonal injury in animals and humans: A review of current thoughts. *Journal of Neurotrauma*, 12 (4), 555-564
- Rall, W. (2011). Core conductor theory and cable properties of neurons. In *Comprehensive Physiology - Handbook of physiology, the nervous system, cellular biology of neurons* (Vol. Chapter 3, pp. 39–97). Washington, D.C.: *Wiley Online Library*. <https://doi.org/10.1002/cphy.cp010103>
- Rvachev, M.M. (2010). On axoplasmic pressure waves and their possible role in nerve impulse propagation. *Biophysical Reviews and Letters*, 5(2), 73–88. <https://doi.org/10.1142/S1793048010001147>
- Siettos, C., and Starke, J. (2016). Multiscale modeling of brain dynamics: from single neurons and networks to mathematical tools. *Wiley Interdisciplinary Reviews: Systems Biology and Medicine*, 8(5), 438–458. <https://doi.org/10.1002/wsbm.1348>
- Smith, D. H., and Meaney, D. F. (2000). Axonal damage in traumatic brain injury. *The Neuroscientist*, 6(6), 483–495. <https://doi.org/10.1177/107385840000600611>
- Smith, D. H., Wolf, J. A., Lusardi, T. A., Lee, V. M., and Meaney, D. F. (1999). High tolerance and delayed elastic response of cultured axons to dynamic stretch injury. *The Journal of Neuroscience*, 19(11), 4263–4269. Retrieved from <http://www.jneurosci.org/content/19/11/4263.long>

- Su, E. and Bell, M. (2016). Diffuse axonal injury, translational research in traumatic brain injury, (*CRC Press/ Taylor and Francis group*), (pp. 1–37). Retrieved from <https://www.ncbi.nlm.nih.gov/books/NBK326722/?report=printable>
- Tahayori, B., Meffin, H., Dokos, S., Burkitt, A.N. and Grayden, D.B. (2012). Modeling extracellular electrical stimulation: II. Computational validation and numerical results. *Journal of Neural Engineering*, 9(6), 65006. <https://doi.org/10.1088/1741-2560/9/6/065006>
- Tasaki, I., and Byrne, P. M. (1990). Volume expansion of nonmyelinated nerve fibers during impulse conduction. *Biophysical Journal*, 57(3), 633–635. [https://doi.org/10.1016/S0006-3495\(90\)82580-7](https://doi.org/10.1016/S0006-3495(90)82580-7)
- Voßen, C., Eberhard, J.P. and Wittum, G. (2007). Modeling and simulation for three-dimensional signal propagation in passive dendrites. *Computing and Visualization in Science*, 10(2), 107–121. <https://doi.org/10.1007/s00791-006-0036-7>
- Wang, H. and Ma, Y. (2010). Experimental models of traumatic axonal injury. *Journal of Clinical Neuroscience*, 17(2), 157–162. <https://doi.org/10.1016/j.jocn.2009.07.099>
- Wright, R.M. and Ramesh, K.T. (2012). An axonal strain injury criterion for traumatic brain injury. *Biomechanics and Modeling in Mechanobiology*, 11(1–2), 245–260. <https://doi.org/10.1007/s10237-011-0307-1>
- Young, P. G., Qidwai, S. M., Bagchi, A., Kota, N., and Cotton, R. T. (2015). Developing a finite element head model for impact simulation in Abaqus. In *SIMULIA Community Conference* (pp. 1–13).
- Yu, N., Morris, C.E., Joós, B. and Longtin, A. (2012). Spontaneous excitation patterns computed for axons with injury-like impairments of Sodium Channels and Na/K pumps. *PLoS Computational Biology*, 8(9). <https://doi.org/10.1371/journal.pcbi.1002664>
- Zhang, P.C., Keleshian, A.M. and Sachs, F. (2001). Voltage-induced membrane movement. *Nature*, 413(6854), 428–432. <https://doi.org/10.1038/35096578>
- Zhang, Y.P., Cai, J., Shields, L.B.E., Liu, N., Xu, X.M. and Shields, C.B. (2014). Traumatic brain injury using mouse models. *Translational Stroke Research*, 5(1), 454–471. <https://doi.org/10.1007/s12975-014-0327-0>

## Chapter 3.      **Electro-Thermal Equivalent 3D Finite Element Model of a Single Neuron**

This chapter is concerned with the assessment and validation of the theory of electro-thermal equivalences for modelling neural electrical activity in finite element analysis. The material in this chapter has been published in *Cinelli, I., M. Destrade, M. Duffy, and P. E. McHugh. 2017. "Electro-thermal equivalent 3D Finite Element Model of a Single Neuron", IEEE Transactions on Biomedical Engineering, DOI 10.1109/TBME.2017.2752258.*

*Abstract — Objective:* A novel approach for modelling the inter-dependence of electrical and mechanical phenomena in nervous cells is proposed, by using electro-thermal equivalences in Finite Element (FE) analysis so that existing thermo-mechanical modelling tools can be applied. *Methods:* First, the equivalence between electrical and thermal properties of the nerve materials is established, and results of a pure heat conduction analysis performed in Abaqus CAE Software 6.13-3 are validated with analytical solutions for a range of steady and transient conditions. This validation includes the definition of equivalent active membrane properties that enable prediction of the Action Potential (AP). Then, as a step towards fully coupled models, electro-mechanical coupling is implemented through the definition of equivalent piezoelectric properties of the nerve membrane using the thermal expansion coefficient, enabling prediction of the mechanical response of the nerve to the AP. *Results:* Results of the coupled electro-mechanical model are validated with previously published experimental results of deformation for squid giant axon, a crab nerve fibre and a garfish olfactory nerve fibre. *Conclusion:* A simplified coupled electro-mechanical modelling approach is established through an electro-thermal equivalent FE model of a nervous cell for biomedical applications. *Significance:* One of the key findings is the mechanical characterization of the neural activity in a coupled electro-mechanical domain, which provides insights into the electro-mechanical behaviour of nervous cells, such as thinning of the membrane. This is a first step towards modelling 3D electro-mechanical alteration induced by trauma at nerve bundle, tissue and organ levels.

### 3.1 Introduction

The complexity of numerical modelling of the biomechanical behaviour of biological tissue is constantly increasing due the use of more realistic geometries and the incorporation of the non-linear behaviour of the tissue at different levels such as cells and fibres (Baillargeon et al., 2014; Crozier et al., 2016). Moreover, the increase in degrees of freedom comes with a higher computational cost (Baillargeon et al., 2014; Clayton et al., 2011; Crozier et al., 2016).

In contrast, numerical modelling of the electrical activity of biological tissue is based on completely different principles, and the requirements differ in terms of equations, boundary conditions and discretisation (Clayton et al., 2011; Crozier et al., 2016). Therefore, the electrical activity of tissue is generally modelled using dedicated electrical modelling software codes (Crozier et al., 2016; Elia et al., 2009).

Detailed electrophysiological models of cellular and tissue processes (Clayton et al., 2011) are now being linked to a large body of existing research for modelling the spread of electrical excitation throughout biological tissue such as nerve and cardiac tissue (Baillargeon et al., 2014; Crozier et al., 2016). From the perspective of combining the electrical and biomechanical behaviours, generally there are two different methods that have been used to integrate the electrical activity of the tissue into a biomechanical model: (i) as a simulated quantity where the output of an electrical model is input into a separate mechanical model (Crozier et al., 2016), or (ii) as an indirect measure of deformation of the tissue due to electrical contraction (Crozier et al., 2016).

Because the developments of models of electrical and mechanical processes have occurred largely independently, electro-mechanical coupling, involving the integration of both techniques, can result in a high computational cost, compromising the efficiency of the model and the scale of the problems that can be addressed. Independent electrical or mechanical models do not easily incorporate the effects of electro-mechanical coupling, such as bending or stretching of ion channels in cellular models, although they have been shown to be important in tissue electro-mechanics (Baillargeon et al., 2014; Clayton et al., 2011; Galbraith et al., 1993; Mueller and Tyler, 2014). Integrating the mechanical response of the tissue into models for electrical activity, and doing so in a computationally efficient way, is, therefore, a key challenge for the generation of models that can advance our fundamental understanding of electro-mechanics in biological tissue (Clayton et al., 2011).

Against this backdrop of limitations, this chapter presents an alternative approach to model coupled electro-mechanical phenomena of biological tissue in a single model, establishing this approach for the case of a single nervous cell. Electro-thermal equivalence is proposed here for modelling the simultaneous inter-dependence of electrical and

mechanical phenomena by using advanced facilities for coupled thermo-mechanical models provided in existing computational modelling tools (Cinelli et al., 2015; Tawfik et al., 2011; Wang, 1995). Abaqus CAE 6.13-3 is used in this work. In contrast to previous works using analogue quantities in modelling (Tawfik et al., 2011; Wang, 1995), here, the equivalences are utilised to (i) establish a thermal analogue implementation of the Cable Equation simulating the non-linear diffusion of electrical charges in nervous cells by using the Heat Equation (Cinelli et al., 2015; Meffin et al., 2012; Rall, 1977), and (ii) implement coupled electro-mechanical effects by applying a thermal expansion coefficient to describe the piezoelectric nature of the nerve membrane (Staworko and Uhl, 2008; Tawfik et al., 2011).

Analysis of neural signalling is normally carried out with computational software and open source electrical software (such as NEURON and NEURITE (Jérusalem et al., 2014)) for simulating electrical signal propagation, as discussed in Section 2.6.2. These software codes solve 1D electrical simulations, in which the material structure of the tissue is approximated or neglected. Hence, advanced electro-mechanical modelling of material characteristics cannot be carried out because of the missing 3D structure. In particular, capabilities for coupled electro-mechanical simulations are not readily available in computational software, but they are well developed for thermo-mechanical analysis. The thermo-electrical analogy therefore enables us to build on these established tools to gain insights into neural activity. The well-established nature of thermo-mechanical analysis ensures that the tools are reliable and can be reproduced and adopted in similar application fields. In addition, the approach enables modelling of fully coupled 3D electro-mechanical systems.

In contrast to other commercial Multiphysics software, such as COMSOL (Tahayori et al., 2012), Abaqus CAE 6.13-3 is an engineering design software that has been developed specifically to account for an extensive range of complex material constitutive relationships in the context of non-linear Finite Element (FE) analysis. In addition, Abaqus is extensively used in bioengineering thanks to the capabilities it provides for extracting detailed results at different levels in multiscale FE models. Although there is an option in Abaqus for simulating electromechanical systems, this tool is mainly used to model piezoelectric materials and it has limited capabilities for defining non-linear electrical properties as required to implement the HH model (Hodgkin and Huxley, 1952). Here, an electro-thermal analogy is proposed to enable more powerful neural modelling, where 3D coupled (equivalent) electro-mechanical models are resolved using established coupled thermo-mechanical computational tools. The equivalent electro-mechanical coupling in Abaqus enables the investigation of complex coupled phenomena at the nerve membrane

layer (Mosgaard et al., 2015), where there is a close link between electrical and mechanical quantities as in damage, trauma or diseases (Demerens et al., 1996; Galbraith et al., 1993).

The first aim of this chapter is the assessment of the electro-thermal equivalence and the identification of equivalent thermal material properties to model the electrical behaviour of biological tissue. The second aim is to investigate the coupled electro-mechanical deformation behaviour of nerve tissue, by combining the electro-thermal equivalences with a coupled thermo-mechanical modelling approach that models the biophysical phenomena at the nerve membrane (Zhang et al., 2001).

First, electro-thermal equivalence is demonstrated for a 3D nerve model and validated against analytical models for a range of non-symmetric boundary conditions under sub-threshold conditions (Hodgkin and Huxley, 1952; Meffin et al., 2012; Tahayori et al., 2012). The electro-thermal equivalent model is then adapted to account for the non-linear electrical behaviour of the nerve membrane, described by HH dynamics (Hodgkin and Huxley, 1952), and validated through comparison with space and voltage clamp experiments (Hille, 1977; Hodgkin and Huxley, 1952).

Secondly, an equivalent thermal expansion coefficient is applied to model the piezoelectric properties of the nerve membrane to investigate coupled electro-mechanical phenomena accompanying the AP (El Hady and Machta, 2015; Mosgaard et al., 2015; Zhang et al., 2001) as a function of physical length scale. Simulated results of deformation are compared with experimental observations of squid giant axon, crab nerve fibre and garfish olfactory nerve fibre (Mosgaard et al., 2015; Zhang et al., 2001).

The overall objective here is to establish, validate and demonstrate the performance of an effective and powerful platform for 3D electro-mechanical tissue modelling that can form the basis of further studies, for example to integrate the effects of trauma and to account for the resulting variations in conduction of signals (Galbraith et al., 1993a), and to scale up the approach to the nerve bundle, tissue and organ levels.

## **3.2 Materials and Methods**

### **3.2.1 Theory of the Equivalence**

The Cable Equation and the Heat Equation are partial differential equations of the same parabolic type (Rall, 1977; Wang, 1995). Hence, the mathematical solution of the steady state and transient Heat Equation, Eq. 3.1, below, can also be applied to the Cable Equation, Eq. 3.2, (Rall, 1977; Wang, 1995).

In the Heat Equation, Eq. 3.1,  $T$  is the temperature [ $^{\circ}C$  or  $K$ ],  $\rho$  is the density [ $kg/m^3$ ],  $c_p$  is the specific heat capacity [ $J/(kg K)$ ],  $k$  is the thermal conductivity [ $W/(mK)$ ], and  $Q$  is the heat source density [ $W/m^3$ ]; correspondingly, in the Cable Equation, Eq. 3.2, applied to the nerve,  $V_m$  is the transmembrane potential [ $V$ ],  $S_v$  [ $1/m$ ] denotes the surface-volume ratio,  $C_m$  [ $F/m^2$ ] is the nerve membrane capacitance,  $\sigma$  [ $S/m$ ] is the electrical conductivity of the membrane, and  $I_{ionic}$  [ $A/m$ ] is the ionic current.

$$\rho c_p \partial T / \partial t - \nabla \cdot (k \nabla T) + Q = 0 \quad \text{Eq. 3.1}$$

$$C_m S_v \partial V_m / \partial t - \nabla \cdot (\sigma \nabla V_m) + S_v I_{ionic} = 0 \quad \text{Eq. 3.2}$$

By substituting electrical for thermal quantities, the equivalence relationship becomes evident. Table 3.1 lists the quantities of the thermal and electrical systems in analogous form, based on the literature (Staworko and Uhl, 2008; Tawfik et al., 2011; Wang, 1995). It is interesting to note that while the equivalence between electrical and thermal conductivities is well known, the equivalence between electrical capacitance per unit area and specific heat capacity is not so obvious, although it is important for incorporating the effect of nerve capacitances in the thermal domain.

Coupling of the electro-mechanical effects of the AP (Hodgkin and Huxley, 1952) is achieved through modelling of the nerve membrane as a piezoelectric material (Mosgaard et al., 2015). By using the electro-thermal analogy (Staworko and Uhl, 2008; Tawfik et al., 2011), the electric field is equivalent to a thermal load, while the piezoelectric constants are equivalent to the thermal expansion coefficients. Therefore, mechanical effects of the piezoelectric properties of the nerve membrane can be incorporated in an equivalent electro-thermal model by defining an appropriate thermal expansion coefficient. The thermo-elastic strain-stress relation is given in Eq. 3.3, where  $\{\boldsymbol{\varepsilon}\}$  is the total strain vector,  $[\boldsymbol{\beta}]$  is the compliance matrix,  $\{\boldsymbol{\sigma}\}$  is the mechanical stress vector,  $\{\boldsymbol{\alpha}\}$  is the thermal expansion coefficients vector and  $\Delta T$  is the temperature difference (Staworko and Uhl, 2008; Tawfik et al., 2011).

$$\{\boldsymbol{\varepsilon}\} = [\boldsymbol{\beta}]\{\boldsymbol{\sigma}\} + \{\boldsymbol{\alpha}\}\Delta T \quad \text{Eq. 3.3}$$

Based on this relationship, the piezo-elastic relation is given in Eq. 3.4 where  $\{\boldsymbol{\delta}\}$  is the piezoelectric strain coefficient vector,  $h$  is the thickness of the piezoelectric layer and  $\Delta V$  is the voltage difference (Staworko and Uhl, 2008; Tawfik et al., 2011).

$$\{\boldsymbol{\varepsilon}\} = [\boldsymbol{\beta}]\{\boldsymbol{\sigma}\} + \{\boldsymbol{\delta}\}(\Delta V / h) \quad \text{Eq. 3.4}$$

Simulating the nerve membrane as the dielectric component of a parallel plate capacitor (Hodgkin and Huxley, 1952; Tawfik et al., 2011), the displacement follows the gradient of the electric field, approximated here as the voltage across the membrane divided by its thickness, using the approach presented in (Staworko and Uhl, 2008; Tawfik et al., 2011), see Eq. 3.4.

**Table 3.1 Electrical-Thermal Equivalences**

Electric Quantities	Symbol	Units	Thermal Quantities	Symbol	Units
Voltage	$V$	[V]	Temperature	$T$	[°C or K]
Current Per Unit Area	$I$	[A/m <sup>2</sup> ]	Heat Flux	$q$	[W/m <sup>2</sup> ]
Charge	$\Phi$	[C]	Energy	$E$	[J]
Electrical			Thermal		
Conductance Per Unit Area	$g$	[S/m]	Conductance per unit area	$c$	[W/(K m <sup>2</sup> )]
Electrical			Thermal Resistance per unit area	$R_{th}$	[(m <sup>2</sup> K)/W]
Resistance Per Unit Area	$R$	[Ω m <sup>2</sup> ]	Thermal Resistance per unit length	$r_{th}$	[K/(mW)]
Electrical			Specific Heat Capacity	$c_p$	[J/(kgK)]
Resistance Per Unit Length	$r$	[Ω/m]	Thermal Conductivity	$k$	[W/(mK)]
Electrical			Expansion Coefficient	$\alpha$	[1/K]
Capacitance Per Unit Area	$C$	[F/m <sup>2</sup> ]	$c_p\rho$	$\beta_t$	[(J K)/m <sup>3</sup> ]
Electrical			Thermal Expansion Coefficient	$\alpha$	[1/K]
Conductivity	$\sigma$	[S/m]			
Temperature Coefficient	$\alpha$	[1/V]			
$C_m S_v$	$\beta_e$	[(C V)/m <sup>3</sup> ]			
Piezoelectric Strain Coefficient	$\delta$	[m/V]			

### 3.2.2 Neuron Structure

Neurons or nervous cells are electrically excitable cells carrying electrical signals, called action potentials (or spikes). Each neuron consists of a long cylindrical nerve fibre called the axon, see Fig. 2.1, which connects between the neuron extremities or dendrites, as discussed in Section 2.1. A thin membrane sheath separates the axon (i.e. axoplasm or

Intracellular Media, ICM) from the external saline solution (Extracellular Media or extracellular space, ECM).

In the literature, the simplest model of a neuron is a 1D uniform cylindrical axon as described by the 1D Cable Equation, Eq. 3.2, where the current flow is predominantly inside the core along the cylindrical axis and the extracellular resistivity is negligible (extracellular iso-potentiality), as written in the paper (Rall, 1977). Previous studies have been performed on the mathematical derivation of the 3D Cable Equation, where longitudinal and transversal stimuli can be modelled to simulate the exchange of electrical charges in one 3D fibre, when located within a bundle of fibres (Meffin et al., 2012; Tahayori et al., 2012). Due to the 3D geometry, a finite thickness for both the ICM and ECM is introduced, whereas the 1D Cable Equation only considers the axon thickness, as shown by Rall (1977). In the 3D case, the confined thickness of the ECM represents the physical distance between fibres within a bundle (Plonsey and Barr, 2007; Meffin et al., 2012; Tahayori et al., 2012), and it is known to have similar finite electrical conductivity as the ICM (Gleixner and Fromherz, 2006; Meffin et al., 2012; Tahayori et al., 2012). Thus, when combining the Cable Equation assumptions with the confined ECM thickness assumption, the extracellular resistance per unit length ( $r_{ECM}$ ) is much greater than the intracellular resistance ( $r_{ICM}$ ), i.e.  $r_{ECM} \gg r_{ICM}$  [ $\Omega/m$ ] (Plonsey and Barr, 2007; Meffin and Kameneva, 2011; Meffin et al., 2012), for better accuracy of the analytical solutions (i.e. with an error of less than 5%) where current is predicted to flow predominantly along the fibre axis (Tahayori et al., 2012).

Recent experimental evidence has uncovered complex interactions of biophysical phenomena at the membrane layer in nervous cells during signalling (Mosgaard et al., 2015; Mueller and Tyler, 2014). Since it has been found that the membrane is the main piezoelectric component of the neurite (Zhang et al., 2001), it is imperative to accurately model its structure in coupled electro-mechanical studies. In contrast to (Elia et al., 2009; Tahayori et al., 2012), in this work, the membrane layer has a finite thickness, so that the thin layer approximation for the membrane is not assumed. Hence, here, an isotropic 3D cylindrical model of a nervous cell (including ICM, membrane and thin ECM) is modelled in FE as a cable of semi-infinite length to simulate the charge distribution across an unmyelinated neurite (Elia et al., 2009; Rall, 1977), see Fig. 3.1.

The length of the cylindrical model,  $l$ , see Fig. 3.1 (a), was chosen to be at least ten times the electronic length constants (Tahayori et al., 2012), here  $500 \mu m$ , see Fig. 3.1 (a). Then the radii are:  $a_{ICM} = 0.477 \mu m$  for the ICM,  $a_M = 0.480 \mu m$  for the membrane, and  $a_{ECM} = 0.500 \mu m$  for the ECM (Plonsey and Barr, 2007; Meffin et al., 2012), see Fig. 3.1 (a). The diameter of this fibre is within the range of the human corpus

callosum (Björnholm et al., 2017). Here, the membrane's thickness is considered to be that of the central dielectric core of a planar capacitor (about 3 nm), without polar head groups (Plonsey and Barr, 2007). The size of each cross-section is chosen to be within the range of physiological values (Meffin and Kameneva, 2011; Tahayori et al., 2012) for a necessary comparison with the analytical solutions (Meffin and Kameneva, 2011; Tahayori et al., 2012).

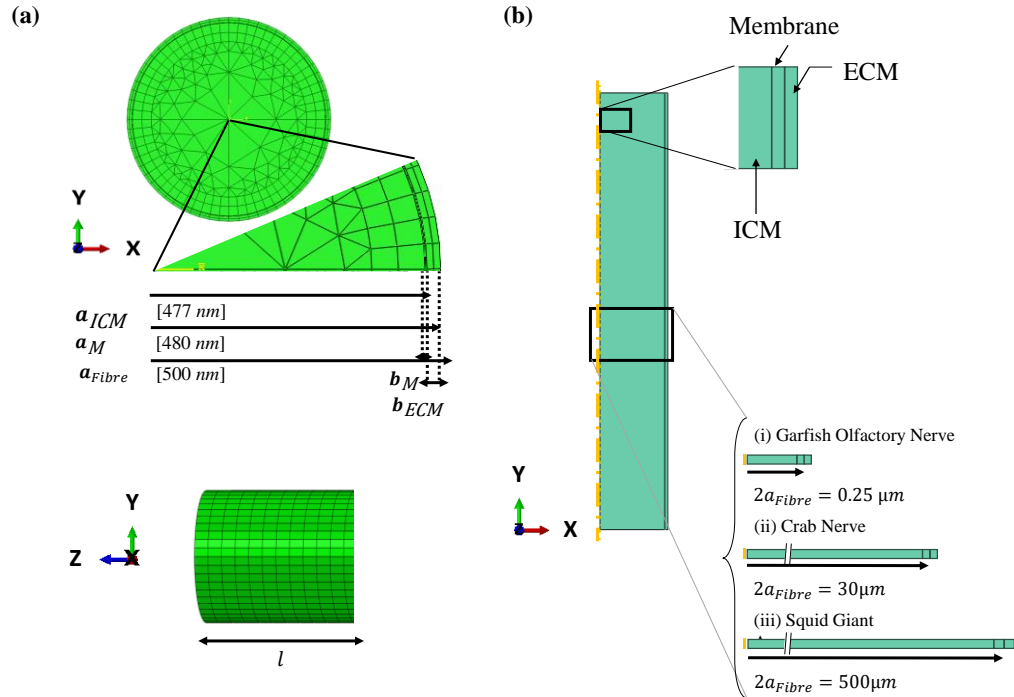


**Fig. 3.1** In (a), a schematic illustration of the unmyelinated nerve and myelinated nerve. The ECM, membrane and ICM are highlighted. The length of the fibre is  $l$ . The radius of a nerve fibre from the ICM to the ECM is  $a_{Fibre}$ . In (b), frontal and lateral views of the mesh of the 3-layer cylindrical model of the nervous cell with 500  $\mu m$  length are shown. The ICM and membrane radii are  $a_{ICM}$  and  $a_M$  respectively. The membrane and ECM thicknesses are  $b_M$  and  $b_{ECM}$ , respectively. In (b), the 3-layer axisymmetric model of the membrane. Underneath, the 3-layer axisymmetric models of squid giant axon, crab nerve fibre and garfish olfactory nerve fibre with diameters equal to 500  $\mu m$  (Hodgkin and Huxley, 1952; Rall, 1977), 30  $\mu m$  (Hille, 1977) and 0.25  $\mu m$  (Easton, 1971) respectively.

### 3.2.3 Material Properties

Table 3.2 lists the values of the material properties, directly inputted into Abaqus CAE 6.13-3, in which the calculated electrical quantities are assigned to the corresponding thermal equivalent quantities. Due to the constant cross-sectional area, the model is a composite continuous compartment (Bédard et al., 2004).

Both ICM and ECM are purely conductive and homogeneous, see Fig. 3.1, with equal conductivities (Gleixner and Fromherz, 2006; Meffin et al., 2012; Tahayori et al., 2012). The resistivity of the ICM,  $\rho_{ICM}$ , and of the ECM,  $\rho_{ECM}$ , are both set equal to  $0.1 \Omega m$ , and derivation of the membrane resistivity is based on a membrane resistance,  $R_m$ , equal to  $10 \Omega m^2$  (Rall, 1977), all within the range considered in previous works (Meffin and Kameneva, 2011; Meffin et al., 2012).

The steady state and time varying electrical behaviours are analysed based on the Electro-Quasi-Static (EQS) approximation for diffusion of charge in biological media (Moulin et al., 2008; Wang, 1995). The EQS leads to a simplification in Maxwell's equations by ignoring the magnetic field, inductive effects (Bossetti et al., 2008), (electromagnetic) wave propagations at low frequency electro-dynamics (less than  $1 kHz$  (Bossetti et al., 2008; Joucla and Yvert, 2012)) and non-ideal capacitive effects, such as dielectric loss factor (Appali et al., 2010; Bédard and Destexhe, 2008).

For simplicity, the frequency dependence of the neuron constituent material properties, such as permittivity ( $\epsilon$ ) and conductivity ( $\sigma$ ), is neglected due to the EQS assumption (Bédard and Destexhe, 2009; Bédard et al., 2004). This also aligns with previous works where the inclusion of nonhomogeneous media (such as the proposed nervous cell structure) has been shown to accurately account for frequency-dependent behaviour when the transmission of electric signals (such as the AP) occurs at frequencies  $\omega$  higher than  $100 Hz$  ( $\omega \epsilon / \sigma \gg 1$ ) (Bédard and Destexhe, 2008; Bédard et al., 2004; Bossetti et al., 2008). The ICM and ECM are assigned relative permittivity values equal to the static relative permittivity of water, i.e. 80 (Plonsey and Barr, 2007; Elia et al., 2009); the value for the membrane is 3.5, based on a capacitance  $C_m$  (Hodgkin and Huxley, 1952) equal to  $10^{-14} F / \mu m^2$ , see Table 3.2. With constant values for  $\sigma$  and  $\epsilon$ , the membrane of the neurite is modelled as a distributed (passive) parallel resistor–capacitor structure in the subthreshold regime (Plonsey and Barr, 2007; Meffin et al., 2012).

The trans-membrane electrical behaviour of a fibre has two distinct conditions of interest: (i) the subthreshold excitation condition (prior to AP initiation), where the membrane is passive, and (ii) the trans-threshold (near-, upper-threshold or active state) condition, where the membrane is active (Plonsey and Barr, 2007). In upper-threshold simulations, the membrane conductivity  $\sigma_m$  changes in response to the membrane voltage as described by the HH dynamics (Hodgkin and Huxley, 1952).

**Table 3.2 Material Electrical Properties**

Material Properties	Units	ICM	Membrane	ECM
Electrical Conductivity	$S/\mu m$	$10^{-5}$	$3.14 \cdot 10^{-13}$	$10^{-5}$
Electrical Capacitance	$F/\mu m^2$	$1.48 \cdot 10^{-15}$	$10^{-14}$	$3.54 \cdot 10^{-14}$
Density	$kg/\mu m^3$	$10^{-18}$	$10^{-18}$	$10^{-18}$

Similarly, the membrane electrical capacitance per unit area (and thus the relative permittivity) is a constant (Hodgkin and Huxley, 1952) for a non-coupled electro-thermal analysis, while it varies to account for electrostriction in the coupled electro-mechanical model (Alvarez and Latorre, 1978). As described in Section 2.4.1, the electrical capacitance per unit area,  $C_m(V)$ , changes as the square of the voltage (Alvarez and Latorre, 1978; El Hady and Machta, 2015). Substituting the values of the fractional increase constant (Alvarez and Latorre, 1978), Eq. 2.10 can be rewrite as Eq. 3.5. The membrane capacitance at physiological conditions,  $C_m(0)$ , is  $1 \mu F/cm^2$  (Alvarez and Latorre, 1978), see Eq. 3.5.

$$C_m(V) = C_m(0)[1 + 0.02(V - \Delta V)^2] \quad \text{Eq. 3.5}$$

Additionally, in the coupled electro-mechanical model, the piezoelectric effect is only relevant in the through-thickness direction, and it is thus assumed to be only one non-zero component for  $\delta$ , approximately  $1 \text{ nm}$  per  $100 \text{ mV}$  (Zhang et al., 2001) in that direction, see Eq. 3.4 and section 2.4.2.

### 3.2.4 Subthreshold Model: Mesh and Boundary Conditions

To ensure numerical accuracy, the minimum FE size is chosen to be smaller than the thickness of the membrane, here  $3 \text{ nm}$ . As shown in Fig. 3.1 (a), the mesh density changes through the thickness of the intracellular media: the inner core was partitioned with a coarse mesh of the wedge element type, and from a radius of  $350 \text{ nm}$  outwards, the mesh is more regular and dense with hexahedral elements. The mesh design was motivated by computational efficiency. The membrane and the extracellular media were defined as solid bi-layers within the mesh. In this way, the same hexahedral element was assigned to the regions where higher levels of charge are exchanged. The model consists of 1,276,922 nodes, 1,426,524 elements, where 1,379,904 are linear hexahedral elements (DC36.3 in

Abaqus) and 46,620 are linear wedge elements (DCC36.5D) for convection/diffusion analysis with dispersion control.

The practical case of a standard stimulating electrode on a neurite has been previously modelled using electrical FE simulation (Meffin and Kameneva, 2011; Meffin et al., 2012; Tahayori et al., 2012), where the current spreads both along the fibre and across its layers. In order to reproduce this phenomenon, the (passive) membrane is modelled as a homogeneous conducting cylinder with a non-uniform voltage  $V$  [V], Eq. 3.6, or current density  $I$  [ $A/m^2$ ] boundary condition, Eq. 3.7, applied as external stimulation (Meffin et al., 2012; Tahayori et al., 2012). In Eq. 3.6 - Eq. 3.8,  $n$  is the mode number of the input signal, which accounts for variable sinusoidal voltage or current distributions acting along the azimuthal coordinate  $\theta$  of the neurite. The temporal frequency  $\omega$  acts over time,  $t$ , as shown in Eq. 3.6 and Eq. 3.7, respectively. The longitudinal width of the current and voltage stimuli is controlled through the standard deviation,  $s$ , of a Gaussian distribution of the input function along the axial dimension,  $z$ , according to Eq. 3.8.

$$V_{input}(z, \theta, t, n) = V(n)G(z) \cos(n\theta) \cos(\omega t) \quad \text{Eq. 3.6}$$

$$I_{input}(z, \theta, t, n) = I(n)G(z) \cos(n\theta) \cos(\omega t) \quad \text{Eq. 3.7}$$

$$G(z) = (2\pi)^{-\frac{1}{2}} e^{-z^2/2s^2} \quad \text{Eq. 3.8}$$

At this stage, the magnitude of the voltage and current stimuli is constrained to be within the subthreshold regime, i.e. the trans-membrane voltage contains no AP.

### 3.2.5 Active Membrane Model: Mesh and Boundary Conditions

For validation against the HH model (Hodgkin and Huxley, 1952), the non-linear dynamic behaviour of the membrane is simulated assuming axisymmetric uniformity of the potential (i.e. longitudinal mode); hence, an isotropic axisymmetric model is used, based on a 2D longitudinal section of the full nerve fibre, see Fig. 3.1 (b) (Plonsey and Barr, 2007). Therefore, in this case all the field quantities are assumed to be independent of the azimuthal angle of the cylinder. The model is made of 15,652 nodes and 15,300 axisymmetric quadrilateral elements designed for convection/diffusion analysis with dispersion control (type DCCAX4D in Abaqus). Thanks to the symmetry of the geometry and boundary conditions, the use of an axisymmetric geometry reduces the computational cost of the simulation. However, our approach to modelling the non-linear dynamic

behaviour is valid for 3D models as well, and as such the 3D model of the nervous cell is also used here, see Fig. 3.1, for the subthreshold model.

The left side of Fig. 3.2 shows the flowchart for implementing the HH model in which the Gaussian voltage distribution input elicits the AP, generating a flow of ionic currents across the membrane as described in (Hodgkin and Huxley, 1952). On the right side of Fig. 3.2, the thermal equivalent implementation of the HH model is illustrated for 3D distributions of voltages and currents, which are simulated as temperature and heat flow distributions, respectively in the 3D FE thermal model of the nervous cell. The inclusion of the HH dynamics (Hodgkin and Huxley, 1952), see Eq. 3.9, leads to the non-linear cable equation, where the speed and shape of the solution are defined by the standard HH voltage gating variables ( $\bar{g}_K, \bar{g}_{Na}, \bar{g}_l; V_K, V_{Na}, V_l$  – see Appendix A for further details).

$$\frac{a_{ICM}}{2R_{ICM}v^2} \frac{\partial^2 V}{\partial t^2} = C_M \frac{\partial V}{\partial t} + \bar{g}_K n^4 (V - V_K) + \bar{g}_{Na} m^3 h (V - V_{Na}) + \bar{g}_l (V - V_l) \quad \text{Eq. 3.9}$$

In Abaqus CAE, the non-linear behaviour of the membrane is implemented using user-defined subroutines to describe the changes in membrane thermal equivalent conductivity with membrane voltage, as in (Hodgkin and Huxley, 1952) (UMATHT, USDFIELD and DISP subroutines in Abaqus).

The linear Cable Equation, Eq. 3.2, and the Heat Equation, Eq. 3.1, are diffusive equations with no (linear) travelling-wave component, whose solutions correspond to passive, diffusive spreading, as can be seen in the book (Nelson, 2004). Here, in the equivalent electro-thermal domain, the AP is a localized voltage distribution along the fibre in a dissipative system, as discussed by Remoissenet (1999), described by an RC circuit, according to the EQS assumption (Bédard et al., 2004). If required, the propagation of the AP can be implemented as a moving heat source at the membrane, derived from a wave-like solution of the Heat Equation.

### 3.2.6 Equivalent Coupled Electro-Mechanical Model: Mesh and Boundary Conditions

Numerous mechanical events have been experimentally observed in neuronal membrane excitability and are thought to play an important role in regulating neuronal activity (El Hady and Machta, 2015; Mosgaard et al., 2015; Mueller and Tyler, 2014). Herein, the electro-thermal equivalences are assessed as a method for investigating the mechanical displacement arising from neural transmission. In this model, the mechanical

features are electrically driven phenomena, implemented through a thermal expansion coefficient that represents the piezoelectric effect (El Hady and Machta, 2015) as illustrated in Fig. 3.2.

The equivalent electro-mechanical coupling is assessed for three different models, simulating the electro-mechanical responses of isolated unmyelinated fibre of the squid giant axon, a crab nerve fibre, and a garfish olfactory nerve fibre with diameters equal to  $500\ \mu\text{m}$  (Hodgkin and Huxley, 1952; Rall, 1977),  $30\ \mu\text{m}$  (Hille, 1977) and  $0.25\ \mu\text{m}$  (Easton, 1971) respectively, see Fig. 3.2. As in (El Hady and Machta, 2015), the width and amplitude of the Gaussian distribution function of the excitation voltage for each fibre is dependent on fibre dimensions, as shown in Fig. 3.5.

Homogeneous, isotropic and incompressible mechanical properties are assigned to the ICM, membrane and ECM for each nervous cell type (El Hady and Machta, 2015) for simplicity. The density of the medium is set to  $10^3\ \text{kg m}^{-3}$ , i.e. the same as water (El Hady and Machta, 2015). Size-independent elastic material properties are assigned to each animal. In Case I, each nervous cell is assumed to be made of different regions with the same mechanical properties (Alvarez and Latorre, 1978; El Hady and Machta, 2015) (where Young's Modulus is  $1.4 \times 10^8\ \text{Pa}$  (Alvarez and Latorre, 1978)). In Case II, only the membrane and the ICM have the same Young Modulus ( $63,981.69\ \text{Pa}$  (Abolfathi et al., 2009)), while the ECM has a different value ( $23,195.14\ \text{Pa}$  (Abolfathi et al., 2009)). This allows for the effects of elastic properties to be assessed.

Each nervous cell type is modelled with an axisymmetric geometry assumption, simulating a nerve fibre with semi-infinite length. The minimum FE size is  $2.14 \times 10^{-4}\ \mu\text{m}$  at the membrane layer. The models consist of: 124,031 nodes and 120,000 4-node axisymmetrical coupled thermo-mechanical elements (CAXA4RT) for the garfish olfactory nerve; 33,033 nodes and 32,000 CAXA4RT elements for the crab nerve fibre and 17,535 nodes and 170,000, CAXA4RT elements for the squid giant axon. An encasté boundary condition is enforced at the origin of each model, while the longitudinal displacement is limited along the axis of symmetry and for the nodes at  $y = 0$ , see Fig. 3.2.

### 3.3 Results

Electro-thermal equivalences are validated for a 3D neuron model (see Fig. 3.1 (a)) in both subthreshold and upper-threshold regimes with non-symmetrical voltage and current boundary conditions. Then, the electro-mechanical coupling is validated under upper-threshold conditions.

In the reported results, the trans-membrane potential is referred to as the membrane potential for subthreshold stimulation and the AP for upper-threshold stimulation. Through the thermo-mechanical analogy, the temperature (NT11) representing voltage is the nodal temperature variable in Abaqus CAE.

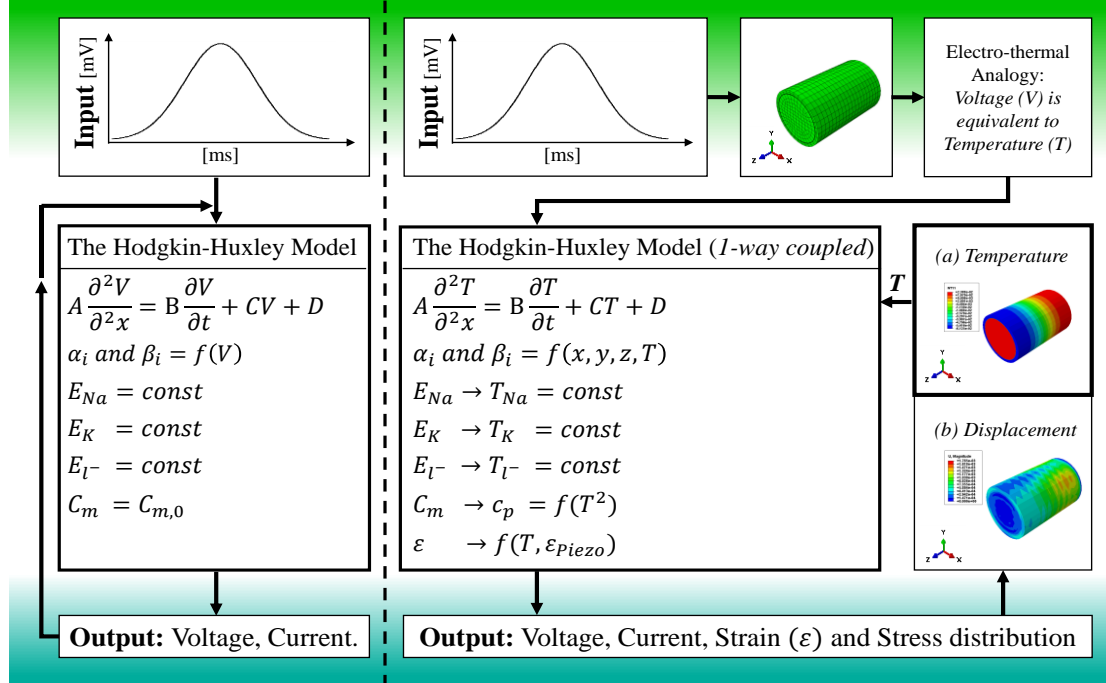


**Fig. 3.2** Flowchart of the code describing the active behaviour of the nerve's membrane: on the left the HH dynamics (Hodgkin and Huxley, 1952) and on the right the *I-way* coupled HH dynamics. Here, a Gaussian voltage distribution elicits the AP in a 3D model of a nervous cell. By using electro-thermal equivalences, the HH dynamics are implemented as an equivalent thermal process, in which the membrane's conductivity changes as in (Hodgkin and Huxley, 1952) and the capacitance,  $C_m$ , changes as in (Alvarez and Latorre, 1978).

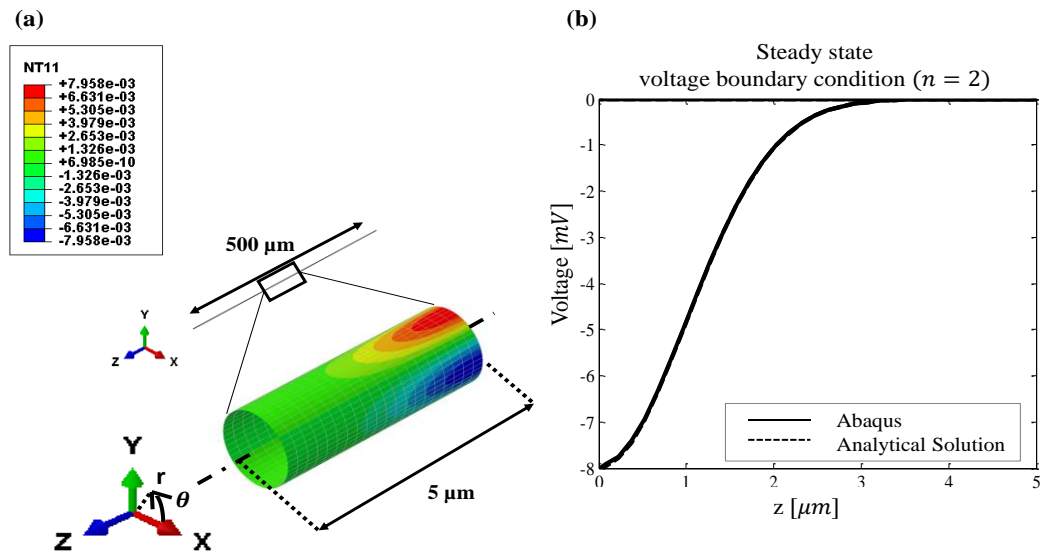
### 3.3.1 Subthreshold Model

Fig. 3.3 shows the 3D model results for the steady state voltage boundary conditions of the nerve membrane. Here, only the results for the subthreshold model with  $n = 2$  are shown. In Fig. 3.3 (a), the contour plots show a part of the neurite's section with  $5 \mu\text{m}$  and  $15 \mu\text{m}$  length, respectively. In Fig. 3.3 (a) and (b), a uniform voltage boundary condition, Eq. 3.6, ( $V(2) = 20 \text{ nVm}$ ) with a Gaussian distribution, Eq. 3.8, was applied at the outer surface of the ECM ( $s = 1 \mu\text{m}$ ), similar to that applied in (Tahayori et al., 2012). In Fig. 3.3 (b), the voltage distribution in the cylinder in the axial direction is shown and compared with results produced by the analytic solution presented in (Tahayori et al., 2012), where

close agreement between both models is confirmed. Similarly, results for current boundary conditions can be found in Appendix A.

### 3.3.2 Active Membrane Model

The equivalent implementation of the HH dynamics has been validated according to the voltage clamp and space clamp procedures (Hodgkin and Huxley, 1952), applying a clamped voltage, Fig. 3.4 (a), and current stimulus,  $I$ , Fig. 3.4 (c), respectively. The sodium,  $I_{Na}$ , potassium,  $I_K$ , and leak,  $I_l$ , currents are the ionic currents of the nerve membrane, see Fig. 3.4 (d), as in (Hodgkin and Huxley, 1952). The generated ionic membrane currents are within physiological values (Hodgkin and Huxley, 1952) and are reported in Fig. 3.4 (b) and (d), respectively, for each input. Additional results about the gating variables can be found in Appendix A.



**Fig. 3.3 Voltage boundary condition.** (a) Spatial variation of the membrane voltage  $[V]$ , here NT11, in steady state ( $\omega = 0$ ) is shown for  $n = 2$  (Tahayori et al., 2012), see Eq. 3.6. The azimuthal coordinate is  $\theta$ . In (b), the voltage distribution in the axial direction at the membrane layer, at  $x = 1 \mu\text{m}$ ,  $y = 0 \mu\text{m}$ , from  $z = 0 \mu\text{m}$  to  $z = 5 \mu\text{m}$  of the 3 layer cylinder model. Here  $V(2) = 20 \text{ nVm}$  and  $s = 1 \mu\text{m}$  (Tahayori et al., 2012), see Eq. 3.6 - Eq. 3.8.

### 3.3.3 Equivalent Electro-Mechanical Coupling

Here, the AP is implemented as a voltage source, whose amplitude is a Gaussian distribution with fixed spatial width that depends on the nerve fibre dimensions, as in (El Hady and Machta, 2015; Hodgkin and Huxley, 1952), see Fig. 3.5.

For each of the three test cases considered, the AP is applied as an equivalent thermal excitation to calculate the membrane displacements, stresses and strains in the middle of the membrane layer (at the peak of the AP), see Fig. 3.5. Here, the piezoelectric coefficient is equivalent to the thermal expansion coefficient, Table 3.1, and it has a finite value (greater than zero) for the nerve membrane. The ECM and ICM have a piezoelectric coefficient value close to zero, so these material sections do not undergo displacement of the same order as those found at the nerve membrane, because experimental evidence of piezoelectricity has been measured at the nerve membrane only (Zhang et al., 2001).

A decrease in thickness of about 23% is found at the membrane, consistent with what is experimentally observed (16% (Heimburg and Jackson, 2005; Mosgaard et al., 2015) and 21.6% (Iwasa et al., 1980)).

Although changes in membrane density strongly affect the membrane capacitance during signalling (Heimburg and Jackson, 2005; Mosgaard et al., 2015), here, the capacitance per unit area is a function of the square of voltage only, calculated approximately as 0.03% during the AP, once again consistent with physiological conditions (less than 1% (Alvarez and Latorre, 1978)). Hence, the membrane deformation is dominated by the piezoelectric effects, with a maximum deformation magnitude of approximately 23% of the membrane thickness.

In Fig. 3.5 (d), the time-dependency of the AP refers to the squid giant axon only, which is in agreement with experimental evidence (from approximately  $-65\text{ mV}$  to  $+40\text{ mV}$  (El Hady and Machta, 2015; Hodgkin and Huxley, 1952)). Similar changes and values are found both for the garfish and crab nerve fibres. In contrast to (Abolfathi et al., 2009; El Hady and Machta, 2015), as a first step to assess the performance of a fully coupled electro-mechanical model, incompressible isotropic mechanical properties are used to characterize each axon model while the piezoelectric effect is only relevant in the through-thickness direction of the membrane layer. Hence, the electrically driven displacement and strain each have a predominant radial component in the membrane. The assumptions focus the coupled electro-mechanical analysis on the assessment of the theory of equivalences and the impact of equivalent thermal phenomena on the structure of a single nervous cell.

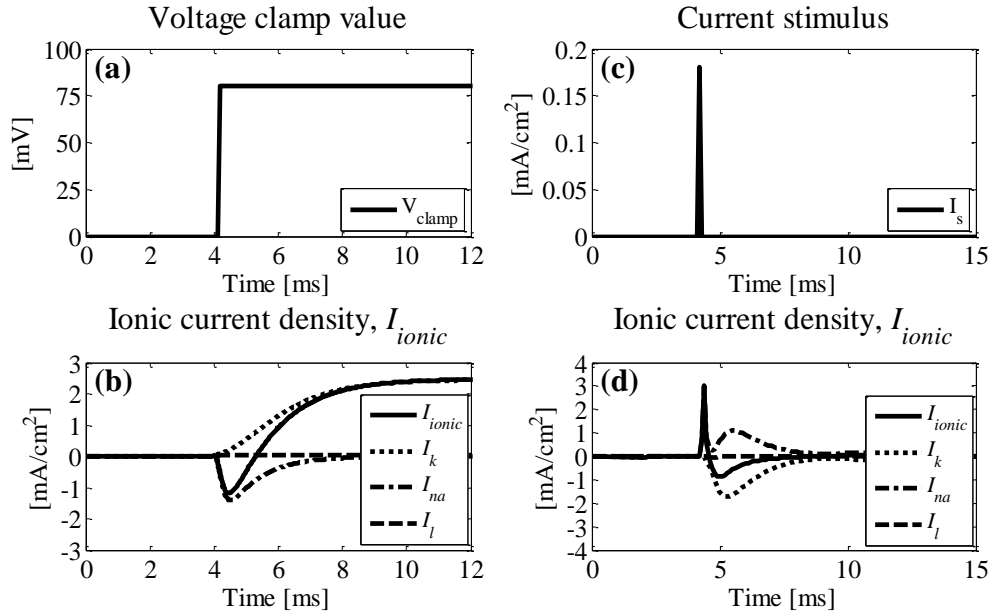


**Fig. 3.4** Voltage clamp procedure with 80 mV clamped voltage, (a), and generated ionic currents in (b). Space clamp procedure and 18 mA cm<sup>-2</sup> current stimulus of 0.2 ms (c) and generated ionic currents in (d).

Fig. 3.5 (a)-(c) shows results for a Young Modulus of  $1.4 \times 10^8 Pa$  (Case I) (Alvarez and Latorre, 1978), and Fig. 3.5 (d) compares the stresses and strains estimated using both Case I (Alvarez and Latorre, 1978) and Case II (Abolfathi et al., 2009) over time. It is interesting to note in Fig. 3.5 (d) that while the strains, which are electrically driven, are quite independent of Young's Modulus, the opposite is true for the stresses, which are highly dependent on Young's Modulus.

### 3.4 Discussion

The main achievements of this chapter are: the analogue implementation of the Heat Equation as the Cable Equation; the validation of electro-thermal equivalences in an uncoupled electrical and a coupled electro-mechanical analysis; and the modelling of a nervous cell as a 3D 3-layer conductor at different physical scales. Previous works have introduced only the use of equivalent quantities in finite element modelling, as can be seen in the paper (Wang, 1995), while others (Meffin and Kameneva, 2011; Meffin et al., 2012; Tahayori et al., 2012) neglect the importance of the electro-mechanical biophysical phenomena at the membrane layer (as electrostriction, swelling and deformation) (Iwasa et al., 1980; Mosgaard et al., 2015; Mueller and Tyler, 2014).

The assessment and validation of the electro-thermal equivalences and equivalent material properties in Abaqus CAE 6.13-3 are necessary to guarantee that the electrical current flow in a 3D neuron model can be represented as a heat diffusion process under longitudinal and transversal stimuli, for both passive and active membranes.

Here, the Heat Equation is used to simulate not just linear equivalent quantities, as shown in the paper (Wang, 1995), but also a non-linear equivalent phenomenon, specifically addressed in the Core Conductor Theory and represented by the Cable Equation for nerve fibres, as discussed by Rall (1977).

Validation of the solution for the Cable Equation in turn enables development of a coupled electro-mechanical model through the development of an equivalent coupled thermo-mechanical model. When compared with other approaches for coupled electro-mechanical modelling, the combined real-time use of separate advanced mechanical and electrical modelling software codes is computationally very expensive and computationally intractable if inhomogeneity and anisotropy in tissue conductivities are considered. Here the analogue thermo-mechanical domain provides computational simplification, particularly for three-dimensional problems in FE.

The simulation of electrical conduction using the electro-thermal equivalence can be implemented in different FE software packages (e.g. ANSYS and COMSOL), and non-linear electrical activity can be implemented directly in COMSOL (Elia et al., 2009), but coupled electro-mechanical solutions to biological systems have not yet been reported for this software. However, the use of Abaqus in the current application presents significant advantages. Compared to COMSOL, Abaqus provides greater control over the range of finite element types used in the model, the mesh structure, the calculated field variables, and the extraction of detailed field variable values at different levels in multi-scale models. Abaqus also facilitates the use of a very broad range of complex non-linear electrical and mechanical material properties, including user-defined material descriptions, which lend themselves particularly well to the representation of biological tissue. Hence, in contrast to previous studies (Elia et al., 2009; Moulin et al., 2008; Tahayori et al., 2012; Ying and Henriquez, 2007), the advanced FE platform for material characterization makes Abaqus CAE an ideal tool for investigating the electro-mechanical coupling in nerves.

The non-linear Cable Equation considered in this chapter focused on the non-linear HH dynamics for an unmyelinated nervous cell (Hodgkin and Huxley, 1952). However, the same equation can be used for a myelinated nerve fibre where the conductivity is periodic and piecewise constant, as is the case for Ranvier's nodes for example (Einziger et al., 2005).

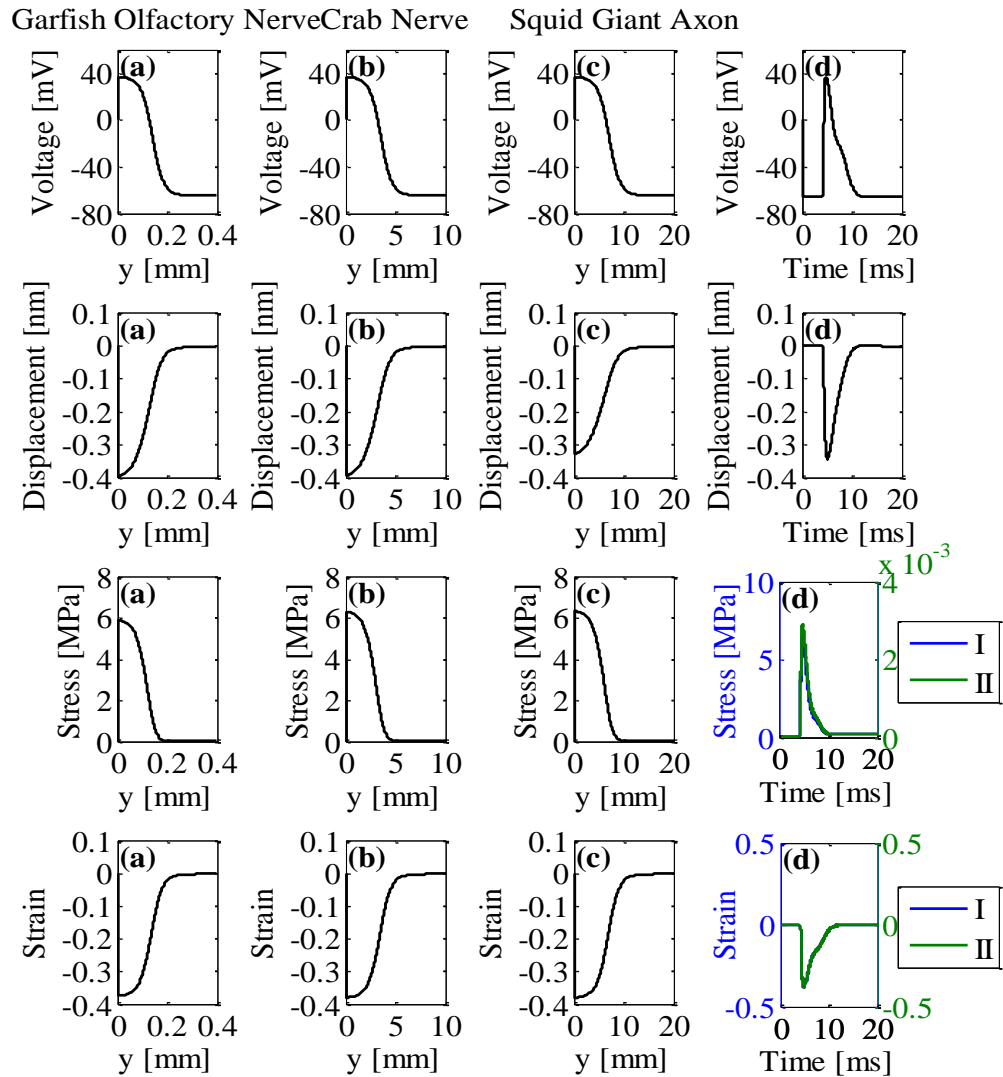


**Fig. 3.5** Quantitative comparison with three experimentally favoured systems of garfish olfactory nerve (column a), crab nerve (column b) and squid giant axon (column c) using model and parameters as described in the text. Columns (a)-(c) present the spatial distribution of the voltage and mechanical responses for the three different cases. Column (d) shows the time dependency of the mechanical features for the squid giant axon case only. The results refer to the 1-way coupling of the HH model. The results are taken in the middle of the membrane layer at  $y = 0$ , where the  $y$  –axis is the axis of symmetry of the model and the  $x$  –axis is the radial distance. For each case, the width of the AP is taken from the experimental literature (El Hady and Machta, 2015). Displacement, strain and stress are taken in the radial direction. In (d), stresses and strains are estimated using different Young’s Moduli, refer to Case I (Alvarez and Latorre, 1978; El Hady and Machta, 2015) and Case II (Abolfathi et al., 2009).

In relation to the application of electro-thermal equivalences to solve coupled electro-mechanical nerve conduction problems, very good agreement between the simulated results and published experimental measurements (over a number of quantities) validates the approach taken, and in particular the assumption of approximating the voltage gradient

(Eq. 3.4) (Staworko and Uhl, 2008; Tawfik et al., 2011). Secondly, by using three different models (squid giant axon, crab nerve fibre and garfish olfactory nerve fibre), the results confirm the validity of the approach over three very different length scales. It is interesting to note that although the electrical properties are different in each case, the strain response exhibits a similar trend across the different scales. This can be understood when one considers that the piezoelectric component of the strain is directly related to the piezoelectric constant (assumed the same for all cases) and the AP which is relatively uniform across all the cases (see Fig. 3.5 (a)). Finally, although strain levels are similar across the scales, the stress levels are hugely dependent on the choice of Young's Modulus. This demonstrates the importance of having accurate tissue mechanical property data in such models for gaining accurate insights into the coupled electro-mechanical behaviour. Additionally, dependence of electrical phenomena on stress through two-way coupling is expected to be significant.

Our model assumes that the mechanical features of the membrane are electrically driven by the AP (El Hady and Machta, 2015; Hodgkin and Huxley, 1952). The membrane is modelled as a parallel plate capacitor (Hodgkin and Huxley, 1952; Mosgaard et al., 2015; Tawfik et al., 2011), in which the piezoelectricity follows the orientation of the electric field (Zhang et al., 2001) and the changes in capacitance are proportional to the square of electric polarization (Alvarez and Latorre, 1978).

Although the HH model (Hodgkin and Huxley, 1952) assumes a constant membrane capacity, the combined use of the depolarisation wave and electrostriction seems to be accepted in the literature (El Hady and Machta, 2015). Here, the dimensional changes of the nerve membrane are not affecting the finite value of the membrane capacitance, as it was assumed to be constant, as in (El Hady and Machta, 2015). Isotropic material properties are assumed in all regions (apart from the orthotropic thermal expansion coefficient in the membrane layer). Analysis with a set of non-isotropic mechanical properties at the membrane layer (Heimburg and Jackson, 2005; Mosgaard et al., 2015) would require the use of other user-defined subroutines in Abaqus.

In conclusion, a method for modelling the mechanical characterization of neural activity in a coupled electro-mechanical domain by using the electro-thermal equivalences in FE has been proposed and validated. In contrast with (El Hady and Machta, 2015; Elia et al., 2009; Moulin et al., 2008; Tahayori et al., 2012; Ying and Henriquez, 2007), this approach can be used to better investigate the combined impact of the electric field and mechanical stresses simultaneously in the alteration of neural patterns and diseases (Shreiber et al., 2009). Thus, this chapter shows the importance of electro-thermal equivalences through the analysis of the electric current in a nervous cell, concluding that the physical meaning of the electric conduction is not altered using an analogue domain. This coupling is based

on a *1-way* coupled HH model in which material properties vary only in response to the simulated voltage (equivalent to temperature) during the cycle. In chapter 4, this modelling approach is expanded for including the electrical changes induced by mechanical loading (*2-way* coupled HH model or fully coupled HH model). The advantages of using a coupled HH model are shown for myelinated and unmyelinated fibres. Future works could extend this approach to modelling of biological systems at the tissue and organ levels and to model the neural activity in injured fibres and bundles (Galbraith et al., 1993), where the material properties change in response to voltage and strain.

### 3.5 Conclusion

This chapter focuses on the assessment and validation of the use of electro-thermal equivalences for modelling the inter-dependence of electrical and mechanical phenomena in FE analysis using thermo-mechanical software tools, considering the case of a single nervous cell. This approach facilitates the modelling of electro-mechanical phenomena, opening the way for realistic 3D electro-mechanical models of neural networks, neuropathological, neurological traumatic brain injuries and diseases (such as multiple sclerosis) (Demerens et al., 1996; Galbraith et al., 1993).

The model is validated against subthreshold and upper-threshold stimuli and is capable of simulating the electric activity of a nervous cell with both voltage and current boundary condition in the steady and transient state. The electrical conduction is well described by this approach, which verifies the spatial-temporal variation of the electro-thermal equivalences by using the Heat Equation as an analogue of the Cable Equation. In the end, the electro-mechanical coupling arises from the mechanical features of the Cable Equation, which, here, is used for simulating both piezoelectricity and electrostriction.

In the context of multi-disciplinary modelling, this methodology can help the integration and interaction of the mechanical modelling of materials with electrical activity for general applications. The inconvenience of having to combine different software packages and codes can therefore be overcome, by utilising the thermal analogue of electrical behaviour in the same modelling software, i.e. Abaqus CAE 6.13-3, that releases full access to both mechanical and equivalent electro-thermal quantities at each node and element of the model.

### References Chapter 3

- Abolfathi, N., Naik, A., Sotudeh Chafi, M., Karami, G., and Ziejewski, M. (2009). A micromechanical procedure for modelling the anisotropic mechanical properties of brain white matter. *Computer Methods in Biomechanics and Biomedical Engineering*, 12(3), 249–262. <https://doi.org/10.1080/10255840802430587>
- Alvarez, O., and Latorre, R. (1978). Voltage-dependent capacitance in lipid bilayers made from monolayers. *Biophysical Journal*, 21(1), 1–17. [https://doi.org/10.1016/S0006-3495\(78\)85505-2](https://doi.org/10.1016/S0006-3495(78)85505-2)
- Appali, R., Petersen, S., and Van Rienen, U. (2010). A comparison of Hodgkin-Huxley and soliton neural theories. *Advances in Radio Science*, 8, 75–79. <https://doi.org/10.5194/ars-8-75-2010>
- Baillargeon, B., Rebelo, N., Fox, D. D., Taylor, R. L., and Kuhl, E. (2014). The living heart project: A robust and integrative simulator for human heart function. *European Journal of Mechanics, A/Solids*, 48(1), 38–47. <https://doi.org/10.1016/j.euromechsol.2014.04.001>
- Bédard, C., and Destexhe, A. (2008). A modified cable formalism for modeling neuronal membranes at high frequencies. *Biophysical Journal*, 94(4), 1133–1143. <https://doi.org/10.1529/biophysj.107.113571>
- Bédard, C., and Destexhe, A. (2009). Macroscopic models of local field potentials and the apparent 1/f noise in brain activity. *Biophysical Journal*, 96(7), 2589–2603. <https://doi.org/10.1016/j.bpj.2008.12.3951>
- Bédard, C., Kröger, H., and Destexhe, A. (2004). Modeling extracellular field potentials and the frequency-filtering properties of extracellular space. *Biophysical Journal*, 86(3), 1829–1842. [https://doi.org/10.1016/S0006-3495\(04\)74250-2](https://doi.org/10.1016/S0006-3495(04)74250-2)
- Bossetti, C. A., Birdno, M. J., and Grill, W. M. (2008). Analysis of the quasi-static approximation for calculating potentials generated by neural stimulation. *Journal of Neural Engineering*, 5(1), 44–53. <https://doi.org/10.1088/1741-2560/5/1/005>
- Björnholm, L., Nikkinen, J., Kiviniemi, V., Nordström, T., Niemelä, S., Drakesmith, M., ... Paus, T. (2017). Structural properties of the human corpus callosum: Multimodal assessment and sex differences. *NeuroImage*, 152(February), 108–118. <https://doi.org/10.1016/j.neuroimage.2017.02.056>

- Cinelli, I., Destrade, M., Duffy, M., and McHugh, P. (2017). Electro-thermal equivalent 3d finite element model of a single neuron. *IEEE Transactions on Biomedical Engineering*, 9294(99). <https://doi.org/10.1109/TBME.2017.2752258>
- Cinelli, I., Duffy, M., and McHugh, P. (2015). Thermo-electrical equivalents for simulating the electro-mechanical behavior of biological tissue. In IEEE (Ed.), *Proceedings of the Annual International Conference of the IEEE Engineering in Medicine and Biology Society*, EMBS (Vol. 2015–November, pp. 3969–3972). Milan: IEEE. <https://doi.org/10.1109/EMBC.2015.7319263>
- Clayton, R. H., Bernus, O., Cherry, E. M., Dierckx, H., Fenton, F. H., Mirabella, L., Zhang, H. (2011). Models of cardiac tissue electrophysiology: progress, challenges and open questions. *Progress in Biophysics and Molecular Biology*, 104(1–3), 22–48. <https://doi.org/10.1016/j.pbiomolbio.2010.05.008>
- Crozier, A., Augustin, C. M., Neic, A., Prassl, A. J., Holler, M., Fastl, T. E., Plank, G. (2016). Image-based personalization of cardiac anatomy for coupled electromechanical modeling. *Annals of Biomedical Engineering*, 44(1), 58–70. <https://doi.org/10.1007/s10439-015-1474-5>
- Demerens, C., Stankoff, B., Logak, M., Anglade, P., Allinquant, B., Couraud, F., Lubetzki, C. (1996). Induction of myelination in the central nervous system by electrical activity. *Proceedings of the National Academy of Sciences of the United States of America*, 93(18), 9887–9892. <https://doi.org/10.1073/pnas.93.18.9887>
- Easton, D. M. (1971). Garfish olfactory nerve: easily accessible source of numerous long, homogeneous, nonmyelinated axons. *Science*, 172(3986), 952–955. Retrieved from <http://www.jstor.org/stable/1731652>
- Einzig, P. D., Livshitz, L. M., Dolgin, A., and Mizrahi, J. (2005). Novel cable equation model for myelinated nerve fiber. *IEEE Transactions on Biomedical Engineering*, 52(10), 112–115. <https://doi.org/10.1109/CNE.2003.1196769>
- El Hady, A., and Machta, B. B. (2015). Mechanical surface waves accompany action potential propagation. *Nature Communications*, 6(6697), 6697. <https://doi.org/10.1038/ncomms7697>
- Elia, S., Lamberti, P., and Tucci, V. (2009). A finite element model for the axon of nervous cells. In COMSOL (Ed.), *COMSOL Europe Conference* (pp. 1–7). Milan: COMSOL Conference 2009 Milan. <https://doi.org/http://www.comsol.com/paper/a-finite-element-model-for-the-axon-of-nervous-cells-6735>

- Galbraith, J. A., Thibault, L. E., and Matteson, D. R. (1993). Mechanical and electrical responses of the squid giant axon to simple elongation. *Journal of Biomechanical Engineering*, 115(1), 13–22. <https://doi.org/10.1115/1.2895464>
- García-Grajales, J. A., Rucabado, G., García-Dopico, A., Peña, J. M., and Jérusalem, A. (2015). Neurite, a finite difference large scale parallel program for the simulation of electrical signal propagation in neurites under mechanical loading. *PLoS ONE*, 10(2), 1–22. <https://doi.org/10.1371/journal.pone.0116532>
- Gleixner, R., and Fromherz, P. (2006). The extracellular electrical resistivity in cell adhesion. *Biophysical Journal*, 90(7), 2600–2611. <https://doi.org/10.1529/biophysj.105.072587>
- Heimburg, T., and Jackson, A. C. (2005). On soliton propagation in biomembranes and nerves. *Proceedings of the National Academy of Sciences*, 102(28), 9790–9795. <https://doi.org/10.1073/pnas.0503823102>
- Hille, B. (1977). Ionic basis of resting and action potentials. In *Comprehensive Physiology* (pp. 99–136). Washington, D.C. <https://doi.org/10.1002/cphy.cp010104>
- Hodgkin, A. L., and Huxley, A. F. (1952). A quantitative description of membrane current and its application to conduction and excitation in nerve. *Journal of Physiology*, 117, 500–544. [https://doi.org/10.1016/S0092-8240\(05\)80004-7](https://doi.org/10.1016/S0092-8240(05)80004-7)
- Iwasa, K., Tasaki, I., and Gibbons, R. (1980). Swelling of nerve fibers associated with action potentials. *Science*, 210(4467), 338–339. <https://doi.org/10.1126/science.7423196>
- Joucla, S., and Yvert, B. (2012). Modeling extracellular electrical neural stimulation: From basic understanding to MEA-based applications. *Journal of Physiology*, 106(3–4), 146–158. <https://doi.org/10.1016/j.jphysparis.2011.10.003>
- Meffin, H., and Kameneva, T. (2011). The electrotonic length constant: A theoretical estimate for neuroprosthetic electrical stimulation. *Biomedical Signal Processing and Control*, 6(2), 105–111. <https://doi.org/10.1016/j.bspc.2010.09.005>
- Meffin, H., Tahayori, B., Grayden, D. B., and Burkitt, A. N. (2012). Modeling extracellular electrical stimulation: I. Derivation and interpretation of neurite equations. *Journal of Neural Engineering*, 9(6), 65005. <https://doi.org/10.1088/1741-2560/9/6/065005>

- Mosgaard, L. D., Zecchi, K. a., and Heimborg, T. (2015). Mechano-capacitive properties of polarized membranes. *Soft Matter*, 11(40), 7899–7910. <https://doi.org/10.1039/C5SM01519G>
- Moulin, C., Glière, A., Barbier, D., Joucla, S., Yvert, B., Mailley, P., and Guillemaud, R. (2008). A new 3D finite-element model based on thin-film approximation for microelectrode array recording of extracellular action potential. *IEEE Transactions on Bio-Medical Engineering*, 55(2 Pt 1), 683–692. <https://doi.org/10.1109/TBME.2007.903522>
- Mueller, J. K., and Tyler, W. J. (2014). A quantitative overview of biophysical forces impinging on neural function. *Physical Biology*. <https://doi.org/10.1088/1478-3975/11/5/051001>
- Nelson, P. (2004). *Biological Physics: Energy, Information, Life*, WH Freeman Publishing, <https://doi.org/10.1063/1.1839381>
- Perge, J. a, Niven, J. E., Mugnaini, E., Balasubramanian, V., and Sterling, P. (2012). Why do axons differ in caliber? *The Journal of Neuroscience*, 32(2), 626–638. <https://doi.org/10.1523/JNEUROSCI.4254-11.2012>
- Rall, W. (2011). Core conductor theory and cable properties of neurons. In *Comprehensive Physiology - Handbook of physiology, the nervous system, cellular biology of neurons* (Vol. Chapter 3, pp. 39–97). Washington, D.C.: Wiley Online Library. <https://doi.org/10.1002/cphy.cp010103>
- Plonsey, R., and Barr, R. C. (2007). *Bioelectricity: A quantitative approach*. (Springer, Ed.), Springer. <https://doi.org/10.1007/978-0-387-48865-3>
- Remoissenet, M. (1999). *Waves called solitons: Concepts and experiments*, Springer. Dijon. Retrieved from <http://www.springer.com/gp/book/9783540659198>
- Shreiber, D. I., Hao, H., and Elias, R. A. (2009). Probing the influence of myelin and glia on the tensile properties of the spinal cord. *Biomechanics and Modeling in Mechanobiology*, 8(4), 311–321. <https://doi.org/10.1007/s10237-008-0137-y>
- Staworko, M., and Uhl, T. (2008). Modeling and simulation of piezoelectric elements - comparison of available methods and tools. *Mechanics*, 27(4), 161–171. Retrieved from <http://journals.bg.agh.edu.pl/MECHANICS/2008-04/mech05.pdf>

- Tahayori, B., Meffin, H., Dokos, S., Burkitt, A. N., and Grayden, D. B. (2012). Modeling extracellular electrical stimulation: II. Computational validation and numerical results. *Journal of Neural Engineering*, 9(6), 65006. <https://doi.org/10.1088/1741-2560/9/6/065006>
- Tawfik, S. A., Stefan Dancila, D., and Armanios, E. (2011). Unsymmetric composite laminates morphing via piezoelectric actuators. *Composites Part A: Applied Science and Manufacturing*, 42(7), 748–756. <https://doi.org/10.1016/j.compositesa.2011.03.001>
- Wang, B.J. (1995). Electro-thermal modelling in Abaqus. In ABAQUS (Ed.), *Abaqus User' Conference* (pp. 771–785). Paris: *ABAQUS Users' Conference 1995*. Retrieved from <http://www.3ds.com/products-services/simulia/products/abaqus/multiphysics/thermal-electric/>
- Ying, W., and Henriquez, C. S. (2007). Hybrid finite element method for describing the electrical response of biological cells to applied fields. *IEEE Transactions on Biomedical Engineering*, 54(4), 611–620. <https://doi.org/10.1109/TBME.2006.889172>
- Zhang, P.C., Keleshian, A. M., and Sachs, F. (2001). Voltage-induced membrane movement. *Nature*, 413(6854), 428–432. <https://doi.org/10.1038/35096578>

## Chapter 4.      **Electro-Mechanical Response of a 3D Nerve Bundle Model to Mechanical Loads Leading to Axonal Injury**

This chapter is about the assessment and validation of the fully coupled electro-mechanical model, where the neural activity is changing as a function of strain, voltage, space and time. The material in this chapter has been published in *Cinelli, I., M. Destrade, M. Duffy, and P. E. McHugh. 2017. “Electro-Mechanical Response of a 3D Nerve Bundle Model to Mechanical Loads Leading to Axonal Injury”, International Journal for Numerical Methods in Biomedical Engineering, DOI 10.1002/cnm.2942 <http://onlinelibrary.wiley.com/doi/10.1002/cnm.2942/abstract#>.*

*Abstract — Objective:* Traumatic brain injuries and damage are major causes of death and disability. A 3D fully coupled electro-mechanical model of a nerve bundle is proposed to investigate the electrophysiological impairments due to trauma at the cellular level. *Methods:* The coupling is based on a thermal analogy of the neural electrical activity by using the finite element software Abaqus CAE 6.13-3. The model includes a real-time coupling, modulated threshold for spiking activation and independent alteration of the electrical properties for each 3-layer fibre within a nerve bundle as a function of strain. *Results:* Results of the coupled electro-mechanical model are validated with previously published experimental results of damaged axons. The cases of compression and tension are simulated here, to induce (mild, moderate and severe) damage at the nerve membrane of a nerve bundle, made of four fibres. Changes in strain, stress distribution, and neural activity are investigated for myelinated and unmyelinated nerve fibres, by considering the cases of an intact and of a traumatized nerve membrane. *Conclusion:* A fully coupled electro-mechanical modelling approach is established to provide insights into crucial aspects of neural activity at the cellular level due to traumatic brain injury. *Significance:* One of the key findings is the 3D distribution of residual stresses and strains at the membrane of each fibre due to mechanically-induced electrophysiological impairments, and its impact on signal transmission.

## 4.1 Introduction

Traumatic Brain Injury (TBI) is caused by mechanical loading to the head due to a sudden acceleration or a blast wave, for example, causing pathologies which range from focal damage of brain tissue to widespread axonal injury (Wright and Ramesh, 2012; Jérusalem et al., 2014). TBI in humans may result from falls, vehicle accidents, sport injuries, military incidents, etc. (Wright and Ramesh, 2012; Zhang et al., 2014; Ma et al., 2016), as discussed in the previous chapters.

The diffuse form of TBI is called Diffuse Axonal Injury (DAI), i.e. a mechanical pathogenesis of an axonal injury, initiated in the deep white matter regions of the brain at the moment of injury (Wright and Ramesh, 2012; Ma et al., 2016). DAI is the most common pathological feature of the mild and severe cases of TBI at cellular and subcellular levels (Smith et al., 2000; Wright and Ramesh, 2012), with progressive course (Ma et al., 2016), responsible for long-lasting neurological impairments following TBI, and high rates of mortality (Smith et al., 2000; Lajtha et al., 2009; Wang et al., 2010). Pathological features of DAI include a wide-ranging variety of tissue lesions of the white matter, such as swelling of axonal mitochondria, thinning of the intermodal axoplasm, and development of myelin intrusions (Maxwell et al., 1997), focal haemorrhages, contusions and other brain injuries (Lajtha et al., 2009; Wright and Ramesh, 2012; Ma et al., 2016).

Although DAI is classified as an independent category of disease from TBI, the pathological mechanism of DAI is very complex and, currently, there are no diagnostic criteria (Ma et al., 2016). A better understanding of mechanically-induced electrophysiological impairments and damage associated with morphological changes of neural cells is urgently needed to improve diagnosis, clinical treatments and prognosis (Lajtha et al., 2009; Ma et al., 2016).

A number of experimental models of axonal injury reproduce DAI by experimental traumatic insult, where a Traumatic Axonal Injury (TAI) induces DAI to investigate the relationship between mechanical forces and structural and functional responses of axons in experiments (Lajtha et al., 2009). Here, TAIs are axonal injury produced in experiments, while DAIs are diagnosed. Experimental studies conducted on single axons (Galbraith et al., 1993) and nerve fibres (Bain and Meaney, 2000) aim to induce TAI by applying pressure (Gallant, 1992; Hosmane et al., 2011), displacement (Bain et al., 2000; Wright and Ramesh, 2012), strain (Galbraith et al., 1993; Shi et al., 2006), shear strain (LaPlaca et al., 2005) and electroporation (Gallant et al., 1997). Although different types of loads seem to initiate TAI, recent studies have shown that the degree of neuronal impairment is directly related to the magnitude and rate of axonal stretch (Galbraith et al., 1993; Bain et al., 2000; Boucher et al., 2012; Wright and Ramesh, 2012). Beyond a critical threshold (Bain et al.,

2000), axons appear to be vulnerable to stretch-induced changes that induce morphological changes at the microscale level, increasing axolemma permeability (Smith et al., 2000; Wright and Ramesh, 2012; Ma et al., 2016).

The alteration of axolemma permeability is evidence of mitochondrial damage and neurofilament compaction (Lajtha et al., 2009; Maxwell and Graham, 1997). Axonal damage is a common manifestation of DAI. Injury-induced axonal damage involves damage of the axonal cytoskeleton, resulting in a loss of membrane integrity and impairment of axoplasmic transport, leading to changes in electrical signal propagation (Galbraith et al., 1993; Yu et al., 2012; Zhang et al., 2014). The alteration of neural activity in a mechanically-injured nerve is called neurotrauma (Galbraith et al., 1993; Geddes et al., 2003; Leung et al., 2008; Yu et al., 2012). Although recent experimental studies highlight complex electro-mechanical phenomena at the nerve membrane layer (Mosgaard et al., 2015; Zhang et al., 2001), the injury-induced electrophysiological changes of the electro-mechanical activity in neural cells are poorly understood (Galbraith et al., 1993; Lajtha et al., 2009). Quantifying the induced electro-mechanical changes can help to differentiate the severity of injury and to understand the alteration in signal propagation at cellular and nerve bundle levels.

Computational electro-mechanical models, coupling mechanics and electrophysiology, are powerful tools to investigate and evaluate neurophysiological, neuropathological processes and neurocognitive damage associated with DAI due to injury at the macroscale (Wright and Ramesh, 2012; Jérusalem et al., 2014). This work presents a novel approach for evaluating and quantifying the changes in neural activity due to TAI by using finite element (FE) models. Previous modelling efforts have simulated 1D damage of a nerve fibre (Jérusalem et al., 2014) and 2D axonal injury of brain tissue (Wright and Ramesh, 2012). In this work, using the FE software Abaqus CAE 6.13-3, advanced 3D models explain the link between TBI and DAI at the microscale level (Wright and Ramesh, 2012; Jérusalem et al., 2014), by considering the case of TAI at the axonal and bundle levels. Our 3D FE model of a nerve bundle includes a representation of nervous cells made of Extracellular Media (ECM), membrane, and Intracellular Media (ICM). As in Chapter 3 and in (Cinelli et al., 2015, 2017b), these three regions have finite thicknesses, so that the resulting model is a 3-layer nerve bundle. The bundle model here is a section of an idealized geometry of a nerve bundle, which consists of four parallel cylindrical unmyelinated or myelinated fibres, see Fig. 4.1. In this chapter, a series of mechanical loads (such as pressure (Hosmane et al., 2011) and displacement (Bain and Meaney, 2000)) are applied to the bundle to induce a certain level of damage at the nerve membrane of a fibre, altering the fibre activation dynamics and transmission (Boucher et al., 2012; Yu et al., 2012).

This model presents a unique framework for investigating how changes in strain and stress distributions alter the function of 3D myelinated and unmyelinated nerve fibres and bundles. In contrast to previous studies (Wright and Ramesh, 2012; Jérusalem et al., 2014), this model includes full coupling between mechanical and electrical domains (Cinelli et al., 2017d, 2017c) where the neural electrical activity, as described in (Hodgkin and Huxley, 1952), is coupled to the mechanical domain through piezoelectricity (Zhang et al., 2001) and electrostriction (Mosgaard et al., 2015), reproducing biophysical phenomena accompanying the Action Potentials (APs) as observed experimentally (El Hady and Machta, 2015; Zhang et al., 2001). Here, the electrical activity is directly coupled to mechanical deformation by using electro-thermal equivalences in a coupled thermo-mechanical FE analysis (Cinelli et al., 2015a). Electro-thermal equivalences and equivalent material properties have been shown to provide an efficient approach to resolve 3D electrical problems in a coupled electro-mechanical analysis in Abaqus CAE 6.13-3 (Cinelli et al., 2015, 2017), as shown in 3.2.1.

This chapter builds on the work reported in Chapter 3 and in (Cinelli et al., 2017e, 2017d, 2017c, 2015a). Here, details show how electro-mechanical coupling is represented through thermo-mechanical equivalence; the nerve bundle model and its geometry; and the damage criterion and its implementation.

The electro-mechanical coupling approach is validated based on the strain-based damage criterion (Boucher et al., 2012; Cinelli et al., 2017e; Jérusalem et al., 2014). This criterion refers to traumatic mechanically-induced damage on a nerve fibre (refer to (Boucher et al., 2012; Jérusalem et al., 2014)) in which the resting ionic potentials of the Hodgkin and Huxley (HH) model are shifted by 20 mV, simulating experimental evidence of damaged nerve fibres (Boucher et al., 2012; Yu et al., 2012), as in (Jérusalem et al., 2014). The injury threshold takes into account axonal strain along the nerve fibre length only (Wright and Ramesh, 2012; Jérusalem et al., 2014). The strain along the fibre length has been shown to be a physiologically relevant injury criterion for multiscale TBI models (Wright and Ramesh, 2012; Jérusalem et al., 2014). Two cases, (i) dynamic pressure and (ii) displacement loads at the bundle level, in which only one fibre is activated, are considered.

This approach has the potential to generate useful insights in studying the mechanics behind neuro-physiology, as observed experimentally in damaged nerve membranes of clinical cases (such as multiple sclerosis) (Demerens et al., 1996; Galbraith et al., 1993; Geddes et al., 2003).

## 4.2 Method

### 4.2.1 Model

The bundle model simulates the exchange of charges in four identical fibres as shown in Fig. 4.1. Each fibre consists of a cylindrical region of ICM enclosed by a thin membrane and surrounded by a region of ECM (Cinelli et al., 2015a), as described in Section 3.2.2.

Two bundle models are used in this study: a fully unmyelinated bundle and a fully myelinated bundle. The neurite radii are:  $a_{ICM} = 0.477 \mu m$ ,  $a_M = 0.480 \mu m$  and  $a_{ECM} = 0.500 \mu m$  (Cinelli et al., 2017c, 2015a) for the ICM, membrane and ECM layers, respectively. As a first step, this analysis is focused on the radial distribution of charges rather than on longitudinal variations. The length of the bundle is  $2.5 \mu m$  for a diameter equal to  $2.41 \mu m$  in both cases, see Fig. 4.1, within the human corpus callosum (Björnholm et al., 2017).

To model a myelinated fibre, the ICM is assumed to be enclosed by a single layer, which is periodically-partitioned along the fibre length, similarly to the histologic section of a myelinated fibre, see Fig. 4.1 (d.1) and (d.2). The insulation sheath of myelin around the nerve fibre is modelled as an insulating layer, which replaces the membrane layer at regular intervals along the fibre (Einzigler et al., 2003a), see Fig. 4.1 (d.1). Different conductivity values are assigned to denote the myelin and membrane sections (Einzigler et al., 2003a), see Fig. 4.1 (d.2). The width of the piecewise conductive membrane regions (or Ranvier's nodes) is  $0.002 \mu m$  and the internode distance is  $1 \mu m$  (Einzigler et al., 2003a), see Fig. 4.1 (d.2). Modelling of myelinated fibres is shown in greater details in the Appendix B.

Incompressible isotropic mechanical properties (El Hady and Machta, 2015) are assumed in both models, with Young's Modulus set equal to 1GPa and a Poisson ratio of 0.49 (El Hady and Machta, 2015) (close to incompressibility). Then, the electrical model parameters for unmyelinated and myelinated fibres are taken from (Cinelli et al., 2015a) and (Antoine Jérusalem et al., 2014), respectively. The resistance per unit length of the ICM and ECM is  $1.89 \Omega m$ , and for the myelin it is  $4 M\Omega m$ . Then, the capacitance per unit area is  $0.148 \mu F/cm^2$  for the ICM,  $3.54 \mu F/cm^2$  for the ECM, and  $3.58 \cdot 10^{-3} \mu F/cm^2$  for the myelin layer. The corresponding values for the membrane are the HH model values (Hodgkin and Huxley, 1952) for steady state conditions and are dependent on voltage, strain and spatial coordinates during loading conditions, see Section 4.2.3.

Hence, this approach establishes a fully 2-way electro-mechanical coupling accounting, at the same time, for the effect of mechanical loads on electrical response and the effect of the electrical activity on the nerve structure.

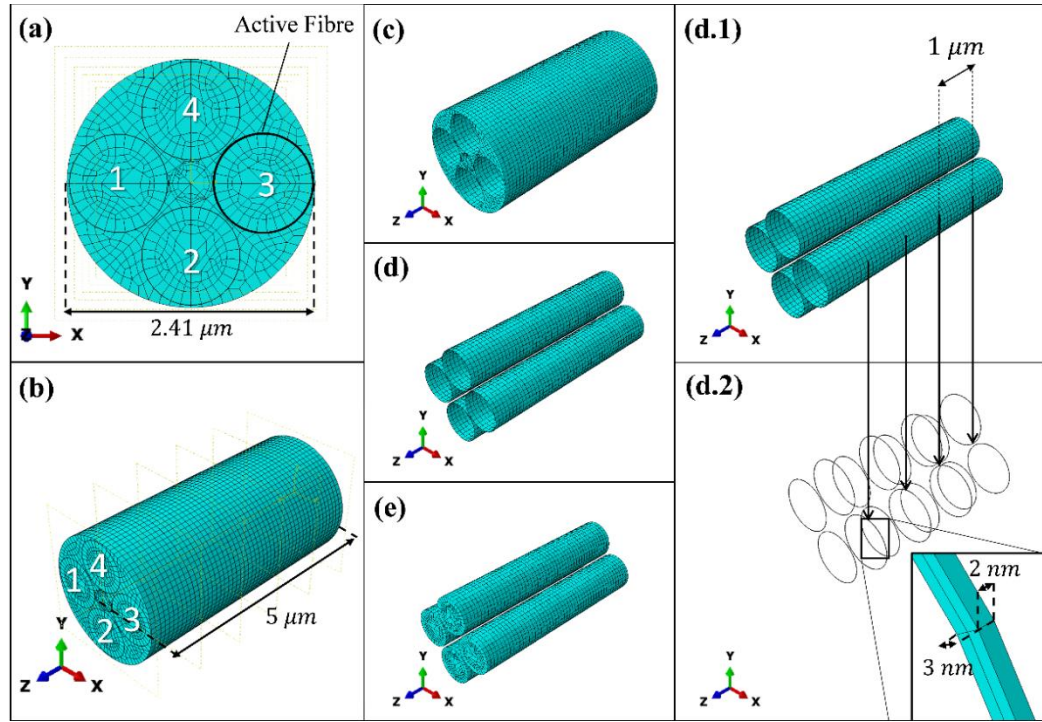


**Fig. 4.1** (a): frontal view and (b): isometric view of the 3-layer nerve bundle, made of four fibres. Fibre #3 is the active fibre, i.e. the fibre activated by a Gaussian voltage distribution (El Hady and Machta, 2015). Fibres #1, #2 and #4 are activated by the charges diffusing from Fibre #3. (c): the ECM; (d): the membrane; (e): the ICM. In the case of myelinated fibres, the membrane layer is periodically-partitioned along the fibre length to model the insulation sheath of the myelin layer, see (d.1), and the Ranvier node, see (d.2). The myelin layer length is  $1 \mu\text{m}$  and the Ranvier's node length is  $2 \text{ nm}$ , while the radial thickness of the layer is equal to  $3 \text{ nm}$  (Cinelli et al., 2017d, 2017c, 2015a; Einziger et al., 2005).

## 4.2.2 Damage Evaluation

Strain-based damage affects the sodium and potassium reversal potentials ( $E_{Na}(\epsilon_m)$  and  $E_K(\epsilon_m)$ ), see Eq. 4.1, of the HH model, simulating the changes in ionic concentration across the nerve membrane depending on the membrane strain ( $\epsilon_m$ ) (Jérusalem et al., 2014). The resting potentials at physiological conditions are  $E_{Na0}$  and  $E_{K0}$  (Hodgkin and Huxley, 1952; Jérusalem et al., 2014) see Eq. 4.1.. If a maximum strain,  $\tilde{\epsilon}$ , is exceeded, then the reversal potentials are zero, otherwise the changes follow Eq. 4.1 if  $\epsilon_m < \tilde{\epsilon}$ , as can be seen in (Jérusalem et al., 2014):

$$\begin{cases} E_{Na}(\epsilon_m) = E_{Na0}(1 - (\epsilon_m/\tilde{\epsilon})^\gamma) \\ E_K(\epsilon_m) = E_{K0}(1 - (\epsilon_m/\tilde{\epsilon})^\gamma) \end{cases} \quad \text{Eq. 4.1}$$

Here, the strain threshold,  $\tilde{\epsilon}$ , is set at 0.21 as an indicator of the onset of functional damage at which there is a 25% probability of having morphological injury during a uniaxial displacement test of a nerve fibre (Bain and Meaney, 2000). The parameter  $\gamma$ ,

equal to 2 (Jérusalem et al., 2014), is an index referring to the sensitivity of the damage to small versus large deformation, see (Jérusalem et al., 2014). Additionally, the reversal potential of the leak ions  $E_{l-}$  is not influenced by the strain but varies based on changes in gradient concentrations of potassium and sodium across the membrane (Jérusalem et al., 2014), see Fig. 4.2. The changes for the leak ions can be derived from the sum of the total membrane currents at resting conditions (Hodgkin and Huxley, 1952; Jérusalem et al., 2014).

### 4.2.3 Implementation

The implementation of the coupled HH model is shown in Fig. 4.2 (on the right), in contrast to the uncoupled HH model (shown on the left). By using the electro-thermal equivalence (Cinelli et al., 2017d, 2017e, 2017c, 2015a), the implementation of the neural activity, the distribution of voltage, and the generated strain can be seen in 3D by using well established coupled thermo-mechanical software simulation tools. In the coupled model (Cinelli et al., 2017e), the membrane electrical conductivity changes in response to the membrane voltage produced during the AP, incorporating the effects of strain (Hodgkin and Huxley, 1952; Antoine Jérusalem Jérusalem et al., 2014), according to Eq. 4.1, while the electrical capacitance per unit area changes with the square of the voltage (Alvarez and Latorre, 1978), see Eq. 3.5 and Fig. 4.2. The HH reversal voltage potentials change due to the strains at the membrane (Boucher et al., 2012; Jérusalem et al., 2014), hence the threshold of spike initiation changes as in (Hodgkin and Huxley, 1952). In all cases, strain is caused by membrane piezoelectricity as described in Eq. 3.4, and external mechanical loading when applied. The model is implemented as a coupled thermo-mechanical model in Abaqus CAE by using user-defined subroutines (DISP, USDFLD and UMATHT) to assign thermal equivalent electrical properties to the membrane of each fibre, independently, based on the spike initiation (Platkiewicz and Brette, 2010), strain (Boucher et al., 2012; Jérusalem et al., 2014) and voltage (Alvarez and Latorre, 1978) generated at the same membrane, see Eq. 3.3 and Eq. 3.4. Electrical model parameters for other regions of the unmyelinated and myelinated fibres are as applied in Chapter 3, taken from (Cinelli et al., 2015a) and (Jérusalem et al., 2014), respectively.

### 4.2.4 Boundary Conditions

In all cases, a voltage Gaussian distribution (with zero-mean and 0.4 variance) is the upper-threshold stimulation applied on Fibre #3 along its length, see Fig. 4.2, while the other

fibres are activated only if the diffused charges from Fibre #3 generate an input voltage higher than the modulated threshold (Platkiewicz and Brette, 2010). The voltage is applied on the surface of the nerve membrane layer through the DISP user-subroutine in Abaqus CAE, as a thermal load (i.e. equivalent to applied voltage as in Chapter 3 (Cinelli et al., 2017e)). The 3D distribution of charges on Fibre #3 modulates the activation of the other fibres, see Fig. 4.1. First, the electro-mechanical coupling has been assessed and validated by activating Fibre #3 with a pre-imposed strain condition (corresponding to a coupled left-shift (*LS*) of 0 or 20 *mV* of the transmembrane voltage) assuming an intact or traumatized membrane, respectively, as in (Boucher et al., 2012; Jérusalem et al., 2014).

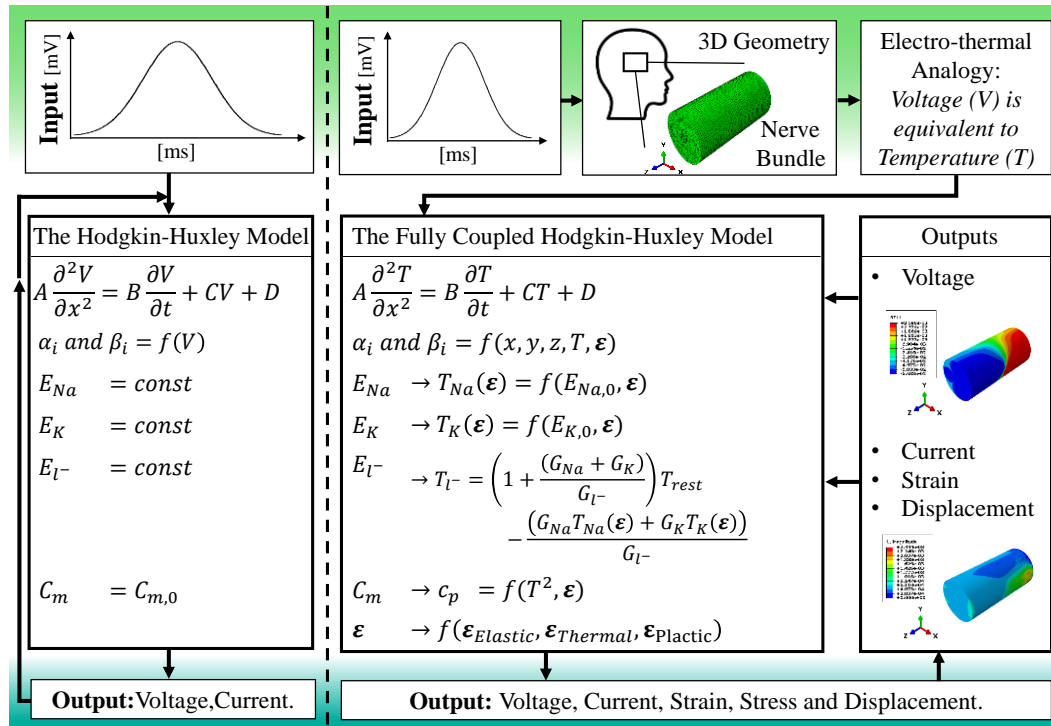


**Fig. 4.2** Flowchart of the code describing the active behaviour of the nerve's membrane: on the left, the HH dynamics (Hodgkin and Huxley, 1952) and on the right, the fully coupled HH dynamics (or 2-way coupling). Here, a Gaussian voltage distribution elicits the AP in a 3D model of a nervous cell. By using electro-thermal equivalences, the HH model is implemented as an equivalent thermal process, in which the membrane's conductivity changes as in (Hodgkin and Huxley, 1952) and the capacitance,  $C_m$ , changes as in (Alvarez and Latorre, 1978). The HH parameters are changing based on the temperature (which is the equivalent quantity of voltage (Cinelli et al., 2017d)) and strain at the membrane (Jérusalem et al., 2014). The strain  $\epsilon$  generated in the model is a function of temperature,  $T$ , and thermal expansion coefficients, see Eq. 3.4 and Eq. 4.1. Voltage, current, strain and stresses distribution are only a few of the 3D results released by Abaqus by equivalence. In Chapter 4 plasticity is not included; in Chapter 5 the analysis includes isotropic plasticity.

An encasté boundary condition is enforced at the origin of each model, while no rotation or shear is allowed by fixing a point on the same side of the model. Then, two cases of mechanical loads applied at the bundle have been considered. As a first step to assess this novel coupling, only frequency-independent loading conditions are considered throughout, after the initial steady-state, so that the solutions are quasi-static (Cinelli et al., 2017e).

In the first case of applied mechanical loading, an instantaneous uniform compression is applied to the bundle to simulate injury conditions. Three values of pressure are modelled simulating mild (less than 55 *kPa*), moderate (55 – 95 *kPa*) and severe (higher than 95 *kPa*) pressure (Hosmane et al., 2011). In the second case, axial strain conditions that reproduce the uniaxial test in (Bain and Meaney, 2000) are applied. Two values of instantaneous uniform stretch are applied as a displacement boundary condition to simulate 5 % and 14 % of total axial deformation,  $\varepsilon$ , at which the probability of inducing morphological injury during the elongation test is 5% and 25%, respectively (Bain and Meaney, 2000).

#### 4.2.5 Validation

This work builds on the work reported in Chapter 3 and in (Cinelli et al., 2017e), in which the theory of electro-thermal equivalences is validated (using both mathematical analysis and computational tools) and verified for the case of nervous cells (Cinelli et al., 2017e), see 3.3. Then, in (Cinelli et al., 2017e), the uncoupled HH model (Hodgkin and Huxley, 1952) is validated and verified for voltage and current boundary conditions, see Fig. 3.5. In this chapter, a further validation is needed to assess the coupled HH model in the 3D nerve bundle model. Our model includes (Jérusalem et al., 2014), as the most recent and completed reference available in literature. Thus, the 2-way coupling is verified against (Jérusalem et al., 2014), and validated though comparison with (Boucher et al., 2012; Jérusalem et al., 2014) and by replicating compression and elongation tests as in the experimental literature (Bain and Meaney, 2000; Hosmane et al., 2011).

Because previous works refer to 1D computational models (Boucher et al., 2012; Jérusalem et al., 2014), the verification is carried out by comparison of output behaviours (of voltage and displacement) within the same model. Hence, the approaches in (Boucher et al., 2012; Jérusalem et al., 2014) are implemented in our 3D nerve bundle model for the same applied boundary conditions. The traumatic mechanically-induced damage approach (Boucher et al., 2012; Jérusalem et al., 2014) is validated by using a coupled Left-Shift (LS) version of the HH model (Boucher et al., 2012) reproducing experimental evidence (Boucher et al., 2012; Yu et al., 2012), as in (Jérusalem et al., 2014). The LS denomination

refers to the induced positive shift of the transmembrane potentials, simulating a nerve membrane subjected to mechanical trauma (Jérusalem et al., 2014). It is called coupled  $LS$  to highlight the close link of mechanical strain on the electrical properties of the nerve membrane. In contrast to (Hodgkin and Huxley, 1952), the ionic currents of the modified HH model include the fraction of Affected ionic Channels by the strain ( $AC$ ) and coupled  $LS$  variables, see Eq. 4.2 and Eq. 4.3 (Boucher et al., 2012). When a trauma occurs at the nerve membrane, the ionic resting potentials undergo a voltage-shift ( $LS$ ), here, equal to  $20\text{ mV}$ , as a reference value for trauma-induced kinetic changes observed in experiments (Boucher et al., 2012). This allows simulation of uniaxial loading experiments (Cao et al., 2012; Riyi Shi and Whitebone, 2006) of a nerve bundle, by implementing a pre-imposed shift in the HH dynamics, simulating the impact of applied mechanical strain at the nerve membrane. Then, the integrity of the nerve membrane is modelled as the fraction of the voltage-time dependent activation and inactivation variables (i.e.  $m$ ,  $n$  and  $h$  (Hodgkin and Huxley, 1952)) of the HH model, shifted by  $LS$  (here, indicated as  $m_{LS}$ ,  $n_{LS}$  and  $h_{LS}$ ), see Eq. 4.2 and Eq. 4.3 (Boucher et al., 2012). The model accounts for the case where only a fraction of nodal channels ( $AC$ ) undergoes a  $LS$ , while the rest of the membrane's channels,  $(1 - AC)$ , remains intact (Boucher et al., 2012). Here, only the extreme cases of the entire membrane being traumatized ( $AC = 1$ ) or intact ( $AC = 0$ ) are shown as illustrative examples. In Eq. 4.2, the sodium current,  $I_{Na}$ , and, in Eq. 4.3, the potassium current,  $I_K$ , (Boucher et al., 2012). The membrane potential is  $V$ , and the sodium,  $\bar{g}_{Na}$ , and potassium,  $\bar{g}_K$ , conductances are, respectively, equal to  $120\text{ mS cm}^{-2}$  and  $36\text{ mS cm}^{-2}$  (Hodgkin and Huxley, 1952).

$$I_{Na} = [m^3 h (1 - AC) + m_{LS}^3 h_{LS} AC] (V - E_{Na}) \bar{g}_{Na} \quad \text{Eq. 4.2}$$

$$I_K = [n^4 (1 - AC) + n_{LS}^4 AC] (V - E_K) \bar{g}_K \quad \text{Eq. 4.3}$$

This model is validated considering two cases of interest and two approaches. The first Case (I) is the nerve membrane at physiological conditions, i.e. intact ( $LS = 0$ ) and non-traumatized ( $AC = 0$ ). In second case (Case II), the membrane loses integrity ( $AC = 1$ ) due to damage ( $LS = 20\text{ mV}$ ). Then, in the first approach, the reversal ionic potentials in Eq. 4.2 and Eq. 4.3,  $E_{Na}$  and  $E_K$ , are constant values, equal to  $50\text{ mV}$  and  $-77\text{ mV}$ , respectively (Hodgkin and Huxley, 1952), as in (Boucher et al., 2012). Here, the signals are changing because of the changes in conductance produced by changes in the voltage-dependent variables ( $m_{LS}$ ,  $n_{LS}$  and  $h_{LS}$ ). In a second approach, the reversal potentials are changing with  $LS$ , see Eq. 4.1, as in (Jérusalem et al., 2014). Therefore, the signals are changing due to the changes in both the conductance and the reversal ionic potentials. Fig.

4.3 shows the changes in membrane potential due to the left-shift voltage implemented as in (Boucher et al., 2012) (indicated with \*) and as in (Jérusalem et al., 2014) (indicated as \*\*). Those two conditions are the ones that can be directly compared to results presented in (Boucher et al., 2012; Jérusalem et al., 2014).

## 4.3 Results

### 4.3.1 Model Analysis

The electrophysiological impairments associated with structural damage of the neuron mechanics affect the electrostriction and the electric field across the membrane, Eq. 3.4, while the piezoelectric properties of the nerve membrane are assumed to be constant, Eq. 3.5, (Cinelli et al., 2017e; El Hady and Machta, 2015; Zhang et al., 2001).

The results in Fig. 4.3 confirm the ability of the model to reproduce the membrane voltage and ionic current waveforms of a damage-induced injury. Here, the coupled *LS* model of HH reproduces the changes in hyperpolarization in a damaged axon, left-shifting the affected ionic channels by  $20\text{ mV}$ , as in slow-severe cases, see (Boucher et al., 2012; Jérusalem et al., 2014). Fig. 4.3 refers to Fibre #3, the only fibre directly activated by the Gaussian voltage distribution input. Similarly, by diffusion, the membrane potential of the other fibres changes according to the level of damage and trauma on Fibre #3. Fig. 4.3 (a) shows the membrane potential and Fig. 4.3 (b) reports the ionic currents of the membrane (for leak ions,  $I_{l^-}$ , potassium,  $I_K$ , and sodium,  $I_{Na}$ ) vs. time in Cases I, II (\*) and II (\*\*). As shown, the mechanically-induced voltage-shift of the resting potentials leads to a time-delay and a lower amplitude of the voltage signal, due to leaky channels, similar to trends observed in (Boucher et al., 2012; Jérusalem et al., 2014). In Case II (\*), the membrane potential is shifted in time by  $13.3\text{ ms}$  and its peak at  $16.9\text{ ms}$  has a magnitude of about  $10\text{ mV}$ . In Case II (\*\*), the membrane potential is shifted by  $13.7\text{ ms}$  and the maximum magnitude is about  $-46.5\text{ mV}$  at  $25.1\text{ ms}$ .

To illustrate the utility of the model in predicting the nerve mechanical response, Fig. 4.4 (a) and Fig. 4.4 (b) show the corresponding displacement vs. time of an unmyelinated nerve membrane and myelinated nerve membrane, respectively, in a damaged bundle along the radial direction (i.e. the  $x$  - axis). Data are taken at the position of maximum radial displacement on Fibre #3. Fig. 4.5 shows the total displacement distribution in an unmyelinated bundle (from (a) to (d)) and in a myelinated bundle (from (e) to (h)) with  $LS = 20\text{ mV}$  and  $AC = 1$ . In both cases, data are plotted at the instant when the mechanical displacement is at its maximum.

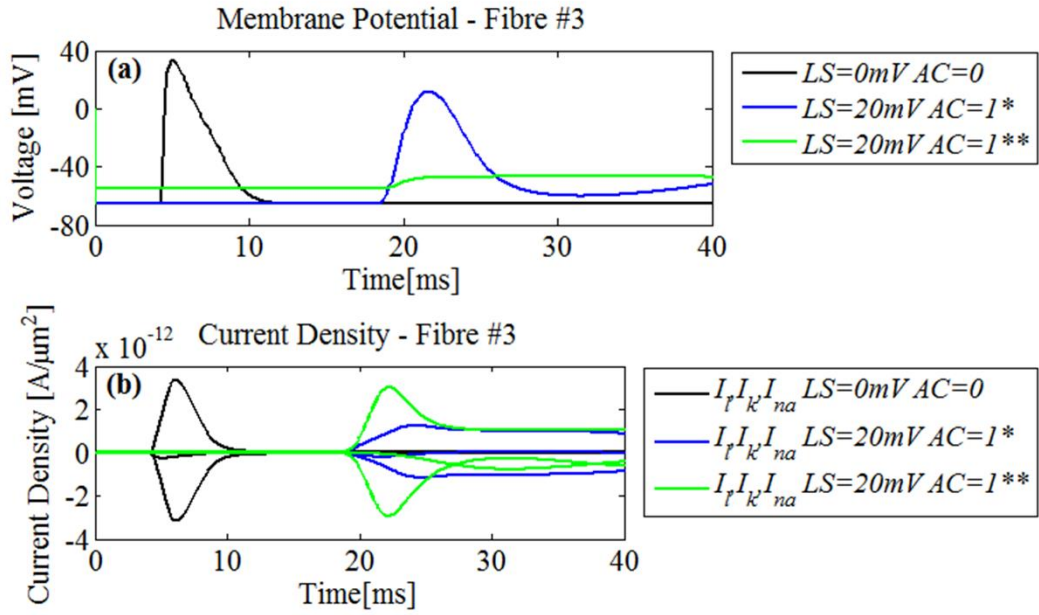


**Fig. 4.3** (a) the membrane’s potential in Case I, AP ( $LS = 0mV; AC = 0$ ); Case II, damaged traumatized membrane ( $LS = 20mV; AC = 1$ ). In \*, the reversal ionic potentials have constant values as in (Boucher et al., 2012), and, in \*\*, they change according to equation Eq. 4.1, as in (Jérusalem et al., 2014). In (b), the Current Density [ $A/\mu m^2$ ] on Fibre #3 for the cases considered.

For each case in Fig. 4.3, residual compressive forces are found in unmyelinated and myelinated fibres, see Fig. 4.4 and Fig. 4.5, due to the biophysical activity of the nerve membrane (Alvarez and Latorre, 1978; Zhang et al., 2001). In an unmyelinated bundle, the displacement peak is  $-3.3 nm$  for Case I,  $-2.5 nm$  for Case II (\*), and  $-0.6 nm$  for Cases II (\*\*). In a myelinated bundle, the peak is  $-0.81 nm$  for Case II (\*) and  $-0.27 nm$  for Case II (\*\*). The peaks of the radial displacements occur at the membrane potential peaks for each case. In a myelinated bundle, lower displacements are found at the membrane than in the unmyelinated case, see Fig. 4.4 (b) and Fig. 4.5 (e)-(h). The myelin layer constrains the deformation of the nerve membrane, reducing the displacement by about an order of magnitude compared to the same unmyelinated fibre, see Fig. 4.4 (b) and Fig. 4.5 (h). Assuming the Ranvier’s node regions are aligned in a bundle, the total displacement of the bundle is driven by the same deformation as the activated fibre, see Fig. 4.5 (h).

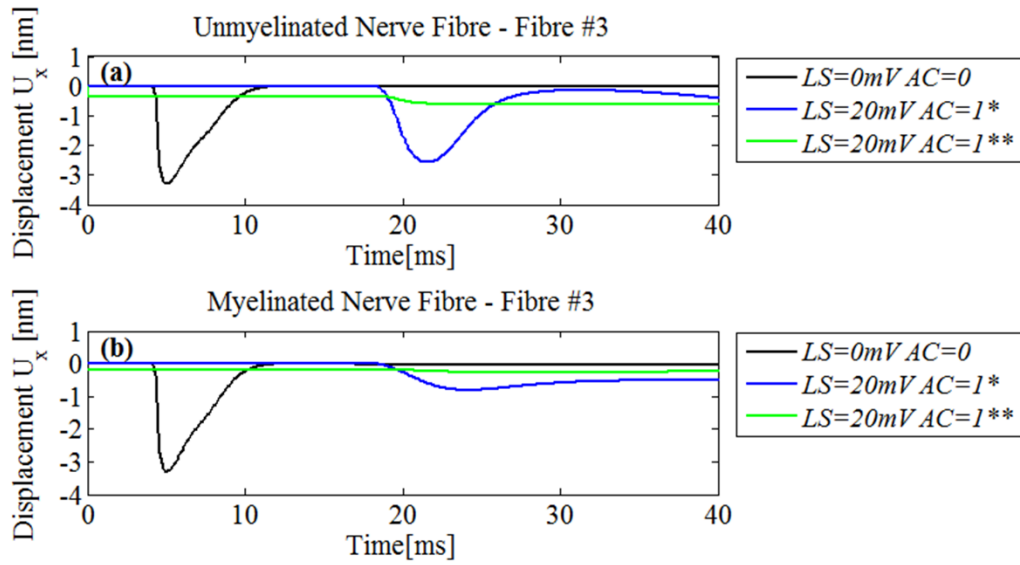


Fig. 4.4 (a): mechanical displacement of the unmyelinated nerve membrane; (b): displacement of a myelinated nerve membrane of the Fibre #3 in the four cases considered (see text) along the radial direction in the bundle (i.e. the  $x$  - axis),  $U_x$ .

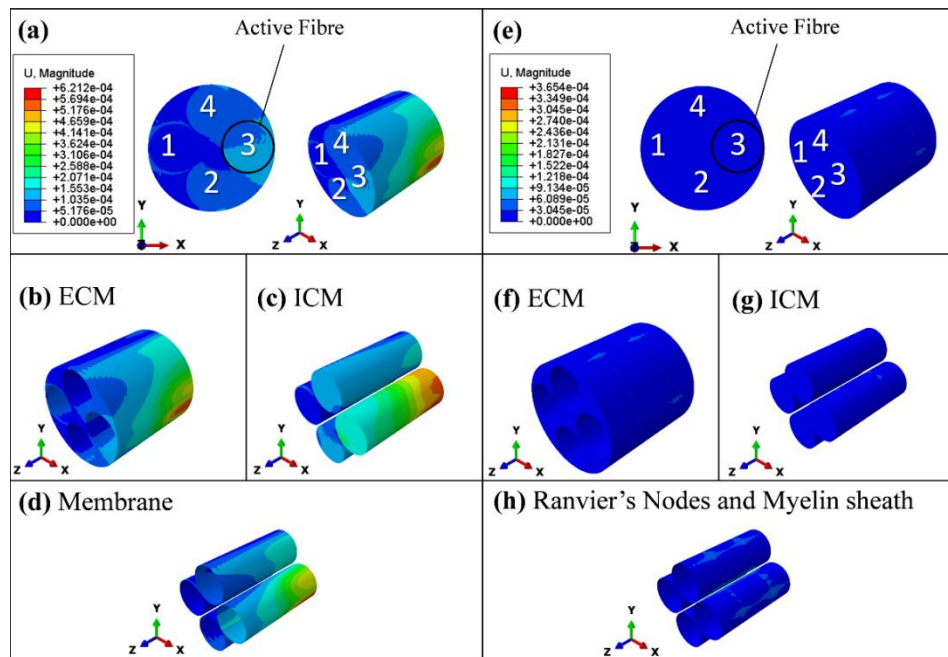


Fig. 4.5 Frontal and isometric views of the total displacement [ $\mu m$ ] in (a) an unmyelinated and (e) a myelinated nerve bundle model. In (b) and (f), the ECM; in (c) and (g), the ICM of the two bundle types. In (d), the isometric view of the nerve membrane and, in (h), the Ranvier nodes and the myelin sheath of the myelinated bundle. (a)-(d) and (e)-(h) are Case II (\*\*)(Jérusalem et al., 2014) applied to an unmyelinated and myelinated nerve bundle. Data are taken at the peak of the membrane potential in both cases.

## 4.3.2 Mechanical Loading Cases of Interest

In this section, the fully coupled electro-mechanical model of Fig. 4.2 is applied to investigate different mechanical loading conditions directly using Eq. 3.1-Eq. 3.6, see Chapter 3, instead of a simulated voltage-shift.

### 4.3.2.1 Pressure Loads

Fig. 4.6 (a) and Fig. 4.6 (b) show the hyperpolarization and current densities of an unmyelinated bundle and a myelinated bundle under mild ( $25\text{ kPa}$ ), moderate ( $68\text{ kPa}$ ) and severe ( $192\text{ kPa}$ ) pressures inducing Traumatic Axonal Injuries (TAI) (Hosmane et al., 2011). The case of extreme pressure ( $1\text{ GPa}$ ) is also considered. In contrast to the reference case of an intact nervous cell ( $P = 0\text{ kPa}$  and  $AC = 0$ ), all pressure loads reduce the magnitude of the AP and shift it over time, correlating with results in Fig. 4.3. Here, the strain applied at the nerve membrane by compressing the bundle shifts the ionic resting potentials of the fully coupled HH model by a quantity which varies depending on the magnitude of the applied load, see Eq. 4.1. Thus, only the  $AC$  variable is considered (not the  $LS$  variable).

Compression levels in the range of  $25\text{ kPa}$  to  $192\text{ kPa}$  have a similar impact on the signal transmission both in terms of reduced magnitude and shift over time; this is found to be due to similar strain values read at the nerve membrane, because of the linear elastic assumption. In these cases, the peak of the membrane potential is about  $-17\text{ mV}$  with  $16\text{ ms}$  of time delay. Here, only slight differences are found for a traumatized vs. non-traumatized nerve membrane ( $AC = 1$  vs.  $0$ ) when mild-to-severe pressures are applied, and therefore only results for  $AC = 0$  are included, see Fig. 4.6.

In contrast, application of extreme pressure changes the resting potential of ions reducing the current flow across the nerve membrane, see Fig. 4.6 (b), and reducing the magnitude of the membrane potential to zero, see Fig. 4.6 (a). An extreme pressure leads to both a reduction in magnitude and an increase of the voltage baseline up to  $-24\text{ mV}$  for an intact membrane, and up to  $-7\text{ mV}$  for a traumatized membrane, see Fig. 4.6 (a) and (b). Here, the homeostatic balance of charges across the nerve membrane vanishes with an extreme pressure applied over a traumatized nerve membrane ( $AC = 1$ ), because the strain levels at the nerve membrane are close to the threshold value assumed in Eq. 4.1.

With mild-to-severe pressure loads from  $25\text{ kPa}$  to  $192\text{ kPa}$ , the contraction of the nerve membrane due to the electrostriction has a similar trend to the case of  $LS = 0\text{ mV}$  and  $AC = 1$ , see Fig. 4.3. Fig. 4.7 (a) and Fig. 4.7 (b) show the radial mechanical displacement on Fibre #3 of an unmyelinated and myelinated fibre, respectively. In both

unmyelinated and myelinated bundles, the membrane potential is shifted through time durations by about  $4.70\text{ ms}$  for the extreme pressure case (not shown here) and by  $16.2\text{ ms}$  for the mild-to-severe cases (Hosmane et al., 2011), respectively, see Fig. 4.7 (a) and Fig. 4.7 (b). Higher deformation at the nerve membrane changes the ionic resting voltages leading to higher mechanical displacements, see Eq. 4.1 and Fig. 4.8.

Then, for the mild to severe cases of TAI-induced pressure (Hosmane et al., 2011), the resting voltage potentials are changed due to the induced deformation in the bundle and the magnitude of the AP is, hence, reduced (Jérusalem et al., 2014), see Fig. 4.7. The peak of the membrane potential is higher in a compressed unmyelinated bundle than in a compressed myelinated one.

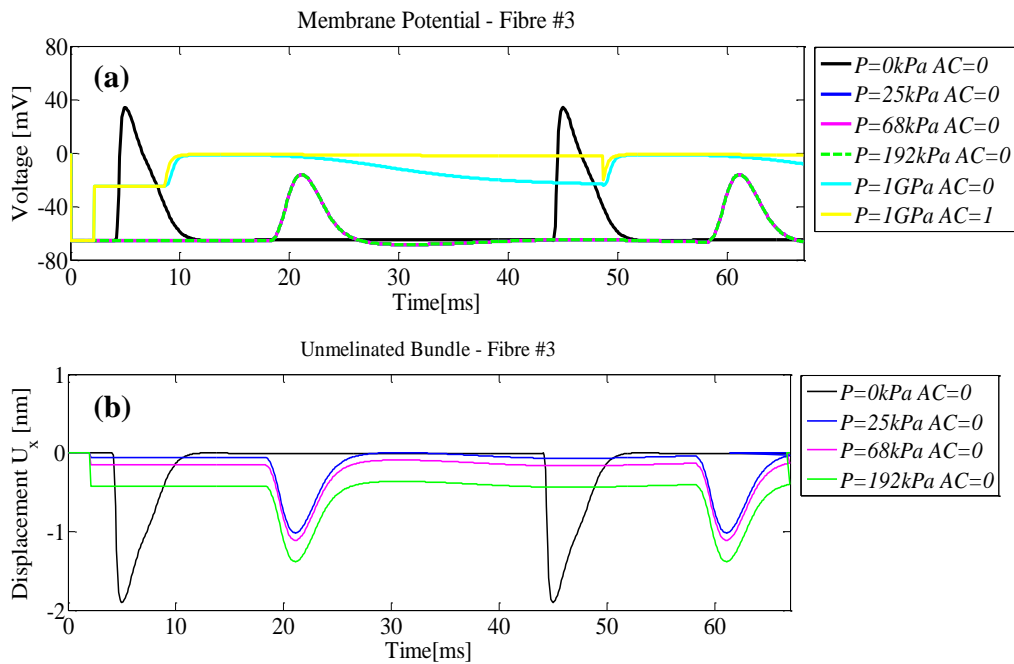


**Fig. 4.6** (a) Membrane Potential [mV] and (b) Current Density [ $A/\mu m^2$ ] on Fibre #3 in the unmyelinated bundle under mild ( $25\text{kPa}$ ), moderate ( $68\text{kPa}$ ) and severe ( $192\text{kPa}$ ) pressures (Hosmane et al., 2011). The extreme case of  $P = 1\text{GPa}$  is also considered.  $AC$  is the fraction of affected ionic channels by the strain:  $AC = 0$  is for an intact membrane and  $AC = 1$  for a traumatized membrane (Boucher et al., 2012). Data are the maximum radial displacement of a node on Fibre #3.

Within the range of pressure levels considered, an unmyelinated layer displaces according to the charges exchanged across the nerve membrane, see Fig. 4.7. On Fibre #3, for the case of mild, moderate and severe pressures, the peak is  $-1.67\text{ nm}$ ,  $-1.82\text{ nm}$ , and  $-2.3\text{ nm}$ , respectively, while the peak of the reference case is at  $-3.4\text{ nm}$ , see Fig. 4.7 (a). In a myelinated bundle, the charge-induced displacement of a myelinated fibre is much less than in an unmyelinated bundle and therefore its displacement is more in response to the loading condition than to electrostriction, see Fig. 4.7 (b). Here, on Fibre #3, for the

cases of mild, moderate, and severe pressures, the peak is  $-0.34\text{ nm}$ ,  $-0.50\text{ nm}$ , and  $-1\text{ nm}$ , respectively, see Fig. 4.7 (b).

This model shows greater membrane displacements in an unmyelinated fibre than in a myelinated fibre, see Fig. 4.7 (a) and Fig. 4.7 (b). The myelin layer constrains the deformation of the Ranvier nodes, which are the only regions throughout the fibre to show voltage-induced membrane displacement (Zhang et al., 2001). At the nodes, the applied compression acts in opposition to the electrostriction, because of the negative value of the membrane potential.

Then, the stresses are about  $8.17 - 8.46\text{ MPa}$  for  $25 - 192\text{ kPa}$ , with slight differences with  $AC$ . Shear stresses are lower than the principal components.

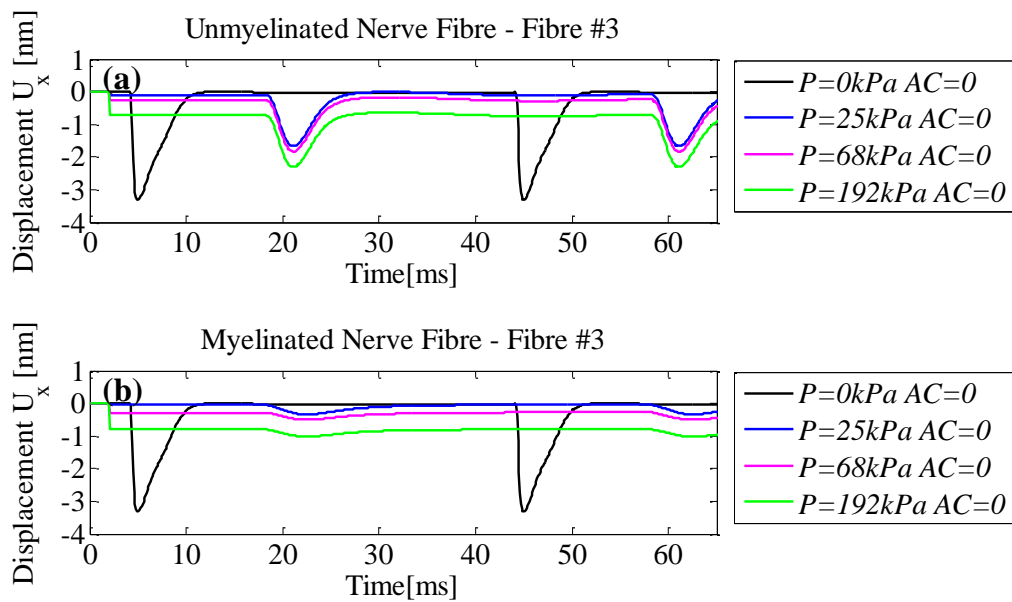


**Fig. 4.7 Radial displacement [nm] of (a) an unmyelinated bundle and (b) a myelinated bundle. Uniform applied pressures are classified as mild ( $25\text{ kPa}$ ), moderate ( $68\text{ kPa}$ ) and severe ( $192\text{ kPa}$ ) pressures (Hosmane et al., 2011). Data are the maximum radial displacement of a node on Fibre #3 in both cases.**

### 4.3.2.2 Displacement Loads

In Fig. 4.8 (a)-(b) and Fig. 4.8 (c)-(d) a displacement boundary condition applied along the length of the unmyelinated and myelinated bundles, respectively, simulates 5% and 14% of total deformation (Bain and Meaney, 2000).

In an unmyelinated bundle, see Fig. 4.8 (a)-(b) and Fig. 4.9 (a)-(d), the membrane potential is shifted over time by about  $19\text{ ms}$  for  $\varepsilon = 5\%$  and  $AC = 0$ , and by  $21\text{ ms}$  for  $\varepsilon = 5\%$  and  $AC = 1$ . For higher deformation, the membrane potential is delayed by  $8\text{ ms}$ , showing similar results both with  $AC = 0$  and  $AC = 1$ , representing the loss of ionic

gradient across the nerve membrane, see Fig. 4.8 (b). Then, the maximum of the membrane potential is about  $-64\text{ mV}$  for  $\varepsilon = 5\%$  (with  $AC = 0$  and  $AC = 1$ ) and  $-60\text{ mV}$  for  $\varepsilon = 14\%$  (with  $AC = 0$  and  $AC = 1$ ).

In contrast, in a myelinated bundle, see Fig. 4.8 (b)-(d) and Fig. 4.9 (e)-(h), no significant differences have been found between intact and traumatized membranes. Here, for 5% and 14% deformation, the membrane potential is shifted up to  $-62\text{ mV}$  and  $-48\text{ mV}$ , respectively, while the peaks are shifted at  $23\text{ ms}$  and  $17\text{ ms}$ , respectively, see Fig. 4.8 (c). Lower current density at the Ranvier's nodes is mainly due to lower voltage gradient and higher localized strain, see Fig. 4.8 (d) and Fig. 4.9 (h). Then, stresses are about  $13 - 41.3\text{ MPa}$ , where the shear stresses are lower than the principal components.

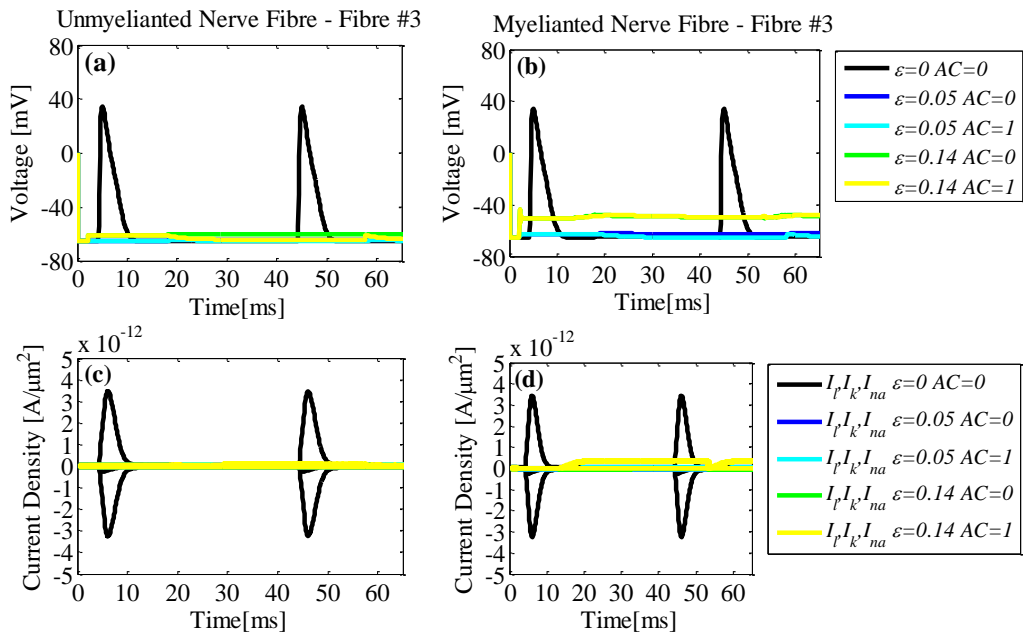


**Fig. 4.8** (a)-(b) Membrane Potential [mV] and (c)-(d) Current Density [ $A/\mu\text{m}^2$ ] on Fibre #3 in the unmyelinated bundle and myelinated bundle, respectively, under 5% and 14% of total deformation  $\varepsilon$  applied (Bain and Meaney, 2000).  $AC$  is the fraction of affected ionic channels by the strain:  $AC = 0$  is for an intact membrane and  $AC = 1$  for a traumatized membrane (Boucher et al., 2012). Data are taken at the maximum displacement along the bundle middle axis, i.e.  $z - axis$ , on Fibre #3.

## 4.4 Discussion

In contrast to previous studies (Wright and Ramesh, 2012; Jérusalem et al., 2014), this chapter shows the advantages of a fully coupled electro-mechanical 3D framework to investigate the details of neural activity, combining real-time fully coupled electro-mechanical phenomena, modulated threshold for spiking activation, and independent alteration of the electrical properties for each fibre in the 3-layer nerve bundle, made of

membrane (or Ranvier’s nodes and myelin sheath), ICM and ECM. The electro-mechanical coupling, based on electro-thermal equivalences (Cinelli et al., 2017e, 2017c, 2017d, 2015a), allows for reliable simulation of changes in electrostriction and neural activity due to mechanical damage, as seen in experiments (Bain and Meaney, 2000; Boucher et al., 2012; Hosmane et al., 2011), see Fig. 3.5.

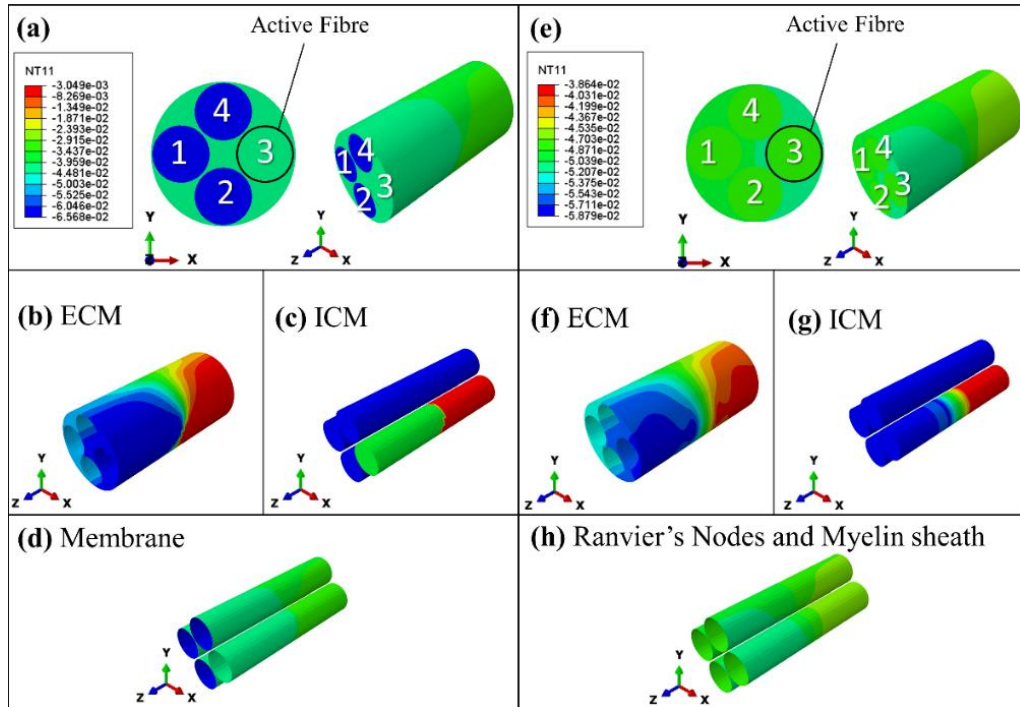


**Fig. 4.9** Voltage distribution (*NT11*) in an unmyelinated nerve bundle, in (a)-(d), and in a myelinated nerve bundle, in (e)-(h), for 5% elongation. Frontal and isometric view of an unmyelinated and myelinated nerve bundle model in (a) and (b), respectively. In (b) and (f), the ECM, in (c) and (g) the ICM of the two bundle types. In (d), the isometric view of the nerve membrane and, in (h), the Ranvier nodes and the myelin sheath of the myelinated bundle.

In this study, two cases of interest provide insights into the electrophysiological impairments of axonal injury due to sudden TAI-induced pressures and displacements. Differences in signal transition arise in the bundle for each fibre, depending on the fibre type. In the bundle, Fibre #3 is activated by imposing a voltage Gaussian distribution, while the other fibres are activated based on the voltage gradient from the active fibre and total strains (i.e. elastic and thermal strain) read at the nerve membrane. Here, the nerve membrane integrity depends on the ionic resting potentials which are a function of the voltage and total strain at the nerve membrane. If the strains at the nerve membrane are lower than 21% (Bain and Meaney, 2000), the resting voltage potentials change accordingly to the strain intensity. Alternately, no ionic gradient can be simulated at the

membrane because the resting voltage values are zero (Jérusalem et al., 2014), as in the case of pressure higher than  $192kPa$  and elongation greater than 14%, see Fig. 4.7 and Fig. 4.9.

During compression, unmyelinated nerve fibres show the greatest changes with mechanical loads due to the higher current density per area exchanged at the membrane, see Fig. 4.7 (a). In contrast, lower density of ions per area can flow through the membrane at the Ranvier's nodes, while the myelin layer constrains the electrostriction accompanying the neural activity, see Fig. 4.7 (b). Then, during elongation, higher strains (along the bundle middle axis (Jérusalem et al., 2014) )are read at the nerve membrane of unmyelinated fibres, while the myelin sheath protects the Ranvier's node regions by redistributing the strains around the bundle, see Fig. 4.8. In both cases, shear stresses are found to be lower than the principal components. However, future work might include shear as boundary conditions, due to their significance in the experimental literature (Smith et al., 1999).

Results show that in the myelinated bundle the activation of the fibres is compromised because they are not able to follow the pattern of activation under pressure and displacement loads. These two loading conditions are cases of clinical interest. A constant pressure on an axon is representative of injuries (Wright and Ramesh, 2012; Ma et al., 2016) and plaques in demyelinating diseases, acting as conduction block for APs of neighbouring axons inhibiting the myelinisation process. On the other hand, results of elongation tests might explain the relatively long time period needed for spontaneous membrane repair after fast strain (Riyi Shi and Whitebone, 2006).

Finally, as highlighted earlier, the results refer to a cylindrical bundle made of four identical fibres with characteristics within the range of the human optic axon (Perge et al., 2012). Although real nerve bundles are made of a higher number of fibres with different calibre (Perge et al., 2012), the use of a simplified geometry was needed to assess electro-mechanical equivalences in a 3D FE model and to limit the computational cost. Chapter 5 is focused on extending this technique to nerve bundles with different calibres (made of unmyelinated and myelinated). Future works may consider mixed bundles containing unmyelinated and myelinated fibres, and activation of multiple fibres.

## 4.5 Conclusion

In this chapter, a fully coupled electro-mechanical framework for modelling the biophysical phenomena accompanying neural activity is proposed. Here, the coupling is based on an electro-thermal analogy by modelling the piezoelectric effect as a thermal

expansion phenomenon in Abaqus CAE 6.13-3. This approach allows us to model and generate insights into aspects of neural activity, such as electrostriction and piezoelectricity, and to correlate these with experimental observations. The model, built on that described in Chapter 3 and in (Cinelli et al., 2017c, 2017e, 2017d, 2015a), generates a fully coupled 3D electro-mechanical simulation of ion channel leaking for nerve fibres under pressure and displacement loads. In conclusion, in this model has been applied to determine the following:

- The time-shift, magnitude and baseline values of a nerve membrane voltage signal are dependent on the total strain, voltage and size of the fibre;
- Lower strain and lower electrophysiological changes are found in myelinated fibre vs. unmyelinated fibre.

This model can contribute to understanding the causes and consequences of TBI and DAI to improve diagnosis, clinical treatments and prognosis by simulating the mechanical changes accompanying the changes in signal transmission in traumatic-axonal-injury-induced loading conditions.

## References Chapter 4

- Alvarez, O., and Latorre, R. (1978). Voltage-dependent capacitance in lipid bilayers made from monolayers. *Biophysical Journal*, 21(1), 1–17. [https://doi.org/10.1016/S0006-3495\(78\)85505-2](https://doi.org/10.1016/S0006-3495(78)85505-2)
- Bain, A. C., and Meaney, D. F. (2000). Tissue-level thresholds for axonal damage in an experimental model of central nervous system white matter injury. *Journal of Biomechanical Engineering*, 122(6), 615–622. <https://doi.org/10.1115/1.1324667>
- Boucher, P. A., Joós, B., and Morris, C. E. (2012). Coupled left-shift of Nav channels: Modeling the Na<sup>+</sup>-loading and dysfunctional excitability of damaged axons. *Journal of Computational Neuroscience*, 33(2), 301–319. <https://doi.org/10.1007/s10827-012-0387-7>
- Cao, C., Yu, A., and Qin, Q.H. (2012). Evaluation of effective thermal conductivity of fiber-reinforced composites. *International Journal of Architecture, Engineering and Construction*, 1(1), 14–29. <https://doi.org/10.7492/IJAEC.2012.002>
- Cinelli, I., Destrade, M., Duffy, M., and McHugh, P. (2017a). Electro-mechanical response of a 3d nerve bundle model to mechanical loads leading to axonal injury. In *Engineering in Medicine and Biology Society (EMBC), 2017 39th Annual International Conference of the IEEE* (pp. 1–4). <https://doi.org/10.1109/EMBC.2017.8036989>
- Cinelli, I., Destrade, M., Duffy, M., and McHugh, P. (2017b). Electro-thermal equivalent 3D Finite Element Model of a Single Neuron. *IEEE Transactions on Biomedical Engineering*, 9294(99). <https://doi.org/10.1109/TBME.2017.2752258>
- Cinelli, I., Destrade, M., Duffy, M., and McHugh, P. (2017c). Neurotrauma evaluation in a 3D electro-mechanical model of a nerve bundle. In IEEE (Ed.), *International IEEE/EMBS Conference on Neural Engineering*, NER (pp. 513–516). <https://doi.org/10.1109/NER.2017.8008402>
- Cinelli, I., Duffy, M., and McHugh, P. (2015). Thermo-electrical equivalents for simulating the electro-mechanical behavior of biological tissue. *Proceedings of the Annual International Conference of the IEEE Engineering in Medicine and Biology Society, EMBS, 2015–Novem*, 3969–3972. <https://doi.org/10.1109/EMBC.2015.7319263>
- Demerens, C., Stankoff, B., Logak, M., Anglade, P., Allinquant, B., Couraud, F., Lubetzki, C. (1996). Induction of myelination in the central nervous system by electrical

- activity. *Proceedings of the National Academy of Sciences*, 93(18), 9887–9892. <https://doi.org/10.1073/pnas.93.18.9887>
- Einzig, P. D., Livshitz, L. M., Dolgin, A., and Mizrahi, J. (2005). Novel cable equation model for myelinated nerve fiber. *IEEE Transactions on Biomedical Engineering*, 52(10), 112–115. <https://doi.org/10.1109/CNE.2003.1196769>
- Einzig, P. D., Livshitz, L. M., Dolgin, A., and Mizrahi, J. (2003). Novel cable equation model for myelinated nerve fiber. *First International IEEE EMBS Conference on Neural Engineering*, 2003. Conference Proceedings. 52(10), 1632–1642. <https://doi.org/10.1109/CNE.2003.1196769>
- El Hady, A., and Machta, B. B. (2015). Mechanical surface waves accompany action potential propagation. *Nature Communications*, 6(6697), 6697. <https://doi.org/10.1038/ncomms7697>
- Galbraith, J. A., Thibault, L. E., and Matteson, D. R. (1993). Mechanical and electrical responses of the squid giant axon to simple elongation. *Journal of Biomechanical Engineering*, 115(1), 13–22. <https://doi.org/10.1115/1.2895464>
- Gallant, P. E. (1992). The direct effects of graded axonal compression on axoplasm and fast axoplasmic transport. *Journal of Neuropathology and Experimental Neurology*, 51(2), 220–230. Retrieved from <http://www.ncbi.nlm.nih.gov/pubmed/1371545>
- Gallant, P. E., and Galbraith, J. A. (1997). Axonal structure and function after axolemmal leakage in the squid giant axon. *Neurotrauma*, 14(11), 811–822. <https://doi.org/10.1089/neu.1997.14.811>
- Geddes, D. M., Cargill, R. S., and LaPlaca, M. C. (2003). Mechanical stretch to neurons results in a strain rate and magnitude-dependent increase in plasma membrane permeability. *Journal of Neurotrauma*, 20(10), 1039–1049. <https://doi.org/10.1089/089771503770195885>
- Hodgkin, A. L., and Huxley, A. F. (1952). A quantitative description of membrane current and its application to conduction and excitation in nerve. *Journal of Physiology*, 117, 500–544. [https://doi.org/10.1016/S0092-8240\(05\)80004-7](https://doi.org/10.1016/S0092-8240(05)80004-7)
- Hosmane, S., Fournier, A., Wright, R., Rajbhandari, L., Siddique, R., Yang, I. H., Thakor, N. (2011). Valve-based microfluidic compression platform: Single axon injury and regrowth. *Lab on a Chip*, 11(22), 3888. <https://doi.org/10.1039/c1lc20549h>

- Jérusalem, A., García-Grajales, J. A., Merchán-Pérez, A., and Peña, J. M. (2014). A computational model coupling mechanics and electrophysiology in spinal cord injury. *Biomechanics and Modeling in Mechanobiology*, 13(4), 883–896. <https://doi.org/10.1007/s10237-013-0543-7>
- Lajtha, A., Javitt, D., and Kantrowitz, J. (2009). Handbook of neurochemistry and molecular neurobiology. Brain and spinal cord trauma. (N. Banik & K. R. Swapan, Eds.), *Springer Reference* (3rd Edition, Vol. 281). Springer. <https://doi.org/10.1016/j.jns.2009.03.019>
- LaPlaca, M. C., Cullen, D. K., McLoughlin, J. J., and Cargill, R. S. (2005). High rate shear strain of three-dimensional neural cell cultures: A new in vitro traumatic brain injury model. *Journal of Biomechanics*, 38(5), 1093–1105. <https://doi.org/10.1016/j.jbiomech.2004.05.032>
- Leung, L. Y., Vandevord, P. J., Leonardi, A., Cengio, D., Bir, C., Yang, K. H., and King, A. I. (2008). Blast Related Neurotrauma: A review of Cellular Injury. *Molecular and Cellular Biomechanics*, 5(3), 155–168.
- Ma, J., Zhang, K., Wang, Z., and Chen, G. (2016). Progress of research on diffuse axonal injury after traumatic brain injury. *Neural Plasticity*, 2016, 7. <https://doi.org/10.1155/2016/9746313>
- Maxwell, W. L., and Graham, D. I. (1997). Loss of axonal microtubules and neurofilaments after stretch-injury to guinea pig optic nerve fibers. *Journal of Neurotrauma*, 14(9), 603–614. <https://doi.org/10.1089/neu.1997.14.603>
- Mosgaard, L. D., Zecchi, K. a., and Heimborg, T. (2015). Mechano-capacitive properties of polarized membranes. *Soft Matter*, 11(40), 7899–7910. <https://doi.org/10.1039/C5SM01519G>
- Perge, J. a, Niven, J. E., Mugnaini, E., Balasubramanian, V., and Sterling, P. (2012). Why do axons differ in caliber? *The Journal of Neuroscience*, 32(2), 626–638. <https://doi.org/10.1523/JNEUROSCI.4254-11.2012>
- Platkiewicz, J., and Brette, R. (2010). A threshold equation for action potential initiation. *PLoS Computational Biology*, 6(7), 25. <https://doi.org/10.1371/journal.pcbi.1000850>

- Shi, R., and Whitebone, J. (2006). Conduction deficits and membrane disruption of spinal cord axons as a function of magnitude and rate of strain. *Journal of Neurophysiology*, 95(6), 3384–3390. <https://doi.org/10.1152/jn.00350.2005>
- Smith, D. H., and Meaney, D. F. (2000). Axonal damage in traumatic brain injury. *The Neuroscientist*, 6(6), 483–495. <https://doi.org/10.1177/107385840000600611>
- Smith, D. H., Wolf, J. A., Lusardi, T. A., Lee, V. M., and Meaney, D. F. (1999). High tolerance and delayed elastic response of cultured axons to dynamic stretch injury. *The Journal of Neuroscience*, 19(11), 4263–4269. Retrieved from <http://www.jneurosci.org/content/19/11/4263.long>
- Wang, H. C., and Ma, Y. Bin. (2010). Experimental models of traumatic axonal injury. *Journal of Clinical Neuroscience*, 17(2), 157–162. <https://doi.org/10.1016/j.jocn.2009.07.099>
- Wright, and Ramesh, K. T. (2012). An axonal strain injury criterion for traumatic brain injury. *Biomechanics and Modeling in Mechanobiology*, 11(1–2), 245–260. <https://doi.org/10.1007/s10237-011-0307-1>
- Yu, N., Morris, C.E., Joós, B. and Longtin, A. (2012). Spontaneous excitation patterns computed for axons with injury-like impairments of Sodium Channels and Na/K pumps. *PLoS Computational Biology*, 8(9). <https://doi.org/10.1371/journal.pcbi.1002664>
- Zhang, Y. P., Cai, J., Shields, L. B. E., Liu, N., Xu, X. M., and Shields, C. B. (2014). Traumatic brain injury using mouse models. *Translational Stroke Research*, 5(1), 454–471. <https://doi.org/10.1007/s12975-014-0327-0>
- Zhang, Keleshian, A. M., and Sachs, F. (2001). Voltage-induced membrane movement. *Nature*, 413(6854), 428–432. <https://doi.org/10.1038/35096578>

## Chapter 5.      **Effects of Nerve Bundle Geometry on Neurotrauma Evaluation**

In this chapter the use of the electro-mechanical coupling in unmyelinated and myelinated nerve bundles of different sizes is investigated. Here, the proposed modelling framework is developed to include mechanical plasticity. This chapter has been published as a journal paper manuscript in *Cinelli I, Destrade M, McHugh P, Duffy M. Effects of nerve bundle geometry on neurotrauma evaluation. International Journal of Numerical Methods in Biomedical Engineering. 2018;34:e3118. <https://doi.org/10.1002/cnm.3118>*.

*Abstract — Objective:* To show that alteration of a neuron structure can induce abnormalities in signal propagation for nervous systems, as seen in traumatic brain injuries, brain damage and brain tumours. *Methods:* The effects of geometrical changes and damage of a neuron structure are investigated in two scaled nerve bundle models, one made of myelinated nerve fibres and the other made of unmyelinated nerve fibres. A 3D finite element model of nerve bundles is proposed as a unique framework in Abaqus CAE 6.13-3, combining a real-time fully coupled electro-mechanical framework, a modulated threshold for spiking activation and independent alteration of the electrical properties for each 3-layer fibre. *Results:* The cases of compression and tension are simulated to induce (mild and severe) damage at the membrane of a nerve bundle made of four fibres. The changes in strain and neural activity for myelinated and unmyelinated nerve fibres are examined in both bundle sizes, by considering in turn the cases of intact and traumatized nerve membrane. Results show lower strain and lower electrophysiological impairments in unmyelinated fibres than in myelinated fibres. Also, higher deformation levels are found in larger bundles, and higher electrophysiological impairments in smaller bundles. *Conclusion:* The insulation sheath of myelin constricts the membrane deformation and scatters plastic strains within the bundle; higher strain levels are found at the nerve membrane in the myelinated bundle; larger bundles deform more than small bundles; small fibres tolerate a higher level of elongation before mechanical failure.

## 5.1 Introduction

As discussed in Chapter 4, head injuries may result in Traumatic Brain Injury (TBI), which is categorized as mild, moderate and severe based on clinical symptoms and post-mortem histology (Hemphill et al., 2015; Hosmane et al., 2011; Ma et al., 2016; Wright and Ramesh, 2012; Zhang et al., 2014). The rapid acceleration-deceleration of the head during TBI generates a diffusive form of microscale damage, such as Diffuse Axonal Injury (DAI) and microvascular damage (Hemphill et al., 2015; Ma et al., 2016; Wright and Ramesh, 2012; Zhang et al., 2014). However, microscale damage is difficult to detect with the current medical imaging technology due to haemorrhages, haematoma and tissue lesions of the neighbouring injured area (Hemphill et al., 2015; Kan et al., 2012; Wright and Ramesh, 2012). This difficulty increases the risk of developing future neurodegenerative disease (Hemphill et al., 2015; Kan et al., 2012).

Previous biomechanical studies of brain injuries have highlighted the importance of the brain microenvironment and of neural tissue responses in the understanding of disease pathogenesis initiated by TBI (Hemphill et al., 2015). They established that tensile axonal strain is the most realistic mechanism for generating DAI at the cellular level (Bain and Meaney, 2000; Cinelli et al., 2017b; Antoine Jérusalem Jérusalem et al., 2014; Wright and Ramesh, 2012).

At the next level, the distribution of diffuse damage is found to be non-uniform throughout the brain tissue, suggesting that tissue regions and cellular structures within the brain are affected differently (Hemphill et al., 2015). Tissue heterogeneity has a significant influence on the mechano-transduction of mechanical forces into physiological and neural responses of nervous cells (Hemphill et al., 2015), and therefore models that accurately account for tissue structure are needed for an effective modelling of damage.

Experiments have also revealed a close link between changes in electrical signal propagation and changes in the geometrical structure of neurons (Zhang et al., 2001). Indeed, a geometrical alteration of neural morphology can modify the propagation properties of the action potential (AP), for instance by delaying propagation (Boucher et al., 2012; Cinelli et al., 2017a, 2017e; Mohagheghian, 2015). This was observed in results presented in Chapter 4. A detailed investigation of non-recoverable deformations of the neural microenvironment (injuries (Antoine Jérusalem et al., 2014; Wright and Ramesh, 2012), trauma (Jérusalem et al., 2014), tumours (Mohagheghian, 2015)) is needed to evaluate and estimate the role of nerve bundle geometry in changing neural activity.

Recent progress in physiological measurements has led to new insights into damaged neuronal behaviour, where electrophysiological and functional deficits of the neural activity are known to be functions of the applied strain and strain rate (Boucher et al., 2012; Geddes

et al., 2003; Jérusalem et al., 2014). Electrophysiological impairments (such as leaking ionic channels (Boucher et al., 2012; Yu et al., 2012)) are associated with structural damage of the neuron tissue. The loss of nerve membrane integrity due to an applied deformation leads to changes in electrical signal propagation (Galbraith et al., 1993; Yu et al., 2012). Furthermore, injury pathologies in nerve fibres are also initiated and influenced by strain and strain rate, which have a significant impact on the time of neural death and pathomorphology, respectively (Bar-kochba et al., 2016). For instance, experimental studies on human axons show that morphological changes may tolerate dynamic stretch at strains up to 65% (Smith et al., 1999), manifesting both an elastic recovery and a delayed elastic response along the fibre length (Smith et al., 1999), as mentioned in the previous chapters.

In this chapter the influence of neuron morphology in neurotrauma is evaluated. Here neurotrauma refers to the alteration of neural activity in a mechanical-injured nerve (Galbraith et al., 1993; Geddes et al., 2003), by using a fully coupled electro-mechanical model in the finite element (FE) software package Abaqus, shown in Fig. 4.2. Our purpose is to evaluate strain distributions leading to neurotrauma in damaged nerve bundles of different types and sizes during signalling. This work aims at improving the understanding the mechano-transduction of mechanical loads below the threshold for mechanical failure, on neural responses in nerve bundles and fibres.

In contrast with previous modelling efforts (Jérusalem et al., 2014; Mohagheghian, 2015), a fully coupled 3D electro-mechanical model of a nerve bundle is proposed (Cinelli et al., 2017b, 2017d), which includes electro-mechanical coupling (Alvarez and Latorre, 1978; El Hady and Machta, 2015; Zhang et al., 2001) of the neural activity. Mechanical loads inducing damage are applied (Cinelli et al., 2017b; Jérusalem et al., 2014) at the nerve membrane layer to investigate the changes in neuronal membrane excitability (Jérusalem et al., 2014) and propagation (Boucher et al., 2012) in response to changes in electrostriction (Mueller and Tyler, 2014). As discussed in Chapter 1 and 3, the electrical and the mechanical fields of the model are coupled by using electro-thermal equivalences and equivalent materials properties in FE analysis (Cinelli et al., 2017d, 2017b). The coupling of the electro-mechanical effects of the AP is achieved (Hodgkin and Huxley, 1952) by modelling the nerve membrane as a piezoelectric material (Zhang et al., 2001), and implementing the thermal analogy of the neural electrical activity (Cinelli et al., 2017d, 2017b).

The modelling approach reported in (Cinelli et al., 2017a) describes a computationally efficient way for coupling the electrical and mechanical domains in finite element analysis. It has been shown to replicate successfully complex biophysical phenomena occurring in nervous cells. The nerve bundle model in (Cinelli et al., 2017a) assumes incompressible rate-independent isotropic mechanical behaviour (Cinelli et al., 2017a; El Hady and Machta,

2015), so that the applied loads induce elastic deformations only while no permanent deformations are generated within that model. In contrast to (Cinelli et al., 2017a), here, the description of the mechanical behaviour of the nerve bundle model incorporates plasticity to represent permanent deformation of the tissue, while sharing the same approach for modelling the coupling between electrical and mechanical domains, proposed in (Cinelli et al., 2017a). The incorporation of plasticity in this way significantly enhances the physiological accuracy of the model in relation to recoverable (elastic) and permanent (plastic) tissue deformation. This aspect is of critical importance when investigating the effects of trauma, as here. Understanding the role of plasticity on induced alterations of the neural activity might lead to new insights into the mechanical and functional performance of nervous cells.

In a development of the model presented in Chapter 4 and in (Cinelli et al., 2017b), here the effects of nerve bundle geometry and type on the electro-mechanical coupling to evaluate permanent electro-mechanical impairments due to plasticity are analysed when mechanical loads are applied. Although nerve axons show some elastic recovery of the pre-stretched geometry under slow loading rates (Smith et al., 1999), the role of plasticity in delaying the mechanical response is fundamental in understanding the pathology due to stretch injury occurring at fast loading rates. Indeed, induced-permanent focal axonal dysfunction and induced-permanent focal electrophysiological impairments may explain the adaptive recovery of neural connections seen in mild-to-moderate TBI, and the potential synaptic rearrangements seen in severe TBI (Jafari et al., 1998; H. C. Wang and Ma, 2010; Wang et al., 2011). So, in contrast to Chapter 4, the fully coupled HH model used for this analysis includes plasticity, see Fig. 4.2.

This chapter shows that variability in axonal calibre affects axonal vulnerability, leading to differential injury responses in myelinated and unmyelinated axons (Hemphill et al., 2015; Perge et al., 2012). Morphological changes of the cellular structures are more likely to happen in unmyelinated than myelinated axons (Hemphill et al., 2015; Jafari et al., 1998; Reeves et al., 2012), and they occur in the form of molecular-based processes such as leaking nerve membrane (Yu et al., 2012) and cytoskeleton disruption (Hemphill et al., 2015; Jafari et al., 1998; Smith et al., 1999; Tang-schomer et al., 2017). Unmyelinated axons are at greater risk compared to myelinated axons, where injuries occur preferentially at the Ranvier's node regions (Hemphill et al., 2015). Additionally, larger calibre axons are shown to be more vulnerable to injury due to their higher metabolic requirements, and they are more prone to develop pathologies (Hemphill et al., 2015; Reeves et al., 2012).

Our proposed 3D finite element model of a nerve bundle includes a representation of a nervous cell made of Extracellular Media (ECM), a membrane, and Intracellular Media (ICM), as in Fig. 4.1. This chapter considers the case of two scaled nerve bundle models

with a ratio of 2:1, where the nerve fibres inside follow the same ratio, while keeping the same thickness for the nerve membrane (Cinelli et al., 2017b, 2017d). The bundles are made of identical unmyelinated or myelinated nerve fibres. Different sizes and nerve types are used to enhance the understanding of neurotrauma in mechanically-injured bundles, as revealed in experiments at the cellular level (Galbraith et al., 1993; Geddes et al., 2003; Yu et al., 2012).

With the purpose of highlighting the importance of a unified electro-mechanical theory for neural applications (El Hady and Machta, 2015; Heimbürg et al., 2014; Hemphill et al., 2015; Mosgaard et al., 2015; Mueller and Tyler, 2014), a modelling approach (Cinelli et al., 2017b, 2017d) is further developed in this chapter to replicate electro-mechanical phenomena accompanying the neural electrical activity (Cinelli et al., 2017b, 2017d; El Hady and Machta, 2015; Mueller and Tyler, 2014). The use of an idealized 3D geometry with plastic material properties allows for the simulation and evaluation of strain and voltage distributions before and after the induced damage.

## 5.2 Method

### 5.2.1 Material Properties

The Nerve Bundle Model assumes incompressible rate-independent isotropic mechanical behaviour (El Hady and Machta, 2015), as described in Chapter 3 and 4. Further, plasticity is included, by assuming the same isotropic plastic behaviour for the nerve membrane, ICM, and myelin layer. The yield stress is calculated with an engineering strain equal to 21 % (Bain and Meaney, 2000) and a Young's Modulus equal to  $1\text{ GPa}$  (El Hady and Machta, 2015). Strain hardening is assumed to occur up to a strain of 65 % (Smith et al., 1999). Thus, the engineering strain and engineering stress values are  $(0.21, 0.21\text{ GPa})$  and  $(0.65, 0.65\text{ GPa})$  for the yield strain limit and strain hardening, respectively. Beyond 65 % strain, the stresses are assumed to be constant.

The electrical model parameters for unmyelinated and myelinated fibres are taken from (Cinelli et al., 2015c) and (Jérusalem et al., 2014), respectively. As mentioned in Section 3.2.3, the piezoelectric effect is only relevant in the through-thickness direction, represented here with orthotropic piezoelectric constants of approximately  $1\text{ nm}$  per  $100\text{ mV}$  (Zhang et al., 2001) in the thickness direction and zero in the longitudinal and circumferential directions, while the electrical capacitance per unit area changes as the square of the voltage as before (Cinelli et al., 2017d, 2017b; El Hady and Machta, 2015).

## 5.2.2 Boundary Conditions

For evaluating the influence of neuron structure in neurotrauma, only one fibre in each bundle is activated, Fibre#3, while the other fibres are activated by the diffusion of charges when the induced damage is minimal or absent (Cinelli et al., 2017b). For the purposes of this chapter, the one-fibre activation assumption allows for quantifying the generated electro-mechanical alterations (Cinelli et al., 2017b) in a simplified context, as a first step towards a more detailed analysis. This assumption allows for understanding the distribution of charges when mechanical damage is induced, focusing on the radial distribution of charges rather than on longitudinal.

In particular, an upper-threshold stimulation voltage with a Gaussian distribution (Cinelli et al., 2017b; Tahayori et al., 2012) is applied on Fibre #3 along its length as before, see Fig. 4.2, while the other fibres are activated only if the diffused charges from Fibre #3 generate an input voltage higher than the modulated threshold (Platkiewicz and Brette, 2010). The 3D distribution of charges on Fibre #3 modulates the activation of the other fibres, see Fig. 4.1.

This chapter considers in turn two cases of applied mechanical loads at the bundle. As a first step to assess the inclusion of plasticity using this novel coupling method, only frequency-independent loading conditions are considered throughout, following the initial steady-state regime (lasting about  $2ms$ ) (Cinelli et al., 2017b, 2017d). The mechanical loads are applied from  $2ms$  to  $67ms$ , as instantaneous loading conditions, and the model runs for  $140ms$  so that the effects of plasticity can be observed post-loading. An encasté boundary condition is enforced at the origin of each model, so that no movement and rotation is allowed at the origin node. Then, no rotation is allowed for all nodes at the origin bundle side.

In the first case, an instantaneous uniform compression to the bundle is applied to simulate injury conditions, with two values of pressure, simulating mild (less than  $55kPa$ ) and severe (higher than  $95kPa$ ) pressures (Hosmane et al., 2011).

In the second case, the axial strain conditions of the uniaxial test are reproduced as those conducted by Bain and Meaney (Bain and Meaney, 2000). Two values of instantaneous uniform stretch are applied as a displacement boundary condition to simulate 5 % and 14 % of total axial deformation,  $\epsilon$ , where the probability of inducing morphological injury during the elongation test is 5% and 25%, respectively (Bain and Meaney, 2000). Additionally, this chapter also considers the cases of 25%, 30% and 60% elongation to investigate the electro-mechanical responses within the range of plasticity (before mechanical failure) (Smith et al., 1999).

## 5.3 Results

### 5.3.1 Pressure Loads

Fig. 5.1 (a) shows the membrane potential of a small bundle made of unmyelinated nerve fibres (SBUN), and Fig. 5.1 (c)-(e) the radial displacement in small (SBUN) and big (BBUN) unmyelinated bundles under mild ( $25kPa$ ) and severe ( $192kPa$ ) pressures, inducing axonal injuries (Hosmane et al., 2011). Then, Fig. 5.1 (b) shows the membrane potential of Small Myelinated Bundle (SBMY), and Fig. 5.1 (d)-(f) the radial displacement in a small (SBMY) and big (BBMY) myelinated bundles, for each pressure case. It should be noted that because they have the same membrane properties, the same voltage responses are found for both small and big bundle models. Here, the strain applied at the nerve membrane by compressing the bundle shifts the ionic reversal potentials of the fully coupled HH model by a quantity which varies depending on the magnitude of the applied load, see Fig. 4.2. Results are taken at the maximum radial displacement on Fibre #3.

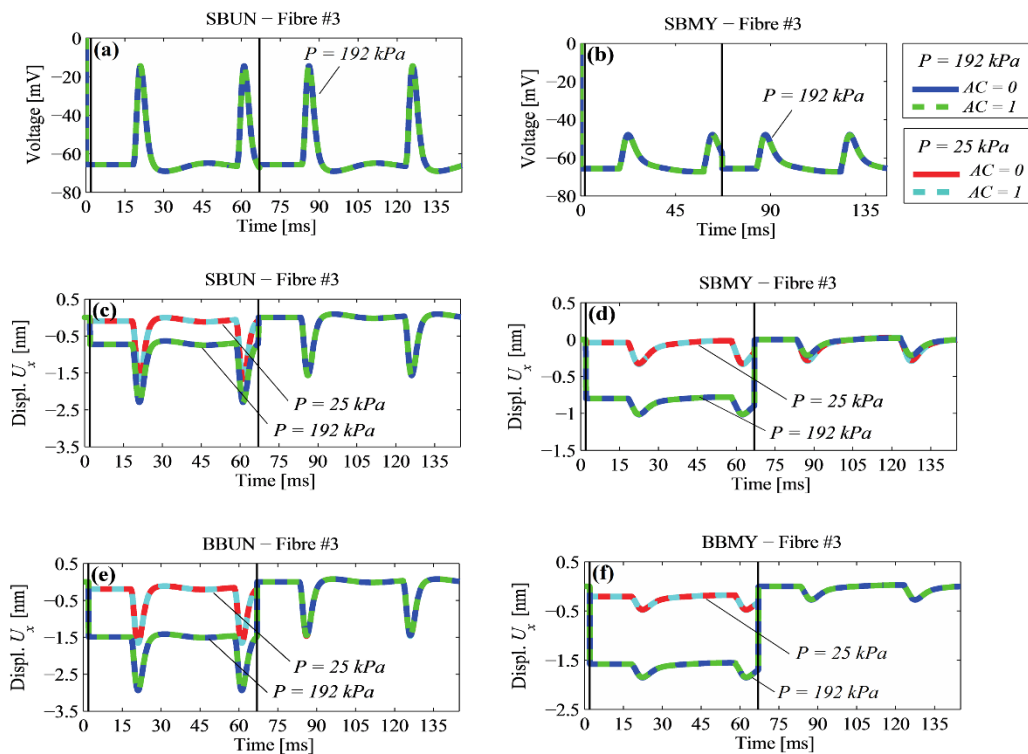


**Fig. 5.1** (a) Membrane Potential [mV] on Fibre #3 in a small unmyelinated bundle (SBUN). (c)-(e) Radial displacement [nm],  $U_x$ , of a SBUN and an unmyelinated big bundle (BBUN). (b) Membrane Potential [mV] on Fibre #3 in a small myelinated bundle (SBMY). (d)-(f) Radial displacement [nm],  $U_x$ , of SBMY and a myelinated big bundle (BBMY). The uniform applied pressures are classified as mild ( $25kPa$ ) and severe ( $192kPa$ ) pressures (Hosmane et al., 2011). Data are the maximum radial displacement of a node on Fibre #3 in both cases.

In this chapter, it is found that mild ( $25\text{ kPa}$ ) and severe ( $192\text{ kPa}$ ) pressure levels have a similar impact on the signal transmission, both in terms of reduced magnitude and shift over time, due to similar strain values read at the nerve membrane. In both small (SBUN) and big (BBUN) unmyelinated bundles, the AP's peak is  $-14.4\text{ mV}$  at  $19\text{ ms}$ , see Fig. 5.1 (a), while in small (SBMY) and big (BBMY) myelinated bundles, the peak is  $-47.54\text{ mV}$  at  $22\text{ ms}$ , see Fig. 5.1 (b).

For any applied load, the reversal voltage potentials are changed due to the induced-strain in the bundle and the magnitude of the AP is reduced (J rusalem et al., 2014). The applied compression leads to changes in reversal potentials, according to the strain values read along the bundle middle axis only (J rusalem et al., 2014). In all cases, only slight differences are found for a traumatized ( $AC = 1$ ) compared to a non-traumatized nerve membrane ( $AC = 0$ ) when mild or severe pressures are applied, see Fig. 5.1 (a)-(b). The fraction of Affected Channels,  $AC$ , impacts the ionic conductance (Boucher et al., 2012) whose changes are not contributing to the total strain along the bundle middle axis direction during compression, see Section 4.2.5. This is because the piezoelectricity of the membrane is modelled radially rather than longitudinally (Cinelli et al., 2017d; Zhang et al., 2001), as discussed in (El Hady and Machta, 2015; Hodgkin and Huxley, 1952; Zhang et al., 2001). Indeed, the applied pressures lead to an axial displacement of less than 1 % of the total length of the bundles in each model. Despite the size of the bundle, traumatized nerve membranes seem to be able to carry and generate signals both during and after uniform compression.

Fig. 5.1 (c) and (e) show the radial displacement on Fibre #3 in SBUN and BBUN, respectively. While the shift in baseline displacement is altered by the applied pressure in both cases, the amplitude of the peak value from the baseline follows the membrane voltage response, and therefore values for the unmyelinated bundles are the same regardless of the bundle size, see Fig. 5.1 (c) and (e).

Table 5.1 lists the values of the displacement shift, during and after loading, at mild ( $25\text{ kPa}$ ) and severe ( $192\text{ kPa}$ ) pressure levels. The maximum values of the Plastic Strain ( $PE$ ) and Total Strain ( $E_{tot}$ ) are computed once the loads are removed.

Fig. 5.1 (a)-(d) show the difference in voltage distribution over the bundle, at the AP peak, in small and big, myelinated and unmyelinated bundles, with non-traumatized nerve membranes ( $AC = 0$ ) bundles, under mild pressure ( $25\text{ kPa}$ ).

The myelinated bundles (Fig. 5.2 (a) and (c)) experience uniform compression. At the peak of the membrane potential applied on Fibre #3, the piezoelectric effect generates an additional contraction on its nerve membrane, dragging parts of Fibres #2 and #4 in its

vicinity. Thus, four peaks of the maximum total strain  $E_{tot}$  on Fibre#3 are found: two are at the regions in proximity to Fibres #2 and #4; and two in the diametrically opposed regions (to conserve the overall volume by incompressibility). Then, on the encastré side of the bundle, where the applied voltage is higher, local regions of high voltage are found on Fibres #2 and #4, due to their vicinity with Fibre #3. So, local contractions on Fibres #2 and #4 act in opposition to the contractions on Fibre#3. The voltage distribution in Fig. 5.2 (a) and (c) is influenced by the final distribution of  $E_{tot}$ . Hence, the voltage is higher at the regions where: the applied voltage Gaussian distribution is high, the nerve membrane is not constrained, and the strains are low.

A similar scenario occurs for myelinated bundles, see Fig. 5.2 (b) and (d). However, here the piezoelectricity is limited to the Ranvier's node regions, whose displacement is constrained by the myelin layer. Accordingly, the  $E_{tot}$  is more uniform at the nerve membrane layer of all the fibres than for unmyelinated bundles. Fibres surrounding the active Fibre #3 are not activated because the charge read at their nerve membrane is lower than the minimum threshold for activation (Hodgkin and Huxley, 1952).

**Table 5.1 Displacement peak and strain on Fibre#3 when compression is applied.**

Boundary Conditions	Intensity	Unmyelinated Nerve Bundles		Myelinated Nerve Bundles	
		SBUN	BBUN	SBMY	BBMY
<b>Displacement Peak [nm]</b>					
<i>During Loading</i>					
Pressure Loads	25 kPa	-1.67	-1.65	-0.34	-0.48
	192 kPa	-2.30	-2.95	-1.02	-1.85
<i>After Loading</i>					
Pressure Loads	25 kPa	-1.47	-1.47	0	0
	192 kPa	-1.47	-1.47	-0.28	-0.26
<b>Strain [%]</b>					
<i>During Loading</i>					
Plastic Strain	25 kPa	0.5	0.5	0	0
	192 kPa				
Max. Total Strain	25 kPa	3.5	3.5	1.5	1.5
	192 kPa				

### 5.3.2 Displacement Loads

Figures 5.3-5.6 illustrate the response of a bundle to a displacement boundary condition applied at one end along its fibre length, simulating 5 %, 14 %, 25 %, 30 % and 60 %

elongation of the total length of the bundle (in line with the experiments conducted by Bain and Meaney (Bain and Meaney, 2000)). Those elongation values are chosen to initiate an elastic response if the applied strain is lower than 21 % (Bain and Meaney, 2000), or a plastic response if it is higher (according to the experiments conducted by Smith et al. (Smith et al., 1999) on cultured axons). The Figures show the membrane potential at the position of maximum displacement on Fibre #3, the maximum principal value of plastic strains ( $PE_z$ ) along the bundle middle axis (Jérusalem et al., 2014) and the total strain  $E_{tot}$ . Appendix D shows how data are selected at the nerve membrane.

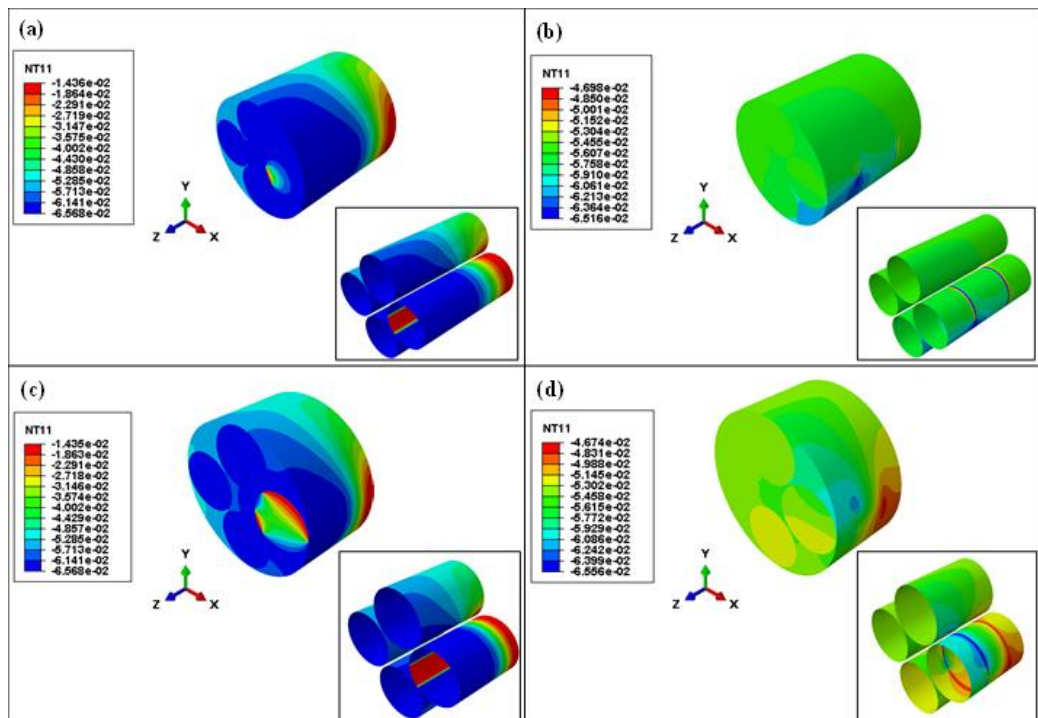


**Fig. 5.2** Voltage distribution ( $NT11$ ), at the AP peak, in (a) SBUN, (b) SBMY, (c) BBUN and (d) BBMY for  $25kPa$  pressure with  $AC = 0$ . The box shows the membrane layer of each model.

Fig. 5.3 shows the membrane voltage distribution in small (a) unmyelinated (SBUN) and (b) myelinated bundles (SBMY). In all elongations, the AP signal is reduced significantly if not eliminated altogether, while there is a clear increasing shift in baseline voltage with increasing applied displacement. The effect of strain on the baseline shift is higher for the myelinated than for the unmyelinated bundles. This finding is in line with previous results, where the voltage read at the nerve membrane varies linearly with the elastic component of the total strain up to 21 % (Bain and Meaney, 2000) when permanent electrophysiological impairments (such as leaking ionic channels (Boucher et al., 2012; Yu

et al., 2012)) alter the osmotic gradient across the membrane, and so the ability to carry and generate action potentials (Galbraith et al., 1993; Jérusalem et al., 2014; Smith et al., 1999). Then, the reversal potentials change depending on the level of elongation, the type of bundle and its size, due to the different distribution of total strain within the bundle.

Additionally, the fraction of nodal channels affected by trauma  $AC$  induces differences in the membrane voltage peaks from the membrane baseline, see Fig. 5.3 (a) and (b), while there are little or no differences membrane baseline value with varying  $AC$ . In the SBUN case, increasing the fraction of affected channels,  $AC$ , increases the difference between the membrane potential peak and the membrane baseline at higher strains only in small unmyelinated bundles. For example, at 60 %, the membrane potential is  $-24.15\text{ mV}$  with  $AC = 0$  and  $-2.134\text{ mV}$  with  $AC = 1$ , see Fig. 5.3 (a). In small myelinated bundles (SBMY), instead, the membrane peaks at 25 % are about the same as the values found at 30 and 60 % of elongation, see Fig. 5.3 (b). Similarly to SBUN, the maximum voltage in SBMY at 60 % elongation is  $-23.21\text{ mV}$  with  $AC = 0$  and  $-2.08\text{ mV}$  with  $AC = 1$ , see Fig. 5.3 (b). Then, at high applied strain, the voltage peaks in big unmyelinated bundles (BBUN) show similar differences when going from  $AC = 0$  to  $AC = 1$  ( $-24.17\text{ mV}$  with  $AC = 0$  and  $-2.15\text{ mV}$  with  $AC = 1$ , not shown here), while in big unmyelinated bundles (BBMY), the peaks are about the same order regardless of  $AC$  ( $-4\text{ mV}$  with  $AC = 0$  and  $-1\text{ mV}$  with  $AC = 1$ , not shown here). However, big bundles show a higher shift in membrane potential at 30 % elongation, which is the maximum elongation for big bundles in this study.

These trends are to be expected, because the fraction of nodal channels affected by trauma  $AC$  impacts the ionic conductance of the nerve membrane (Boucher et al., 2012). Hence, with  $AC = 1$ , a membrane plateau is reached because of the combined changes in ionic conductance (Boucher et al., 2012) and in reversal potentials (Jérusalem et al., 2014). The plateau shape occurs due to the similar values of the reversal potentials in a membrane in which the ion mobility of potassium and sodium are similar.

In unmyelinated fibres, the membrane voltage is shifted following elongation and no AP is generated because of the higher strain components along the fibre length, where the strain is highest (Jérusalem et al., 2014). In contrast, similarly to compression, the myelin layer induces a different distribution of strain at the Ranvier's node regions of the nerve membrane layer, where strains along the bundle middle axis are lower than in unmyelinated bundles, as observed in experiments (Hemphill et al., 2015; Jafari et al., 1998; Reeves et al., 2012). Therefore, those fibres are more likely to generate an AP after elongation. This is the reason why in SBMY, the potential does not have a plateau shape when  $AC = 1$  as in myelinated fibres, see Fig. 5.3. Then, in the BBMY, the fibre is still able to generate action

potential, both during and after loading, although there is a shift in membrane voltage baseline, as seen in the other cases. This suggests that the myelin layer induces a different distribution of strain within the fibre to preserve its functionality.

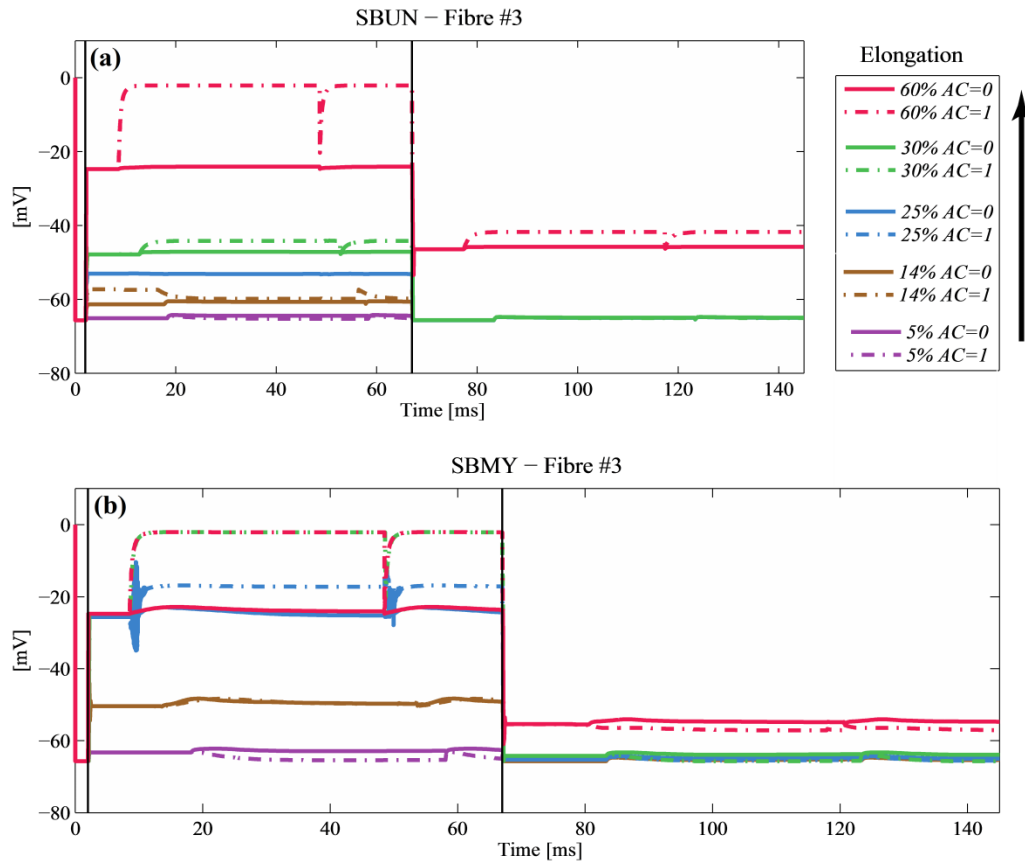


**Fig. 5.3** (a)-(b) Membrane Potential [mV] on Fibre #3 in SBUN and SBMY, under 5% to 60% of elongation (Bain and Meaney, 2000). The load is applied from 2 ms to 67 ms, only. AC is the fraction of affected ionic channels by the strain:  $AC = 0$  is for an intact membrane and  $AC = 1$  for a traumatized membrane (Boucher et al., 2012). Data are taken at the maximum displacement along the bundle middle axis, i.e.  $z$  - axis, on Fibre #3.

After the load is removed (i.e. after 67 ms), only in the case of 60 % elongation is the membrane baseline for SBUN shifted, up to  $-45.7$  mV ( $AC = 0$ ) and to  $-41.7$  mV ( $AC = 1$ ), as the ionic gate channels are kept open by the permanent plastic strains at the nerve membrane. Similarly for SBMY after loading, the membrane voltage baseline goes to  $-55.64$  mV only for 60 % elongation ( $AC = 0$  and  $AC = 1$ ), while it remains about  $-65$  mV for the other elongation values, see Fig. 5.3. As seen by Jérusalem et al. (Jérusalem et al., 2014), this chapter reports that the larger the elongation, the greater the shift of the membrane potential to a higher peak value, where the reversal potentials are affected differently by the strain magnitude.

This effect can be better appreciated in Fig. 5.4 and Fig. 5.5, where membrane voltage peaks and corresponding strains are taken at the node of maximum axial displacement and the node of maximum peak voltage on Fibre#3, respectively. Fig. 5.4 shows the peak of the membrane potential in (a) small and (c) big bundles, and the corresponding plastic strains, (b) and (d), during elongation, at the node of maximum axial displacement along the bundle middle axis (i.e. along the  $z$  – axis).

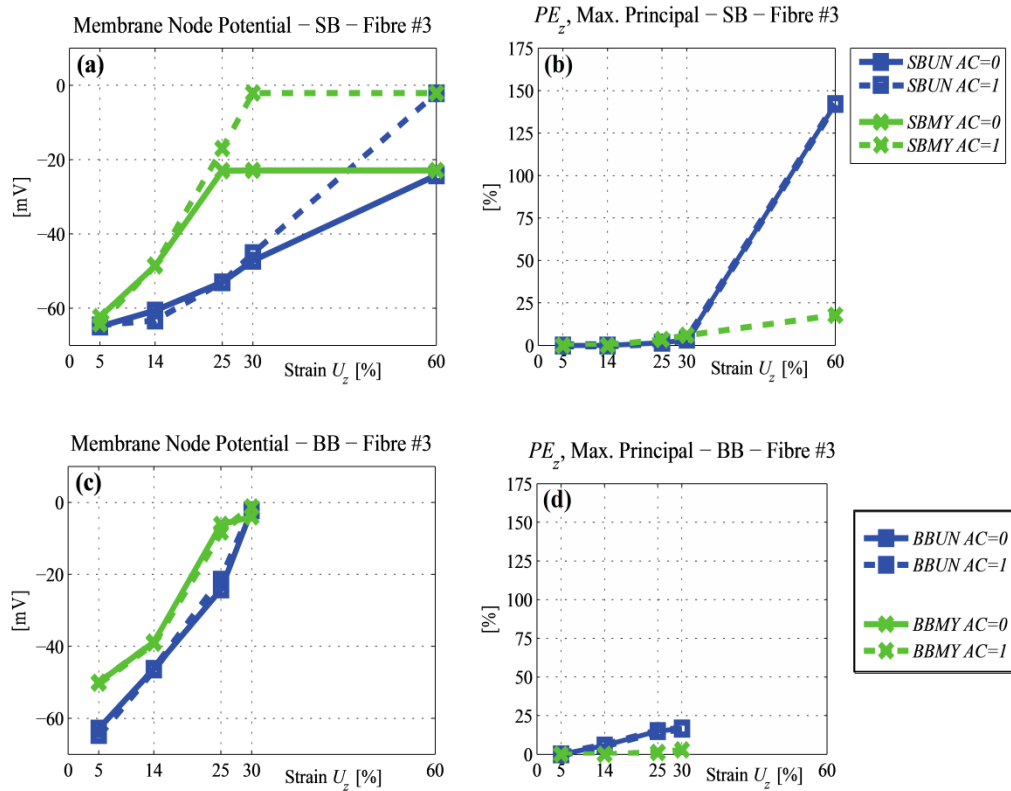


**Fig. 5.4** (a), (c) show the peak values of the membrane potential  $[mV]$  in the SB and BB, respectively. (b), (d) show the maximum values of the maximum principal plastic strain ( $PE_z$ ) at the node of interest, along the bundle axis. Data are taken on Fibre #3 at the node at which the displacement along the bundle axis is maximum. Displacement boundary conditions are equal to 5%, 14%, 25%, 30% and 60%. In BB, failure occurs at 60% applied displacement.

The membrane potential, see Fig. 5.4 (a)-(c), shows only slight changes with the fraction of nodal channels affected by trauma  $AC$  for strains lower than 30 %. Although the voltage in SBMY levels off at lower strains than in SBUN, at 60%, the differences in membrane potential are not dependent on fibre type, but only on  $AC$ , see Fig. 5.4 (a). In SBUN and SBMY, the same value of maximum potential is reached at 60 %, which is about  $-20 mV$  with  $AC = 0$  and about  $0 mV$  with  $AC = 1$ , see Fig. 5.4 (a). The corresponding  $PEs$  are lower than 25 % for applied elongation values lower than 30 %, and higher than 25 % for applied elongation values higher than 30 %, see Fig. 5.4 (b) and (d).

while they are much higher in SBUN (143 %) than in SBMY (20 %) at 60 % elongation, see Fig. 5.4 (b). However, the local maximum peak voltage, relative to Fibre#3, reaches a constant value above 25 % elongation, see Fig. 5.5 (a). Differences in maximum at lower elongations, see Fig. 5.6 (a), are due to elastic and thermal strains (i.e. the thermal equivalent of piezoelectric strain (Cinelli et al., 2017b)), see Fig. 5.5 (b), because of the small plastic strains found for the same conditions, see Fig. 5.4 (b).

In contrast, when doubling the size of the bundles, the changes in membrane potential are of the same order of magnitude for unmyelinated and myelinated bundles in all elongation cases. Additionally, in contrast to what happens to small bundles,  $AC$  has a little influence on these voltage variations, see Fig. 5.4 (c).

Similarly, the local maximum peak voltage read on Fibre#3 does not show great variation with either fibre type or  $AC$  during elongation tests, see Fig. 5.5 (a). Again, slight differences in plastic strains ( $PE$ ) are found going from  $AC = 0$  to  $AC = 1$ , see Fig. 5.4 (b) and (d), suggesting that the changes in ionic conductance (Boucher et al., 2012) has a smaller impact, compared with the applied strain, in generating plastic strain at the nerve membrane. At high strain (here, at 30 %), the peaks, read in both bundles, reach the same value, independent of the fibre type and  $AC$  value, see Fig. 5.4 (c). Although there is a large shift in potential, the plastic strains are lower than 25 % in both BBUN and BBMY. At the same applied strains, the plastic strain is not the main component of the maximum value of the total strain  $E_{tot}$  read at the bundles, see Fig. 5.6 (d), which are up to 75 % in BBUN and 120 % in BBMY.

Data show that plastic strains are responsible for the functional and mechanical failure in small unmyelinated bundles (SBUN), while functional recovery is more likely to happen in small myelinated bundles (SBMY) because the elastic component is 70 % of the  $E_{tot}$  at 60 % elongation, see Fig. 5.5 (b). Then, larger bundles show higher variation in membrane voltage due to the higher number of changes exchanged per unit area on the fibre. However, the  $E_{tot}$  at 30 % elongation are comparable to the values found in small bundles at 60 %, despite the lower plastic strains ( $PE$ ) at the membrane. Failure occurs for elongation higher than 30 % suggesting that the  $E_{tot}$  are mainly along the bundle middle axis. Strains along the fibre length are those with greater impact on the membrane voltage (Jérusalem et al., 2014), and are responsible for the voltage shift in all the bundles considered here.

Then, myelinated bundles (both SBMY and BBMY) show smaller  $PE$  in contrast with unmyelinated bundles (both SBUN and BBUN) at the same elongation. Particularly, at 30 % elongation, the plastic strain is less than 10 % in myelinated bundles (5.90 % in SBMY and 2.88 % in BBMY) and greater than 15 % in unmyelinated bundles (15.42 % in SBUN and 16.56 % in BBUN). The myelin layer seems to redistribute the induced

permanent damage on the whole fibre, rather than on the fibre length, as in unmyelinated bundles. Thus, at the same loading conditions, myelinated fibres and bundles are stronger than the unmyelinated ones.

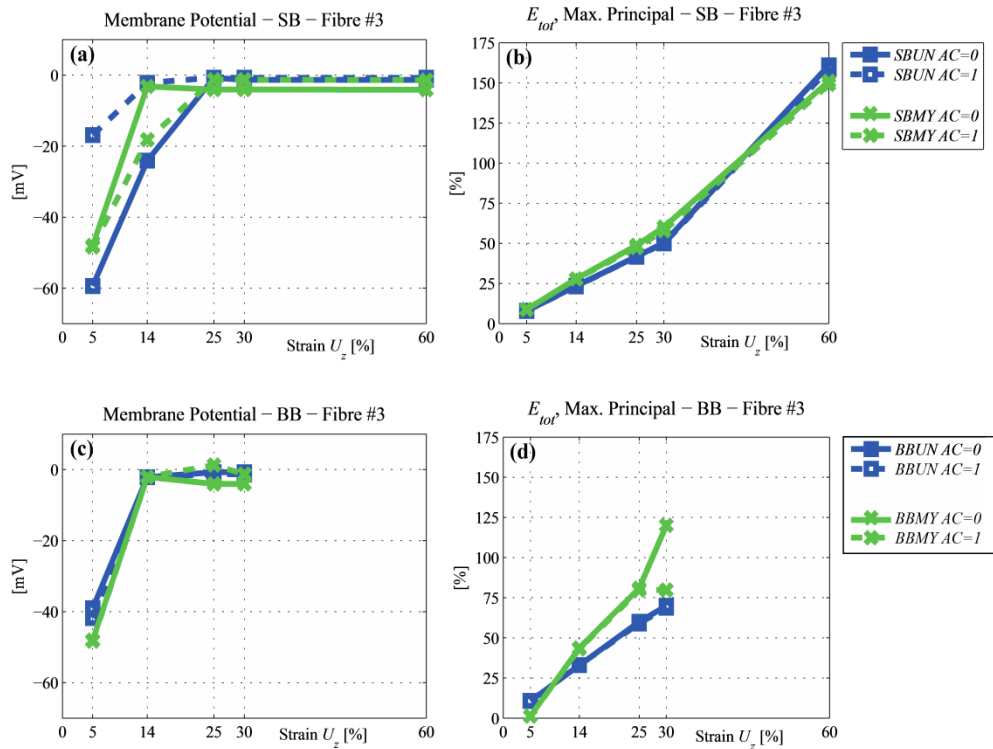


**Fig. 5.5** (a), (c) show the peak values of the membrane potential [mV] found on Fibre#3, in the SB and BB, respectively. In (b), (d), the maximum value of the total strain ( $E_{Tot}$ ) is the maximum found on Fibre#3. Displacement boundary conditions are equal to 5%, 14%, 25%, 30% and 60%. In BB, failure occurs at 60% applied displacement.

Fig. 5.6 (a)-(d) show the difference in total displacement distribution, at the AP's peak for 30% elongation and no traumatized nodal channels ( $AC = 0$ ). Similarly, to Fig. 5.2, the voltage distribution is affected by the total generated strain  $E_{tot}$  at the nerve membrane layer of each fibre. Here, the fibres are pulled along the bundle middle axis while Fibre#3 is contracting, dragging Fibre#2 and #4. The maximum value of the total strain  $E_{tot}$  is lower around the centre of the bundle due to the balance of negative radial and positive axial strains. Here the plastic strains ( $PE$ ) are consistently higher than those generated by applied pressure, see Fig. 5.1. Again, the voltage is higher in the regions where lower strains are found.

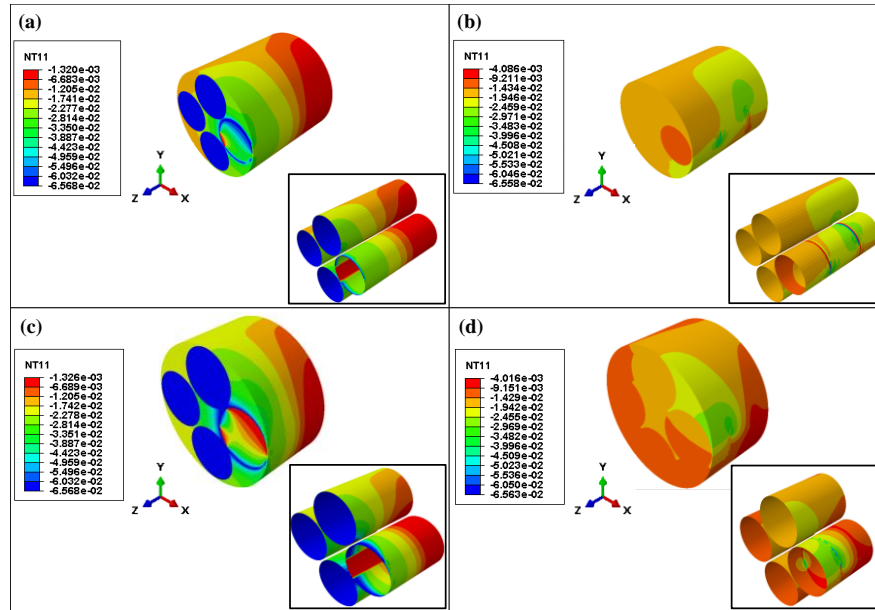


**Fig. 5.6** Isometric view of (a) SBUN and (b) SBMY for 60% elongation; and, (c) BBUN and (d) BBMY for 30% elongation with  $AC = 0$ . Data are taken at the peak of the AP. NT11 is the equivalent voltage variable in [V]. The box shows the membrane layer of each model.

## 5.4 Discussion

In contrast to previous studies (J rusalem et al., 2014; Wright and Ramesh, 2012), this chapter shows the advantages of a fully coupled electro-mechanical 3D framework to investigate the details of neural activity, combining real-time fully coupled electro-mechanical phenomena, a modulated threshold for spiking activation and independent alteration of the electrical properties for each fibre in the 3-layer nerve bundle (Cinelli et al., 2017b, 2017d). The use of coupled electro-mechanical finite element modelling for neural engineering (Cinelli et al., 2017d) opens the way to a different investigation of the neuron nature itself. The use of a 3D geometry allows for a physical representation of the neuron cell and morphology in signal propagation with trauma (Cinelli et al., 2017d; Galbraith et al., 1993; Gallant, 1992; Geddes et al., 2003; Smith et al., 1999; Zhang et al., 2014). Estimating the strain and stress distributions in damaged nerve fibres and bundles is a key issue both for clinical care and medical devices (Hemphill et al., 2015; Ma et al., 2016; R. Shi and Pryor, 2002; Wright and Ramesh, 2012).

Here, two cases of interest provide insights into the electrophysiological impairments of axonal injury due to sudden trauma-induced loading conditions. The boundary conditions in this study replicate the experiments conducted on nerve bundles and axons under both pressure (Hosmane et al., 2011) and elongation (Bain et al., 2001; Geddes et al., 2003; Smith et al., 1999). Additionally, the use of a 3D geometry highlights the

difference in voltage and strain distributions in unmyelinated and myelinated fibres in bundles of different size.

Differences in signal transmission arise in the bundle for each fibre, depending on the fibre type. In the bundle, Fibre #3 is activated by imposing a voltage Gaussian distribution on the fibre, while the other fibres are activated based on the voltage gradient from the active fibre and total strains (elastic, equivalent thermal and plastic strains) read at the nerve membrane.

The inclusion of plasticity shows the impact of permanent deformation on signal propagation after a mechanical load is applied. Permanent deformations occur if the strains at the nerve membrane are higher than 21 % according to Bain and Meaney (Bain and Meaney, 2000), so the reversal voltage potentials change permanently accordingly to the strain intensity. In the cases considered here, the signal read at the nerve membrane on Fibre #3 varies between ranges of voltage value lower than the AP described by Hodgkin and Huxley (Hodgkin and Huxley, 1952), or the membrane potential is about the baseline value. This means that the distribution of voltage in the bundle is changed, and the other fibres are not activated, because the voltage read at their nerve membranes is a subthreshold stimulation, so that an AP cannot be elicited, see Fig. 5.3.

During compression, the neural activity is changed according to the elastic strain at the nerve membrane, where plastic strains of 0.5 % are found in unmyelinated fibres, but no plastic strains in myelinated fibres for the range of pressure levels applied. Although high pressure values are chosen, compare to those found in TBI (Hosmane et al., 2011), the applied strains do not compromise the functionality of the membrane and its ability to generate signals, even when assuming changes in ionic conductance (Boucher et al., 2012). Additionally, the resulting total strains at the membrane are lower than 3.5 % and 1.5 % in unmyelinated and myelinated bundles. Thus, during compression, the fibre is far from mechanical failure thanks to the small strains generated at the membrane. Fibres and bundles appear to be stronger in compression than in elongation. A uniform compression of the bundle induces only a 1% elongation of the bundle, leading to small changes in neural activity and lower values of plastic strains (*PEs*) are found at the membrane.

During elongation, results show that the neural activity is more easily affected by deformations in small bundles than in larger bundles, where at 14% of elongation a plateau indicates a new osmotic gradient across the nerve membrane. As in experiments, the larger the fibre, the higher the voltage read at the membrane (Dominique M. Durand, 2000; Galbraith et al., 1993; Smith et al., 1999), and hence the higher the deformations, whose plastic component is shown in Fig. 5.4. It is also found that the myelin layer constrains the mechanical deformation of the nerve membrane at the Ranvier nodes, generating a different distribution of plastic strain around the fibre. This important property of myelin

preserves the functionality of the membrane by distributing the applied uniaxial strain within the bundle. It is revealed thanks to 3D finite element modelling.

Small myelinated bundles tolerate lower plastic strain than unmyelinated bundles, as seen in previous studies (Hemphill et al., 2015; Jafari et al., 1998; Reeves et al., 2012). However, smaller plastic strains are found in bigger myelinated bundles, where plastic damage occurs locally around the fibre rather than along the fibre length, see Fig. 5.3. This could be thought of as a way to preserve good communication between neurons cells under stretch. The nervous cell reading the signals carried by a damaged myelin fibre might not consider it as a valuable source of information because of its reduced magnitude. For higher deformations, the AP is not elicited because of the very low ionic gradient across the nerve membrane (Cinelli et al., 2017c), altering the signal propagation from cell-to-cell, and in turn, the communication between cells.

The assumption of instantaneous loading is a first step towards the electro-mechanical analysis of changes associated with TBI. Rate-dependent loadings could be included in future works. Injury pathologies in nerve fibres are also initiated and influenced by strain and strain rate, which have a significant impact on the time of neural death and pathomorphology, respectively (Bar-kochba et al., 2016). Experimental studies on human axons show morphological changes of axons at different stages of dynamic stretch injury (Smith et al., 1999). Axons can tolerate stretching up to twice their original length under slow loading rates (within the range of minutes (Tang-schomer et al., 2017)), with elastic recovery of the initial pre-stretched geometry (Bar-kochba et al., 2016; Tang-schomer et al., 2017). However, dynamic loading conditions with a short pulse duration (lower than  $50s^{-1}$  (Tang-schomer et al., 2017)), initiate undulating distortions along their entire length (Bar-kochba et al., 2016; Smith et al., 1999; Tang-schomer et al., 2017), and recovery of the pre-stretched geometry was found to be non-uniform. Axonal regions can manifest both an elastic recovery and a delayed elastic response, i.e. a gradual recovery, along the same fibre length (Smith et al., 1999). For example, mechanical failure of squid giant axons was found at 25 – 30% stretch at a strain rate of  $10s^{-1}$  (Galbraith et al., 1993), while human axons, with a diameter of about  $0.5 - 1 \mu m$ , tolerate dynamic stretch injury at strains up to 65% according to Smith et al. (Smith et al., 1999).

Future studies might also include viscoelastic mechanical properties for a more accurate description of the mechanical behaviour of nervous fibres under loading (Jérusalem et al., 2014). An elastic isotropic plastic model, as in this paper, might not be comprehensive enough to tackle mechano-sensing properties arising during loading at different strain rates (Jérusalem et al., 2014), such as the reversible behaviour of specific ionic channels after stretch, recovery and axonal growth (Jérusalem et al., 2014; Riyi Shi and Whitebone, 2006).

Finally, as highlighted earlier, our model assumed an idealized geometry of a nerve bundle. Further works must tackle the effect of a realistic geometry of nervous cells, by considering fibre alignments in different directions and multiple fibre activation.

Chapter 6 focuses on applying this approach to estimate injury at the microscale induced during simulated frontal head impacts.

## 5.5 Limitations

This work aims at evaluating the electro-mechanical coupling (Cinelli et al., 2017a) in a nerve bundle model, where isotropic plastic behaviour is assigned to the nerve membrane, intracellular media, and myelin layer. This modelling approach has not been extended yet to simulate temperature variation and its implications, as has been shown to occur in nervous cells during signalling (Andersen et al., 2009; Hodgkin and Huxley, 1952; Rattay, 2005). The inclusion of the temperature would allow for an evaluation of the changes in conduction velocity in relation to the induced damage intensity, not accounted for in this chapter.

To illustrate the relative effects of nerve bundle scale and the inclusion of plasticity, the electrophysiological parameters of this paper were taken from the literature used to validate the basic coupled electro-mechanical model (Cinelli et al., 2017b; Hodgkin and Huxley, 1952; Jérusalem et al., 2014). This chapter aims at highlighting the applicability of the electro-mechanical coupling proposed in (Cinelli et al., 2017a) to diffuse axonal injury for its relevance in clinical applications. However, future studies might take into account different material properties for simulating alterations occurring in specific regions of the brain due to diseases (Demerens et al., 1996), brain aging (Ziegler, 2012), human disorders (Bercury and Macklin, 2015), or in other human body regions (as the human cochlea (Rattay, 2005; Rattay et al., 2013)).

As mentioned in the Methods section, this study is carried out assuming an idealized geometry of a nerve bundle to limit the complexity and computational cost arising from the use of 3D morphological images of neuronal structure (Cinelli et al., 2017b; Lytton et al., 2017). Then, although the axon calibre has been shown to vary in animals (Perge et al., 2012; Wang et al., 2008) and in humans (Björnholm et al., 2017; Liewald et al., 2014; Rattay, Potrusil, Wise, et al., 2013), here, we have assumed fibres with diameters of about 1 to 2  $\mu\text{m}$  only, as examples of human nerve fibres. However, the human brain is made of fibres with a wider range of diameters (Björnholm et al., 2017; Liewald et al., 2014). So, the calibre of fibres considered in this paper is representative of small fibres ( $d < 0.4 \mu\text{m}$ ) only found in the human corpus callosum (Björnholm et al., 2017), but not large fibres

( $d > 5 \mu m$ ) (Björnholm et al., 2017). Thus, future works may consider testing this modelling approach for a wider range of axon calibre to understand the distribution of functional and mechanical failure within the human brain under mechanical loading (Björnholm et al., 2017; Liewald et al., 2014; Rattay, 2005). However, whereas the results reported in this work refer to two nerve bundle models only, the electro-mechanical coupling (Cinelli et al., 2017a) in this paper builds on a previous validation, carried out in three different animal models with diameters varying between  $0.25 - 500 \mu m$  (Cinelli et al., 2017b).

## 5.6 Conclusion

A fully coupled electro-mechanical framework is proposed for modelling the biophysical phenomena accompanying neural activity, such as electrostriction and piezoelectricity, by relying on the electro-thermal analogy. This framework is a new approach in neural engineering, embracing the main findings of experimental observations. The model, built on previously chapters (Cinelli et al., 2017b, 2017d, 2017e, 2017a) incorporates the effect of plasticity to generate a fully coupled 3-dimensional simulation of ion channel leaking for nerve fibres under pressure and displacement loads. Accounting of the limitations of this work, a list of the main conclusion points is reported below to recapitulate the key findings:

- Lower strain and lower electrophysiological changes are found in myelinated fibres than in unmyelinated fibres;
- The myelin layer redistributes the generated plastic strain within the bundle;
- Fibres and bundles are stronger under compression than elongation;
- During elongation, mechanical failure occurs at lower elongation in BBMY, than in BBUN, SBMY and SBUN;
- Larger bundles deform more than small bundles;
- Larger bundles fail because of elastic strain, not plastic strain;
- Trauma affects small bundles more than larger bundles;
- Plastic strains are not influenced by the trauma level at the nerve membrane (as measured by  $AC$ );
- Trauma ( $AC$ ) does not influence the membrane baseline voltage during compression or elongation;
- Trauma does not influence voltage and plastic strain in larger bundles.

## References Chapter 5

- Alvarez, O., and Latorre, R. (1978). Voltage-dependent capacitance in lipid bilayers made from monolayers. *Biophysical Journal*, 21(1), 1–17. [https://doi.org/10.1016/S0006-3495\(78\)85505-2](https://doi.org/10.1016/S0006-3495(78)85505-2)
- Andersen, S. S. L., Jackson, A. D., and Heimburg, T. (2009). Towards a thermodynamic theory of nerve pulse propagation. *Progress in Neurobiology*, 88(2), 104–113. <https://doi.org/10.1016/j.pneurobio.2009.03.002>
- Bain, A. C., and Meaney, D. F. (2000). Tissue-level thresholds for axonal damage in an experimental model of central nervous system white matter injury. *Journal of Biomechanical Engineering*, 122(6), 615–622. <https://doi.org/10.1115/1.1324667>
- Bain, A. C., Raghupathi, R., and Meaney, D. F. (2001). Dynamic stretch correlates to both morphological abnormalities and electrophysiological impairment in a model of traumatic axonal injury. *Journal of Neurotrauma*, 18(5), 499–511. <https://doi.org/10.1089/089771501300227305>
- Bar-Kochba, E., Scimone, M. T., Estrada, J. B., and Franck, C. (2016). Strain and rate-dependent neuronal injury in a 3D in vitro compression model of traumatic brain injury. *Scientific Reports*, 6(April), 30550. <https://doi.org/10.1038/srep30550>
- Boucher, P. A., Joós, B., and Morris, C. E. (2012). Coupled left-shift of Nav channels: Modeling the Na<sup>+</sup>-loading and dysfunctional excitability of damaged axons. *Journal of Computational Neuroscience*, 33(2), 301–319. <https://doi.org/10.1007/s10827-012-0387-7>
- Björnholm, L., Nikkinen, J., Kiviniemi, V., Nordström, T., Niemelä, S., Drakesmith, M., ... Paus, T. (2017). Structural properties of the human corpus callosum: Multimodal assessment and sex differences. *NeuroImage*, 152(February), 108–118. <https://doi.org/10.1016/j.neuroimage.2017.02.056>
- Cinelli, I., Destrade, M., Duffy, M., and McHugh, P. (2017a). Effects of nerve bundle geometry on neurotrauma evaluation. In *International IEEE/EMBS Conference on Neural Engineering*, NER (pp. 517–520). <https://doi.org/10.1109/NER.2017.8008403>
- Cinelli, I., Destrade, M., Duffy, M., and McHugh, P. (2017b). Electro-mechanical response of a 3D nerve bundle model to mechanical loads leading to axonal injury.

*International Journal for Numerical Methods in Biomedical Engineering*.  
<https://doi.org/10.1002/cnm.2942>

- Cinelli, I., Destrade, M., Duffy, M., and McHugh, P. (2017c). Electro-mechanical response of a 3D nerve bundle model to mechanical loads leading to axonal injury. In *Engineering in Medicine and Biology Society (EMBC), 2017 39th Annual International Conference of the IEEE* (pp. 1–4).  
<https://doi.org/10.1109/EMBC.2017.8036989>
- Cinelli, I., Destrade, M., Duffy, M., and McHugh, P. (2017d). Electro-thermal equivalent 3d finite element model of a single neuron. *IEEE Transactions on Biomedical Engineering*, 9294(99). <https://doi.org/10.1109/TBME.2017.2752258>
- Cinelli, I., Destrade, M., Duffy, M., and McHugh, P. (2017e). Neurotrauma evaluation in a 3D electro-mechanical model of a nerve bundle. In IEEE (Ed.), *International IEEE/EMBS Conference on Neural Engineering, NER* (pp. 513–516).  
<https://doi.org/10.1109/NER.2017.8008402>
- Cinelli, I., Duffy, M., and McHugh, P. (2015). Thermo-electrical equivalents for simulating the electro-mechanical behavior of biological tissue. In IEEE (Ed.), *Proceedings of the Annual International Conference of the IEEE Engineering in Medicine and Biology Society, EMBS* (Vol. 2015–Novem, pp. 3969–3972). Milan: IEEE.  
<https://doi.org/10.1109/EMBC.2015.7319263>
- Demerens, C., Stankoff, B., Logak, M., Anglade, P., Allinquant, B., Couraud, F., Lubetzki, C. (1996). Induction of myelination in the central nervous system by electrical activity. *Proceedings of the National Academy of Sciences*, 93(18), 9887–9892.  
<https://doi.org/10.1073/pnas.93.18.9887>
- Durand, D. M. (2000). Electric stimulation of excitable tissue. In E. J. D. Bronzino (Ed.), *The biomedical engineering handbook: Second edition*. (Vol. 42, p. 23). Boca Raton: CRC Press LLC, 2000. <https://doi.org/10.1201/9781420049510>
- El Hady, A., and Machta, B. B. (2015). Mechanical surface waves accompany action potential propagation. *Nature Communications*, 6, 6697.  
<https://doi.org/10.1038/ncomms7697>
- Galbraith, J. A., Thibault, L. E., and Matteson, D. R. (1993). Mechanical and electrical responses of the squid giant axon to simple elongation. *Journal of Biomechanical Engineering*, 115(1), 13–22. <https://doi.org/10.1115/1.2895464>

- Gallant, P. E. (1992). The direct effects of graded axonal compression on axoplasm and fast axoplasmic transport. *Journal of Neuropathology and Experimental Neurology*, 51(2), 220–230. Retrieved from <http://www.ncbi.nlm.nih.gov/pubmed/1371545>
- Geddes, D. M., Cargill, R. S., and LaPlaca, M. C. (2003). Mechanical stretch to neurons results in a strain rate and magnitude-dependent increase in plasma membrane permeability. *Journal of Neurotrauma*, 20(10), 1039–1049. <https://doi.org/10.1089/089771503770195885>
- Heimburg, T., Blicher, A., Mosgaard, L. D., and Zecchi, K. (2014). Electromechanical properties of biomembranes and nerves. *Journal of Physics: Conference Series*, 558, 12018. <https://doi.org/10.1088/1742-6596/558/1/012018>
- Hemphill, M. A., Dauth, S., Yu, C. J., Dabiri, B. E., and Parker, K. K. (2015). Traumatic brain injury and the neuronal microenvironment: A potential role for Neuropathological Mechanotransduction. *Neuron*, 85(6), 1177–1192. <https://doi.org/10.1016/j.neuron.2015.02.041>
- Hodgkin, A. L., and Huxley, A. F. (1952). A quantitative description of membrane current and its application to conduction and excitation in nerve. *Journal of Physiology*, 117, 500–544. [https://doi.org/10.1016/S0092-8240\(05\)80004-7](https://doi.org/10.1016/S0092-8240(05)80004-7)
- Hosmane, S., Fournier, A., Wright, R., Rajbhandari, L., Siddique, R., Yang, I. H., Thakor, N. (2011). Valve-based microfluidic compression platform: Single axon injury and regrowth. *Lab on a Chip*, 11(22), 3888. <https://doi.org/10.1039/c1lc20549h>
- Jafari, S. S., Nielson, M., David, I., and Maxwell, W. L. (1998). Axonal cytoskeletal changes after nondisruptive axonal injury. II. Intermediate sized axons. *Journal of Neurotrauma*, 15(11), 955–966.
- Jérusalem, A., García-Grajales, J. A., Merchán-Pérez, A., and Peña, J. M. (2014). A computational model coupling mechanics and electrophysiology in spinal cord injury. *Biomechanics and Modeling in Mechanobiology*, 13(4), 883–896. <https://doi.org/10.1007/s10237-013-0543-7>
- Kan, E. M., Ling, E., and Lu, J. (2012). Microenvironment changes in mild traumatic brain injury. *Brain Research Bulletin*, 87(4–5), 359–372. <https://doi.org/10.1016/j.brainresbull.2012.01.007>
- Lajtha, A., Javitt, D., and Kantrowitz, J. (2009). Handbook of neurochemistry and molecular neurobiology. Brain and spinal cord trauma. (N. Banik & K. R. Swapan,

- Eds.), *Springer Reference* (3rd Edition, Vol. 281). Springer.  
<https://doi.org/10.1016/j.jns.2009.03.019>
- Liewald, D., Miller, R., Logothetis, N., Wagner, H. J., and Schüz, A. (2014). Distribution of axon diameters in cortical white matter: an electron-microscopic study on three human brains and a macaque. *Biological Cybernetics*, 108(5), 541–557.  
<https://doi.org/10.1007/s00422-014-0626-2>
- Lytton, W. W., Arle, J., Bobashev, G., Ji, S., Klassen, T. L., Marmarelis, V. Z., Sanger, T. D. (2017). Multiscale modeling in the clinic: Diseases of the brain and nervous system. *Brain Informatics*, 4(4), 219–230. <https://doi.org/10.1007/s40708-017-0067-5>
- Ma, J., Zhang, K., Wang, Z., and Chen, G. (2016). Progress of research on diffuse axonal injury after traumatic brain injury. *Neural Plasticity*, 2016, 7.  
<https://doi.org/10.1155/2016/9746313>
- Mohagheghian, F. (2015). Effect of geometry on propagation of action potentials in neurons; An in silico analysis. In 2015 IEEE 35th *International Conference on Electronics and Nanotechnology (ELNANO) Effect* (pp. 378–380). Retrieved from <http://ieeexplore.ieee.org/document/7146924/>
- Mosgaard, L. D., Zecchi, K. a., and Heimbürg, T. (2015). Mechano-capacitive properties of polarized membranes. *Soft Matter*, 11(40), 7899–7910.  
<https://doi.org/10.1039/C5SM01519G>
- Mueller, J. K., and Tyler, W. J. (2014). A quantitative overview of biophysical forces impinging on neural function. *Physical Biology*. <https://doi.org/10.1088/1478-3975/11/5/051001>
- Perge, J. a, Niven, J. E., Mugnaini, E., Balasubramanian, V., and Sterling, P. (2012). Why do axons differ in caliber? *The Journal of Neuroscience*, 32(2), 626–638.  
<https://doi.org/10.1523/JNEUROSCI.4254-11.2012>
- Platkiewicz, J., and Brette, R. (2010). A threshold equation for action potential initiation. *PLoS Computational Biology*, 6(7), 25.  
<https://doi.org/10.1371/journal.pcbi.1000850>
- Rattay, F. (2005). Functional Electrical Stimulation of the Central Nervous System: Analysis of the Primarily Excited Structures, (July), 122.

- Rattay, F., Potrusil, T., Wenger, C., Wise, A. K., Glueckert, R., and Schrott-Fischer, A. (2013). Impact of morphometry, myelination and synaptic current strength on spike conduction in human and cat spiral ganglion neurons. *PLoS ONE*, 8(11). <https://doi.org/10.1371/journal.pone.0079256>
- Reeves, T. M., Smith, T. L., Williamson, J. C., and Phillips, L. L. (2012). Unmyelinated axons show selective rostrocaudal pathology in the corpus callosum following traumatic brain injury. *Journal of Neuropathology and Experimental Neurology*, 71(3), 198–210. <https://doi.org/10.1097/NEN.0b013e3182482590>.Unmyelinated
- Shi, R., and Pryor, J. D. (2002). Pathological changes of isolated spinal cord axons in response to mechanical stretch. *Neuroscience*, 110(4), 765–777. [https://doi.org/10.1016/S0306-4522\(01\)00596-6](https://doi.org/10.1016/S0306-4522(01)00596-6)
- Smith, D. H., Wolf, J. A., Lusardi, T. A., Lee, V. M., and Meaney, D. F. (1999). High tolerance and delayed elastic response of cultured axons to dynamic stretch injury. *The Journal of Neuroscience*, 19(11), 4263–4269. Retrieved from <http://www.jneurosci.org/content/19/11/4263.long>
- Tahayori, B., Meffin, H., Dokos, S., Burkitt, A. N., and Grayden, D. B. (2012). Modeling extracellular electrical stimulation: II. Computational validation and numerical results. *Journal of Neural Engineering*, 9(6), 65006. <https://doi.org/10.1088/1741-2560/9/6/065006>
- Tang-schomer, M. D., Patel, A. R., Baas, P. W., and Smith, D. H. (2017). Mechanical breaking of microtubules in axons during dynamic stretch injury underlies delayed elasticity, microtubule disassembly, and axon degeneration. *The FASEB Journal*, 24(5), 1401–1410. <https://doi.org/10.1096/fj.09-142844>
- Wang, H. C., and Ma, Y. Bin. (2010). Experimental models of traumatic axonal injury. *Journal of Clinical Neuroscience*, 17(2), 157–162. <https://doi.org/10.1016/j.jocn.2009.07.099>
- Wang, J., Hamm, R. J., and Povlishock, J. T. (2011). Traumatic axonal injury in the optic nerve: evidence for axonal swelling, disconnection, dieback, and reorganization. *Journal of Neurotrauma*, 28(7), 1185–1198. <https://doi.org/10.1089/neu.2011.1756>
- Wright, R. M., and Ramesh, K. T. (2012). An axonal strain injury criterion for traumatic brain injury. *Biomechanics and Modeling in Mechanobiology*, 11(1–2), 245–260. <https://doi.org/10.1007/s10237-011-0307-1>

- Yu, N., Morris, C.E., Joós, B. and Longtin, A. (2012). Spontaneous excitation patterns computed for axons with injury-like impairments of Sodium Channels and Na/K pumps. *PLoS Computational Biology*, 8(9). <https://doi.org/10.1371/journal.pcbi.1002664>
- Zhang, Y. P., Cai, J., Shields, L. B. E., Liu, N., Xu, X. M., and Shields, C. B. (2014). Traumatic brain injury using mouse models. *Translational Stroke Research*, 5(1), 454–471. <https://doi.org/10.1007/s12975-014-0327-0>
- Zhang, Keleshian, A. M., and Sachs, F. (2001). Voltage-induced membrane movement. *Nature*, 413(6854), 428–432. <https://doi.org/10.1038/35096578>
- Ziegler, G. (2012). Models of the aging brain structure and individual decline. *Frontiers in Neuroinformatics*, 6(March), 1–16. <https://doi.org/10.3389/fninf.2012.00003>

## Chapter 6.      **Electro-Mechanical Alterations in Nerve Fibres of the Human Corpus Callosum**

The focus of this chapter is on the assessment of the coupled electro-mechanical modelling approach in a model with anatomically accurate dimensions those found in the Human Corpus Callosum. This modelling approach is compared with the results shown in Chapter 5.

### **6.1 Introduction**

By modelling the myelin sheath as shown in (Einziger et al., 2003b; a) and Chapter 5, the myelin thickness is neglected, and it is collapsed at the nerve membrane section, as described in Appendix B. Here, the myelin is modelled as a piecewise constant periodic section repeated along the nerve membrane length, with the same thickness of the nerve membrane layer,  $3\text{ nm}$ . The lengths of the myelin sheath and the Ranvier's node regions are chosen based on the ratio equal to 0.002, as shown in (Einziger et al., 2003b; a), and their final lengths are  $1\ \mu\text{m}$  and  $2\ \text{nm}$ , respectively. The final length is chosen to limit the computational cost of the model, although nerve fibres in humans have a similar length ratio but a longer final length. This approach allows us to investigate the current flow through a 3D non-homogeneous conductor. In Appendix B, it is shown that this current flow can be modelled by the Cable Equation by using thermo-electrical equivalences in 3D. In this section, a different nerve bundle model is considered for investigating the implications of anatomically accurate dimensions of the bundle in the use of the thermo-electrical equivalences. In the nerve bundle, shown in Fig. 6.1, the myelin sheath and Ranvier's node regions are modelled as those found in the Human Corpus Callosum (HCC), a myelinated bundle. An application of this model is to investigate the alterations in displacement, voltage and plastic strain when considering realistic dimensions of human nerve fibres.

### **6.2 Method**

The radius of each fibre is equal to  $0.5\ \mu\text{m}$  (Aboitiz et al., 1992; Liewald et al., 2014) and the membrane thickness is equal to  $3\ \text{nm}$ , see Fig. 6.1. The myelin sheath thickness is found from the difference between the myelin diameter and the inner diameter of the intracellular medium (ICM), and it is equal to  $9\ \text{nm}$  (Liewald et al., 2014). The myelin

thickness can also be found from the ratio of the inner ICM diameter over the outer diameter of the myelin sheath, equal to 0.84 in HCC (Liewald et al., 2014). The thickness of the surrounding extracellular medium (ECM) is kept equal to  $20\text{ nm}$ , as described by (Meffin et al., 2012). Here, the Ranvier’s node region length is chosen equal to  $1.5\ \mu\text{m}$  (Arancibia-cárcamo et al., 2017), so the myelin sheath length is calculated to be  $750\ \mu\text{m}$  from the ratio of 0.002 (Einziger et al., 2003b; a), see Fig. 6.1. Then, the nerve membrane section is extended from the Ranvier’s nodes underneath the myelin sheath, in contrast to the case shown in Chapters 4 and 5, where the membrane section is made of alternating units of insulating and conductive regions within the same radial section, see Appendix B. As in nature, the electrically active region of the nerve membrane is limited to the Ranvier’s node, while the region underneath the myelin is purely passive as it is insulated by the surrounding myelin, see Fig. 6.1 (b). For this reason, the charge flow skips the myelin region when an action potential is elicited, and the speed of conduction is faster than that of an unmyelinated fibre (Rall, 1977).

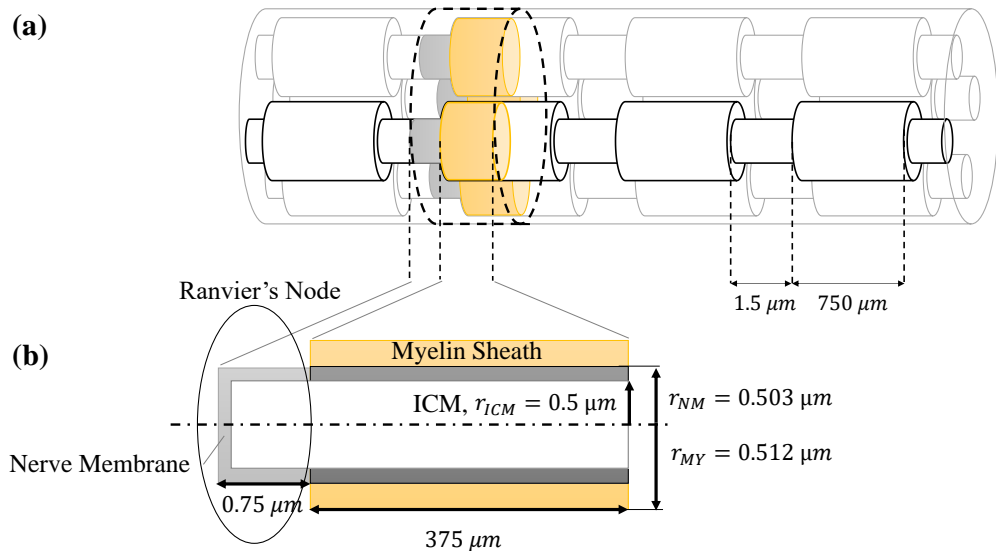


**Fig. 6.1** Diagram of the HCCMY. In (a), the HCCMY is made of repeated units of myelin sheath with length equal to  $750\ \mu\text{m}$ , separated by the Ranvier’s Node regions with length equal to  $1.5\ \mu\text{m}$  (not drawn to scale). The four fibres are surrounded by the extracellular medium (EC). Here, we assumed that the fibres are parallel and identical. Thanks to the symmetry, the coloured part is the part modelled in Abaqus. In (b), a section of a fibre of the HCCMY. The intracellular medium (ICM) radius is  $0.5\ \mu\text{m}$ , the nerve membrane (NM) thickness is  $3\text{ nm}$ , and the myelin sheath thickness is  $90\text{ nm}$ . The darker grey part of the nerve membrane section in pure resistive material, while the light grey part is the Ranvier’s Node region where the Action Potential can be elicited.

We assume a nerve bundle model where all the fibres are parallel, so that the myelin sheath and Ranvier’s nodes are perfectly aligned, see Fig. 6.3.1 (a). With this assumption,

the idealized representation of the HCC is made of repeated units, and taking advantage of symmetry, the modelled regions are halved, where  $0.75 \mu\text{m}$  and  $375 \mu\text{m}$  are the lengths of the Ranvier's node and the myelin sheath, respectively, see Fig. 6.3.1 (a) and Fig. 6.2. An encastè boundary condition is applied at the Ranvier's node side, similarly to Chapter 4, and the active region is the Ranvier's node region on Fibre#3 only. Here, an upper-threshold stimulus is applied as a gaussian voltage distribution limited to the Ranvier's node region only.

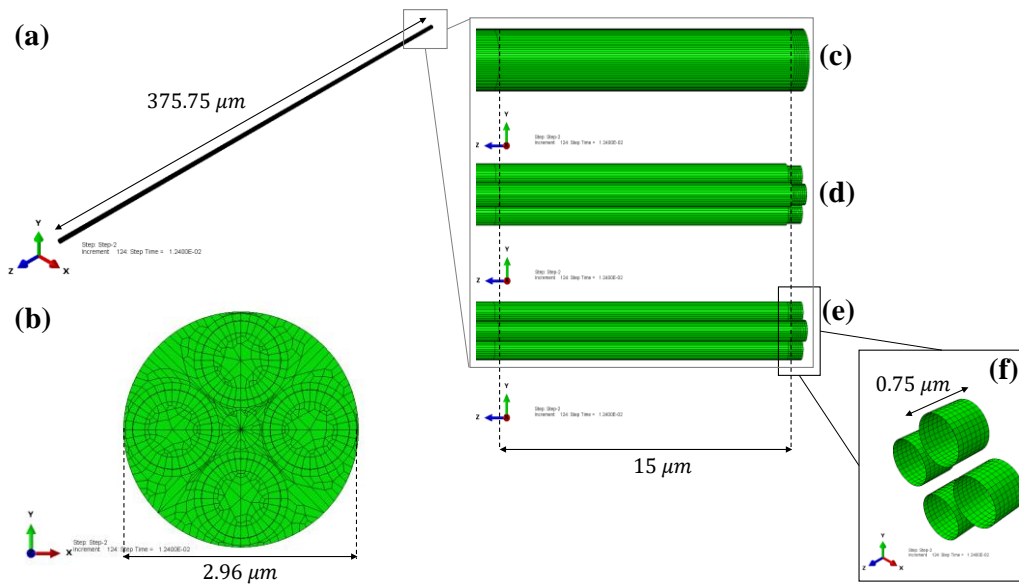


**Fig. 6.2** The HCCMY is long  $375.75 \mu\text{m}$ , see (a), and has a diameter of  $2.96 \mu\text{m}$ , see (b). The myelin sheath is  $375 \mu\text{m}$  while the Ranvier's node is  $0.75 \mu\text{m}$ . In (c), a side of the HCCMY is shown, made by a  $15 \mu\text{m}$  long myelinated section and a  $0.75 \mu\text{m}$  is shown. In (d), the myelin and the membrane nodes are shown without the extracellular medium around. Then, (e) shows the membrane layer, where the active part, i.e. the Ranvier's Node, has a length equal to  $0.75 \mu\text{m}$ , see (f).

### 6.3 Results

Similarly to the nerve bundle model shown in Chapter 4 and 5, displacement, voltage and strains are the outputs of interest. The data are taken on the active nerve fibre, Fibre#3, both for the small myelinated bundle (SBMY), and the human corpus callosum bundle (HCCMY), see Appendix D and E. Displacement boundary conditions are applied (from 5 % to 30 % with  $AC = 0$  and  $AC = 1$ ) to HCCMY, similarly to Chapters 4 and 5. Data in Fig. 6.3 are the membrane nodal potentials taken at the membrane peak, at the node at which the displacement along the bundle  $z - axis$  is maximum. This point is found to be at the boundary between the Ranvier's node and the myelin sheath in all cases as indicated in Figs. 6.5, 6.6 and 6.7. Data in Fig. 6.4 refer to the maximum of the voltage and strain

magnitude found read on Fibre #3, without referring to a specific node. The membrane potential at the node is about the maximum of the voltage found on the Fibre #3, see Fig. 6.3 and 6.4. This confirms that the nodal data represent the region where the voltage undergoes maximum alteration. Indeed, at the node of interest, the electro-mechanical alterations of the ionic gate dynamics are shown to be significant (García-grajales and Peña, 2014; Cinelli et al., 2017), and include the piezoelectric effect and the electrostriction.

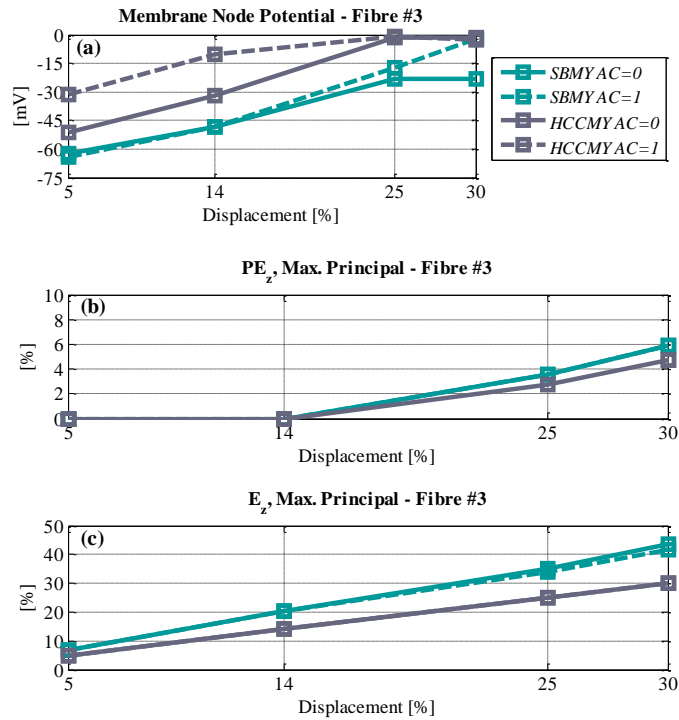


**Fig. 6.3** Data are nodal quantities when displacement boundary conditions (from 5 % to 30 %) are applied at the small myelinated bundle (SBMY) and the human corpus callosum bundle (HCCMY) with AC=0 and AC=1. Data are taken on Fibre #3 at the node at which the displacement along the bundle axis is maximum. (a) shows the peak values of the membrane potential [mV] at the node. Then, (b) shows the maximum principal value of the plastic strain [%], and, in (c), the total strain at the node of interest, along the bundle axis.

In Fig. 6.3 and 6.4 the membrane voltage, plastic strains,  $PE_z$ , and total strains,  $E_{Tot}$ , are shown for SBMY and HCCMY. In Fig. 6.3 (a) the membrane potential at the node of maximum axial displacement in HCCMY is higher than the same found in SBMY, regardless of the value of AC. A similar trend was found in large myelinated bundles (BBMY), see Fig 5.4 and 5.5. Larger fibres can see greater voltage potentials, as seen in Chapter 5 and (Durand, 2000). When considering the case that all the ionic channels of the Ranvier's node are affected by deformation ( $AC = 1$ ), the peak of the membrane potential

at the node of interest is higher than the same value found with  $AC = 0$ , where the ionic channels are not affected by the applied displacement. In SBMY, this is evident at high displacements only at which the applied deformations lead to greater changes in the ionic reversal potentials. Here, their final values are still lower than those of the HCCMY due to the limited surface area where charges can be exchanged. The Ranvier’s node regions in HCCMY have a greater area compared to SBMY, so the current per unit area is lower. Then, the trend of the maximum voltage found on the active Fibre, Fibre #3, is similar in all cases, see Fig. 6.4 (a). However, differences can also arise due to the mechanical structure and the choice of the element for the mesh. In all cases, it is found that the nerve membrane functionality is preserved for applied displacement levels lower than 25 % (i.e. there is some level of membrane potential elicited) indicating that an osmotic gradient is still present across the nerve membrane. When the membrane voltage potential reaches zero, the osmotic gradient is not present, and we assumed that the membrane loses its functionality, so that it is not capable of eliciting an action potential.

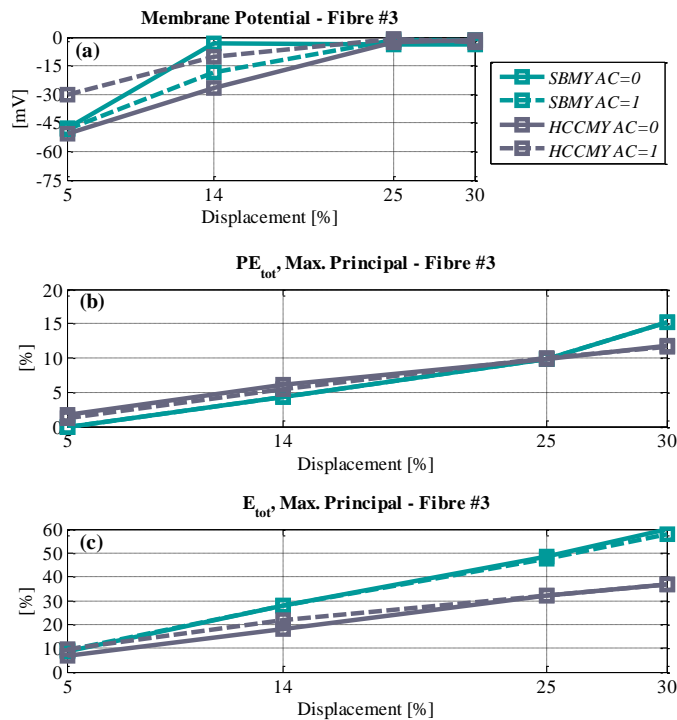


**Fig. 6.4** Data are the maximum quantities of Fibre #3 when displacement boundary conditions (from 5 % to 30 %) are applied at the small myelinated bundle (SBMY) and the human corpus callosum bundle (HCCMY) with AC=0 and AC=1. (a) shows the peak values of the membrane potential [mV] on Fibre #3. Then, (b) shows the maximum principal value of the plastic strain [%], and, in (c), the total strain on Fibre #3.

The plastic strains are proportional to the applied strain with a similar trend observed for both the HCCMY and SBMY cases, see Fig. 6.3 (b) and 6.4 (b). This might be due to the choice of keeping the ratio of the myelin sheath length over the Ranvier’s node length equal to 0.002 (Einzigler et al., 2003b; a) in both cases. Similarly, Fig. 6.3 (c) and 6.4 (c) show that the total strain at the node of maximum displacement or the maximum in the active fibre, respectively, are proportional to the applied strain. The use of a realistic model, HCCMY, shows that the generated plastics and total strains are lower than those found in a simplified nerve bundle, SBMY, for the boundary conditions considered here. The mechanical failure of the fibre is represented by fibre disconnection, that here is assumed to occur at high deformation (at 30% or higher), see Chapters 4 and 5. Fig. 6.3 and 6.4 show that mechanical failure is induced by elastic strains rather than plastic strains, where the total strain can reach about 60 % in the active fibre vs. 15 % found for plastic strain. This is in line with evidence of mechanical failure at high deformations (Smith et al., 1999), and with the assumption that the myelin sheath redistributes the plastic strains at the bundle level preserving its functionality at higher deformations, see Chapters 4 and 5.

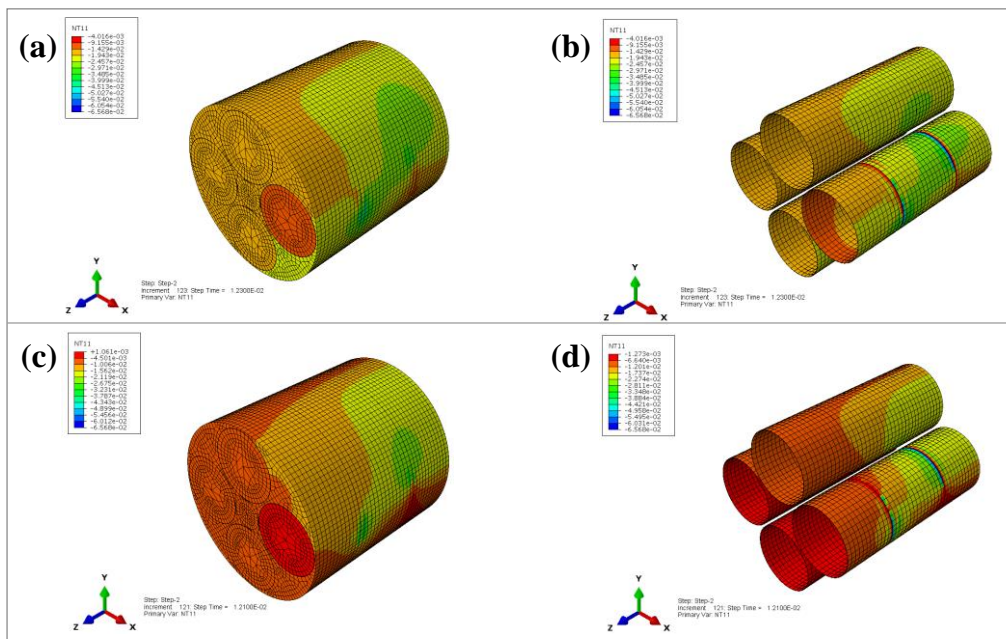


**Fig. 6.5** Isometric view of the small bundle model made by myelinated fibres under 30% applied deformation. The voltage distribution [V] is taken at the peak of the membrane potential with  $AC=0$  in (a)-(b), and  $AC=1$  in (c)-(d).

The voltage distribution of the SBMY, see Fig. 6.5, is shown in contrast to that of the HCCMY with  $AC = 0$  and  $AC = 1$ , see Fig. 6.6 and 6.7, respectively. HCCMY refers only to half of the real Ranvier’s node and myelin sheath region, see Fig. D1, which is a section of that represented by SBMY where two Ranvier’s node regions are modelled. The

equivalent part of the membrane section of SBMY in Fig. 6.5 (b) and (d) for  $AC = 0$  and  $AC = 1$ , respectively is Fig. 6.6 (d) and 6.7 (d) of HCCMY, although the dimensions are different. Similarly, the equivalent voltage distributions of the bundles can be seen at the ECM in Fig. 6.5 (a)-(c) (SBMY), and Fig. 6.6 (c) and 6.7 (c) (HCCMY).

The voltage distributions are similar in HCCMY with  $AC = 0$  and  $AC = 1$  but with different values, see Fig. 6.6 and 6.7. As in Fig. 6.5, the distribution at the Ranvier’s node regions shows areas where the voltage magnitude has low and high values, see Fig. 6.6 and 6.7. The voltage magnitude found on neighbouring Fibres #2, #1 and #4 is the same in both the SBMY and HCCMY regardless of  $AC$ , and it is lower than  $10\text{ mV}$  in all cases. So, neighbouring fibres can undergo depolarization in both models.

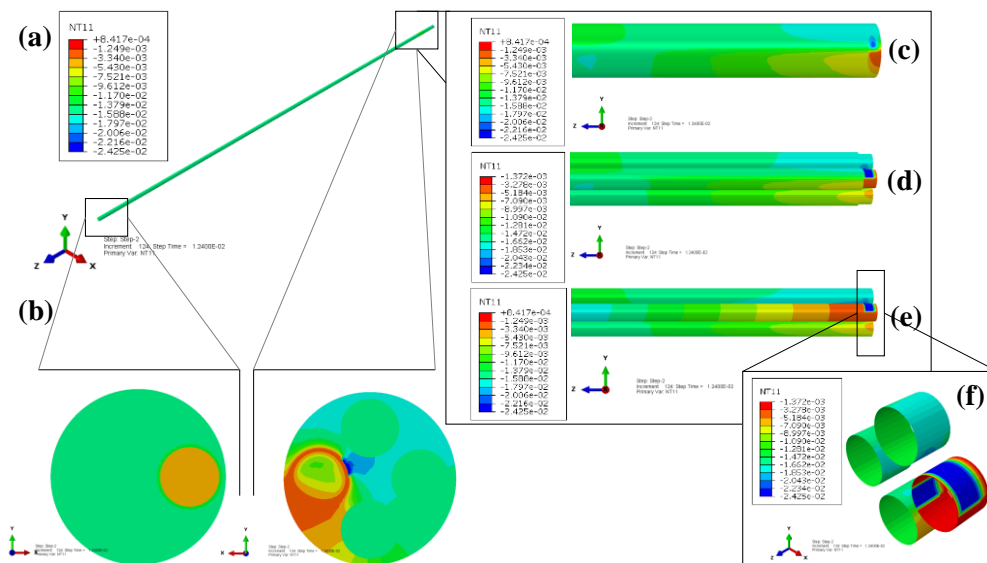


**Fig. 6.6** The HCCMY is shown at the peak of the membrane potential when a 30% displacement boundary conditions is applied with  $AC=0$ . In (b), the frontal and back view of the HCCMY. In (c), a section of the HCCMY including the myelin and the Ranvier’s Node. In (d), the myelin and the Ranvier’s node without the extracellular medium and intracellular medium. In (e), the membrane section, where the conductive part, the Ranvier’s node, is shown in (f).

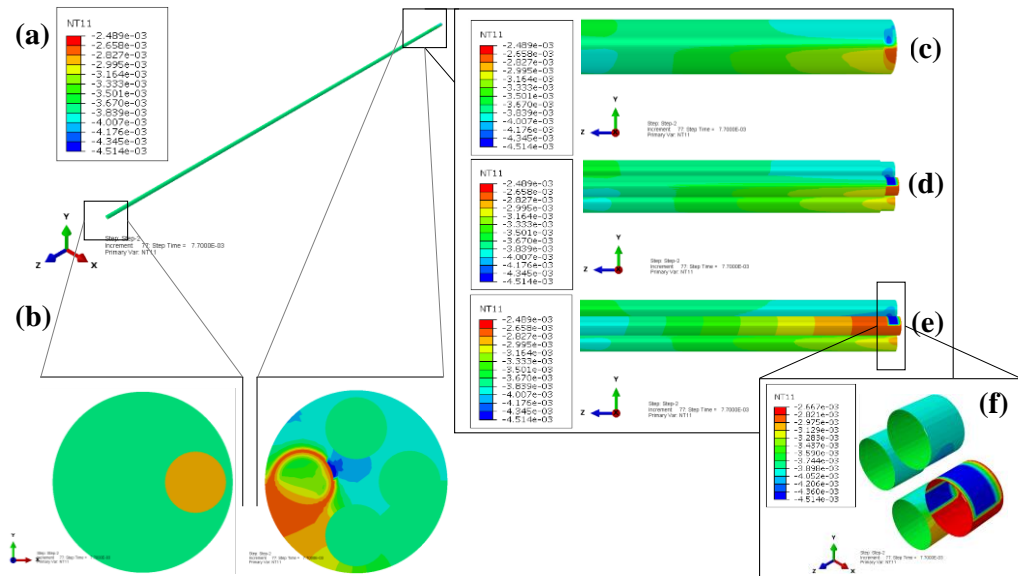


**Fig. 6.7** The HCCMY is shown at the peak of the membrane potential when a 30% displacement boundary conditions is applied with  $AC=1$ . In (b), the frontal and back view of the HCCMY. In (c), a section of the HCCMY including the myelin and the Ranvier's Node. In (d), the myelin and the Ranvier's node without the extracellular medium and intracellular medium. In (e), the membrane section, where the conductive part, the Ranvier's node, is shown in (f).

To illustrate the relative contribution of piezoelectricity in the coupled model, Fig. 6.8 shows the maximum principal value of the total strain, the plastic strain and the piezoelectric (thermal equivalent) strain of the HCCMY versus applied displacement. As the piezoelectric effect is only relevant in the through-thickness direction of the nerve membrane, see Chapter 3 and 5, Fig. 6.8 reports the radial component of the thermal strain only, as all the other components are null. As mentioned in Chapter 3, the nerve membrane is the only part of the model to have a finite piezoelectric coefficient greater than zero. Clearly, piezoelectricity is a significant contributor to the overall strain levels under the conditions considered. Although the thermal strain values in Fig. 6.8 are taken at the HCCMY only, those are also representative of those in the SBMY, as the piezoelectric coefficient is the same in both models.

Assuming a zero-piezoelectric coefficient at the nerve membrane (as that of ECM and ICM, see Chapter 3), the voltage-induced displacement is negligible, so that the corresponding strain and stresses are negligible at the nerve membrane, and their value is dependent only by the magnitude of the applied boundary conditions. By carrying coupled equivalent thermal-displacement simulations with null expansion coefficients at both the nerve membrane, ECM and ICM, the results generated by the model are not significant for the purposes of this thesis as the values would be dependent on its mechanical properties

only. Appendix F shows the insights of a the piezoelectric coefficient in relation to voltage , plastic strain and total strain.

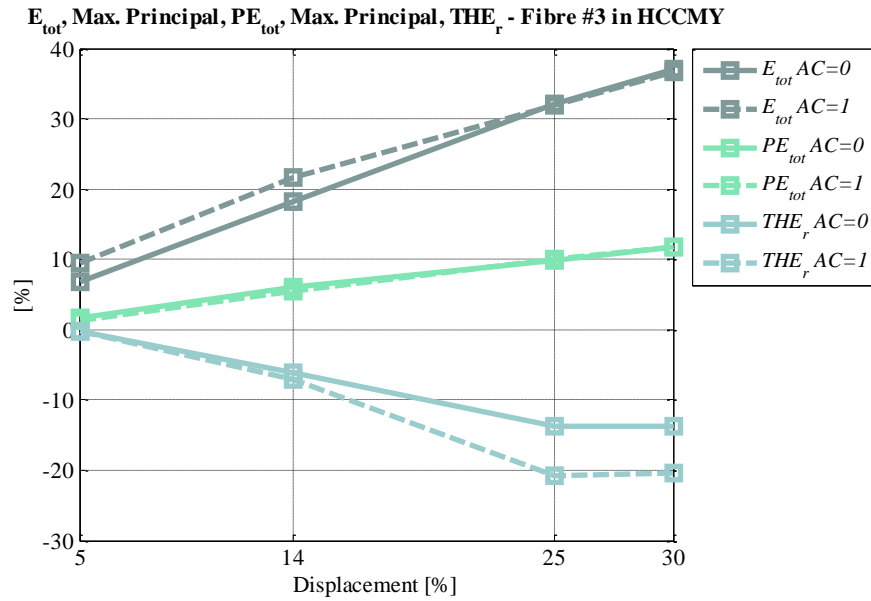


**Fig. 6.8** The maximum principal of the total strain,  $E_{Tot}$ , the total plastic strain,  $PE_{Tot}$ , and the thermal strain through the membrane thickness,  $THE_r$ , of the HCCMY are plotted against the applied strain. These values refer to Fibre #3.

## 6.4 Limitations

The HCCMY is a model that requires higher computational cost compared to the SBMY due to its geometry which includes a very high ratio of membrane axial length: membrane thickness and therefore a very large mesh design is required, see Appendix D and E. As a result, the HCCMY cannot complete all the steps of the simulation carried out for the previous SB and BB models (*step 1*: steady state, *step 2*: loading; and, *step 3*: after loading) for each of the applied deformations. The model runs up to the first applied upper-threshold stimulus at about the peak of the membrane potential; that is, it stops running during *step 2*. Additionally, no simulations could be carried out at 60 % of applied displacement. Therefore, the data in Fig. 6.3, 6.4, 6.6 and 6.7 in HCCMY  $AC = 1$  are taken at different time steps than in SBMY for the same applied boundary conditions. However, the time steps are very close to those of the SBMY, and are taken about the time at which the membrane potential peak is reached. Although the data in HCCMY and SBMY are not taken at the same time step, the time window is very close and it differs of about a few milliseconds only. Nonetheless, as discussed above, the results for the HCCMY show similar trends to those found in the SBMY. Also, it is worth noting that the voltage

distribution along the myelin sheath remains approximately constant at a distance from the Ranvier's nodes, and therefore future work could consider shorter models focussed on the region of interest around the Ranvier's nodes. In the end, here, we neglect the variation of the membrane potential speed, the recovery of the functionality (seen experimentally (Smith et al., 1999; Rickett, Connell and Bastijanic, 2011; Ochs et al., 2000)) and the presence of other ions (as calcium (Loverde, Pfister and Heidemann, 2015)).

## 6.5 Conclusion

In summary, results generated by the model with anatomically accurate nerve fibres (HCCMY) show similar trends to those found for the smaller, more computationally efficient (SBMY). The conclusions, listed below, are made accounting of the limitations of this work within this context.

Considering that:

- The calibre of HCCMY is slightly greater of that of SBMY,  $0.5 \mu m$  vs.  $0.477 \mu m$ .
- The Ranvier's node regions are  $0.75 \mu m$  in HCCMY vs.  $2 nm$  of the same in SBMY.
- The myelin thickness is  $9 nm$  in HCCMY (Liewald et al., 2014) vs.  $3 nm$  (Einziger et al., 2003b; a; Plonsey and Malmivuo, 1995) in SBMY.
- The radius of the ICM, nerve membrane and myelin are:  $0.5 \mu m/0.503 \mu m/0.512 \mu m$  in HCCMY, and  $0.477 \mu m/0.5 \mu m/0.5 \mu m$  in SBMY.
- The length of HCCMY is  $375.75 \mu m$  vs.  $2.5 \mu m$  of the SBMY.
- The ratio of myelin sheath length over the Ranvier's node lengths is equal to 0.002 in both cases.

We found that:

- At the maximum applied axial displacement, the maximum values of nodal quantities show that: the voltage is higher in HCCMY than in SBMY; the strains are lower in HCCMY than in SBMY.
- The maximum values of the quantities generated on Fibre #3 show that: the voltage has similar values in both models (HCCMY and SBMY); the plastic strains are about the same values; the elastic strain is lower in HCCMY than in SBMY.
- Membrane potential varies on Fibre #3 with similar trends and values of the same order of magnitude.
- Plastic strains and total strains vary with similar trends and are the same order of magnitude.

- Predicted total strain levels are lower in the anatomically accurate model than in the smaller model.
- Elastic strains are higher than plastic strains in both models, so the voltage alterations are influenced more by elastic strains than by the plastic strains.
- Under applied axial strain, the point of maximum displacement is found at the boundary between the myelin sheath and the Ranvier's node.
- Ionic currents are decreasing as the voltage value with  $AC = 1$  are higher than with  $AC = 0$ .
- Generated plastic strain levels are similar in both models (HCCMY and SBMY). The plastic strains might vary with the ratio of myelin sheath length over the Ranvier's node lengths (Fields, 2016; Tricaud, 2018).

These results agree with experimental evidence. Below, the key points are summarized:

- The change in membrane voltage peak is proportional to the applied strain, as seen in Chapters 4 and 5, and as found in experiments (Shi and Whitebone, 2006; Rickett, Connell and Bastijanic, 2011; Ochs et al., 2000).
- The myelin sheath is thought to redistributing the plastic strain around the fibre, as shown in Chapters 4 and 5, lower strain are found in myelinated bundle. Evidence show that, at lower strain, the alteration of membrane potential at the Ranvier's node is not significant thanks to the myelin sheath layer (Gray and Ritchie, 1954). Here, in HCC, the strain are the same order of magnitude and trend of those observed in the previous Chapters. Thus, the myelin sheath layer seems to preserve the functional and mechanical activity of the nerve bundle in both models (SSBMY and HCCMY).
- Evidence show a decrease of the membrane potential with the applied strain (Li and Shi, 2006; Rickett, Connell and Bastijanic, 2011; Loverde, Pfister and Heidemann, 2015; Ochs et al., 2000; Shi and Whitebone, 2006; Bain and Meaney, 2000), as it alters the ionic reversal potentials of the ionic gating dynamics.
- Conduction is limited at high strain, as the membrane axial resistivity is increased (Ochs et al., 2000; Gray and Ritchie, 1954). Here, the decrease of local ionic currents is evident when the applied strain is affecting the ionic reversal potentials and the ionic gating currents, i.e. when  $AC$  is equal to 1, so when all the ionic gating of the membrane is altered by the applied strain.

## References Chapter 6

- Aboitiz, F., Scheibel, A. B., Fisher, R. S., and Zaidel, E. (1992). Fiber composition of the human corpus callosum. *Brain Research*, 508(1–2). Retrieved from <https://www.sciencedirect.com/science/article/pii/000689939290178C?via%3DiHub>
- Arancibia-cárcamo, I. L., Ford, M. C., Cossell, L., Ishida, K., and Attwell, D. (2017). Node of Ranvier length as a potential regulator of myelinated axon conduction speed. *ELife*, 6(1–15), 1–49. <https://doi.org/10.7554/eLife.23329>
- Bain, A. C., and Meaney, D. F. (2000). Tissue-level thresholds for axonal damage in an experimental model of central nervous system white matter injury. *Journal of Biomechanical Engineering*, 122(6), 615–622. <https://doi.org/10.1115/1.1324667>
- Cinelli, I., Destrade, M., Duffy, M., and McHugh, P. (2017). Electro-mechanical response of a 3D nerve bundle model to mechanical loads leading to axonal injury. In *International Journal of Numerical Methods in Biomedical Engineering* (pp. 978–981). <https://doi.org/DOI: 10.1002/cnm.2942>
- Durand, D. M. (2000). Electric Stimulation of Excitable Tissue. In E. J. D. Bronzino (Ed.), *The Biomedical Engineering Handbook: Second Edition*. (Vol. 42, p. 23). Boca Raton: CRC Press LLC, 2000. <https://doi.org/10.1201/9781420049510>
- Einzigler, P. D., Livshitz, L. M., Dolgin, a., and Mizrahi, J. (2003a). Novel cable equation model for myelinated nerve fiber. *First International IEEE EMBS Conference on Neural Engineering, 2003. Conference Proceedings.*, 112–115. <https://doi.org/10.1109/CNE.2003.1196769>
- Einzigler, P. D., Livshitz, L. M., Dolgin, A., and Mizrahi, J. (2003b). Generalized Cable Equation Model for Myelinated Nerve Fiber. *IEEE Transactions on Biomedical Engineering*, 52(10), 1632–1642. <https://doi.org/10.1109/CNE.2003.1196769>
- Fields, R. D. (2016). Myelin—More than Insulation. *Science*, 344(6181), 264–266. <https://doi.org/10.1126/science.1253851.Myelin>
- García-grajales, A. J. J. A., and Peña, A. M. J. M. (2014). A computational model coupling mechanics and electrophysiology in spinal cord injury. *Biomechanics and Modeling in Mechanobiology*, 13(4), 883–896. <https://doi.org/10.1007/s10237-013-0543-7>
- Gray, B. J. A. B., and Ritchie, J. M. (1954). Effects of stretch on single myelinated nerve fibres. *J. Physiol.*, (124), 84–99. <https://doi.org/10.1113/jphysiol.1954.sp005087>

- Li, J., and Shi, R. (2006). A device for the electrophysiological recording of peripheral nerves in response to stretch. *Journal of Neuroscience Methods*, 154, 102–108. <https://doi.org/10.1016/j.jneumeth.2005.12.007>
- Liewald, D., Miller, R., Logothetis, N., Wagner, H. J., and Schüz, A. (2014). Distribution of axon diameters in cortical white matter: an electron-microscopic study on three human brains and a macaque. *Biological Cybernetics*, 108(5), 541–557. <https://doi.org/10.1007/s00422-014-0626-2>
- Loverde, J. R., Pfister, B. J., and Heidemann, S. R.. (2015). Developmental axon stretch stimulates neuron growth while maintaining normal electrical activity , intracellular calcium flux , and somatic morphology. *Frontiers in Cellular Neuroscience*, 9(August), 1–15. <https://doi.org/10.3389/fncel.2015.00308>
- Meffin, H., Tahayori, B., Grayden, D. B., and Burkitt, A. N. (2012). Modeling extracellular electrical stimulation: I. Derivation and interpretation of neurite equations. *Journal of Neural Engineering*, 9(6), 065005. <https://doi.org/10.1088/1741-2560/9/6/065005>
- Ochs, S., Pourmand, R., Si, K., and Friedman, R. N. (2000). Stretch of mammalian nerve in vitro: Effect on compound action potentials. *Journal of Peripheral Nervous System*, 5, 227–235.
- Rall, W. (1977). Core conductor theory and cable properties of neurons. *Handbook of Physiology - The Nervous System I*, Chapter 3, 39–97. <https://doi.org/10.1002/cphy.cp010103>
- Rickett, T., Connell, S., and Bastijanic, J. (2011). Functional and Mechanical Evaluation of Nerve Stretch Injury. *Journal of Medical Systems*, 35(5), 787–793. <https://doi.org/10.1007/s10916-010-9468-1>
- Shi, R., and Whitebone, J. (2006). Conduction deficits and membrane disruption of spinal cord axons as a function of magnitude and rate of strain. *Journal of Neurophysiology*, 95(6), 3384–3390. <https://doi.org/10.1152/jn.00350.2005>
- Smith, D. H., Wolf, J. A., Lusardi, T. A., Lee, V. M., and Meaney, D. F. (1999). High tolerance and delayed elastic response of cultured axons to dynamic stretch injury. *The Journal of Neuroscience*, 19(11), 4263–4269.
- Tricaud, N. (2018). Myelinating Schwann Cell Polarity and Mechanically-Driven Myelin Sheath Elongation. *Frontiers in Cellular Neuroscience*, 11(January), 1–12. <https://doi.org/10.3389/fncel.2017.00414>

## Chapter 7.      **Head-To-Nerve Analysis of Electro-Mechanical Impairments of Diffuse Axonal Injury**

The focus of this chapter is on the use of the coupled electro-mechanical modelling approach in estimating axonal injury induced during simulated head impacts. This is achieved by using two independent models, one at the microscale for the nerve bundle and the other at the macroscale one for the head. This chapter has been published as a journal paper manuscript in *Cinelli, I., Destrade, M., McHugh, P., Trotta, A., Gilchrist, M., and Duffy, M. 2018. Head-to-nerve analysis of electromechanical impairments of diffuse axonal injury. Biomechanics and Modeling in Mechanobiology. <https://doi.org/10.1007/s10237-018-1086-8>.*

*Abstract — Objective:* To investigate mechanical and functional failure of Diffuse Axonal Injury (DAI) in nerve bundles following frontal head impacts, by finite element simulations. *Methods:* Anatomical changes following traumatic brain injury are simulated at the macroscale by using a 3D head model. Frontal head impacts at speeds of 2.5 – 7.5 m/s induce mild to moderate DAI in the white matter of the brain. Investigation of the changes in induced electro-mechanical responses at the cellular level is carried out in two scaled nerve bundle models, one with myelinated nerve fibres, the other with unmyelinated nerve fibres. DAI occurrence is simulated by using a real-time fully coupled electro-mechanical framework, which combines a modulated threshold for spiking activation and independent alteration of the electrical properties for each 3-layer fibre in the nerve bundle models. The magnitudes of simulated strains in the white matter of the brain model are used to determine the displacement boundary conditions in elongation simulations using the 3D nerve bundle models. *Results:* At high impact speed, mechanical failure occurs at lower strain values in large unmyelinated bundles than in myelinated bundles or small unmyelinated bundles; signal propagation continues in large myelinated bundles during and after loading, although there is a large shift in baseline voltage during loading; a linear relationship is observed between the generated plastic strain in the nerve bundle models and the impact speed and nominal strains of the head model. *Conclusion:* The myelin layer protects the fibre from mechanical damage, preserving its functionalities.

## 7.1 Introduction

Current research interests in brain modelling aim at understanding head injury (Dixit 2017; Garcia-Gonzalez 2018; Samaka 2013; Horgan 2004, 2003; Wright 2012; Young 2015), axonal injury (Cinelli 2017a, 2017b, 2017c; Garcia-Grajales 2015; Jérusalem 2014; Mohammadipour 2017; Wright 2012), sport concussions (McCroly 2017), neuronal morphology (Abdellah 2018; Kanari 2018), and brain connectivity (Wazen 2014) when medical conditions are present, such as Alzheimer’s disease, depression and epilepsy (Wazen 2014). Brain models vary according to application (Dixit 2017; Samaka 2013) and can be based on computed tomography and magnetic resonance tomography images (Horgan 2004, 2003) or can be based on magnetic resonance imaging (Garcia-Gonzalez 2017, 2018; Wazen 2014). Accuracy and precision of finite element models of the brain are achieved by design, where the brain anatomy is replicated by the inclusion of a certain number of layers, and where material properties aim to conform to reality (Dixit 2017; Samaka 2013). However, most macro-scale brain models do not account for a detailed representation of the micro-scale structure of nervous cells to limit the computational cost (Dixit 2017; Samaka 2013; Mohammadipour 2017; Wright 2012), although cell models have been developed in this regard (Abdellah 2018; Cinelli 2017a, 2017b; Garcia-Grajales 2015; Jérusalem 2014; Kanari 2018; Mohammadipour 2017; Wright 2012). Recent published works of finite element models of nervous cells tend to simulate both the mechanical structure and the functionality of the cell (Cinelli 2017a, 2017b; Garcia-Grajales 2015; Jérusalem 2014; Mohammadipour 2017), as its relevance has been demonstrated in experimental works (Galbraith 1993; El Hady 2015; Mosgaard 2015; Mueller 2014; Zhang 2001).

Traumatic Brain Injury is a common result of head impact. In Europe, fall-related, work-related and all injury-related deaths due to TBI are as high as 47.4% (Li et al., 2016), 8.5% (Li et al., 2016) and 37% (Majdan et al., 2016), respectively. Brain injuries are associated with increased mortality and decreased life expectancy compared to the general population (Majdan et al., 2016). Furthermore, people with TBI incur substantial direct (health care) and indirect (loss of productivity and care-giver related) costs (Majdan et al., 2016). Multiple factors such as individual anatomy, head acceleration, magnitude and direction of forces, protective equipment, etc., explain the high heterogeneity of TBI (Hemphill et al., 2015; Siedler et al., 2014). Neurochemical, metabolic, neuroinflammation, blood perfusion and other molecular-based processes change the mechanobiology and the cellular microenvironment of the brain as a consequence of the localization of stresses following TBI (Hemphill et al., 2015; Kan et al., 2012). The challenge in understanding the biomechanics of TBI leads to an increase in difficulty in

treating and preventing the development of cognitive and behavioural problems (Hemphill et al., 2015; Kan et al., 2012).

Additionally, TBI has effects at the cellular level. The neuropathology of TBI includes focal damage of brain tissue or widespread axonal injury (Jérusalem et al., 2014; Wright and Ramesh, 2012). TBI-induced dynamic deformations increase the risk of axonal stretch and shear injuries to axons scattered throughout the brain parenchyma (Lajtha et al., 2009; Wright and Ramesh, 2012), generating structural and functional damage (such as leaking nerve membranes (Yu et al., 2012) and cytoskeleton disruption (Hemphill et al., 2015; Smith et al., 1999; Tang-schomer et al., 2017)), leading to rupture of the axon (Hemphill et al., 2015; Siedler et al., 2014; Smith et al., 1999). As discussed in Chapter 5, strain and strain-rate are known to play important roles in the induced-electrophysiological impairments and functional deficits at the axonal level (Boucher et al., 2012; Geddes et al., 2003; Jérusalem et al., 2014).

In particular, mild and severe TBI impacts lead to Diffuse Axonal Injury (DAI), which refers to the damage experienced by neural axons in the deep white matter regions of the brain (Ma et al., 2016; Wright and Ramesh, 2012). DAI is associated with a high risk of developing future neurodegenerative disease (Hemphill et al., 2015; Kan et al., 2012), and the progressive course of DAI is responsible for long-lasting neurological impairments associated with high rates of mortality (Lajtha et al., 2009; Smith and Meaney, 2000; H. C. Wang and Ma, 2010). Currently, no clinical treatments and prognosis can be used against DAI because of the complexity in diagnosis when using medical imaging, due to haemorrhages, hematomas and tissue lesions of the neighbouring injured area (Hemphill et al., 2015; Lajtha et al., 2009; Ma et al., 2016; Wright and Ramesh, 2012). In effect, DAI can only be established post-mortem.

Computational models of TBI biomechanics can simulate brain trauma based on the principles of mechanics. By replicating head impact dynamics, they enable a detailed investigation of the mechanical and physiological changes linked to anatomical and functional damage of the brain. In this way, modelling presents itself as a tool that could aid in diagnosis as it allows for the evaluation of mechanical quantities and physiological measurements (such as temperature, pressure and others). in the brain tissue that cannot be detected by current medical technology.

With the purpose of enhancing the understanding of electro-mechanical DAI occurrences, in this work a multi-scale approach is adopted, and use two independent models to replicate the anatomical and functional changes induced by TBI events: (i) at the *macroscale*, the induced anatomical changes are simulated by using an advanced 3D biomechanical Head Model (the University College Dublin brain trauma model – UCD Head Model (Horgan and Gilchrist, 2003, 2004)); (ii) at the *microscale*, the structural and

functional changes of complex electro-mechanical impairments at the cellular level are simulated by using a 3D coupled electromechanical Nerve Bundle Model (Cinelli et al., 2017b, 2017d). These models replicate the brain macro-environment and the neural micro-environment, respectively. The sequential use of two independent models is needed to limit the computational cost that would arise from the combined modelling of macro and micro features within the same 3D model.

In this chapter, short-term frontal head impacts are simulated by using the Head Model to estimate the deformation of the white matter regions at the instant of impact. Then, the magnitudes of TBI-induced strains in the Head Model are used to determine the displacement boundary conditions to be applied to the Nerve Bundle Model. The worst-case condition of uniaxial stretching is applied to the fibre bundles, where it has been found that tensile axonal strain is the most realistic mechanism for generating DAI (Bain and Meaney, 2000; Jérusalem et al., 2014; Wright and Ramesh, 2012). Similarly to Chapter 5, the variation of the membrane voltage (in terms of its peak and baseline values) is investigated during and after the applied elongation. However, in this chapter, electrophysiological and structural occurrences are simulated at the axonal level using realistic TBI elongation simulations. DAI-induced neural strains and voltage changes are analysed using the Nerve Bundle Model in relation to strain levels predicted by the Head Model for different impact speeds.

In the field of head trauma biomechanics, the Head Model developed at University College Dublin (Horgan and Gilchrist, 2003) is a 3D Finite Element (FE) representation of the human head complex, proposed as a tool for the assessment of brain injury mechanisms (Horgan and Gilchrist, 2003, 2004). The main anatomical features of the UCD Head Model include the cerebrum, cerebellum and brainstem, intracranial membranes, pia, cerebrospinal fluid layer, dura, a varying thickness three-layered skull (cortical and trabecular bone layers), scalp and the facial bone (Horgan and Gilchrist, 2003), see Fig. 7.1. It has been validated against a series of cadaveric head impact experiments, simulating the Nahum's test (Horgan and Gilchrist, 2003), and Trosseille's and Hardy et al.'s tests, see account by Horgan et al. (Horgan and Gilchrist, 2004). The validation includes both rotational and translational acceleration components (Horgan and Gilchrist, 2003, 2004). In the current study, the Head Model is used to simulate frontal head impacts only, where rotations and accelerations are neglected.

Recent experimental evidence of neural activity highlights complex electro-mechanical phenomena happening at the nerve membrane layer (Alvarez and Latorre, 1978; Cinelli et al., 2017a, 2017c; Galbraith et al., 1993; Geddes et al., 2003; Zhang et al., 2001) during signalling (Mosgaard et al., 2015; Zhang et al., 2001). The inclusion of an accurate representation of DAI-related electrophysiological impairments is needed to improve

diagnosis, treatment and prognosis of related pathologies (Jérusalem et al., 2014; Lajtha et al., 2009; Ma et al., 2016; Wright and Ramesh, 2012). Our Nerve Bundle Model is a 3D idealized representation of a nerve bundle (Cinelli et al., 2017a, 2017c), located in the deep white matter of the brain (Wright and Ramesh, 2012), see Fig. 4.1. As described previously, each fibre is made of Extracellular Media (ECM), see Fig. 4.1 (c), Intracellular Media (ICM), see Fig. 4.1 (e), and a membrane, see Fig. 4.1 (d). At the nerve membrane layer, the Nerve Bundle Model includes a fully coupled 3D electro-mechanical representation of the neural activity, combining piezoelectricity and electrostriction with changes in strain, including total strain (elastic, electro-thermal equivalent and plastic strain) (Cinelli et al., 2017d, 2017b, 2017c). In this chapter, the case of two scaled nerve bundle models with a ratio of 2:1 are considered, where the nerve fibres inside follow the same ratio, while the thickness of the nerve membrane is maintained constant. The neurite radii of the small bundle (SB) model are:  $a_{ICM} = 0.477 \mu m$ ,  $a_M = 0.480 \mu m$  and  $a_{ECM} = 0.500 \mu m$  (Cinelli et al., 2015c). The neurite radii of the second, bigger bundle (BB) are double those of SB, while the membrane thickness is the same ( $3nm$ ). Here, only the cases of a fully unmyelinated bundle or a fully myelinated bundle are considered, as in Chapter 5.

This work is a development on the work reported in previous chapters and in (Cinelli et al., 2017b, 2017d) whereby the boundary conditions used in the Nerve Bundle Model are directly linked to frontal head impacts simulated with the Head Model. Thus, control over the boundary conditions of both models aims at simulating realistic clinical events, speeding up the transfer of the findings from computational studies to clinical care.

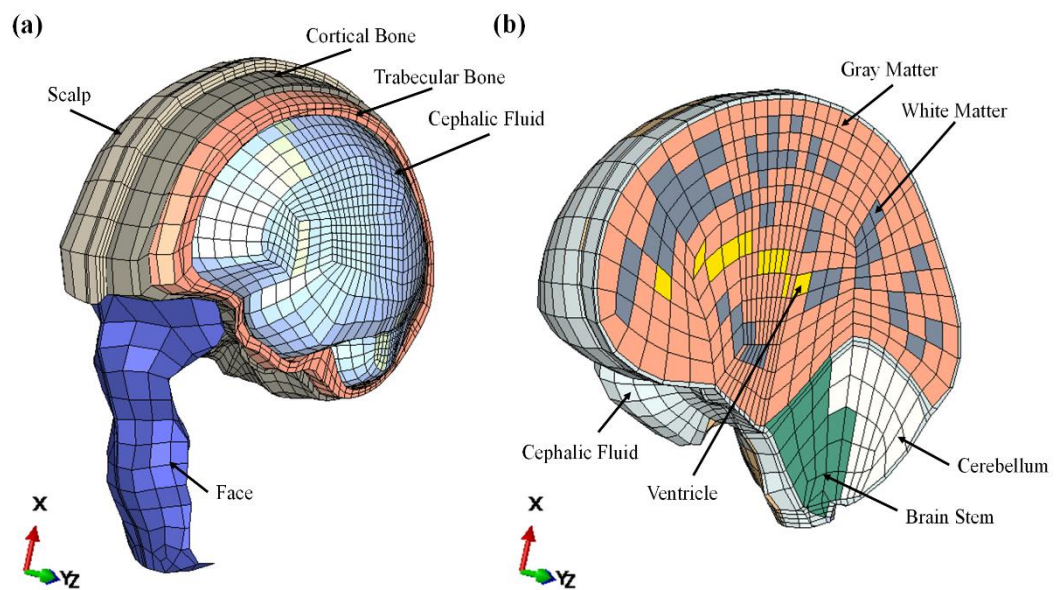


**Fig. 7.1** The UCD Head Model (Horgan and Gilchrist, 2003, 2004): in (a), the face, scalp, cortical and trabecular bone, and cephalic fluid; in (b), gray matter, white matter, cerebellum and brain stem.

## 7.2 Method

### 7.2.1 Material Properties

Details of the Head Model formulation and material properties can be found in the papers by Horgan et al. (Horgan and Gilchrist, 2003, 2004), but to summarise, the model utilises linear viscoelasticity combined with hyper-elasticity and large deformation kinematics to represent the brain tissue. Details of material properties of the Nerve Bundle Model are the same as those assumed previously and can be found at 5.2.1.

### 7.2.2 Boundary Conditions

A frontal impact is simulated to induce axonal injuries in the deep white matter of the brain. The Head Model is launched freely with an initial velocity (from 2.5 to 7.5  $m/s$ ) against an encasté plane (i.e. the *floor* part) (Horgan and Gilchrist, 2003). The speed values are within the range of values considered to induce mild and moderate DAI in white matter (Wright and Ramesh, 2012). The loading axis of the velocity impact is assumed to be aligned parallel to the force of gravity. Since the neck is not included in the model, a free boundary condition is used to simulate a frontal head impact and only short-duration impact responses ( $< 6 ms$  (Horgan and Gilchrist, 2003)) are considered (Horgan and Gilchrist, 2003).

For the Nerve Bundle Model (Cinelli et al., 2017d, 2017b), the encasté boundary condition is applied at the origin of the model at one end, and no rotations are allowed, while a displacement boundary condition is applied at the opposite end (as in uniaxial elongation). Then, an upper-threshold stimulation voltage with a Gaussian distribution is applied on Fibre #3 along its length, see Fig. 4.1, while the other fibres are activated only if the diffused charges from Fibre #3 generate an input voltage higher than the modulated threshold (Cinelli et al., 2017b). As before, the 3D distribution of charges on Fibre #3 modulates the activation of the other fibres, see Fig. 4.1.

Invoking the *macro-micro* link, the magnitude of the displacement boundary conditions of the Nerve Bundle Model are taken from the nominal strain value found in the white matter regions of the Head Model following impact. Here, DAI is simulated as the TBI-induced tissue deformations would stretch the nerve bundle longitudinally only. Frequency-independent loading conditions are considered throughout, after an initial steady-state interval (lasting about 2ms). In the same manner as applied in Chapter 5, the mechanical loads are applied to the Nerve Bundle Model from 2 ms to 67 ms, as instantaneous loading

conditions, and the model is set to run for 140 *ms* so that the effects of plasticity can be observed post-loading.

### 7.3 Results

Following a frontal head impact with initial speed  $v$  [*m/s*], the maximum principal value of the Nominal Strains ( $NE$ ) [%], found in the white matter region of the Head Model, vary with  $v$ , see Fig. 7.2.

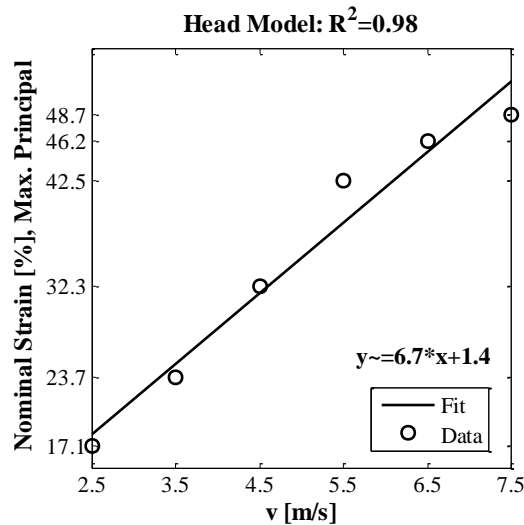


**Fig. 7.2** Variation in the maximum principal value of the nominal strains [%] in the Head Model vs. the speed impact values,  $v$  [*m/s*], used in the frontal head impacts of the Head Model. Linear regression fit also included.

Although an assumption of large deformation kinematics is included in the head model, the  $NE$  variation is near linear with  $v$ . This justifies the investigation of the electrophysiological features of the Nerve Bundle Models based on the quasi-static assumption where only small deformations are considered (see Section 3.2.3).

Fig. 6.3 shows the Head Model, in (a)-(c), and the Nerve Bundle Model, in (d)-(i). This figure refers to the case of impact at 7.5 *m/s*, only. The head impacts the floor at 7.5 *m/s* as shown in (a), where the gravity force is aligned to the  $z$  –axis of the Head Model. At the time of contact with the floor (i.e. 3.75 *ms*), (b) and (c) show the cerebellum and white matter region of the model, respectively.

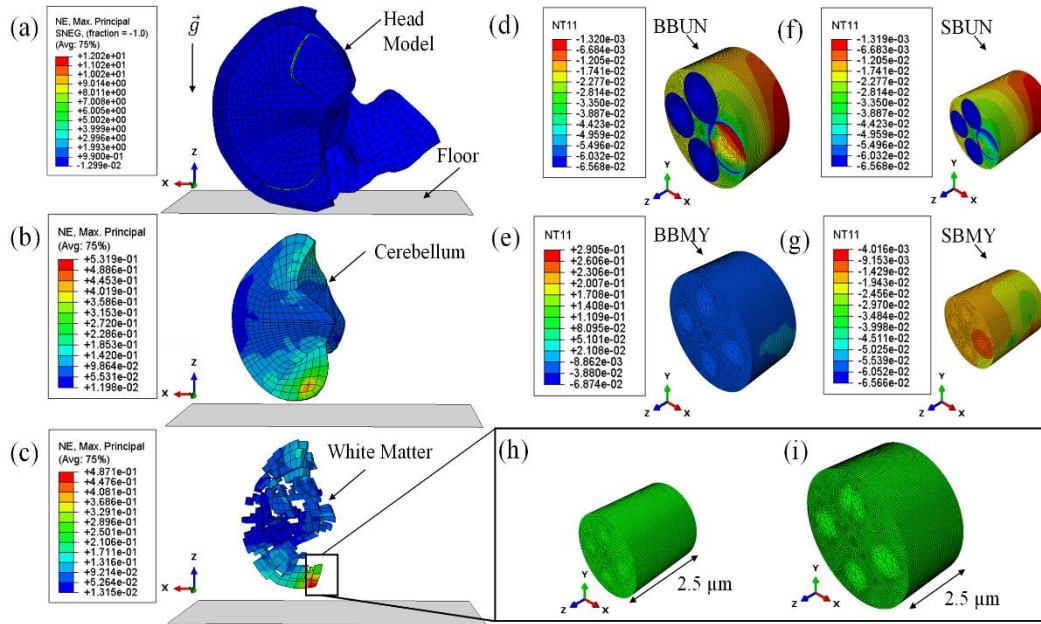


**Fig. 7.3** (a)-(c) the Head Model (Horgan and Gilchrist, 2003, 2004) and in (d)-(i) the Nerve Bundle Model. The head impacts the floor at 7.5 m/s, in (a), and, at the instant of contact with the floor, maximum principal nominal strains are shown for the cerebellum, see (b), and white matter regions of the Head Model, see (c). A displacement boundary condition is applied to the Nerve Bundle Model with magnitude determined from the maximum value of the strain found in the white matter, see (c), for the same case of impact. The voltage (NT11) is shown during elongation, at the peak of the membrane potential. The voltage distribution is shown for: BBUN (d), BMY (e), SBUN (f) and SBMY (g). In (h) and (i) a representation of the mesh and geometry of SB and BB used in this work. The maximum value of each contour plot is reported here in brackets for clarity. For the Head Model the maximum of the nominal strain is 12.02, for the cerebellum is 0.5319, and for the White Matter is 48.71. Then, peak of the voltage in the BBUN is  $-1.320$  mV, for the BMY is  $0.2905$  mV, for the SBUN  $-1.309$  mV and for the SBMY is  $-4.016$  mV.

The contour plots refer to the *NE* in the Head Model. From this, the *NE* in the Head Model is used to generate the magnitude of the displacement boundary conditions applied in the Nerve Bundle Models. Fig. 7.3 (h) and (i) show the differences in the mesh and size of the model use for the SB and BB cases in this work. The voltage distribution (*NT11*), equivalent to temperature (Cinelli et al., 2017d, 2017b), is shown in (d) for BBUN, in (e) for BMY, in (f) for SBUN and in (g) for SBMY. Here, the voltage refers to the maximum value reached during elongation simulation, in which the magnitude of the displacement boundary condition is 48.7 % strain, see (c), and refers to the case of 7.5 m/s impact, see (a).

Then, the alteration of mechanical and electrical variables of the Nerve Bundle Models is shown in Fig. 7.4 and Fig. 7.5 for the range of nominal strain value found in the Head

Model; the cases of small unmyelinated (SBUN), small myelinated (SBMY), big unmyelinated (BBUN) and big myelinated (BBMY) bundles are considered. A head impact at 2.5  $m/s$  generates a mild-intensity axonal injury at the nerve axon level, because the magnitude of the  $NE$  is lower than the threshold considered, 21% (Bain and Meaney, 2000), for initiating plasticity, and equal to 17.1 % (see Fig. 7.2). In contrast, impacts at 3.5 to 7.5  $m/s$  generate strains within 23.7 % to 48.7 % (beyond the yield strain limit), inducing moderate-intensity axonal injury at the nerve axon level (Bain and Meaney, 2000; Smith et al., 1999). The plastic strain values of the Nerve Bundle Model are permanent strains generated during elongation, and consequently are found to remain after loading (see Section 5.3.2). Fig. 7.4 (a)-(b) and (d) shows that for SBUN, SBMY and BBMY, the magnitude of the maximum principal values of the Plastic Strain ( $PE$ ) (%) read at the nerve membrane, have a near-linear relation with the  $NE$  found in the Head Model for all the values considered, and that the  $PEs$  vary between 0 and 15%. In contrast, in the BBUN, the  $PEs$  are found to be within 0% and 150%, showing a more non-linear relation with the  $NE$ , see Fig. 7.4 (c). As expected from results presented in Chapter 5, it is found that bigger bundles undergo larger deformations compared to small bundles, and that the myelin sheath has an important role in redistributing the applied strains, preserving the mechanical structure of the fibre (Cinelli et al., 2017b, 2017c). In the BBUN, the entire nerve membrane layer is exposed to the applied deformation during elongation, while, in the BBMY, the myelin sheath protects the Ranvier's node regions from higher deformation by holding up part of the applied strains. Thus, the  $PEs$  read at the Ranvier's node regions in BBMY are lower than the  $PEs$  found in BBUN.

Fig. 7.5 shows the membrane potential peak and baseline values on Fibre #3 of the Nerve Bundle Models (a)-(c) during loading, and (b)-(d) after loading; values are plotted against the maximum principal value of the  $NE$  found in the white matter region of the Head Model, following impact. In Fig. 7.5 (a)-(c), each point is the peak and baseline voltage respectively, read at the nerve membrane when the elongation displacement boundary condition is applied on one end of the Nerve Bundle Model. The values are taken at the position where maximum displacement along the fibre middle axis occurs.

The membrane voltage (peak and baseline) changes in relation to the total strains read at the membrane, along the fibre length (Cinelli et al., 2017b) and from the corresponding changes in the ionic reversal potentials (Cinelli et al., 2017b, 2017d), see Fig. 3.2. For total strain lower than the 21% (Cinelli et al., 2017b) the ionic reversal potentials vary to produce a different homeostatic ionic gradient across the nerve membrane. For higher strain, the reversal potentials reach a saturation level, simulating loss of charges across the nerve membrane due to permanent deformations at the nerve membrane. This is seen in

terms of saturation in membrane voltage levels with increasing  $NE$  for all cases except SBUN in Fig. 7.5 (a)-(c).

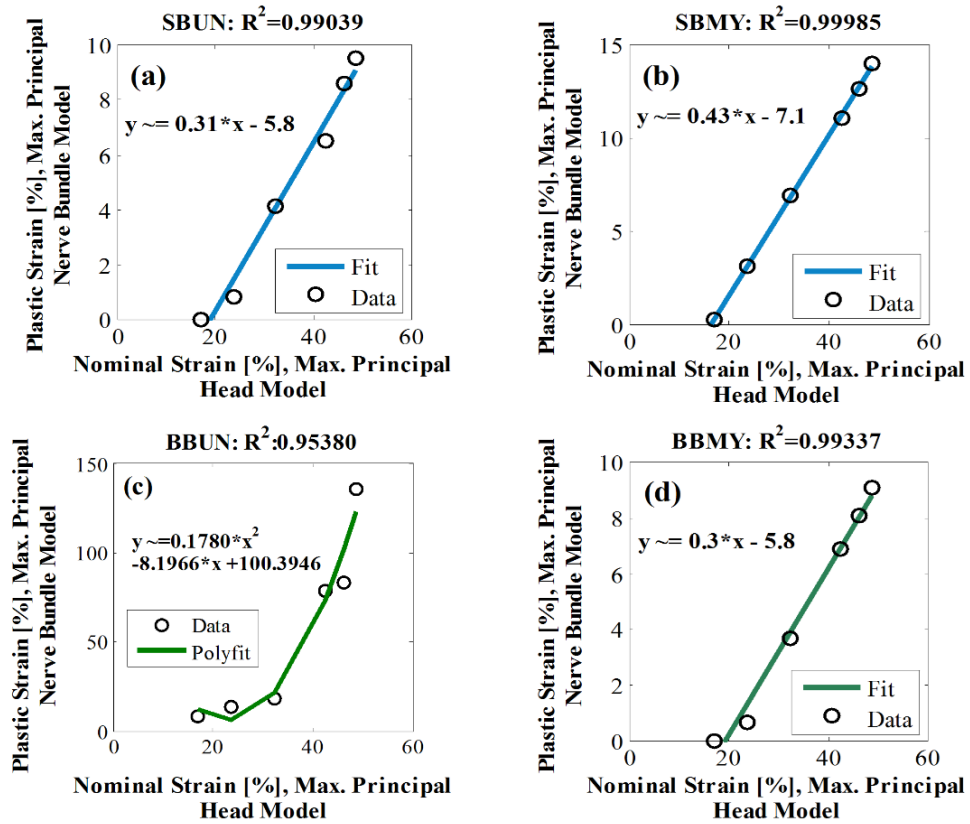


**Fig. 7.4** Variation in the maximum principal value of the plastic strains [%] in the Nerve Bundle Model, read at the nerve membrane, vs. the maximum principal value of the nominal strains [%] in the Head Model for (a) SBUN, (b) SBMY, (c) BBUN and (d) BBMY. Regression fits also included.

The voltage differences found during and after elongation, see Fig. 7.5, arise from the elastic recovery that occurs as soon as the load is removed, while the  $PEs$  remain after loading. Results found after-loading, shown in Fig. 6.5 (b)-(d), are taken at the same node as during loading for ease of comparison. The dashed line refers to the ability of the fibre to generate signals (here, it is found for BBMY only), in contrast with small oscillations of the membrane voltage around the baseline value (solid lines). The levels of oscillation can be deduced by comparing corresponding peak and baseline values, where only the BBMY case shows an appreciable difference both during and after loading, see Fig. 7.5. Again, the reason is because the myelin sheath layer redistributes the plastic strain around the Ranvier's node regions, thus the corresponding changes in the ionic reversal potentials are lower than the other cases. In all cases except the BBUN, there is a general increase in

membrane voltage with *NE* after loading, while the non-linear variation for BBUN is explained by the non-linearity in *PE* (see Fig. 7.3).

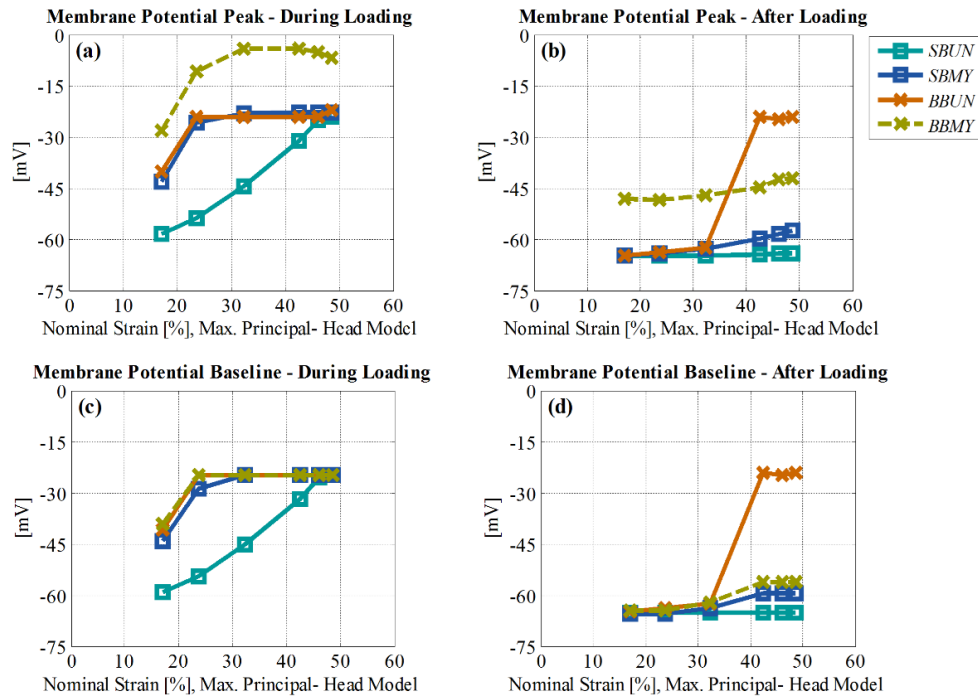


**Fig. 7.5** The membrane potential peak [mV], read at the nerve membrane, vs. the maximum principal value of the nominal strains [%] found in the Head Model; (a) and (c) show the potential values during elongation, while (b) and (d) show the potential values after elongation. On the top, (a) and (b), are for the membrane potential peak, read on Fibre#3. On the bottom, (c) and (d), are for the membrane baseline.

To further illustrate how these results, relate to the impact conditions, Appendix C shows results of *PEs* in the Nerve Bundle Model vs. the speed of impact of the Head Model, and the membrane voltage peak and baseline vs. the speed of impact.

## 7.4 Discussion

DAI arises from damage of the white matter following TBI (Ma et al., 2016; Wright and Ramesh, 2012). The current literature on the subject discusses at length the neurological and non-neurological consequences of DAI (Kan et al., 2012; Lajtha et al., 2009; Smith and Meaney, 2000; Wang and Ma, 2010) the need for need for better diagnosis (Hemphill et al., 2015; Lajtha et al., 2009; Ma et al., 2016; Wright and Ramesh, 2012), and the lack of suitable treatments (Hemphill et al., 2015; Lajtha et al., 2009; Wright and Ramesh, 2012).

Within this context, computational modelling can be used to simulate complex anatomical and functional damage induced by TBI at different scales, with the goal of improving the understanding of brain injuries and the quality of clinical care. In this work, induced damage following TBI is simulated at the macroscale by using a Head Model (Horgan and Gilchrist, 2003, 2004), while damage to cellular mechanisms, i.e. the electro-mechanical impairments of diffuse axonal injury (DAI), is simulated by using a Nerve Bundle Model (Cinelli et al., 2017b, 2017d). The use of two independent, although linked, models is needed to have full control over the applied boundary conditions at the different size scales. Investigation of the structural damage caused by strain levels determined during impact at the macroscale is implemented using an estimation of the plastic strain at the nerve membrane, which is the irrecoverable component of the total strain. The corresponding voltage changes simulated in the Nerve Bundle Model are a measure of the functional damage at the axonal level.

The results show that plastic strains found in the Nerve Bundle Model are linearly related to both the nominal strains generated in the white matter of the Head Model during impact, and the impact speed values themselves, see Fig. 7.2 and Fig. 7.4. Although large deformation is assumed in the Head Model, the quasi-static assumption of the Nerve Bundle Model is justified by the linear deformation of the head regions, following impact, see Fig. 7.2 and Section 6.3.

By elongating the bundles at strain levels predicted from simulated frontal head impacts of the Head Model, it is interesting to note that permanent strains at the membrane are higher in the large unmyelinated bundle, while they are lower than 21% in the other Nerve Bundle Models over the range of impact speeds considered, see Fig. 7.4. Following a high speed frontal head impact, the model predicts that mechanical failure may occur in larger unmyelinated nerve bundles, due to the high plastic strain produced at the membrane, see Fig. 7.4 and Fig. 7.5 (a)-(d). In this work, physical disconnection of fibres within the nerve bundle models (or axotomy (Wang et al., 2011)) is not accounted in the simulation for the range of speeds considered. However, this chapter assumes that high plastic strains in the bundle are indicative of disconnection and so, mechanical failure.

Related to this, the functionality of the fibre is also affected by the (axial) component of the total strain, while it also depends on the high number of charges exchanged per unit area (Cinelli et al., 2017b). The *macro-to-micro* link allows for analysing the structural and functional failure in nerve bundles with different calibre, following frontal head impacts. Thus, the permanent alterations of the membrane potential are DAI-induced electrical changes that can be linked directly both to the speeds of impact and to the nominal strain of the white matter.

Deforming the bundle, permanent deformations occur at the nerve membrane and at the Ranvier's node regions of unmyelinated and myelinated nerve fibres, respectively, which in turn change the ionic reversal potentials and consequently the homeostatic gradient of the nerve membrane. The shift of the membrane potential to positive values is proportional to the level of stretch applied to the bundle (Cinelli et al., 2017b) where the ionic gate channels are physically stretched and kept opened by the applied loads. Due to the magnitude of nominal strains applied (beyond the yield strain limit), these structural and functional changes are not reversible after loading for all the conditions considered here. Small fluctuations of the membrane potential around the voltage baseline could be interpreted as the loss of the ability of the membrane to generate an AP, thereby leading to functional failure. The use of the *macro-to-micro* link for analysing functional damage could be thought as an estimation of the cellular functionality following DAI, without the use of invasive devices.

For speed impact values of up to 7.5 m/s, it is found that after loading (i.e. without the elastic component of the total strain) the voltage alterations simulated by the fully coupled Hodgkin and Huxley model (Cinelli et al., 2017b) (see Fig. 3.2) are shown to be near-linearly related with the nominal strains in the Head Model for the small bundles (SBUN and SBMY) and big myelinated bundle (BBMY). A higher order relation is needed to describe the non-linear voltage alterations caused by strain levels beyond the yield strain for the big unmyelinated bundle (BBUN), and for all bundle types during loading.

In contrast to unmyelinated fibres, myelinated fibres preserve the ability to conduct signals even at high deformations applied to the bundle, because the mechanically induced voltage alterations are significant at the Ranvier's node regions only, rather than along the whole fibre length. The myelin layer is thought to protect the fibre (Cinelli et al., 2017e, 2017b, 2017c) by constraining the deformation at the Ranvier's node regions, allowing for a faster recovery of the normal membrane potential baseline value after loading. Therefore, the myelin sheath seems to protect the fibre from mechanical and functional failure. Here, the large myelinated bundle is the only bundle type still able to carry a signal after impact, although there is a significant shift in membrane voltage (and therefore change in reversal potentials) during loading.

As seen in experimental studies (Galbraith et al., 1993; Smith and Meaney, 2000; Smith et al., 1999), strain-rate dependence in elongation is shown to play an important role in understanding damage of axonal cytoskeleton, changes in ionic gating channels and disconnection. Future work can consider further development of the current models to include strain rate dependence in elongation tests at the cellular level, in addition to rotation and acceleration in head impacts. Finally, the inclusion of a more realistic geometry of the

nerve bundle and the inclusion of mechanical anisotropy in the fibre would lead to a more accurate result.

## **7.5 Clinical Applications**

Modelling helps in understanding the complexity of the neural electrical activity when experimental evidence is not enough to investigate biophysical phenomena in nervous cells. Although computational models are very dependent on the final application, the findings can be used both for answering open questions in research and for improving clinical care. From the results shown in Fig. 7.5, it is possible to conclude that the regions of the brain that are less affected by frontal head impacts are those where large myelinated nerve bundles can be found, while regions where the myelin sheath is absent are those more likely to undergo mechanical and functional failure. This suggests that fibre disconnection might be distributed in the brain regions populated by unmyelinated nerve bundles, and its severity can be seen in relation to the velocity of the impact it was caused by, see Fig. 7.4 and 7.5. This conclusion might be of interest for understanding ‘how’, ‘why’ and ‘where’ mechanical and functional failure occurs after frontal head impacts. Thus, these findings may improve diagnosis of diffuse axonal injury as the model indicates the type of nerve fibre (so the corresponding brain region) most likely to be affected by failure, so that the treatment and the long-term effects could be decided and estimated more accurately. Future studies are needed for including nerve fibres of different calibre, as mentioned in Chapter 5, and their orientation as a head impact may not be frontal and may occur under acceleration.

Then, the use of this modelling approach might be used in research and development of medical devices, as neural interfaces, electrodes, and neuromodulation techniques. In the field of neurotechnology, research and devices have been designed with focus on the electrical activity of the nervous cells only. Modelling the induced mechanical effects by applied voltage or current might benefit the safety and the accuracy of a medical device.

## **7.6 Conclusion**

This work reports the results of an investigation of electro-mechanical impairments of DAI, following TBI events of frontal head impacts. The findings of this work could be easily transferable to clinical applications, thanks to the close link between boundary conditions in both models. The main findings can be summarized as:

- At high impact speeds (that cause high nominal strain in the white matter), disconnection of fibres is more likely to occur in large unmyelinated bundles due to the high plastic strains found at the nerve membrane;
- Signal propagation is preserved in the large myelinated bundle;
- There is a linear relation between the generated plastic strain of the nerve bundle model and the impact velocity and the nominal strains of the head model;
- The myelin layer protects the fibre from mechanical failure, preserving its functionalities.

## References Chapter 7

- Alvarez, O., and Latorre, R. (1978). Voltage-dependent capacitance in lipid bilayers made from monolayers. *Biophysical Journal*, 21(1), 1–17. [https://doi.org/10.1016/S0006-3495\(78\)85505-2](https://doi.org/10.1016/S0006-3495(78)85505-2)
- Bain, A. C., and Meaney, D. F. (2000). Tissue-level thresholds for axonal damage in an experimental model of central nervous system white matter injury. *Journal of Biomechanical Engineering*, 122(6), 615–622. <https://doi.org/10.1115/1.1324667>
- Boucher, P. A., Joós, B., and Morris, C. E. (2012). Coupled left-shift of Nav channels: Modeling the Na<sup>+</sup>-loading and dysfunctional excitability of damaged axons. *Journal of Computational Neuroscience*, 33(2), 301–319. <https://doi.org/10.1007/s10827-012-0387-7>
- Cinelli, I., Destrade, M., Duffy, M., and McHugh, P. (2017a). Electro-mechanical response of a 3D nerve bundle model to mechanical loads leading to axonal injury. *International Journal for Numerical Methods in Biomedical Engineering*. <https://doi.org/10.1002/cnm.2942>
- Cinelli, I., Destrade, M., Duffy, M., and McHugh, P. (2017b). Electro-mechanical response of a 3D nerve bundle model to mechanical loads leading to axonal injury. In *Engineering in Medicine and Biology Society (EMBC), 2017 39th Annual International Conference of the IEEE* (pp. 978–981). <https://doi.org/10.1109/EMBC.2017.8036989>
- Cinelli, I., Destrade, M., Duffy, M., and McHugh, P. (2017c). Electro-thermal equivalent 3D finite element model of a single neuron. *IEEE Transactions on Biomedical Engineering*, 9294(99). <https://doi.org/10.1109/TBME.2017.2752258>
- Cinelli, I., Destrade, M., Duffy, M., and McHugh, P. (2017d). Neurotrauma evaluation in a 3D electro-mechanical model of a nerve bundle. In IEEE (Ed.), *International IEEE/EMBS Conference on Neural Engineering, NER* (pp. 513–516). <https://doi.org/10.1109/NER.2017.8008402>
- Cinelli, I., Duffy, M., and McHugh, P. (2015). Thermo-electrical equivalents for simulating the electro-mechanical behavior of biological tissue. In IEEE (Ed.), *Proceedings of the Annual International Conference of the IEEE Engineering in Medicine and Biology Society, EMBS* (Vol. 2015–Novem, pp. 3969–3972). Milan: IEEE. <https://doi.org/10.1109/EMBC.2015.7319263>

- Galbraith, J. A., Thibault, L. E., and Matteson, D. R. (1993). Mechanical and electrical responses of the squid giant axon to simple elongation. *Journal of Biomechanical Engineering*, 115(1), 13–22. <https://doi.org/10.1115/1.2895464>
- Geddes, D. M., Cargill, R. S., and LaPlaca, M. C. (2003). Mechanical stretch to neurons results in a strain rate and magnitude-dependent increase in plasma membrane permeability. *Journal of Neurotrauma*, 20(10), 1039–1049. <https://doi.org/10.1089/089771503770195885>
- Hemphill, M. A., Dauth, S., Yu, C. J., Dabiri, B. E., and Parker, K. K. (2015). Traumatic brain injury and the neuronal microenvironment: A potential role for neuropathological mechanotransduction. *Neuron*, 85(6), 1177–1192. <https://doi.org/10.1016/j.neuron.2015.02.041>
- Horgan, T. J., and Gilchrist, M. D. (2003). The creation of three-dimensional finite element models for simulating head impact biomechanics. *International Journal of Crashworthiness*, 8(4), 353–366. <https://doi.org/10.1533/ijcr.2003.0243>
- Horgan, T. J., and Gilchrist, M. D. (2004). Influence of FE model variability in predicting brain motion and intracranial pressure changes in head impact simulations. *International Journal of Crashworthiness*, 9(4), 401–418. <https://doi.org/10.1533/ijcr.2004.0299>
- Jérusalem, A., García-Grajales, J. A., Merchán-Pérez, A., and Peña, J. M. (2014). A computational model coupling mechanics and electrophysiology in spinal cord injury. *Biomechanics and Modeling in Mechanobiology*, 13(4), 883–896. <https://doi.org/10.1007/s10237-013-0543-7>
- Kan, E. M., Ling, E., and Lu, J. (2012). Microenvironment changes in mild traumatic brain injury. *Brain Research Bulletin*, 87(4–5), 359–372. <https://doi.org/10.1016/j.brainresbull.2012.01.007>
- Lajtha, A., Javitt, D., and Kantrowitz, J. (2009). Handbook of Neurochemistry and Molecular Neurobiology. Brain and spinal cord trauma. (N. Banik & K. R. Swapan, Eds.), *Springer Reference* (3rd Edition, Vol. 281). Springer. <https://doi.org/10.1016/j.jns.2009.03.019>
- Li, M., Zhao, Z., Yu, G., and Zhang, J. (2016). Epidemiology of traumatic brain injury over the world : A systematic review. *Austin Neurology & Neurosciences*, 1(2), 1–14.

- Ma, J., Zhang, K., Wang, Z., and Chen, G. (2016). Progress of research on diffuse axonal injury after traumatic brain injury. *Neural Plasticity*, 2016, 7. <https://doi.org/10.1155/2016/9746313>
- Majdan, M., Plancikova, D., Brazinova, A., Rusnak, M., Nieboer, D., Feigin, V., and Maas, A. (2016). Epidemiology of traumatic brain injuries in Europe: A cross-sectional analysis. *The Lancet Public Health*, 1(2), e76–e83. [https://doi.org/10.1016/S2468-2667\(16\)30017-2](https://doi.org/10.1016/S2468-2667(16)30017-2)
- Mosgaard, L. D., Zecchi, K. a., and Heimborg, T. (2015). Mechano-capacitive properties of polarized membranes. *Soft Matter*, 11(40), 7899–7910. <https://doi.org/10.1039/C5SM01519G>
- Siedler, D. G., Chuah, M. I., Kirkcaldie, M. T. K., Vickers, J. C., and King, A. E. (2014). Diffuse axonal injury in brain trauma : insights from alterations in neurofilaments. *Frontiers in Cellular Neuroscience*, 8(December), 1–10. <https://doi.org/10.3389/fncel.2014.00429>
- Smith, D. H., and Meaney, D. F. (2000). Axonal damage in traumatic brain injury. *The Neuroscientist*, 6(6), 483–495. <https://doi.org/10.1177/107385840000600611>
- Smith, D. H., Wolf, J. A., Lusardi, T. A., Lee, V. M., and Meaney, D. F. (1999). High tolerance and delayed elastic response of cultured axons to dynamic stretch injury. *The Journal of Neuroscience*, 19(11), 4263–4269. Retrieved from <http://www.jneurosci.org/content/19/11/4263.long>
- Tang-schomer, M. D., Patel, A. R., Baas, P. W., and Smith, D. H. (2017). Mechanical breaking of microtubules in axons during dynamic stretch injury underlies delayed elasticity, microtubule disassembly, and axon degeneration. *The FASEB Journal*, 24(5), 1401–1410. <https://doi.org/10.1096/fj.09-142844>
- Wang, H. C., and Ma, Y. Bin. (2010). Experimental models of traumatic axonal injury. *Journal of Clinical Neuroscience*, 17(2), 157–162. <https://doi.org/10.1016/j.jocn.2009.07.099>
- Wang, J. Hamm, R. J., and Povlishock, J. T. (2011). Traumatic axonal injury in the optic nerve: evidence for axonal swelling, disconnection, dieback, and reorganization. *Journal of Neurotrauma*, 28(7), 1185–1198. <https://doi.org/10.1089/neu.2011.1756>

- Wright, R. M. (2012). A computational model for traumatic brain injury based on an axonal injury criterion. *The Johns Hopkins University*. Retrieved from <https://pqdtopen.proquest.com/doc/1041257250.html?FMT=ABS>
- Wright, R.M., and Ramesh, K. T. (2012a). An axonal strain injury criterion for traumatic brain injury. *Biomechanics and modeling in mechanobiology*, 11(1–2), 245–260. <https://doi.org/10.1007/s10237-011-0307-1>
- Yu, N., Morris, C.E., Joós, B. and Longtin, A. (2012). Spontaneous excitation patterns computed for axons with injury-like impairments of Sodium Channels and Na/K pumps. *PLoS Computational Biology*, 8(9). <https://doi.org/10.1371/journal.pcbi.1002664>
- Zhang, Y. P., Cai, J., Shields, L. B. E., Liu, N., Xu, X. M., and Shields, C. B. (2014). Traumatic brain injury using mouse models. *Translational Stroke Research*, 5(1), 454–471. <https://doi.org/10.1007/s12975-014-0327-0>
- Zhang, Keleshian, A. M., and Sachs, F. (2001). Voltage-induced membrane movement. *Nature*, 413(6854), 428–432. <https://doi.org/10.1038/35096578>

## Chapter 8.      **Conclusions and Recommendations**

This chapter summarises and discusses the work presented in this thesis. A summary of the main findings of the technical chapters (from Chapter 3 to Chapter 6) and a discussion on their possible application towards future works are provided.

### **8.1 Thesis Summary**

Finite element modelling is a powerful tool to investigate specific functions of the human body. However, when representing multiphysical phenomena, the high computational costs, due to the simultaneous replication of events in multiple domains, might significantly affect the reliability of the model. Thus, accuracy is often limited by a missing *coupling*, which would allow for the simulation of real-time evidence of cross-linkages between disciplines, based on different principles.

This gap is evident in neural engineering, where published experimental evidence about the *electro-mechanical* nature of the neural activity can no longer be ignored. There, a coupling between electrical and mechanical domains is needed to improve the accuracy of simulations and ultimately the understanding of the nervous system.

In this thesis, a modelling approach is proposed to simulate coupled electro-mechanical phenomena in finite element modelling, replicating the multiphysics underlying the neural activity. Models of 3D nerve fibres and nerve bundles undergo mechanical loads leading to damage, as in the case of injury. Consideration is given to diffuse axonal injury for its clinical relevance. This work intends to show the importance of electro-mechanical neural activity for evaluating functional and structural performance of the nervous cells and its significance to improve clinical diagnosis and treatment.

The coupling is investigated in two steps due to its complexity. As a first step, the use of equivalent physical quantities is discussed in Chapter 3 as the most appropriate way to establish the coupling between mechanical and electrical domains in finite element modelling. In particular, the coupling is based on the Theory of Equivalences that allows the implementation of the non-linear Cable Equation, describing the diffusion of electrical charges across the nerve membrane, by using the Heat Equation. The advantages in simulating the electrical neural activity using a thermal analogy are the three-dimensional representation of the model and the close link with well-established coupled thermo-

mechanical computational modelling tools, available in existing engineering design software. This coupling opens the way to real-time replication of complex non-linear 3D electrical phenomena in software that account for an extensive range of material constitutive relationships, so that results can be extracted at different levels in multiscale finite element models. This approach is proven to represent non-active and also active neural behaviour, including Hodgkin and Huxley dynamics, piezoelectricity and electrostriction. Validation and verification refer to the representation of electrical phenomena within a mechanical domain only (or *1-way* coupling), in relation to the case of a single nerve fibre.

Then, as the second step, this modelling approach is extended to include the impact of mechanical loadings (in particular, the *strain*) on the electrical activity (i.e. *2-way* coupling), so that changes in electrical activity lead to mechanical alterations and vice versa. In Chapter 4, consideration is given to the *strain* component of the applied mechanical loads over the nerve fibre and nerve bundle models. Due to the variations in the strain, the ionic reversal potentials change, and so does the membrane resting potential. The flow of a particular type of ion across the nerve membrane occurs because of the deformation of the nerve membrane layer, the deformation of ionic gate channels within the membrane thickness, and the different membrane resting potential at which there is no net ionic current flow. Thus, this framework is able to simulate a real-time coupled, modulated threshold for spiking activation and independent alteration of the electrical material properties as a function of strain, voltage, space and time. This approach allows us to simulate original results that are difficult to reproduce and detect with the current technology, such as changes in fibre activation due to applied compression or elongation.

The benefits of simulating the multiphysics behind neural activity are clear when non-linear mechanical properties, i.e. plasticity, are here included, as described in Chapter 5. With the assumption that intracellular media, nerve membrane, Ranvier's node regions and myelin all undergo similar plastic behaviour during loading, the role of permanent deformation on the electrical activity uncovers important information about the features of unmyelinated and myelinated fibres. Thanks to a 3D electro-mechanical analysis, the myelin sheath around myelinated fibre is shown to have important mechanical properties besides being a piecewise constant insulating layer along the fibre length. The myelin layer scatters the plastic strain around the fibre preserving its functionality, by distributing the applied strain within the bundle rather than along the fibre length. So, myelinated fibres are found to be more resistant to elongation than unmyelinated fibres, regardless of the fibre and bundle calibres. Additionally, the structural integrity of the myelinated fibre is affected more by elastic strain than by plastic strain. In contrast, unmyelinated fibres are shown to be more sensitive to plastic strains that induce changes in a higher number of

ionic channels distributed along the fibre length in the nerve membrane layer. In the end, nerve fibres are found to be more resistant to compression than to elongation, regardless of their type and calibre.

Understanding the consequences of structural and functional damage of the nervous system is fundamental for clinical practice, as in the case of brain injuries. Especially, in relation to diffuse axonal injuries, this framework could be used as a computational tool to improve clinical diagnosis and treatment by estimating cellular functionality, without the use of invasive medical devices. Chapter 6 shows that knowing the speed of frontal head impacts helps with finding the level of plastic deformation a nerve bundle undergone during impact. Quantifying the level of permanent deformation at the microscale is important for estimating the functional damage in relation to the intensity of an injury. In particular, a near-linear relation was found between the strain at the tissue level in the brain regions (or the speed values of impact), and the plastic strain at microscale, in regions where small bundles or large myelinated bundles only are present. Then, the strain at the tissue level in the brain are in a near-linear relation with the membrane potential peak in fibres and bundles, with the exception of large unmyelinated bundles.

The alteration in magnitude of the membrane potential peak from the baseline may be considered as an estimation of the cellular functionality. When membrane peak and membrane baseline have similar values, it is an indication that the neural electrical activity is strongly affected by damage, which alters the integrity of the nerve membrane. In this case, the physiological concentration of potassium, sodium and leak ions cannot be reached because the ionic gate channels are kept open by the induced damage at the nerve membrane, compromising the excitability of the nerve membrane.

Identifying quantities in a near-linear fit is important for diagnosing injuries in relation to the part of the brain that is thought to be more affected than other regions, following frontal head impacts. This might be considered as an indicator of the area where diffuse axonal injury would more likely be initiated. Then, consequently, this might also contribute to improving the accuracy of the diagnosis.

## **8.2 Recommendations for Future Research**

The Theory of Equivalence proposed here is a modelling approach that is shown to be relevant in neural engineering for revealing electro-mechanical phenomena accompanying the neural activity. However, a similar approach could have other applications within the biomedical field, as in modelling the membrane motor in the cochlear outer hair cell or in scaling up to the tissue level as an alternative way to model the electro-cardio mechanics

(Baillargeon et al., 2014; Clayton et al., 2011; Crozier et al., 2016). Additionally, it could also be used in design and optimization of medical devices and material characterization studies.

Furthermore, the theory is relevant for any application and in any field where the electro-quasi static assumption applies; that is when the electric energy density exceeds the magnetic energy, and the electric field is conservative and equal to the Coulomb field (Bossetti et al., 2008; Bédard and Destexhe, 2008; Larsson, 2006). Thence, the current Theory of Equivalence includes capacitive effects only, and neglects the inductive effects. Larsson (2006) discusses the different quasi-static theories (electro-quasi-static, magneto-quasi-static and the Darwin model) as intermediate levels of representation between statics and general electrodynamics, described by the full set of Maxwell's Equations. Thus, it may be more informative to base the theory on the Darwin model, as described in the paper (Larsson, 2006), to account for both capacitive and inductive effects, as a step forward for the inclusion of magnetic induction.

The work performed in this thesis combines the Hodgkin and Huxley model, which won the 1963 *Nobel Prize in Physiology or Medicine*, with other experimental evidence relative to neural activity. Up to now, it seems that a unified theory embracing all the electro-thermo-mechanical features of the neural activity has not been published. At the moment, the work reported in this thesis could be considered a most complete modelling approach for electro-mechanics. However, a further evaluation of the electro-mechanical neural activity should be carried out again when a unified theory, including the coupled thermodynamics, will be established. Additionally, future works could include a finite element implementation of the soliton model for nerve pulse propagation, with lipid fluid to gel transition of the nerve membrane and coupled release of heat (Heimburg and Jackson, 2007). This would require the use of other user-defined subroutines in Abaqus CAE/Explicit.

In view of the assessment of a novel coupling approach, this work focuses on the inclusion of electrical activity and the electro-mechanical coupling itself under steady-state conditions, neglecting complex constitutive models of material-transitional phase's characterization. Therefore, another possible future research avenue is the inclusion of the microscopic fluid-like viscoelastic mechanical behaviour of the membrane, for a more realistic description of the mechanical dependencies between the outer and inner sides of the nerve membrane and the surrounding media. So, rate-dependent loading conditions could be included to study elastic recovery of the initial pre-stretched geometry, undulating distortions along the fibre length, recovery of the pre-stretched geometry and the corresponding damage. The inclusion of dynamic loading conditions might be significant in studies about axonal growth, capillary perfusion in nerve bundle and axonal elongation.

Again, these potential studies may require the use of other user-defined subroutines in Abaqus, and the use of Abaqus Explicit for the inclusion of large deformation.

Then, the inclusion of a more realistic geometry could tackle the electro-mechanical effects of fibre alignments in different directions, bundles made of fibres with different calibre and type, and bundles made of a higher number of fibres. Additionally, the activation of multiple fibres could also be included in studies for a more realistic representation of the signal propagation process.

Eventually, although the use of two independent models is needed to describe the *macro-to-micro* link in brain injuries, future studies may extend the electro-mechanical coupling to the tissue level through homogenization, by describing the macroscale electro-mechanics of tissue resulting from the activity of a high number of fibres, and so neglecting the modelling of single nerve membrane layers. Furthermore, the application of this homogenised modelling approach could be included in the grey and white matter regions of a head model, to simulate the distribution of the electro-mechanical waves during local compression, blast, or loading involving accelerations and stress gradients.

The results reported in this thesis may provide a support for other computational neuroscientific approaches, such as neural network and brain mapping. When investigating functional and structural alterations induced by impact or diseases, consideration of other computational studies may help to clarify the physics of the phenomenon and the boundary conditions.

### **8.3 Conclusions and Final Remarks**

The focus of this thesis is on the development of a computational model that can be used to improve the understanding of the complex biophysical phenomena coupled to neural electrical activity, with the ultimate goal of increasing the awareness of neural electro-mechanics.

This is accomplished by establishing a coupling in finite element modelling which is tested in 3D single neuron models and 3D nerve bundle models, made of unmyelinated and myelinated nerve fibres. Then, this framework is also tested in simulated frontal head impacts, uncovering a relation that can be of interest in diagnosis of diffuse axonal injuries.

The following specific conclusions can be drawn from the work performed in this thesis:

- By simulating thermal equivalent electrical activity, the physics of the electrical conduction is not altered in a passive and active nervous fibre.

- The signal propagation in time, distribution in space and signal magnitude depends on the voltage and total strain applied during fibre excitation;
- The myelin layer scatters the plastic strain around the fibre, preserving its functionality under mechanical loadings;
- Myelinated fibres are found to be more resistant to elongation than unmyelinated fibres;
- Nervous fibres are found to be more resistant to compression than elongation;
- During elongation, mechanical failure occurs for lower strain levels in larger bundles than in small bundles;
- Following a high-speed frontal head impact, large unmyelinated bundles undergo higher plastic deformation, and so are thought to be the first undergoing disconnection.

---

## References Chapter 8

- Baillargeon, B., Rebelo, N., Fox, D. D., Taylor, R. L., and Kuhl, E. (2014). The living heart project: A robust and integrative simulator for human heart function. *European Journal of Mechanics, A/Solids*, 48(1), 38–47. <https://doi.org/10.1016/j.euromechsol.2014.04.001>
- Bédard, C., and Destexhe, A. (2008). A modified cable formalism for modeling neuronal membranes at high frequencies. *Biophysical Journal*, 94(4), 1133–1143. <https://doi.org/10.1529/biophysj.107.113571>
- Bossetti, C. A., Birdno, M. J., and Grill, W. M. (2008). Analysis of the quasi-static approximation for calculating potentials generated by neural stimulation. *Journal of Neural Engineering*, 5(1), 44–53. <https://doi.org/10.1088/1741-2560/5/1/005>
- Clayton, R. H., Bernus, O., Cherry, E. M., Dierckx, H., Fenton, F. H., Mirabella, L., Zhang, H. (2011). Models of cardiac tissue electrophysiology: progress, challenges and open questions. *Progress in Biophysics and Molecular Biology*, 104(1–3), 22–48. <https://doi.org/10.1016/j.pbiomolbio.2010.05.008>
- Crozier, A., Augustin, C. M., Neic, A., Prassl, A. J., Holler, M., Fastl, T. E., Plank, G. (2016). Image-based personalization of cardiac anatomy for coupled electromechanical modeling. *Annals of Biomedical Engineering*, 44(1), 58–70. <https://doi.org/10.1007/s10439-015-1474-5>
- Heimburg, and Jackson. (2007). The thermodynamics of general anaesthesia. *Biophysical Journal*, 92(9), 3159–3165. <https://doi.org/10.1529/biophysj.106.099754>
- Larsson, J. (2006). Electromagnetics from a quasistatic perspective. *American Journal of Physics*, 75(3). <https://doi.org/10.1119/1.2397095>

## Appendix A

This Appendix is published as *Supplementary Material* of Cinelli, I., M. Destrade, M. Duffy, and P. E. McHugh. 2017. “Electro-thermal equivalent 3D Finite Element Model of a Single Neuron”, *IEEE Transaction on Biomedical Engineering*, DOI 10.1109/TBME.2017.2752258, see Chapter 3.

### A.1. Subthreshold Model

In Fig. A. 1 (a) and (b), a uniform current density boundary condition, Eq. 3.7, ( $J(2) = 5000 \mu\text{A}/\text{m}$ ) with Gaussian distribution, Eq. 3.7, was applied at the ECM ( $s = 10 \mu\text{m}$ ), refer to (Tahayori et al., 2012). The voltage distribution in the cylinder in the axial direction is shown in Fig. A. 1 (b), where again excellent agreement is confirmed with the analytic solution.

The thickness of the membrane has negligible influence on the results for voltage and current boundary conditions (Tahayori et al., 2012), see Fig. A. 2.

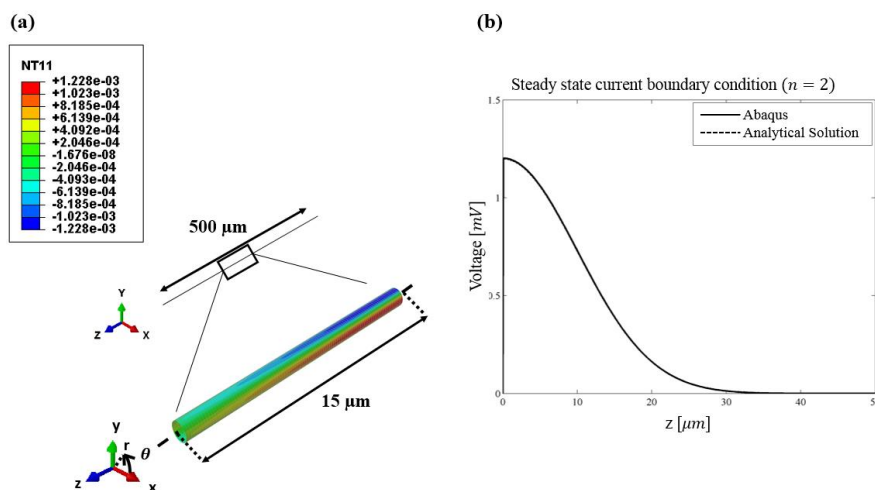


**Fig. A. 1** Current boundary condition. (a) Spatial variation of the membrane voltage [V], here NT11, in steady state ( $\omega = 0$ ) is shown for  $n = 2$  (Tahayori et al., 2012). In (b), the voltage distribution in the axial direction at the membrane layer, at  $x = 1 \mu\text{m}$ ,  $y = 0 \mu\text{m}$ , from  $z = 0 \mu\text{m}$  to  $z = 50 \mu\text{m}$ . Here  $J(2) = 5000 \mu\text{A}/\text{m}$  and  $s = 10 \mu\text{m}$  (Tahayori et al., 2012), see Eq. 3.6 and Eq. 3.7.

## A.2. Active Membrane Model

The trans-membrane potential is first analysed using the passive RC material model in the subthreshold regime, and then as an AP in the upper-threshold regime, using the Hodgkin and Huxley model (Hodgkin and Huxley, 1952), see Section 3.2.4-3.2.5. This model assumes that sodium and potassium ion fluxes are independent of each other (Plonsey and Barr, 2007; Hodgkin and Huxley, 1952).

The behaviour of the membrane can be examined in terms of the behaviour of individual ion channels, and then as the summation of the behaviour of a large number of ion channels, through the equation provided by Hodgkin and Huxley (Hodgkin and Huxley, 1952). The dynamics of voltage-gated channels is described by the ion conductance variables of sodium, potassium and leak ions ( $\bar{g}_K, \bar{g}_{Na}, \bar{g}_l$ ), respectively, that quantify the proportion of the particles on one side of the membrane from their resting potential ( $V_K, V_{Na}$  and  $V_l$ ) (Hodgkin and Huxley, 1952). Then, the total change in membrane conductance due to gating activation depends on the sum of each voltage-gated channel (Hodgkin and Huxley, 1952).

The current carried by ions crossing the membrane,  $I_{ionic}$ , see Eq. A. 1, is the total contribution of each of the ionic fluxes, where  $V_K, V_{Na}$  and  $V_l$  are the equilibrium potential for potassium, sodium and leak ions (Hodgkin and Huxley, 1952). Additionally, Eq. A. 1 is the contribution of ions charging the membrane capacitor,  $I_c$ , see Eq. A. 2 and Eq. A. 3.

In order to selectively measure each constituent current contribution (i.e.  $I_{ionic}$  and  $I_c$ ) to the total membrane current,  $I_m$ , see Eq. A. 3, the activation mechanism is modelled as if it is accomplished by both the voltage clamp and space clamp measurement procedure, as can be seen in the paper (Hille, 1977). A detailed description of the experiment can be found in (Plonsey and Barr, 2007; Hille, 1977; Hodgkin and Huxley, 1952).

In the voltage clamp procedure, current source supplies two electrodes (or axial wire or microelectrode) for voltage recording, placed at diagonally opposite sides of the membrane or inside the axon (Plonsey and Barr, 2007; Hille, 1977; Hodgkin and Huxley, 1952).

The trans-membrane voltage is maintained at some constant preselected value and the current, flowing between these electrodes, is measured (Hille, 1977; Hodgkin and Huxley, 1952). The voltage clamp opens the ionic gates generating a current flow in the membrane ( $I_m$ ) to maintain the clamped value. In the general case,  $I_m$  is proportional to the second derivative of the voltage with axial distance (from the point of stimulus). In Eq. A. 3,  $I_m$  is composed solely of  $I_{ionic}$  because  $I_c$  is zero when the trans-membrane voltage is constant (Plonsey and Barr, 2007; Hille, 1977; Hodgkin and Huxley, 1952; Meffin et al., 2012), see Eq. A. 2.

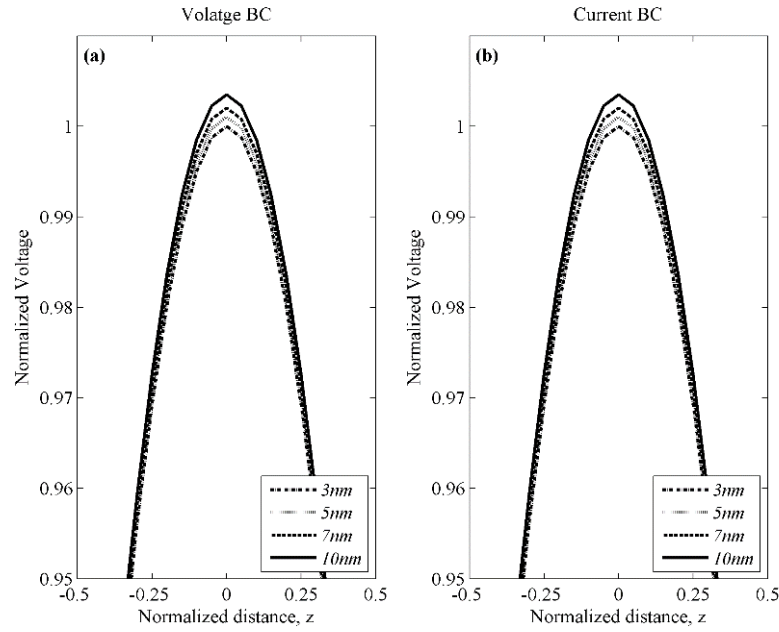


**Fig. A. 2** Normalized voltage taken at membrane, with voltage and current boundary along the  $z$  –axis of the nerve cell model with membrane thicknesses equal to 3, 5, 7 and 10  $nm$ .

In the space clamp procedure, a thin stimulation electrode (axial wire) is placed along the centreline of the axon, which is simultaneously stimulated throughout the entire length by a current source,  $I_s$ , (Plonsey and Barr, 2007; Hille, 1977; Hodgkin and Huxley, 1952). This procedure ensures full uniformity, where there are no potential gradients in the axial direction at any time and no radial current in the membrane after the stimulus, i.e.  $I_m$  is zero (Plonsey and Barr, 2007; Hille, 1977; Hodgkin and Huxley, 1952), and  $I_c$  is equal and opposite to  $I_{ionic}$ . In contrast, during the stimulus,  $I_s$  is equal to the applied stimulus current,  $I_s$ , (Plonsey and Barr, 2007) and the  $I_c$  can be calculated from Eq. A. 2.

$$I_{ionic} = \bar{g}_K n^4 (V - V_K) + \bar{g}_{Na} m^3 h (V - V_{Na}) + \bar{g}_l (V - V_l) \quad \text{Eq. A. 1}$$

$$I_c = C_M \frac{\partial V}{\partial t} \quad \text{Eq. A. 2}$$

$$I_m = I_c + I_{ionic} \quad \text{Eq. A. 3}$$

### A.3. Validation of the Active Membrane Model

The implementation of the Hodgkin and Huxley model successfully predicts the results for voltage clamp and space clamp experiments (Plonsey and Barr, 2007; Hodgkin and Huxley, 1952), which are the main procedures to experimentally evaluate and characterise

the electrophysiological behaviour of a variety of excitable cells (Hille, 1977; Hodgkin and Huxley, 1952).

The active behaviour of the membrane is investigated using the axisymmetric model of the nerve cell (see Fig. 2), where longitudinal uniformity of potential at each time is assumed. The voltage clamp and space clamp procedures are used to validate the implementation of the Hodgkin and Huxley model (Hodgkin and Huxley, 1952), and results are shown in Fig. A. 3 and Fig. A. 4, respectively. The magnitude of the input stimulus is chosen to increase the trans-membrane potential from the resting potential,  $\sim -60\text{ mV}$ , to an upper-threshold stimulation after 4 ms, that is when the trans-membrane potential is greater than  $-55\text{ mV}$  (Hodgkin and Huxley, 1952).

The voltage clamp procedure is carried out with a clamped voltage of  $60\text{ mV}$  in Fig. A. 3 (a) - (e), and  $80\text{ mV}$  in Fig. A. 3 (f) - (j). The results can be compared with (Plonsey and Barr, 2007; Hodgkin and Huxley, 1952). The ionic fluxes of the Hodgkin and Huxley dynamics are activated thanks to the clamped voltage, which forces the opening of selective ion channels during the measurement, see Fig. A. 3 (b), (g). Then, the changes in  $g_K$  and  $g_{Na}$ , Fig. A. 3 (c) and (h), correspond closely to the measured values (Hodgkin and Huxley, 1952). The changes in the  $I_c$ , Eq. A. 2, and  $I_{ionic}$ , Eq. A. 1, are dependent on the magnitude of the input as is shown in (Hodgkin and Huxley, 1952), see Fig. A. 3 (d) and (i). In contrast, Fig. A. 3 (e) and (j) shows that  $I_c$  is maximum during the trigger of the clamped voltage and remains close to zero during a constant trans-membrane potential.

In the space clamp procedure,  $I_m$  is equal to the applied stimulus current,  $I_s$ , for  $0.2\text{ ms}$  (Plonsey and Barr, 2007) here  $I_s$  is set at  $0.06$ , Fig. A. 4 (a) - (e), and  $0.18\text{ mA cm}^{-2}$ , Fig. A. 4 (f) - (j). The results can be compared with (Plonsey and Barr, 2007; Hille, 1977). During the stimulus, the membrane is charged, and the trans-membrane potential is depolarised. This leads to the opening of the ion channels, see Fig. A. 4 (b) and (g). The  $g_K$  and  $g_{Na}$  rise rapidly, due to the fast activation, and relax slowly to the resting state as a result of their kinetics, Fig. A. 4 (c) and (h). The current pulse strengths of the ionic fluxes,  $I_{Na}$  and  $I_K$ , through the membrane, and the generated  $I_{ionic}$ , are dependent on the magnitude of the input, Fig. A. 4 (d) and (i). The resulting  $I_c$  is shown in Fig. A. 4 (e) and (j).

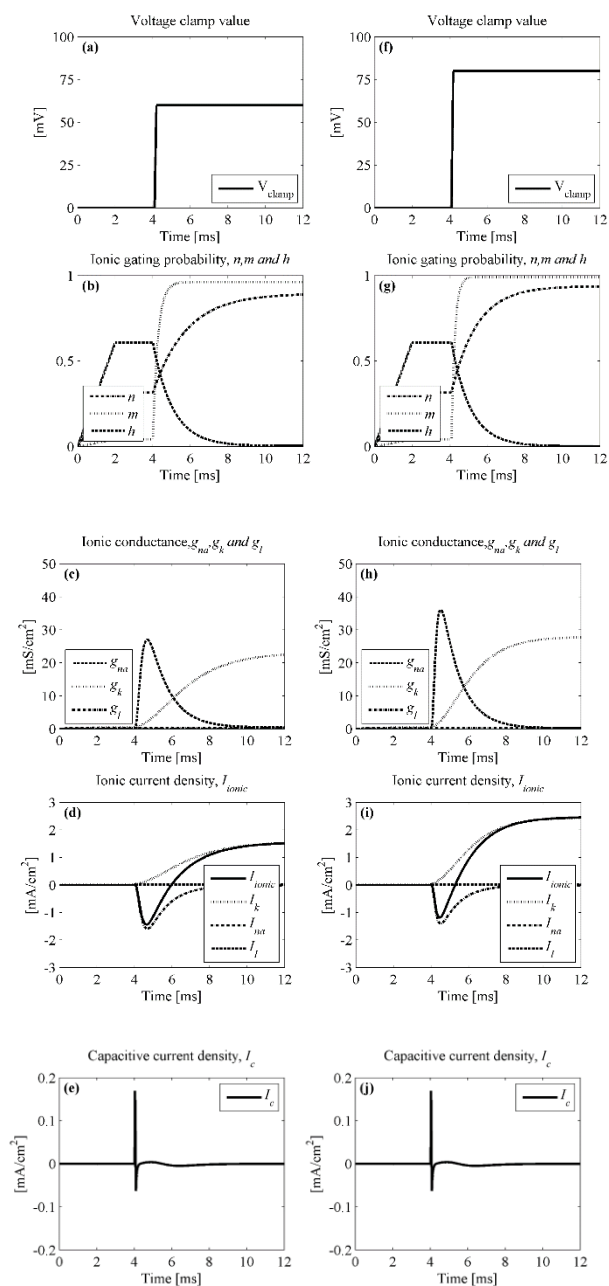


**Fig. A. 3** Voltage clamp procedure with 60 mV (from (a) to (e)) and 80 mV (from (f) to (l)) clamped voltage. The results are shown for clamped voltage as input in (a) and (f); the dynamics of gating activation (no units) in (b) and (g); sodium and potassium conductance in (c) and (h); sodium, potassium and membrane currents in (d) and (i); and capacitive current in (e) and (j). Currents are in [mA/cm<sup>2</sup>].

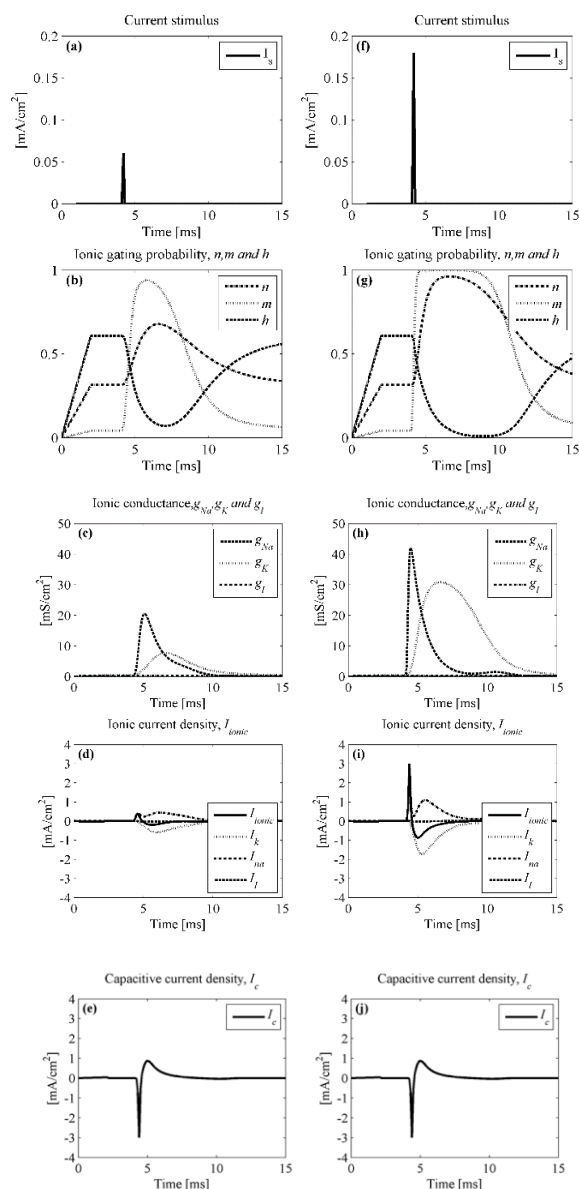


**Fig. A. 4** Space clamp procedure with 6 (from (a) to (e)) and 18 mA cm<sup>-2</sup> (from (d) to (j)) current stimulus of 0.2 ms each. The results are shown for current stimulus as input in (a) and (f); the dynamics of gating activation (no units) in (b) and (g); sodium and potassium conductance in (c) and (h); sodium, potassium and membrane currents in (d) and (i); and capacitive current in (e) and (j). Currents are in [mA/cm<sup>2</sup>].

---

## References Appendix A

- Hille, B. (1977). Ionic basis of resting and action potentials. In *Comprehensive Physiology* (pp. 99–136). Washington, D.C. <https://doi.org/10.1002/cphy.cp010104>
- Hodgkin, A. L., and Huxley, A. F. (1952). A quantitative description of membrane current and its application to conduction and excitation in nerve. *Journal of Physiology*, 117, 500–544. [https://doi.org/10.1016/S0092-8240\(05\)80004-7](https://doi.org/10.1016/S0092-8240(05)80004-7)
- Meffin, H., Tahayori, B., Grayden, D. B., and Burkitt, A. N. (2012). Modeling extracellular electrical stimulation: I. Derivation and interpretation of neurite equations. *Journal of Neural Engineering*, 9(6), 65005. <https://doi.org/10.1088/1741-2560/9/6/065005>
- Plonsey, R., and Barr, R. C. (2007). *Bioelectricity: A quantitative approach*. (Springer, Ed.), *Bioelectricity: A Quantitative Approach* (Third Edit). Springer. <https://doi.org/10.1007/978-0-387-48865-3>
- Tahayori, B., Meffin, H., Dokos, S., Burkitt, A. N., and Grayden, D. B. (2012). Modeling extracellular electrical stimulation: II. Computational validation and numerical results. *Journal of Neural Engineering*, 9(6), 65006. <https://doi.org/10.1088/1741-2560/9/6/065006>

---

## Appendix B

This Appendix was presented as poster the Engineering in Medicine and Biology Society (EMBC), 2016 38th Annual International Conference of the IEEE, see Posters.

### B.1. Myelinated Fibre

Chapter 3 discusses the use of electro-thermal equivalences for an unmyelinated nerve fibre with subthreshold and upper-threshold stimuli. Here, the use of electro-thermal equivalences in three different 3D myelinated nerve models is shown.

Myelinated axons can be represented as cylindrical volume conductors where conductive regions (Ranvier's nodes) are alternated with insulating regions over the whole length of the fibre (Einzigler et al., 2005), see Fig. 2.1. The conduction of signals occurs at the Ranvier's nodes only, coincident with the regions of maximum conductivity (D.M. Durand, 2000; Rall, 1977), see Fig. 2.1. The propagation speed is much higher in myelinated axons than in unmyelinated axons because the charges travel along the fibre skipping the insulating regions, rather than being exchanged all along the nerve membrane (D.M. Durand, 2000; Rall, 1977), see Fig. 2.1. Due to the insulation sheath of myelin around the nerve fibre, the flow of current through the membrane decreases because the membrane capacitance is smaller (D.M. Durand, 2000; Rall, 1977).

Previous studies have already shown the use of the Cable Equation for describing the charge flow in myelinated axons (D.M. Durand, 2000; Einzigler et al., 2003b). First, equivalent forms of the Cable Equation have been investigated extensively for electrical stimulations of composite axons to derive a macroscopic dynamic model using a homogenisation technique (Basser, 1993; D.M. Durand, 2000). Second, further studies about the generalized transmission-line and Cable Equation models at the micro-scale, show that the flow of charges in myelinated axons is equivalent to the conduction in an unmyelinated fibre where an average membrane conductance and an extended source replace the piecewise constant membrane conductivity profile (Einzigler et al., 2005). Then, a further mathematical analysis shows the validity of the generalized Cable Equation model in subthreshold and upper-threshold stimuli (associated with the HH dynamics) (Einzigler et al., 2005).

Due to the use of the electro-thermal equivalences, three modelling approaches have been chosen to replicate the flow of charges in a 3D heterogeneous conductor, allowing for the equivalent use of the Cable Equation (Einzigler et al., 2005). The approaches are:

(A) Similarly to the histologic section, the myelin is modelled as an external layer all around the axon, and it has a finite thickness, see Fig. B. 1.

(B) The physical extension of the myelin layer is neglected, and the axon is surrounded by a unique layer (i.e. central section). This is periodically partitioned as a heterogeneous conductive layer where the myelin sheath regions have the same thickness of the nerve membrane. Hence, the central section is periodically portioned in two regions with different electrical conductivity

(C) The piecewise conductive regions are implemented through the user-defined subroutine UMATHT, where the conductivity can be coded as periodic function without physically partitioning the central section layer.

## B.2. Method

### B. 2.1. Geometry and Material Properties

A cylindrical section of an axon is considered. It consists of an ICM, a central section (that is the nerve membrane or a hybrid region) and ECM, see Fig. B. 1. The radius of ICM, central section and ECM are  $0.477 \mu m$ ,  $0.480 \mu m$  and  $0.500 \mu m$  respectively. The length of the cylindrical model is chosen to be at least ten times the electronic length constants (Tahayori et al., 2012), here  $10 \mu m$ .

The size of conductive section is chosen within the range of physiological values (Basser, 1993; Einziger et al., 2005; Rall, 1977) for a necessary comparison with the analytical solutions (Cinelli et al., 2015b; Einziger et al., 2005). The distance between two adjacent Ranvier's nodes is  $L_p = 1 \mu m$  and its width is  $L_r = 0.002 \mu m$  (Einziger et al., 2005; Rall, 1962), see Fig. B. 1 (a) and (b) for comparison of a myelinated and unmyelinated neurite. In particular,  $L_r/L_p$  is equal to 0.002 and  $L_p/L_c$ , is equal to 1 where  $L_c$  is the characteristics length constant, here equal to  $1 \mu m$  (Einziger et al., 2005), see Fig. B. 1. Referring to the three-modelling approach, details about the geometry for each of them are listed below:

(A) In the 3D myelinated nerve model (MNM), a myelin sheath encloses the ICM and the central section, which coincides with the nerve's membrane. The ratio of the inner diameter of the axonal membrane and the outer diameter of the myelin sheath was equal to 0.7 (Basser, 1993; D.M. Durand, 2000). In order to create the periodic membrane conductivity profile, a physical partition of the myelin layer was performed throughout the length of the fibre (Einziger et al., 2005), see Fig. B. 1 (a).

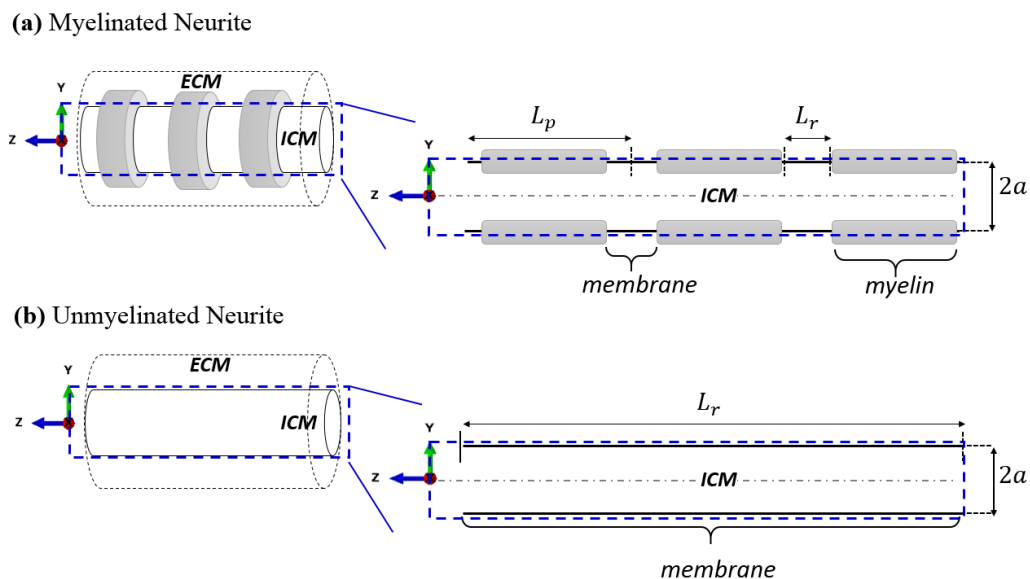


**Fig. B. 1** Cross sections of a general representation of myelinated (Einziger et al., 2005) and unmyelinated (Cinelli et al., 2015c) fibre, respectively in (a) and (b). The periodic black sections in (a) along the length of the fibre ( $z$ -axis) are the myelinated units, instead the region with maximum conductivity are labelled with  $L_r$ , see (a) and (b). Here  $L_p = 1$  and its width is  $L_r = 0.002$  (Einziger et al., 2005). The radius of the neurite (axoplasm and central section) is indicated with the letter  $a$ .

(B) In the mixed 3D myelinated nerve model (M-MNM), the flow of current is evaluated in a 3-layer model where the myelin thickness coincides with the membrane thickness and the central section is physically partitioned, as it is shown in Fig. B. 1 (a). The use of the Cable Equation in myelinated fibre is investigated analytically by assigning different conductivity values at regularly spaced intervals within the same layer, which correspond to the membrane's thickness (Einziger et al., 2005).

(C) An axisymmetric myelinated nerve model (A-MNM) then simulates the flow of charges through a 3-layer fibre, where the thickness of the myelin sheath is neglected. Here, the periodic profile is implemented through the user defined subroutine UMATHHT assigned to the central section, see Fig. B. 1 (b). Its material properties have been changed over the fibre length for different values of  $L_p$  and  $L_r$ , without partitioning the section. The central section could be thought of as a hybrid-membrane region where at the  $L_p$  sections it has myelin properties, while at the  $L_r$  section having the membrane properties. In this way, the activation function is implemented through the UMATHHT, so the extended source response can be analysed in an equivalent unmyelinated neurite through the Heat Equation (Cinelli et al., 2015b; Einziger et al., 2005).

### B. 2.1. Mesh

As shown in Fig. B. 2 the mesh density changes through the thickness of the intracellular media: the inner core was partitioned with a coarse mesh of the wedge element type, and from a radius of  $0.2385 \mu\text{m}$  outwards (that is half of the ICM radius), the mesh is more regular and dense with hexahedral elements. A higher number of elements were assigned to the regions where higher levels of charge are exchanged, that is the central section and the outer radial half of the ICM. The MNM is made by 129528 nodes and 124248 DCC36.5D elements. Each  $L_r$  section consists of 4 nodes with minimum element length of  $6.67 \cdot 10^{-4} \mu\text{m}$ . The A-MNM is made by 180036 nodes and 175000 DCCAX4D elements, where  $1.5 \cdot 10^{-3} \mu\text{m}$  is the minimum element size. In this case, all the central section has been partitioned with the minimum element size due to the ratio  $L_r/L_p = 0.002$ . The user-defined subroutines allows both  $L_c$  and the ratio  $L_p/L_c = 1$  to be easily changed. Instead the M-MNM has 116508 nodes and 110322 DCC36.5D elements with  $4.00543 \cdot 10^{-4} \mu\text{m}$  minimum element size. Finally, 98064 nodes and 90240 DCC36.5D elements are used in the nerve bundle model, where the minimum element size coincides with the membrane layers.

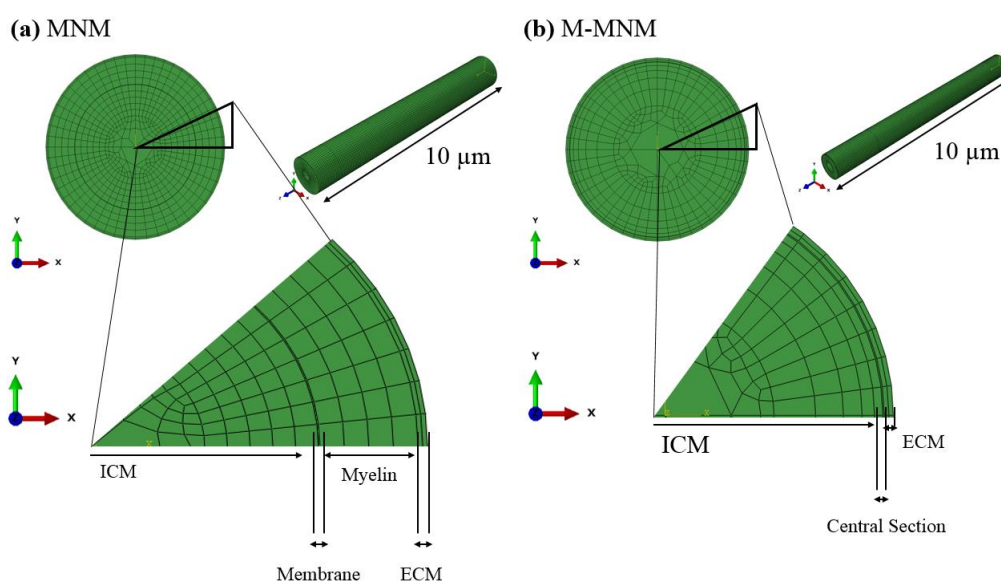


**Fig. B. 2** In (a) and (b), a general and a focus view of the 4-layers MNM and 3-layers M-MNM. In the MNM, the myelin sheath is a solid part with periodic profile around the membrane, instead in the M-MNM the central sections have been partitioned at regularly space intervals with conductive and isolating properties.

## B. 2.2. Boundary Conditions

Assuming an infinite ECM conductivity, a concentrated heat source, placed at half of the ICM radius, resembles an induced current flow decreasing along the fibre length as an exponential function, like a conventional unmyelinated fibre (Einzigler et al., 2005). In Fig. B. 3, the transmembrane potentials are calculated using a point source assuming a magnitude equal to  $2 \cdot 10^{-11}$  A (Einzigler et al., 2005).

## B.3. Results

In Fig. B. 3 shows the analytical verification of charge flow in a heterogeneous composite volume conductor, by using the electro-thermal equivalences. As shown in In Fig. B. 3, an internal localized charge (placed at midway intracellularly) generates an exponential decrease of charges along the membrane length in the M-MNM. In the MNM the charges are more quickly lost along the section because the resistivity per unit length is distributed along the whole fibre length (see contrast, in the A-MNM, the charge reflection at the axis of symmetry leads to an overestimation of the transmembrane potential along the length).

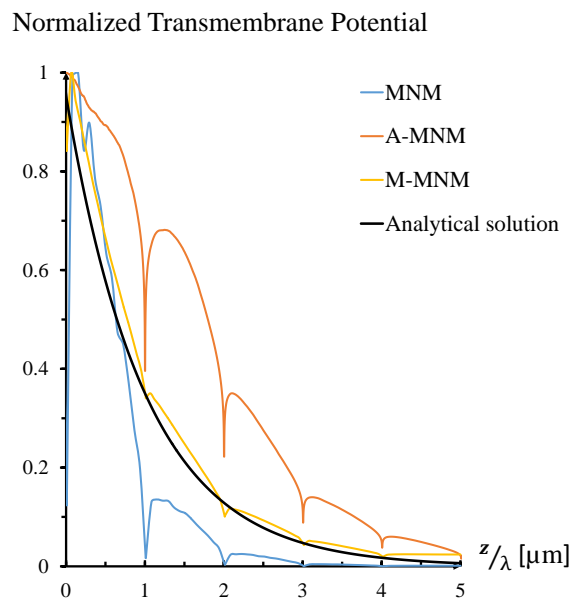


**Fig. B. 3** In (a) a focus view of the normalized transmembrane potential over  $5 \mu m$  of the whole fibre length for the MNM, A-MNM and M-MNM. The results are compared with the analytical solution for a point source (Einzigler et al., 2005). In (b) and (c) the contour plots of voltage and current density in the M-MNM in the central section.

---

## References Appendix B

- Basser, P. J. (1993). Cable equation for a myelinated axon derived from its microstructure. *Medical & Biological Engineering & Computing*, 31 Suppl(AUGUST 1993), S87–S92. <https://doi.org/10.1007/BF02446655>
- Cinelli, I., Duffy, M., and McHugh, P. E. (2015). Thermo-electrical equivalents for simulating the electro-mechanical behavior of biological tissue. In IEEE (Ed.), *Proceedings of the Annual International Conference of the IEEE Engineering in Medicine and Biology Society, EMBS* (Vol. 2015–Novem, pp. 3969–3972). Milan: IEEE. <https://doi.org/10.1109/EMBC.2015.7319263>
- Durand, D. M. (2000). Electric Stimulation of Excitable Tissue. In E. J. D. Bronzino (Ed.), *The Biomedical Engineering Handbook: Second Edition*. (Vol. 42, p. 23). Boca Raton: CRC Press LLC, 2000. <https://doi.org/10.1201/9781420049510>
- Einzig, P. D., Livshitz, L. M., Dolgin, A., and Mizrahi, J. (2005). Novel cable equation model for myelinated nerve fiber. *IEEE Transactions on Biomedical Engineering*, 52(10), 112–115. <https://doi.org/10.1109/CNE.2003.1196769>
- Einzig, P. D., Livshitz, L. M., Dolgin, A., and Mizrahi, J. (2003). Novel cable equation model for myelinated nerve fiber. *First International IEEE EMBS Conference on Neural Engineering, 2003. Conference Proceedings.*, 112–115. <https://doi.org/10.1109/CNE.2003.1196769>
- Rall, W. (1962). Electrophysiology of a dendritic neuron model. *Biophysical Journal*, 2(2), 145–167. [https://doi.org/10.1016/S0006-3495\(62\)86953-7](https://doi.org/10.1016/S0006-3495(62)86953-7)
- Rall, W. (2011). Core conductor theory and cable properties of neurons. In *Comprehensive Physiology - Handbook of physiology, the nervous system, cellular biology of neurons* (Vol. Chapter 3, pp. 39–97). Washington, D.C.: *Wiley Online Library*. <https://doi.org/10.1002/cphy.cp010103>
- Tahayori, B., Meffin, H., Dokos, S., Burkitt, A. N., and Grayden, D. B. (2012). Modeling extracellular electrical stimulation: II. Computational validation and numerical results. *Journal of Neural Engineering*, 9(6), 65006. <https://doi.org/10.1088/1741-2560/9/6/065006>

## Appendix C

This Appendix refers to Chapter 7. Fig. C. 1 shows the near-linear relation between the maximum principal value of the plastic strains [%] in the Nerve Bundle Model and the speed impact values,  $v$  [m/s], used in the frontal head impacts of the Head Model. Here, the nominal strains in the white matter of the Head Model (17.1 %, 23.7 %, 32.3 %, 42.5 %, 46.2 % and 48.7%) correspond to the speed impact values (2.5, 3.5, 4.5, 5.5, 6.5 and 7.5  $m/s$  ).

These results confirm the trends shown in Fig. 6.4, providing the equation for each case.

On the active fibre, Fibre #3, during 17.1% of applied elongation, the membrane peak is lower than  $-40mV$  for all the bundle types, with the exception of the BBMY where the peak reaches  $-29.2 mV$ , see Fig. C. 2 (a). Increasing the elongation up to 23.7 %, a voltage plateau of about  $-25 mV$  is reached in the SBMY and BBUN. In contrast, in the BBMY, the voltage plateau is about  $-4.02 mV$  at 32.3%, while it is equals to  $-24.2 mV$  at 49.7% in SBUN, see Fig. C. 2 (a). In Fig. C. 2 (c), the voltage baseline is shifted to about  $-24 mV$  after 23.7% elongation in the SBMY, BBMY and BBUN, while in the SBUN case the same value is reached after 42.5% elongation. Only in the BBMY, the membrane peaks are distinct from the membrane baseline, see Fig. C. 2 (a) and (c). After elongation, the membrane voltage peaks vary between  $-65 mV$  and  $-60 mV$  in both the SBUN and SBMY for all strain values, see Fig. C. 2 (b). In contrast, in the BBMY, the peaks are about  $-45 mV$  for all strains, while, the voltage read in BBUN goes from  $-62 mV$  at 32.3 % strain, up to  $-24 mV$  at 42.5 – 49.7%, see Fig. C. 2 (b). A similar trend is found for the voltage baseline, see Fig. C. 2 (d).

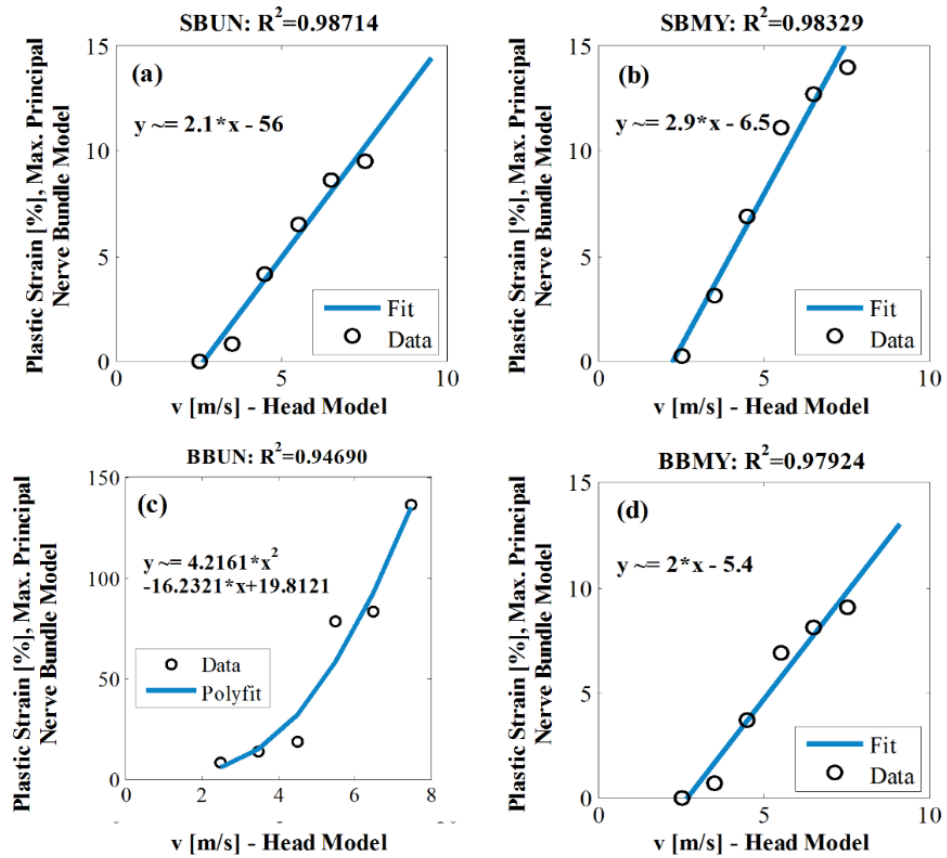


**Fig. C. 1** Variation in the maximum principal value of the plastic strains [%] in the Nerve Bundle Model, read at the nerve membrane, vs. the speed impact values,  $v$  [m/s], used in the frontal head impacts of the Head Model. Regression fits are also shown; the fits refer to SBUN, SBMY, BBUN and BBMY in (a) to (d), respectively.

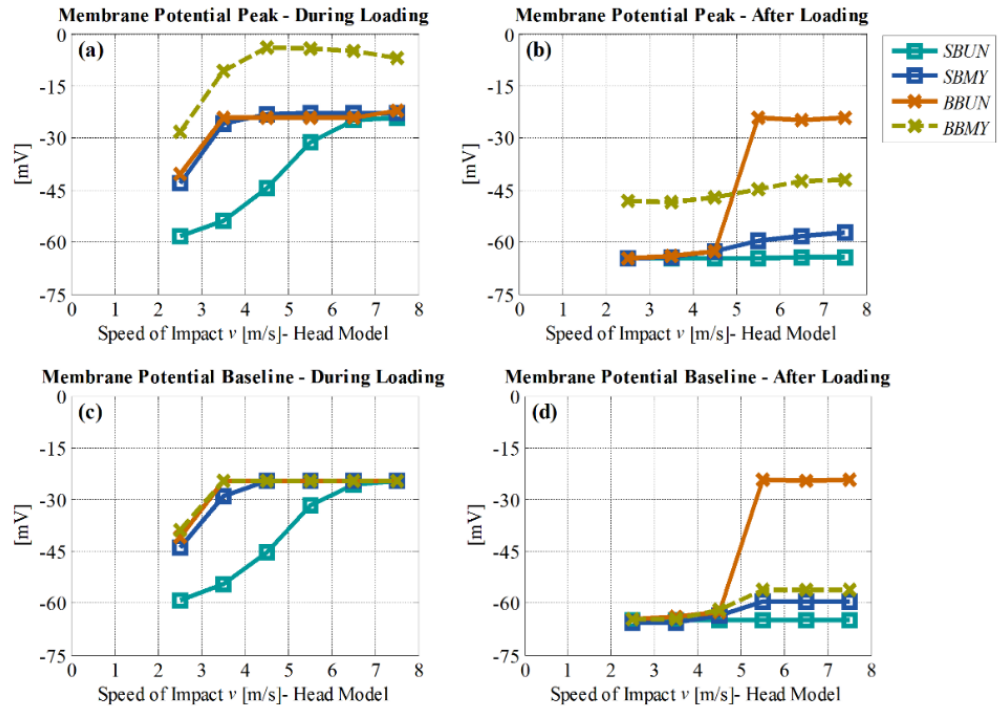


**Fig. C. 2** The membrane potential peak [mv], read at the nerve membrane, vs. the speed of impact values,  $v$  [m/s] used in the Head Model; (a) and (c) show the potential values during elongation, while (b) and (d) show the potential values after elongation. On the top, (a) and (b), are for the membrane potential peak, read on Fibre#3. On the bottom, (c) and (d), are for the membrane baseline.

## Appendix D

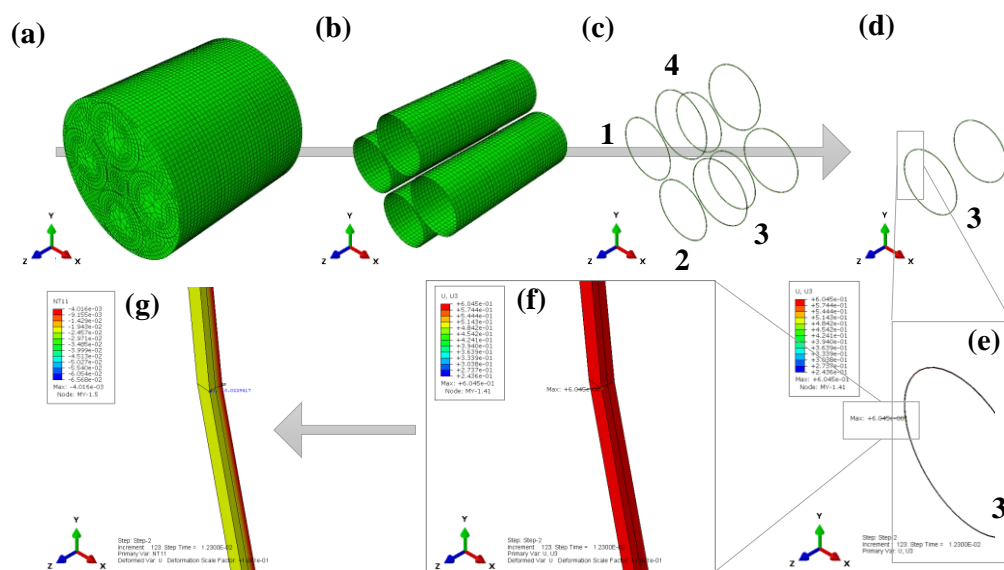


**Fig. D. 1** (a)-(e) selecting the region of interest. In (a), isometric view of the Small Myelinated Bundle (SBMY); in (b), the membrane section that includes the myelin layer and the membrane nodes; in (c), the membrane nodes, and in (d) the membrane nodes of the active fibre, Fibre#3. (e)-(g) extracting nodal quantities when displacement boundary conditions are applied. In (e)-(f), the active membrane nodes at the membrane peak where the maximum refers to the maximum displacement along the  $z$  - axis. In (g), the voltage [V] at the node of interest where the displacement is maximum. Here, (e)-(g) refer to a 30 % applied deformation with  $AC = 0$ .

## Appendix E

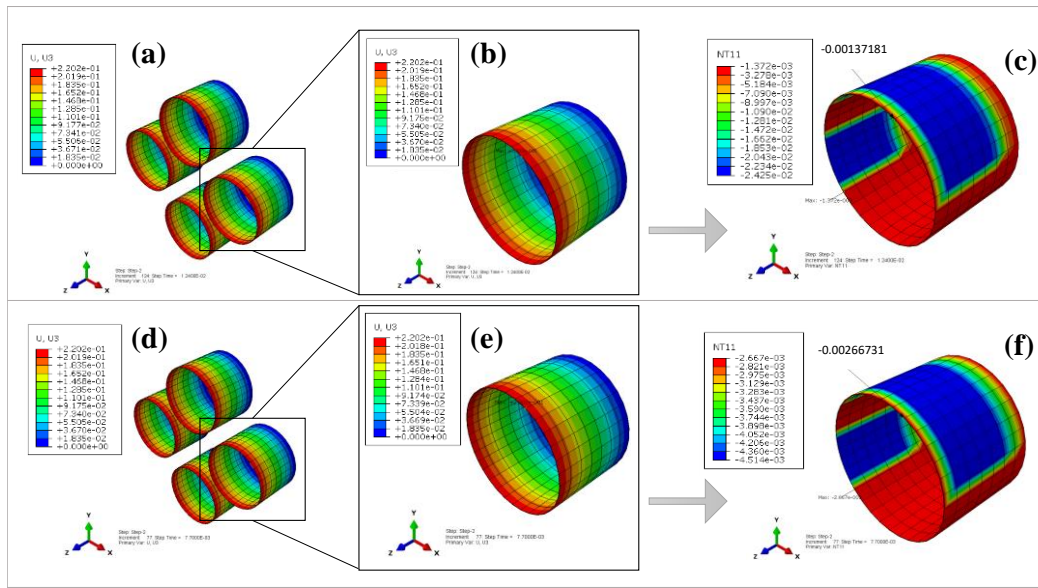


**Fig. E. 1** Data collection procedure: extracting nodal quantities when displacement boundary conditions are applied at the Ranvier's node regions of HCCMY. In (a) and (d) the displacement along the z – axis in the Ranvier's node regions, in (b) and (e) an isometric view of the active node on Fibre #3. In (c) and (f) the voltage [V] distribution on the active node.

## Appendix F

This Appendix refers to Chapter 6, showing insights of the piezoelectric coefficient and generated thermal strains. One section of Ranvier's node only undergoes 5% to 30% elongation. This is a  $0.25 \mu m$  length section, whose radius is equal to  $0.5 \mu m$ . Here, the membrane thickness and the extracellular media thickness are equal to  $3 nm$  and  $20 nm$ , respectively.

The piezoelectric coefficient,  $c$ , is a finite value equal to 0,  $-3.34$  (see Chapter 3 and (Zhang et al., 2001)), and  $-6.68 V^{-1}$ . The extreme values represent the case of an uncoupled electro-mechanical simulation, ( $c = 0$ ), and to the case where the piezoelectric coefficient is the double of the value found in experimental literature, ( $c = -6.68$ ), (Zhang et al., 2001). Although three different coefficient values are chosen, the thickness of the nerve membrane was kept equal to  $3 nm$ , respectively. Fig. F1 (a) and (b) show that varying the piezoelectric coefficient, at the node of maximum displacement, the nodal potential and the plastic strains have similar values in the three cases, while the thermal strain (throughout the thickness of the nerve membrane) are proportional to the piezoelectric value, see Fig. F1 (c).

Fig. F2 shows maximum values found at the nerve membrane during elongation. Here, the membrane potential show similar values in the three cases, see (a). Then, a higher value of the piezoelectric coefficient induces greater plastic strains at the nerve membrane, see Fig. F 2 (b), as the role of the piezoelectricity become significant, see Fig. F 1 (c), so that higher thermal strains lead to higher plasticity for the same elongation value. The value of the total strain is similar when  $c$  is 0 or  $-3.34$ , while are slightly higher when  $c$  is  $-6.68$ , see Fig. F 2 (c). Thus, assuming a zero-piezoelectric coefficient leads to an underestimation of the plastic strains at the nerve membrane, while assuming a greater piezoelectric coefficient would lead to higher plastic and total strain. It is important to notice that any change in the value of the piezoelectric coefficient is linked to a change in the nerve membrane thickness, that here is kept the same for all the three cases.

The results in this Appendix shows slightly different data compared to those in Fig. 6.8, as the data are taken with the same procedure but at a different time step. The Limitation section of Chapter 6 reports the computational limitations of the model HCCMY. Instead, here, one section of the Ranvier's node only undergoes elongation for limiting the computational cost. Here, the data are taken at the peak of the action potential during elongation, while the data in Chapter 6 are taken when the membrane potential is about the maximum value during elongation. As Fig. F 1 and F 2 refer to one fibre only, the generated plastic strain might be different comparing to the case of the nerve bundle because of the neighbouring fibres around Fibre #3 may undergo activation.

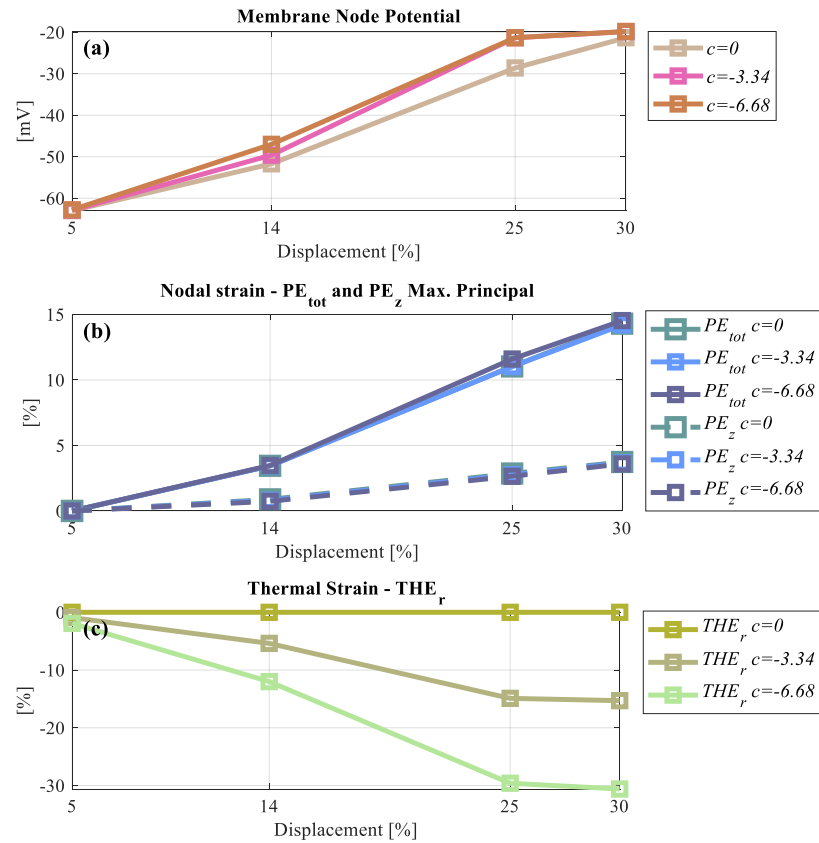


**Fig. F. 1** Data refer to the node at the nerve membrane that undergoes maximum displacement during elongation. (a) show the nodal potential, (b) the max principal value of the total plastic strain,  $PE_{tot}$ , and axial strain,  $PE_z$ , and (c) the thermal strains through the nerve membrane thickness.

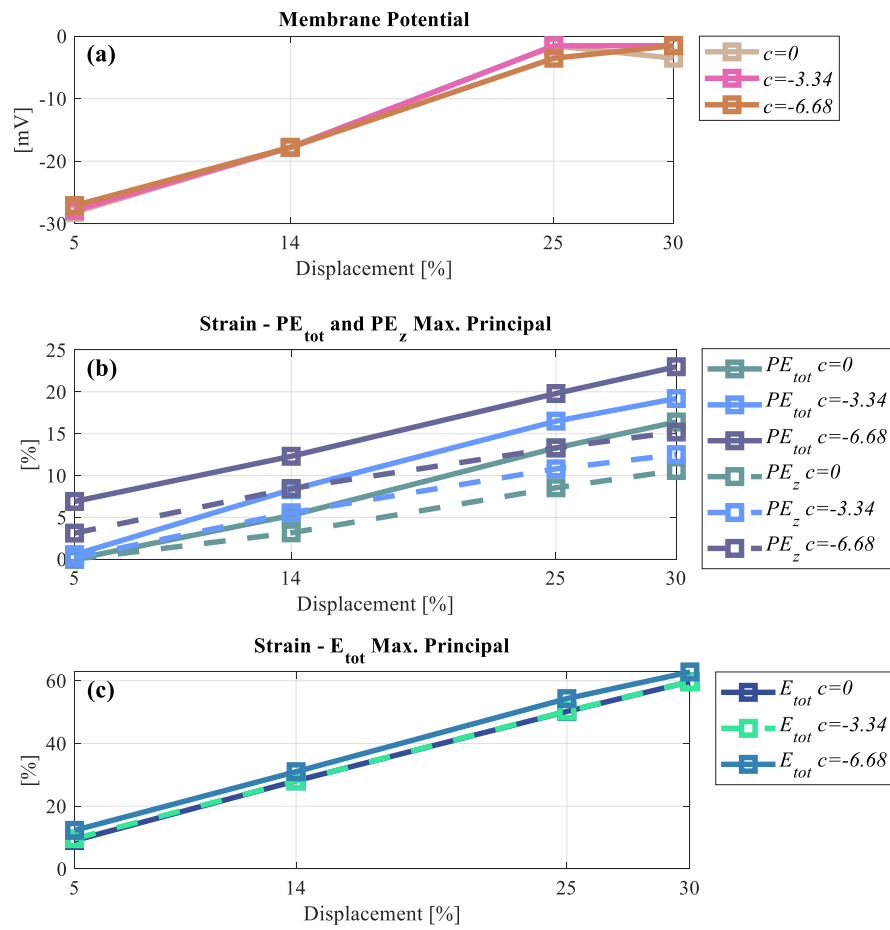


Fig. F. 2 Data refer to the maximum found at the nerve membrane during elongation. (a) show the membrane potential, (b) the max principal value of the total plastic strain,  $PE_{tot}$ , and axial strain,  $PE_z$ , and (c) the total strain,  $E_{tot}$ .

## Acronyms

AP – Action Potential

HH – Hodgkin and Huxley

EQS – Electro-Quasi Static assumption

TBI – Traumatic Brain Injury

DAI – Diffuse Axonal Injury

TAI – Traumatic Axonal Injury

ICM – Intracellular Medium

ECM – Extracellular Medium

SBUN – Small Unmyelinated Nerve Bundle

BBUN – Big Unmyelinated Nerve Bundle

SBMY – Small Myelinated Nerve Bundle

BBMY – Big Myelinated Nerve Bundle

AC – Affected Channels

LS – Left-Shift

PE – Plastic Strain

NE – Nominal Strain

$E_{tot}$  – Total Strain